

# **Impact Crater Formation on the Icy Galilean Satellites**

Veronica J. Bray

Thesis submitted for the degree of Doctor of Philosophy  
And Diploma of Imperial College

Department of Earth Science and Engineering  
Imperial College London

February 2009

For Mum

# Acknowledgements

First and foremost, I would like to thank my PhD supervisors Gareth Collins and Joanna Morgan, who not only helped me through the many facets of completing a PhD, but who also provided me with invaluable experiences and opportunities, which have already helped me on my way. Needless to say, I owe you my career!

This thesis is for my Mum who has helped me every step of the way and made it possible for me to get to where I am. Thank you for your endless encouragement, support and sacrifice. Without you, and the sterling work of Som Gill, I would never have been able to reach for my dreams. A big thanks to my inspiring Big and Bossy sister, Emma, for not getting too impatient when all the rocks I asked you to identify as a 5 year old were flint. Flint or no, I still think you know everything!

Thanks to all those who have helped and advised me academically during my time at Imperial College: notably Mike Warner and Mark Burchell for excellent thesis comments and a relatively pain free viva, Zibi Turtle and Paul Schenk for letting me get my hands on their data, and to Matt Genge, Matt Jackson, Andrew Berry, Phil Bland, Barry Coles, Ralph Lorenz and Richard Ghail, who all know that the most productive science occurs with a drink in one's hand.

I'd also like to express my deepest gratitude to those many family members and friends, both in London and Tucson, who have helped keep me sane(ish) through the years: to Dad, Brian, Lynn, Lucy, Lola and Jill - you are much loved and much missed, to The UCL and Imperial College Crowds (especially Emz, Helen, Ulrike, Margaret, Kate, Ben, Cian, Andy McA., Hannah, Caroline and Susie), The Harrow Lot, The KPG Nutters, The LPL Crowd, The boys from No Anchovies, and finally, I'd like to thank all the hot guys that ran shirtless outside my office window during my final months of write-up – you sure made the time pass more quickly!

# Abstract

The possible existence of liquid water beneath the ice crusts of Ganymede and Europa makes these bodies of great scientific interest as the accessibility of the oceans has implications for astrobiology and future human exploration of the solar system. Study of the cratering trends on these bodies provides one means of assessing the depth of the ice layer above the sub-surface oceans. This work combines observational and numerical modelling data to develop a quantitative model for impact cratering in pure H<sub>2</sub>O ice.

Topographic profiles of craters on Ganymede are presented and used to construct scaling trends, which are then compared to similar trends for the Moon and Mars in order to assess differences in the cratering process in rock, ice and ice-rock mixes. The progression of central peak and central pit crater morphology as crater diameter increases, is used to develop a paradigm for central peak collapse and pit formation on Ganymede.

These observed cratering trends are used to test the results of hydrocode simulation of impact cratering. These simulations were used to determine an appropriate material strength model, and its specific parameters, for the simulation of impact crater formation in un-layered ice. This optimal strength model is then applied to impact cratering in a layered ice and water target. The results from this numerical modelling are compared to the European cratering trends and used to estimate the thickness of Europa's ice crust.

# Contents

<b>1</b>	<b>Introduction to Impact Cratering</b>	<b>15</b>
1.1	Impact Cratering on Rocky Bodies	16
1.1.1.	Simple craters	16
1.1.2.	Flat-Floored and Central Peak Craters	18
1.1.3.	Peak-Ring Craters and Central-Peak Basins	19
1.1.4.	Multi-Ring Basins	21
1.2	The Impact Process	21
1.2.1.	Contact and Compression	22
1.2.2.	Excavation	22
1.2.3.	Modification	23
1.2.4.	Viscous Relaxation	23
1.3	The Effect of Target Properties	28
1.3.1.	Existing lines of Weakness	28
1.3.2.	Original Topography of the Target	31
1.3.3.	Target Layering	31
1.4	Impact Cratering on the Icy Galilean Satellites	32
1.4.1.	Simple and Central Peak Craters	32
1.4.2.	Central Pit Craters	32
1.4.3.	Anomalous Dome Craters	33
1.4.4.	Palimpsests/Europan Macula	33
1.5	The study of Impact Cratering	35
1.5.1.	Observational Data Analysis	35
1.5.2.	Experimental Data	40
1.5.3.	Thesis Structure	41

<b>2</b>	<b>The Comparison of Craters on the Moon and Ganymede</b>	<b>43</b>
2.1	Introduction to Topographic Profiling Techniques ... ..	44
2.1.1.	Stereo Image Analysis ('Stereo Photogrammy') ... ..	46
2.1.2.	Photoclinometry (PC)/shape-from-shading in 2 Dimensions ...	46
2.2	Method ... ..	47
2.3	General Cratering Trends ... ..	49
2.3.1.	Depth-Diameter Ratios ... ..	49
2.3.2.	Rim Heights ... ..	52
2.3.3.	Crater Wall Slopes ... ..	54
2.4	Central Peak Craters ... ..	55
2.4.1.	Central Peak Dimensions ... ..	55
2.4.2.	All Peaks are Created Equal, but Some are More Equal Than Others	61
2.4.3.	The Development of Central Peaks ... ..	63
2.5	Transitional Crater Morphology ... ..	64
2.5.1.	Smooth-Floored Craters ... ..	64
2.5.2.	The Odd Couple – Gula and Achelous ... ..	65
2.6	Observational Summary and Implications ... ..	67
2.6.1.	Degree of Crater Collapse ... ..	67
2.6.2.	Effective Strength of the Target ... ..	68
2.6.3.	Central Peak Development ... ..	68
2.6.4.	Implications for Numerical Modelling ... ..	69
<b>3</b>	<b>The Enigma of Central Pits</b>	<b>71</b>
3.1	Introduction to Central Pit Craters ... ..	72
3.1.1.	Occurrence on Mars ... ..	73
3.1.2.	Occurrence on Other Rocky Bodies ... ..	73
3.2	Formation of Central Pits ... ..	76
3.2.1.	Impact into a Layered Target ... ..	76
3.2.2.	Collapse of a Central Peak in Weak Ice ... ..	77
3.2.3.	Explosive Release of Volatiles ... ..	77
3.2.4.	Draining of Impact Melt ... ..	79
3.3	Observational Data for Central Pits ... ..	79
3.3.1.	Pit Diameters ... ..	80
3.3.2.	Pit Depth and Volume ... ..	83
3.3.3.	Pit Summit Relations ... ..	83
3.4	The Continuing Trends of Central Features ... ..	86
3.5	Additional Features of Central Pit Craters ... ..	89
3.6	Summary and Implications ... ..	91

3.6.1.	Pit Growth in Different Materials	...	...	...	...	91
3.6.2.	Pit and Summit Formation	...	...	...	...	92
3.6.3.	Life After 30 (km)	...	...	...	...	93
3.6.4.	A Model of Pit Formation	...	...	...	...	94
<b>4</b>	<b>Introduction to the iSALE Hydrocode</b>					<b>98</b>
4.1	Modelling impact Cratering with iSALE	...	...	...	...	99
4.1.1.	Numerical Representation of Time and Space	...	...	...	...	100
4.1.2.	The Equation of State (EoS)	...	...	...	...	102
4.1.3.	Constitutive Model I – Static Strength	...	...	...	...	104
4.1.4.	Constitutive Model II – Additional Weakening During Impact	...	...	...	...	107
4.1.5.	Testing and Continuing Code Developments	...	...	...	...	113
4.2	Updating iSALE for Modelling Impact into Ganymede	...	...	...	...	114
4.2.1.	The Tillotson EoS for Ice	...	...	...	...	114
4.2.2.	Development of an Alternative EoS for Ice	...	...	...	...	117
4.2.3.	The Constitutive Model for Ice	...	...	...	...	120
4.3	Summary	...	...	...	...	123
<b>5</b>	<b>Modelling Crater Formation in Ice</b>					<b>125</b>
5.1	Modelling Impact into Ganymede - Approach	...	...	...	...	126
5.1.1.	Preparation: Reducing Errors and Run-Time	...	...	...	...	126
5.1.2.	Impactor Properties	...	...	...	...	128
5.1.3.	Initial Target Conditions	...	...	...	...	132
5.1.4.	Weakening During Impact	...	...	...	...	132
5.1.5.	Comparison to Observations	...	...	...	...	133
5.2	Comparing Strength Models	...	...	...	...	133
5.2.1.	Empirical Model Results	...	...	...	...	135
5.2.2.	Acoustic Fluidization Model Results	...	...	...	...	137
5.2.3.	Summary and Discussion of Model Suitability	...	...	...	...	138
5.3	Model Sensitivity to EoS and Strength Parameters	...	...	...	...	141
5.3.1.	Sensitivity to Acoustic Fluidization Parameters	...	...	...	...	141
5.3.2.	Effect of the Equation of State	...	...	...	...	144
5.4	Modelling Summary and Implications	...	...	...	...	146
<b>6</b>	<b>Strength Model Scaling for Pure Ice</b>					<b>149</b>
6.1	Approach	...	...	...	...	150
6.1.1.	Determining the Scaling Trend for Pure Ice	...	...	...	...	150
6.1.2.	Testing the Scaling Trend	...	...	...	...	151

6.2 Results	152
6.2.1. Development of the Strength Model Scaling	152
6.2.2. Testing the Strength Model I – The Simple-to-Complex Transition	159
6.2.3. Testing the Strength Model II – Extension to Larger Crater Sizes	161
6.3 Summary and Implications	165
6.3.1. Parameter Scaling	165
6.3.2. Recreating Observed Central Peak Crater Morphology	167
6.3.3. Modelling Simple craters and the S-C Transition	168
6.3.4. Central Peak Development – Basal Collapse Modelled	168
6.3.5. The Need for Material Layering	169
<b>7 Modelling Impact into Europa</b>	<b>170</b>
7.1 Introduction to Europa	171
7.1.1. Planetary Setting	171
7.1.2. The Importance of Ice Thickness - Implication for Astrobiology	172
7.2 How Thick is Europa’s Crust?	173
7.2.1. Estimates from Gravity and Magnetic Data	174
7.2.2. Estimates from Heat Flow Data and Visco-Elastic Deformation	175
7.2.3. Rafts, Diapirs and Cycloidal Patterns	176
7.2.4. The Role of Impact Craters in Determining Ice Thickness	178
7.2.5. The Nature of Europa’s Upper Layers	179
7.3 Approach to Modelling Impact into Europa	180
7.3.1. Target Set-Up – Introduction of a Material Layer	181
7.3.2. Material Properties for Impactor and Target	183
7.3.3. Comparison to Observations	183
7.4 Results	184
7.4.1. Simulation of a ~ 14 km Crater on Europa	184
7.4.2. Comparison to the European Cratering Trend	186
7.5 Summary and Implications	188
7.5.1. How Thick is Europa’s Crust?	188
7.5.2. ...5km ...Really?	189
7.5.3. Comparison to Other Ice Thickness Estimates	189
<b>8 Conclusions</b>	<b>190</b>
8.1 Ganymede Observations	191
8.1.1. Central Peaks Form Via Floor Uplift, Not Rim Collapse	
8.1.2. Central Peaks Collapse to Form Peak-Rings, Even on the Icy Satellites	192
8.1.3. Central Pits – The Enigma Remains	193
8.2 Bridging the Gap – A Message to Modellers	193
8.2.1. Match Results to Fresh Crater Depths and Average Wall Slope Trends	194

8.2.2.	Recreate the Correct Style of Peak Formation	...	...	...	194
8.2.3.	Model Peak and Peak-Ring Development Separately From Pit Formation	...	...	...	195
8.3.	Numerical Modelling of Impact into Ice	...	...	...	195
8.3.1.	The A. F. Model Recreates the Correct Morphology, Block Size and Peak Formation Mechanism	...	...	...	195
8.3.2.	Model Improvement is Still Required	...	...	...	196
8.3.3.	Europa's Crustal Thickness is Estimated to be ~ 5 km	...	...	...	197
8.4.	Future Work	...	...	...	197
8.4.1.	Advancing the Reliability of Hydrocode Modelling of Icy Impacts	...	...	...	198
8.4.2.	Continued Acquisition of Observational Data	...	...	...	198
8.4.3.	Combined Modelling and Observational Projects	...	...	...	199
8.5.	Statement of Achievement/Contribution	...	...	...	200
<b>Appendices</b>					<b>202</b>
Appendix A	Database of Ganymede Crater Profiles	...	...	...	202
Appendix B	Program to Compute the Hugoniot of Ice	...	...	...	244
Appendix C	Section of iSALE Script Implementing the Relationship of Melting Temperature with Ambient Pressure	...	...	...	247
<b>Bibliography</b>					<b>248</b>

# List of Figures

1.1.	Sketched profiles of a typical simple and central peak crater	...	...	17
1.2.	Images of lunar complex craters (flat-floored, central peak, peak-ring, multi-ring)			19
1.3.	A series of Magellan images showing peak-ring craters on Venus	...	...	20
1.4.	Examples of ‘central peak basins’ on the Moon	...	...	21
1.5.	Diagrams illustrating the different stages of the impact process	...	...	24
1.6.	Image and Sketched outline of Meteor Crater in Arizona	...	...	29
1.7.	Sketches and an example image of different crater morphologies produced by variations in lunar regolith layer thicknesses	...	...	30
1.8.	Image and sketched topographic profile of a summit pit crater on Mars displaying a multiple layer ejecta blanket	...	...	31
1.9.	Mosaic showing the variety of complex crater morphologies observed on Ganymede	...	...	34
1.10.	Depth-diameter relationship for impact craters on Earth in sedimentary and crystalline targets	...	...	36
1.11.	Depth-diameter plot of craters on Ganymede	...	...	38
1.12.	Crater diameter at the simple-to-complex transition on the terrestrial planets and the icy Galilean satellites	...	...	39
2.1.	The process of profile collection	...	...	45
2.2.	Diagram illustrating the measured crater dimensions	...	...	48
2.3.	Depth-diameter plot of craters included in this work	...	...	50
2.4.	The relationship between crater diameter and rim height	...	...	53

2.5.	The relationship between crater diameter and wall slope on the Moon and Ganymede ... ..	54
2.6.	Image and topographic profile of a typical central peak crater on Ganymede	56
2.7.	The relationship between crater diameter and central peak dimensions ...	57
2.8.	Relative central peak dimensions on Ganymede ... ..	58
2.9.	Approximate volumes of the central peaks in Ganymede craters ... ..	60
2.10.	The relationship between crater diameter and central peak slope on Ganymede and the Moon ... ..	60
2.11.	Examples of central peak craters with anomalous central peaks ... ..	62
2.12.	The paradigm of central peak collapse ... ..	63
2.13.	Image and topographic profile of a smooth-floored crater ... ..	64
2.14.	Images and topographic profiles of The Odd Couple – Gula and Achelous ...	65
3.1	Images of central pit craters on Ganymede and Mars ... ..	72
3.2	Image of the Lansberg crater on the Moon ... ..	74
3.3	The Serra da Cangalha and Gosses Bluff impact structures on Earth ...	75
3.4	Ponded-pitted material within the Tooting crater on Mars ... ..	78
3.5	Diagram illustrating the additional measurements made for pit craters ...	79
3.6	Images and topographic profiles of the summit pit craters included in this work	80
3.7	The relationship between crater diameter and pit diameter ... ..	82
3.8	The relationship between crater diameter and pit depth ... ..	84
3.9	The relationship between crater diameter and pit volume ... ..	84
3.10	The relationship between crater diameter and summit diameter ... ..	85
3.11	The relationship between summit volume and pit volume ... ..	85
3.12	The relationship between crater diameter and central feature width ... ..	87
3.13	The relationship between crater diameter and central feature height ... ..	87
3.14	The relationship between crater diameter and central feature volume ...	88
3.15	The relationship between crater diameter and central feature slope ... ..	88
3.16	Images and topographic profiles of the central pit craters included in this work that display an internal ring ... ..	90
3.17	The relationship between crater diameter and internal ring diameter on Ganymede and terrestrial bodies ... ..	91
3.18	The paradigm of summit pit and internal ring formation ... ..	95
3.19	The paradigm of floor pit formation ... ..	96
4.1	Schematic illustration of a one-dimensional hydrocode computation ...	101

4.2	The treatment of mixed material cells by the iSALE hydrocode	...	...	102
4.3	Variance in net pressure with time within a fragmented rock mass in response to acoustic waves – the mechanism of Acoustic Fluidization	...	...	109
4.4	A mathematical approximation of Acoustic Fluidization – The Block Model			112
4.5	The observed Hugoniot curve for water ice	...	...	115
4.6	Hugoniot curve computed using the Tillotson equation of state	...	...	117
4.7	Comparison of computed Hugoniot curves	...	...	118
4.8	Comparison of the Hugoniot produced using the Tillotson and the Third-Order Tillotson equation of state	...	...	119
4.9	Ice strength as a function of pressure for fractured and intact ice	...	...	120
4.10	Variation of ice strength with ambient temperature	...	...	121
4.11	Melting temperature of ice at different pressures	...	...	122
5.1	Effect of different resolution on simulated crater morphology	...	...	127
5.2	Effect of different mesh size on simulated crater morphology	...	...	129
5.3	Effect of impact velocity on simulated crater morphology	...	...	131
5.4	Final crater profiles produced using the empirical and A.F. models	...	...	134
5.5	Empirical model results – simulation stills	...	...	136
5.6	Acoustic Fluidization model results – simulation stills	...	...	138
5.7	Depth-diameter and wall slope variation with change in A.F. parameters	...		141
5.8	Rim height variation with change in A.F. parameters	...	...	142
5.9	Central peak width and height variation with change in A.F. parameters	...		142
5.10	Sensitivity of final crater profiles to changes in A.F. parameters	...	...	143
5.11	Comparison of simulation results using different equations of state	...	...	145
5.12	Post-impact temperature at the crater centre using different equations of state			146
6.1	Establishing a suitable decay time for a 300 m projectile	...	...	151
6.2	Best-fit simulation results of 3.5 to 17.5 km craters	...	...	153
6.3	Depth-diameter of simulated craters	...	...	154
6.4	Comparison of observed and simulated rim heights	...	...	155
6.5	Comparison of observed and simulated wall slopes	...	...	156
6.6	Comparison of observed and simulated central feature size	...	...	157
6.7	Trends in the best-fit A.F. parameters	...	...	158
6.8	Simulated simple crater result	...	...	160
6.9	Comparison of Ganymede crater depth trend and simulation results	...		161
6.10	Comparison of transient central uplift and final central peak dimensions	...		162

6.11	A series of simulation stills showing the decay of the A. F. region with time	164
6.12	Block model scaling for lunar and Ganymede craters ... ..	167
7.1	Images of the Galilean satellites ... ..	171
7.2	Comparison of terrestrial ice rafting and European chaos ... ..	172
7.3	Ice thickness variation over time since Europa's entrance into the orbital resonance with Io and Ganymede ... ..	175
7.4	Cycloidal double ridges on Europa ... ..	177
7.5	Galileo image of the Cilix crater ... ..	178
7.6	Simplified illustration of Europa's crustal structure ... ..	180
7.7	Example mesh used for Europa simulations ... ..	181
7.8	Radial profiles of craters produced by simulated impact into different ice depths	185
7.9	Comparison of European crater depth trend and simulation results – 14 km crater	186
7.10	Comparison of European crater depth trend and simulation results – all results	187

## List of Tables

2.1.	Description of the crater types profiled in the course of this work	...	...	51
2.2.	Summary of scaling trends for the Moon and Ganymede	...	...	59
3.1	Central Pit Scaling Trends for Mars and Ganymede	...	...	86
4.1	Tillotson Equation of State Parameters for Water and Ice Ih	...	...	116
4.2	Material Properties Employed for the Simulations Presented in Chapter 5	...	...	123
5.1	Impactor Properties and Best-fit Strength Model Parameters for a 15 km Crater	...	...	134
5.2	Final Crater Dimensions Simulated Using Different Equations of State	...	...	135
6.1	Best-fit Simulated Crater Dimensions	...	...	154
6.2	Best-fit Acoustic Fluidization Parameters	...	...	159
6.3	Best-fit Acoustic Fluidization Parameters Predicted Using Scaling Trends	...	...	159
6.4	Block Sizes Predicted from Best-fit Viscosities	...	...	166
7.1	Summary of crustal thickness estimates	...	...	174
7.2	Calculation of Target Heat Flow for Different Crustal Thicknesses	...	...	182
7.3	Depth-Diameter Measurement of Simulated Craters	...	...	187

# Chapter 1

## Introduction to Impact Cratering

Knowledge of the interior structure of solar system bodies is vital for theories of planetary formation and evolution. These in turn provide clues to early solar system processes. For planetary bodies on which sub-surface profiling is not viable, one of the most powerful means of investigating the near-surface properties is the study of impact craters. Impact cratering is a fundamental process affecting the surfaces of all the solid bodies in the solar system. It is a highly complex process that depends upon not just the size, velocity and composition of the impacting body, but also the gravity, material properties and structure of the target. As a result, craters offer direct probes of a body's sub-surface and allow near-surface structure to be inferred on the basis of their morphology.

The exotic morphologies observed for complex craters on the icy Galilean moons are thought to be due to the icy lithospheres being mechanically distinct from terrestrial crusts; the presence of shallow sub-surface liquid layers is another likely factor (Moore et al., 2001; Turtle and Pierazzo, 2001; Schenk, 2002). In the search for liquid water in our solar system, icy bodies with liquid water layers beneath their ice crusts are receiving increasing attention. Indeed, one of the continuing debates of outer solar system research centres on the thickness of Europa's ice crust as it affects both the habitability and accessibility of its sub-surface ocean (Gaidos et al., 1999; Chyba, 2000) and may subsequently have implications to human exploration of the solar system. Many attempts have been made to estimate or measure its thickness using a variety of different techniques, as discussed in Chapter 7. One such technique is the study of impact crater morphology (e.g. Turtle and Pierazzo, 2001; Schenk,

2002) as the upper crustal layering affects crater formation and thus the final morphology of craters.

Before the morphologies created as a result of sub-surface layering can be de-convolved from those occurring as a direct result of the cratering process in ice, the cratering process itself must be understood. Developing our understanding of impact crater formation in ice requires a means to recreate the impact process under controlled conditions so that the factors affecting the process can be assessed. It is also necessary that sufficient observational data exist to validate experimental results.

This thesis includes both an observational and a numerical modelling component to advance and compliment existing work, allowing more accurate modelling of impact cratering in ice targets. New topographic data is collected for the Jovian moon of Ganymede and used to test numerical modelling of impact crater formation in unlayered ice. Once scaling trends and material models for cratering in pure ice have been established, the same strength model is applied to modelling impact into layered ice and water targets and the results compared to cratering trends on Europa. Results are used to estimate the thickness of Europa's crust and to evaluate whether a Ganymede-based strength model can be applied to modelling impact into Europa. This chapter provides an introduction to the cratering types found on rocky and icy bodies, the underlying processes that create such a range of impact crater morphologies and outlines the techniques used to study them.

## **1.1. Impact Craters on Rocky Bodies**

On silicate/rocky targets, craters typically follow a morphologic progression with increasing crater size. This size-morphology progression was first recognised for lunar craters by Gilbert (1983) and begins from simple, bowl-shaped craters to larger complex craters with a range of morphologies. The crater types commonly seen on rocky bodies are outlined in this section for later comparison with the more exotic crater forms found on the icy satellites.

### **1.1.1. Simple Craters**

Simple craters are bowl-shaped (Figure 1.1A), rimmed pits ranging in size from centimetre scales up to tens of kilometres and are created by the impact of a projectile moving at speeds exceeding a few kilometres per second. The slope of the crater wall is steepest close to the rim, decreasing in slope angle smoothly towards the crater centre forming an almost parabolic profile to the crater (Dence, 1973). As collapse of small cavities is governed by the internal friction of the target rocks, simple craters display an average rim slope roughly equal to the

angle of repose of the target material ( $\sim 30^\circ$  for dry sand) independent of gravity (Melosh, 1986; Ji and Shen, 2006).

The rim-to-floor depth of simple craters is generally 0.2 times the rim-to-rim diameter (Pike, 1977) and is shallower than the transient crater (see 1.2.2) from which they form. This is due to the presence of a basal breccia lens which can range in volume from 40% (Brent Crater, Grieve, 1978) to 70% (Meteor Crater, Roddy et al., 1975) of the total crater volume (Figure 1.1A). The lens of Meteor Crater in Arizona, USA is composed from a mix of rocks from all layers intersected by the crater (Shoemaker, 1963), indicating that collapse from the crater walls contributes to the breccia lens formation.

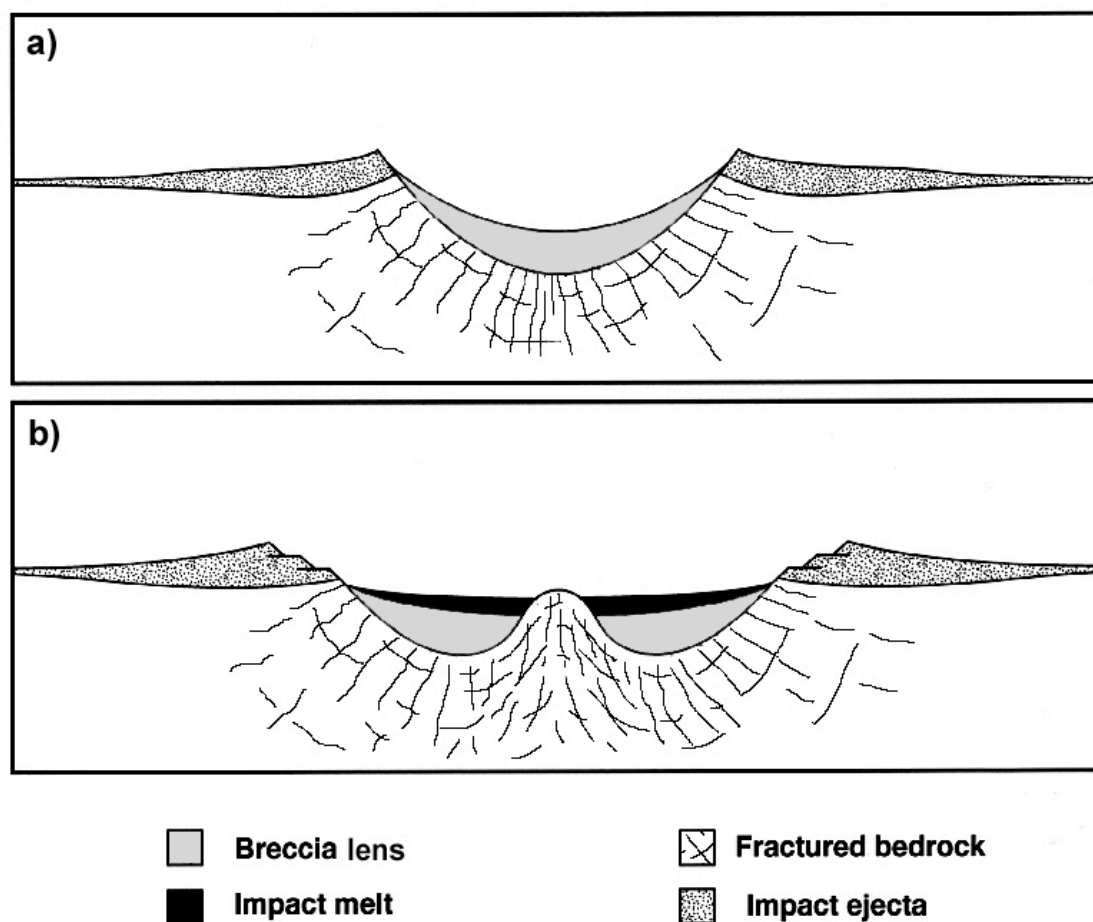


**Figure 1.1:** Sketched profiles of a typical A) simple crater and B) central peak crater. The breccia lenses are composed of a mix of impact melt and fragments of target rock. A representative number of radial and concentric fractures have been marked; fractures are more closely spaced close to the impact point.

The rims of simple craters created by hyper-velocity impact rise above the pre-impact surface with a height equal to about 4% of the crater diameter (Melosh, 1989). Craters produced by the impact of slower-moving ( $< 1 \text{ km s}^{-1}$ ) projectiles tend to be more irregular in profile and have broader rims that are less well defined. For example, ‘secondary’ craters created by the low velocity impact of ejecta from a larger ‘primary’ crater display broader, subdued rims and can be distinguished from small primaries on this basis. There is no lower limit to the size of simple craters and lunar simple craters have been recorded for crater diameters of  $\sim 15 \text{ km}$  down to the limit of resolution. The transition between simple to complex crater morphologies occurs at crater diameters inversely proportional to the target body’s gravity (see 1.5.1).

### 1.1.2. Flat-Floored and Central Peak Craters

As impactor size increases, the excavation of material during impact reaches greater depths within the target. Without a large enough strength at depth, the material pushed down during a large impact may begin to rebound after it reaches its maximum depth to form a variety of interior morphologies not present in smaller craters (Melosh and Ivanov, 1999).

Above crater diameters of  $\sim 15 \text{ km}$  on the Moon, the interior walls of the crater become steeper, close to the angle of repose, joining a floor that is flattened relative to simple craters. Figure 1.2A shows an example of this type of ‘flat-floored’ crater; the rim-wall landslide deposits are one indication of more significant collapse than that occurring during simple crater formation. Such rim collapse occurs on a large scale, often forming internal terraces (Pearce and Melosh, 1986).

At slightly larger diameters the rebound of the crater floor produces more notable central features. Central peaks occur in craters with diameters between 20 and 140 km on the Moon, and are characterised by central uplifts protruding from their flat floors (Figure 1.1B and 1.2B). The diameter of the central peak ( $D_{cp}$ ) increases with crater diameter ( $D$ ), (Pike, 1985):

$$D_{cp} = 0.22D. \quad (1.1)$$

Investigation into Terrestrial central peak craters suggests that the flat floors are produced by breccia infill of the annular trough between peak and rim (Dressler and Sharpton, 1997) (Figure 1.1B). The lack of breccia in the central peak itself indicates that the uplift of the central region occurs rapidly, before debris has had time to slide from the crater walls.

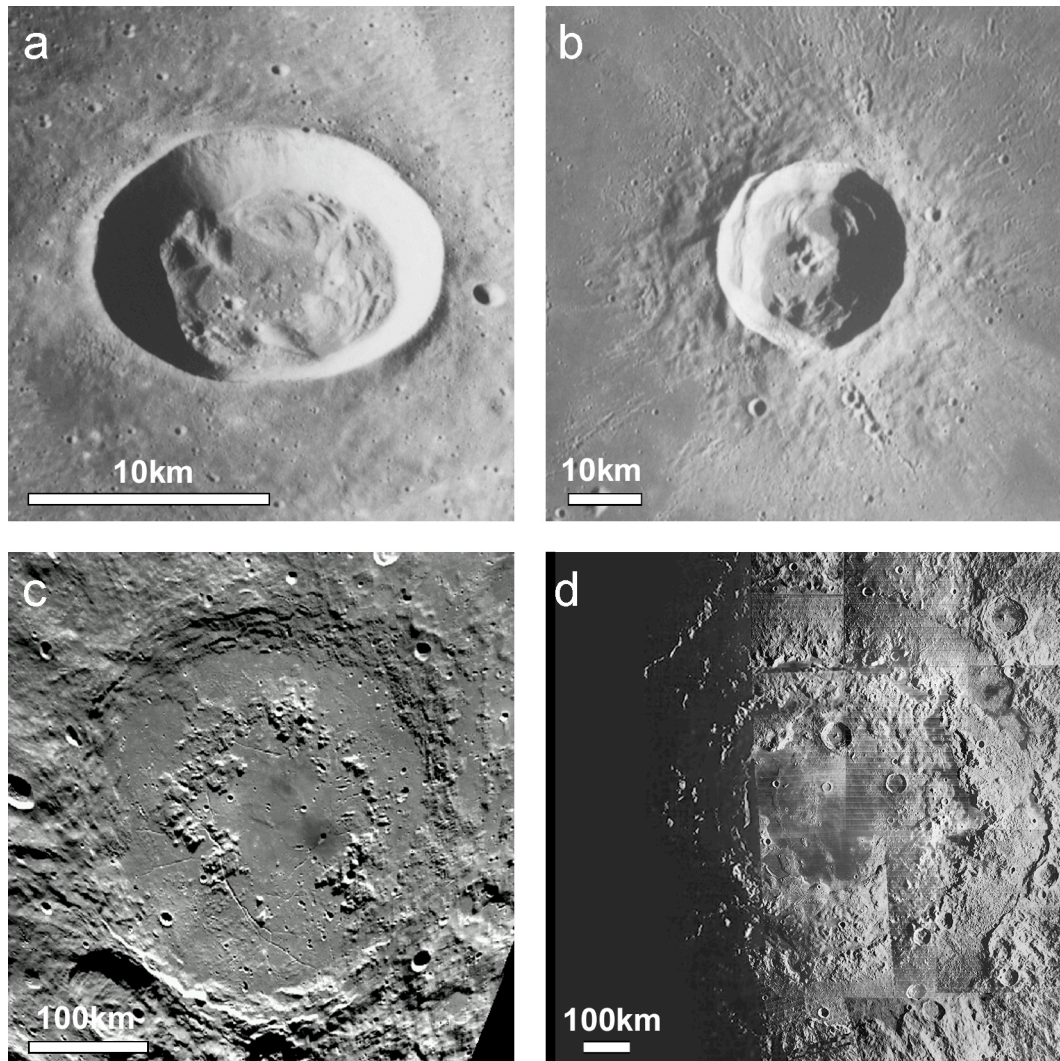


**Figure 1.2:** Images of lunar complex craters. A) The 17 km flat-floored Bessel crater (Apollo image AS15-9328), B) Euler, a 28 km central peak crater (Apollo image AS17-2922). C) Schrödinger, a 320 km peak-ring crater (Mosaic of Clementine images. Image processing by Ben Bussey). D) The Orientale impact basin, ~ 930 km in diameter (Mosaic of Lunar Orbiter IV images. Image processing by Stefan Lammel).

### 1.1.3. Peak-Ring Craters and Central Peak Basins

As crater diameter increases, central peak craters develop into peak-ring craters which display a concentric ring of raised massifs within the crater (Figure 1.2C). On the Moon, peak-ring craters are recorded over crater diameters of 140 to 450 km and contain inner rings with diameters ( $D_i$ ) that are approximately half of the crater diameter,  $D$  (Wood and Head, 1976). The transition to peak-ring morphology occurs at smaller crater diameters on Venus and peak-rings are documented over crater diameters of 30 to 270 km. Although the onset of peak-ring formation differs for bodies of different gravity, similar to the simple-to-complex (s-c)

transition, the diameter of peak-rings is commonly half the rim-to-rim crater diameter on all the terrestrial planets (Melosh, 1989):

$$D_r \approx 0.5 D. \quad (1.2)$$

An alternative  $D_r/D$  trend has been proposed for Venus by Alexopoulos and McKinnon (1994) who suggest that  $D_r/D$  ratio increases with growing crater diameter, as depicted in Figure 1.3. They record an increase of  $D_r/D$  from  $\sim 0.2$  for the smallest peak-ring craters on Venus (30 to 35 km in diameter) to  $\sim 0.8$  for craters above 70 km in diameter. The increasing  $D_r/D$  ratio apparent to Alexopoulos and McKinnon (1994) has been used to support the hypothesis that peak-rings form from the dynamic collapse, downward and outward, of an unstable central peak. The occurrence of peak-rings so consistently after central peaks in the size-morphology progression of craters on terrestrial bodies indicates that this morphological progression is a direct consequence of the impact cratering process rather than due to variation of target properties.

The transition from central peak to peak-ring morphologies is gradual; taking place over some 100 km on the Moon. During this transition, craters can have central peaks, peak-rings or both. Hartmann and Wood (1971) class craters that show both a peak and inner ring as ‘central peak basins’. Craters with this ‘transitional’ morphology are observed on the Moon, Mars and Mercury (Alexopoulos and McKinnon, 1994). Figure 1.4 shows two end member examples on the Moon.

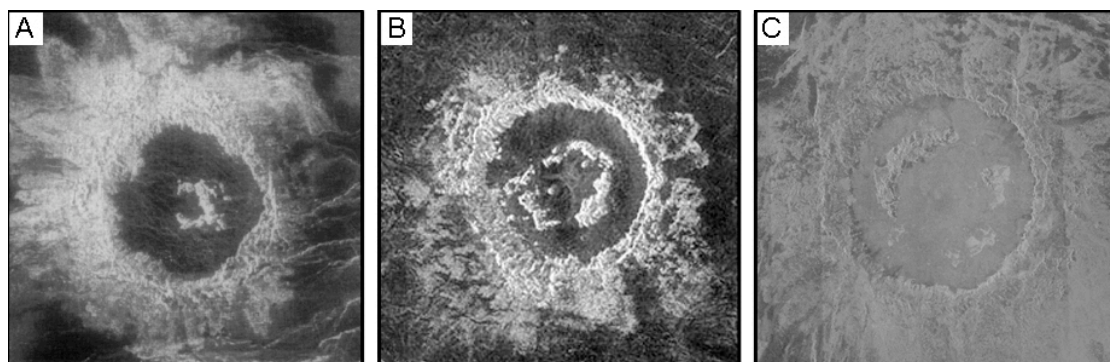


**Figure 1.3:** A series of Magellan images showing peak-ring craters on Venus. A) The 48.5 km Cunitz with an approximate inner ring diameter of 10.8 km. B) Barton, a 50 km crater with an inner ring diameter of 23 km. C) Greenaway, a 92.3 km crater with an inner ring 45.6 km in diameter. The  $D_r/D$  ratios for examples A, B and C are 0.22, 0.46 and 0.49 respectively.

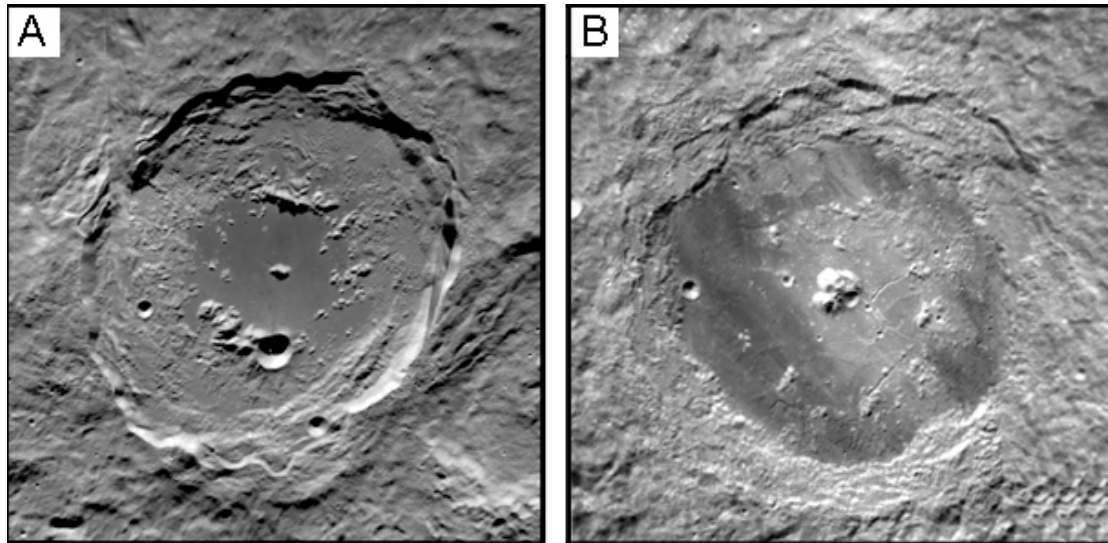


**Figure 1.4:** Examples of ‘central peak basins’ on the Moon. A) Anroniadi is a 143 km wide crater with a small peak, surrounded by an incomplete ring of peaks and hills with a diameter of 65 km. B) Compton, a 165 km diameter crater with the opposite transitional morphology from Anroniadi - a strong central peak with an 80 km wide ring of small and widely spaced peaks. The distribution of lava/melt is also different between the two craters: surrounding the peak in the centre of Anroniadi, while filling the annular trough between ring and rim of Compton.

#### **1.1.4. Multi-Ring Basins**

The next transition in the traditional size-morphology progression is the development of multi-ringed basins (Figure 1.2D) which possess at least two asymmetric, inward-facing scarped rings, one of which may be the original crater rim (Hartmann and Wood, 1971; Spudis et al., 1984). The transition to multi-ring basins occurs at crater diameters of  $\sim 450$  km on the Moon and does not follow the  $1/g$  dependence, indicating that the process initiating multi-ring basin formation differs from that controlling the earlier transitions in morphology. The exact morphology of multi-ring structures varies spatially and on different bodies when compared to the typical basin morphology recorded for the Orientale basin on the Moon (Figure 1.2D) (Wieczorek and Phillips, 1999). Thus, multi-ring basins are likely to be affected by differences in crustal structure and composition (Melosh and McKinnon, 1978). Other morphologies created as a result of target variation are presented later in this chapter.

## **1.2. The Impact Process**

Before further discussing the effects of target structure on impact crater morphology, it is helpful to review current understanding of the impact process itself and introduce terminology

and ideas. Despite being a continuous process, it is convenient to divide impact crater formation into 3 stages, each governed by a different set of physical phenomena.

### **1.2.1. Contact and Compression**

On airless bodies, the first stage of impact cratering begins when the projectile contacts the target surface. During the contact and compression phase the majority of the projectile energy is transferred to the target, leading to heating, compression and acceleration of target material away from the point, or points (for irregular impactors), of impact. The projectile itself is simultaneously heated and decelerated. The rapid momentum change generates a supersonic shockwave that expands, propagating away from the impact point, into both the projectile and target.

Shock pressures developed during these early stages generally reach hundreds of GPa (Ahrens and O'Keefe, 1977), exceeding the yield strength of both projectile and target. Unloading from such pressures causes melting and/or vaporization of material. The contact and compression stage is considered to end when the projectile has unloaded from this high pressure (Melosh and Ivanov, 1999). The duration of the contact and compression stage is dependent on the projectile's composition, size and impact velocity and only lasts ~ 1 second, even in large impacts.

### **1.2.2. Excavation**

The passage of the shockwave through the target leaves the material behind it in motion, leading to a flow of material away from the point(s) of impact. Once initiated, this 'excavation flow' continues independent of the shockwave to open up a hemispherical cavity – the transient crater (Figure 1.5D). Calculations and laboratory experiments suggest that on cessation of the excavation flow, the transient crater is approximately a paraboloid of revolution (Dence, 1973) with a depth-diameter ratio between 0.25 and 0.33 (Melosh, 1989). The excavated material is deposited outside the crater to form the rim, and more distantly as the ejecta blanket.

During the contact and compression stage, stresses are high enough that material strength can be ignored. However, as the stresses in the target material lessen during the excavation stage, the growth of the transient crater becomes retarded by any retained cohesive strength and dry friction within the target, and by gravity (Collins, 2002). In large impact events the gravity is the most significant factor, halting the excavation when insufficient energy remains to lift the target material against its own weight (Nolan et al. 1996). It is estimated that the excavation stage lasts seconds to minutes depending on event size (Melosh, 1989). After this, the forces retarding the excavation flow begin to collapse and modify the transient crater.

### 1.2.3. Modification

The transient crater is gravitationally unstable – it has an internal mass deficit and mass excess at the rim. Collapse of this crater under gravity brings the region back towards equilibrium and will occur when the residual material strength ( $Y$ ) is exceeded by the stresses ( $\sigma$ ) causing the crater to collapse (Melosh and Ivanov, 1999). As fully fractured rock has little or no cohesive strength, the collapse of small transient cavities is controlled primarily by the internal friction of the target rocks (Schmidt and Housen, 1987; Ivanov and Kostuchenko, 1998). In larger impact events, the departure from gravitational stability is such that the collapse of the transient is governed by the gravity of the target body rather than its material strength. Simple craters result from the collapse of relatively small transient craters, while the more dramatic collapse of larger cavities results in complex morphology. The crater diameter at which this transition occurs depends, in part, on the gravity of the target body (see 1.5.1).

After the collapse of the transient is complete, the crater continues to shallow over geologically longer time periods on a path to gravitational stability – a level plain. This process is time-dependent and is affected by crustal strength and crater size. The most prevalent post-impact modification on Earth is erosion of the exposed topography and infill of craters by fluvial or alluvial sediments (Pater and Lissauer, 2001). Infill by lavas also occurs and is particularly evident in the lunar maria. On the icy satellites viscous relaxation is considered to be the most effective method of long-term modification of impact craters (Pater and Lissauer, 2001).

### 1.2.4. Viscous Relaxation

The excavation of material during impact crater formation, combined with the lower density of the fragmented sub-crater debris relative to the surrounding area, creates an isostatically uncompensated feature. This produces a circular ‘gravity low’ anomaly which has aided the identification of some terrestrial impact structures (e.g. Chicxulub, Hilderbrand et al., 1991).

The forces present after crater formation act to isostatically compensate for the loss of material and density reduction. Over time, the crater floor will rise in response to these forces and the rims become subdued, moving the crater topography towards isostatic equilibrium. The mass movement of solid material during this isostatic rebound is possible as no known material is truly ‘solid’. All materials flow under applied stress over long enough time scales. The rate of this flow is temperature dependant and can be imperceptibly slow at low temperatures.

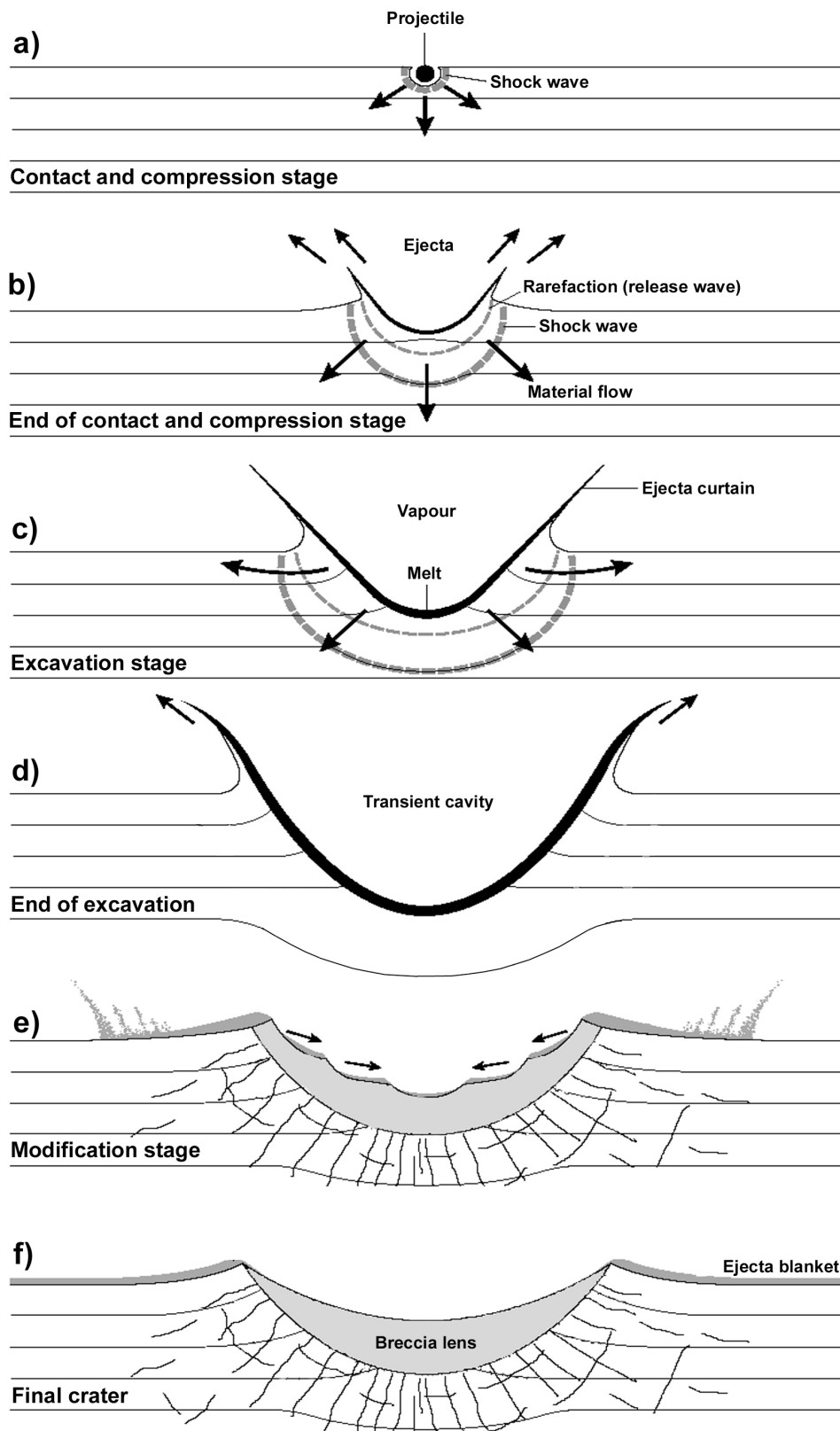


**Figure 1.5:** Diagrams illustrating the different stages of the impact process. Images A to D depict the growth of the transient crater before the modification shown in E. The diagram has been modified from French (1999).

### The Effect of Temperature

After the initial application of a differential stress (e.g. that caused by the isostatic disequilibrium of a crater), all material will reach a steady state in which the creep rate ( $\dot{\epsilon}$ ) is related to temperature and the magnitude of the stress by Equation 1.3:

$$\dot{\epsilon} = A(\tau) \exp(-fT_m / T_a), \quad (1.3)$$

where  $A$  is a function of the applied stress ( $\tau$ ),  $T_m$  is the melting temperature of the material,  $T_a$  is the absolute temperature of the material and  $f$  is a dimensionless constant usually between 23 and 25 for geologic materials (Weertman and Weertman, 1975).

Thus the flow rate is expected to be higher in crusts composed of relatively low-melting point materials, and is expected to become significant once the ambient temperature approaches 50% of the melting temperature. As a result, although viscous relaxation of crater topography occurs to some extent on all solid bodies, viscous relaxation is most noticeably prevalent on icy bodies due to the melting temperature of ice being close to the ambient surface temperature of the body ( $\sim 100$  to  $130$  K for the Galilean moons).

As temperature generally increases linearly with depth in most planetary bodies, the flow rate is expected to increase exponentially allowing material at depth to move in a relatively fluid-like manner. This is indeed the case when we consider the Earth's upper layers: creep in the solid upper crust is imperceptibly slow; at greater depths the ambient temperature of the mantle reaches about half of the melting temperature of pyroxene/olivine ( $\sim 1200$  K), allowing the mantle to flow as a fluid over geological time scales.

### The Effect of Strain Rate

The flow rate of geologic materials is not purely dependent on temperature, and also varies with the magnitude of the applied stress and the time scale over which it is applied. Maxwell rheology describes a substance that behaves elastically over short time scales, but can flow under long-term stresses and has been incorporated into models of the Earth's mantle (The Rheid model, Carey, 1953). The Maxwell time ( $t_M$ ) is a measure of the 'solidity' of these visco-elastic substances and is defined as the length of time a substance must flow under an applied load before the creep strain ( $\epsilon_{t_M}$ ) equals the elastic strain ( $\epsilon_{e1}$ ). For time,  $t < t_M$ , the material in question can be regarded as an elastic solid, whereas fluid behaviour will become predominant for strains applied over a period greater than the Maxwell time.

The Maxwell time is related to the strain rate dependent viscosity ( $\eta = \tau/2\dot{\epsilon}$ ) and shear modulus ( $G$ ) of a material by Equation 1.4:

$$t_M = \frac{\eta}{G}. \quad (1.4)$$

The upper crustal rocks of the Earth and Moon have viscosities in excess of  $10^{25}$  Pa.s giving a Maxwell time in excess of  $10^9$  years; ergo, they behave as elastic solids over the full length of geologic time and are therefore considered ‘solid’. The viscosity of the mantle has been estimated to be  $< 10^{21}$  Pa.s based on isostatic rebound rates of the crust after periods of glaciation (Turcotte and Schubert, 1982). Maxwell times for mantle rocks are of the order of thousands of years, allowing them to flow fluidly over geologic time scales.

The Maxwell time of the Ganymede surface is significantly larger than that of glacier ice on Earth due to the lower ambient temperatures (90 to 160 K). This prevents viscous creep of surface features on the icy moons from being observed over human time scales. However, the bowed floors and subdued topography of craters on Ganymede show appreciable flow to have taken place over geologic time. Indeed, the palimpsest and anomalous dome morphologies seen of the largest and oldest of the Ganymede craters are thought to be a direct result of the action of viscous relaxation (Section 1.4.4, Passey and Shoemaker, 1982).

### The Effect of Crater Diameter

As the largest craters on the icy satellites appear to have undergone a greater amount of viscous relaxation relative to smaller cavities, a dependence of relaxation rate on crater size is inferred. This can be explained when considering the stresses acting on the crater cavity as they also scale with crater size.

The shear stress ( $\tau$ ) beneath a bowl-shaped crater of depth  $H$ , formed in a material of uniform viscosity, is approximately  $\frac{1}{4} \rho g H$  as derived by Melosh (1989). Assuming that the crater material relaxes via Newtonian flow, the strain rate ( $\varepsilon$ ) of the material flowing towards the centre of the crater is:

$$\varepsilon = \frac{1\sigma}{2\eta} = \frac{\rho g H}{8\eta}, \quad (1.5)$$

where  $\sigma$  is the applied stress,  $\eta$  and  $\rho$  are the viscosity and density of the material respectively, and  $g$  is the gravity of the body. The rate of uplift of the crater floor ( $dH/dt$ ) can be estimated by multiplying this strain rate by the crater diameter:

$$-\frac{dH(t)}{dt} = D\varepsilon = \frac{D\rho gH(t)}{8\eta}. \quad (1.6)$$

Integrating this over the time taken to for the craters depth to decrease from  $H(0)$  to  $H$ , this gives:

$$H(t) = H(0) \exp\left(-\frac{t}{t_r}\right), \quad (1.7)$$

where  $t_r$  is the relaxation time:

$$t_r = \frac{8\eta}{\rho g D}. \quad (1.8)$$

Simple calculations assuming an average effective viscosity of  $10^{24}$  Pa.s over 3 Ga suggest that all Ganymede craters above  $\sim 6$  km in diameter will have decreased in depth by more than 10% over this time. Equation 1.8 shows the uplift rate of the crater floor to be dependent on both the viscosity of the material and the crater diameter, thus explaining the observed difference in general relaxation state of small and large craters on the icy moons. Another consequence of this relation is that crater rims of large craters persist longer than the comparatively broad crater bowl, as seen in relaxed Ganymede crater morphologies (Figure 1.9).

It should be noted that the simple relationship between relaxation time and crater diameter shown in Equation 1.8 is complicated by the variance of viscosity with depth that occurs on planetary bodies. Differentiated ice-silicate bodies are thought to consist of an icy crust overlying denser silicates (Consolmagno and Lewis, 1977); the silicates form a high viscosity substratum to the lower viscosity ice crust. In the case of the icy Galilean satellites and some of the more active Saturnian moons, the viscosity-structure is further complicated by the presence of sub-surface oceans, as the viscosity of the ice crust decreases with proximity to these oceans. This more sophisticated relationship is considered by Parmentier and Head (1981), who relate the relaxation time of topography to material viscosity that decreases exponentially with depth (Equation 1.9).

$$t_r = \frac{2\eta k}{\rho g} \left( \frac{\sinh(kd) - (kd)}{\cosh(kd) \sinh(kd) + kd} \right), \quad (1.9)$$

where  $k$  is the wave number ( $k = \pi/\text{wavelength}$ ) and  $d$  is the depth of the relatively rigid crust. For short wavelength features, Equation 1.9 effectively becomes equal to the simplified version in Equation 1.8, showing that short wavelength features will relax at the same slow rate for both uniform and layered viscosity models. Conversely, larger craters will relax notably faster in materials whose viscosity decreases as a function of depth, as is thought to be the case for Ganymede (Durham et al., 1983).

### **1.3. The Effect of Target Properties**

Impact craters on the icy moons display unusual morphologies not yet outlined in this work. These exotic morphologies appear to be influenced or formed as a result of a sub-surface ocean, demonstrating the importance of target layering on impact crater formation. The impact process can be affected by a number of factors related to both target and projectile properties; the complications introduced by variations in target structure are outlined in this section.

#### **1.3.1. Existing Lines of Weakness**

The final crater shape and ejecta patterns can be affected by existing joints, faults or other lines of weakness in the target (Gault et al., 1968). An example of such an effect can be seen when considering Meteor Crater in Arizona which is more square than circular (Figure 1.6). This peculiar shape was caused by two perpendicular sets of vertical joints in the sedimentary basement rocks (Shoemaker, 1963). The excavation flow exploited these pre-existing lines of weakness, traveling more easily in directions parallel to the joints, allowing the transient crater to expand further in these directions.

Complex craters respond to joint placement in a very different way to simple craters such as Meteor Crater. During complex crater collapse, the rim material slides away from the footwall parallel to lines of weakness. This preferential material slump creates concentrated terrace segments and polygonal crater rims (e.g. Figure 2.14).

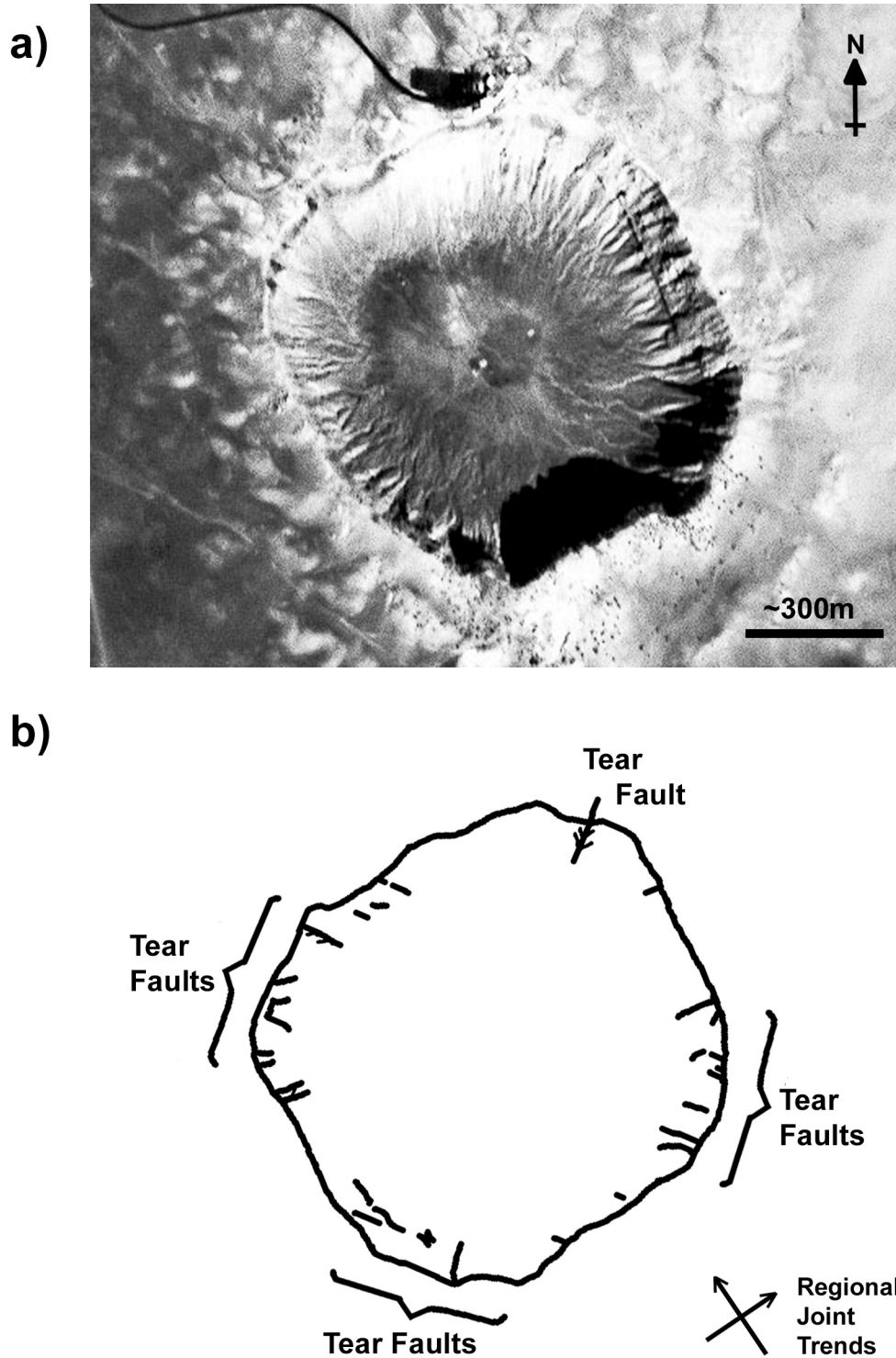


**Figure 1.6:** A) Image of Meteor Crater in Arizona taken by the High Resolution Camera onboard the ESA Proba satellite. B) Outline of Meteor Crater's rim-crest to demonstrate its shape is more square than circular. Two prominent orthogonal joint sets cut the crater, the regional trend of these joints is noted. Diagram from Melosh (1989), using data from Shoemaker (1963)

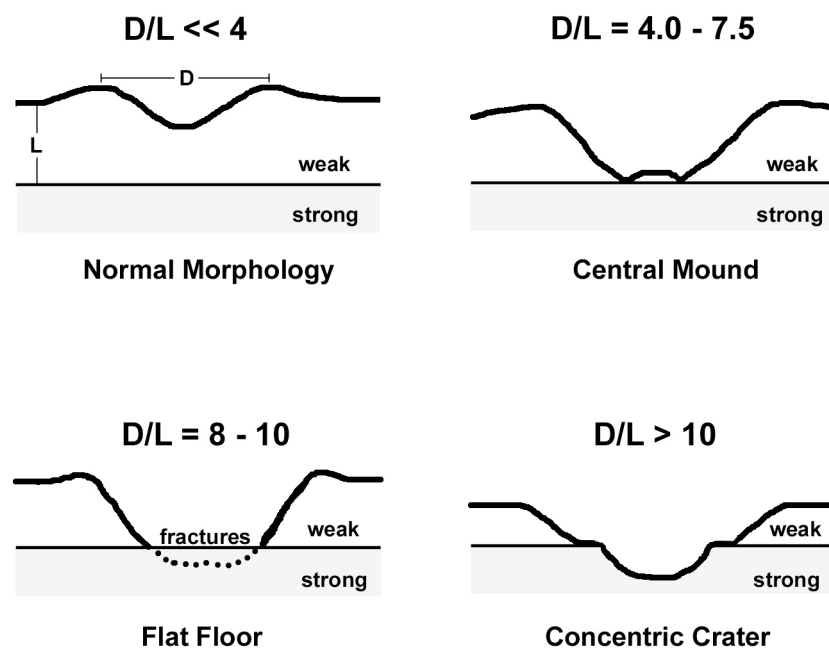
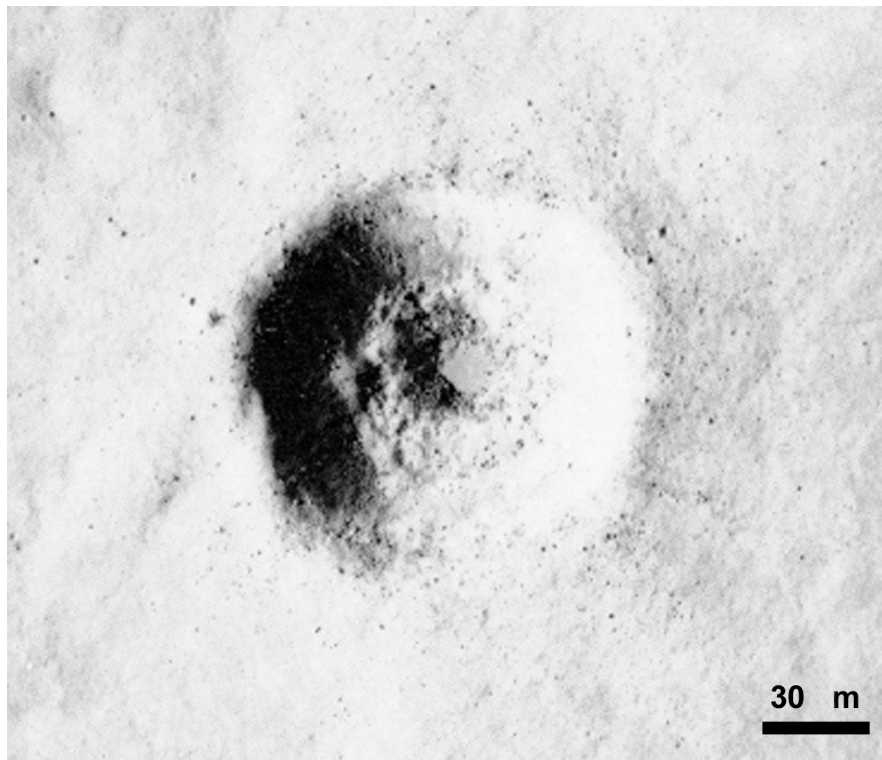


**Figure 1.7:** A) Image of a 1.2 km simple crater on the Moon. The wide bench on its interior wall has been used to infer that the Moon's surface in this area consists of a weak layer about 100 m thick overlying a more resistant rock unit. Apollo Panoramic Photograph AS15-9287. B) Sketches of different crater morphologies produced when the ratio of crater diameter and the thickness of the upper weak layer changes (From Melosh, 1989; after Quaide and Oberbeck, 1968).

### 1.3.2. Original Topography of the Target

Simple craters that form in a sloped surface are expected to be elongated in the downhill direction. This is not as obvious for larger complex craters on sloped targets as, if large enough, their circular shape is generally maintained. However, complex craters on sloping surfaces often display increased collapse and slumping on their uphill rims (Heather and Dunkin, 2002).

### 1.3.3. Target Layering

A well studied case of layering in the target affecting crater morphology is that of lunar craters formed in unconsolidated regolith that overlies more resistant mare basalts (e.g. Figure 1.7A). Oberbeck and Quaide (1968) found that the exact morphology in such cases is dependent on the thickness of the weak upper layer, as displayed in Figure 1.7B. As a result, the diameter of craters such as that in Figure 1.7A has been used to estimate lunar regolith thickness in those areas.

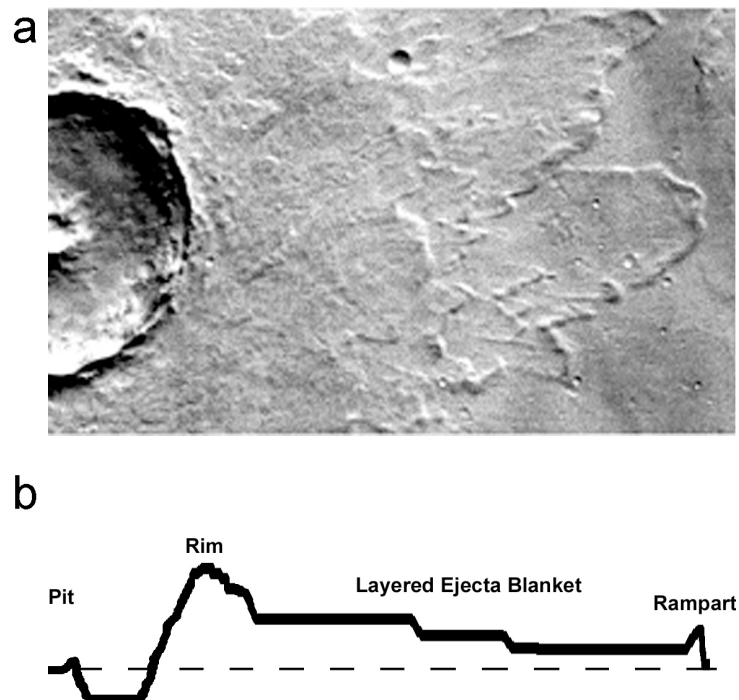


**Figure 1.8:** A) A 25 km 'summit-pit' crater on Mars displaying a multiple layer ejecta blanket (THEMIS image I03218002). B) Sketched topographic profile; vertically exaggerated and not to scale, to better illustrate the structure of rampart ejecta blankets.

Weak ice or water beneath a stronger rock or ice surface may be the controlling factor that leads to central pit crater morphology on the icy Galilean satellites and Mars and is discussed further in the next section. A water-saturated substrate beneath the surface not only aids the fluidization process within the crater, but has also been suggested as a possible mechanism for the fluidization of ejecta blankets and the formation of Martian ‘rampart ejecta’ (Carr et al., 1977) which features a raised rampart, a low concentric ridge or an outward facing escarpment (Figure 1.8). However, ejecta interaction with the Martian atmosphere has also been suggested (Schultz and Gault, 1979), and a consensus is yet to be reached.

## **1.4. Impact Craters on the Icy Galilean Satellites**

As for rocky bodies, craters on the icy satellites also follow a morphologic progression beginning with simple craters and progressing onto more complex morphologies. However, with increasing size, craters in icy media become less like their silicate counterparts. This difference becomes particularly apparent for large craters on the icy Galilean moons, which display characteristics with no obvious analogs on other planetary bodies (e.g. Palimpsests and anomalous dome craters) (Figure 1.9).

### **1.4.1. Simple and Central Peak Craters**

Simple craters on the icy moons mirror those on silicate bodies implying a comparable formation process and near-surface rheology. The transition between simple and complex morphology (the s-c transition, Section 1.5.1) occurs at smaller crater diameters on icy bodies such as Ganymede, and central peak craters are observed at crater diameters of 2 km (Schenk 2001). Central peak craters on icy bodies structurally resemble their counterparts on terrestrial bodies, except they are shallower and their rim terraces are less pronounced (Schenk, 1991; 2002). The shallower depths imply a lower material strength relative to silicate rocks; this is discussed later in this chapter.

### **1.4.2. Central Pit Craters**

Although craters on the large icy satellites exhibit the simple and central peak morphologies seen on the terrestrial planets, no peak-ring craters have been observed on these bodies (Chapman and McKinnon, 1986; McKinnon et al., 1991; Croft et al., 1995). Central pit craters are an unusual morphological class of impact crater seen most commonly on the large

icy satellites Ganymede and Callisto, where they replace the peak-ring morphology expected for similar diameter craters on rocky bodies.

Pit craters are characterized by flattened or upbowed floors with a pit at or near the centre (e.g. Figures 1.8 and 1.9). Their rims display wider terrace zones than central peak craters extending 1 to 7 km into the crater interior (Passey and Shoemaker, 1982). The central pits tend to have raised rims in smaller central pit craters but are usually rimless in larger craters (Schenk and Moore, in prep.). Central pit craters are by far the dominant morphology of craters between  $\sim 25$  and 55 km diameter on Ganymede (Schenk, 1991). This crater type is described in more detail in Chapter 3.

### 1.4.3. Dome craters

In craters between  $\sim 55$  and  $\sim 180$  km in diameter on Ganymede, central pits are partially to extensively filled by sub-circular domed deposits of smooth, high albedo material (e.g. Moore and Malin, 1988; Schenk, 1993). These domes can rise 500-1000 m above their base and widen as crater diameter increases (Schenk, 1993).

Older examples of this crater type are referred to as ‘anomalous dome craters’ as the dome becomes the predominant feature of the crater to remain topographically expressed after rim degradation and viscous relaxation related rebound of the crater floor. Central dome and anomalous dome craters have no analogue in terrestrial cratering and are hypothesised to form as a result of deeply penetrating impacts breaching the brittle ice crust and exposing a relatively fluid layer. Warm sub-surface ice then rises to the surface in the crater centre and freezes to form a dome of fresh ice (Schenk, 1993).

### 1.4.4. Palimpsests

The very oldest and largest of the preserved crater-forms on Ganymede are the palimpsests; they are nearly featureless circular regions of high albedo with no discernable crater rim or rim-like features (Passey and Shoemaker, 1982). Smooth, sub-circular regions at the centre of Ganymede palimpsests are thought to be solidified impact melt water (Jones et al., 2003). Palimpsests are currently believed to form as a result of highly-fluidized ejecta emplacement following an impact and penetration into an ice crust above water (Passey and Shoemaker, 1982; Jones et al. 2003). The original crater diameters are estimated to be  $\geq 36$  km on the basis of secondary crater positions (Jones et al., 2003).

Crater counts and cross-cutting relationships suggest that the formation of these features predated the emplacement of Ganymede’s youngest geologic terrain (the ‘bright terrain’) (Shoemaker et al., 1982), making them approximately older than 1 Ga (Zahnle et al., 1998).

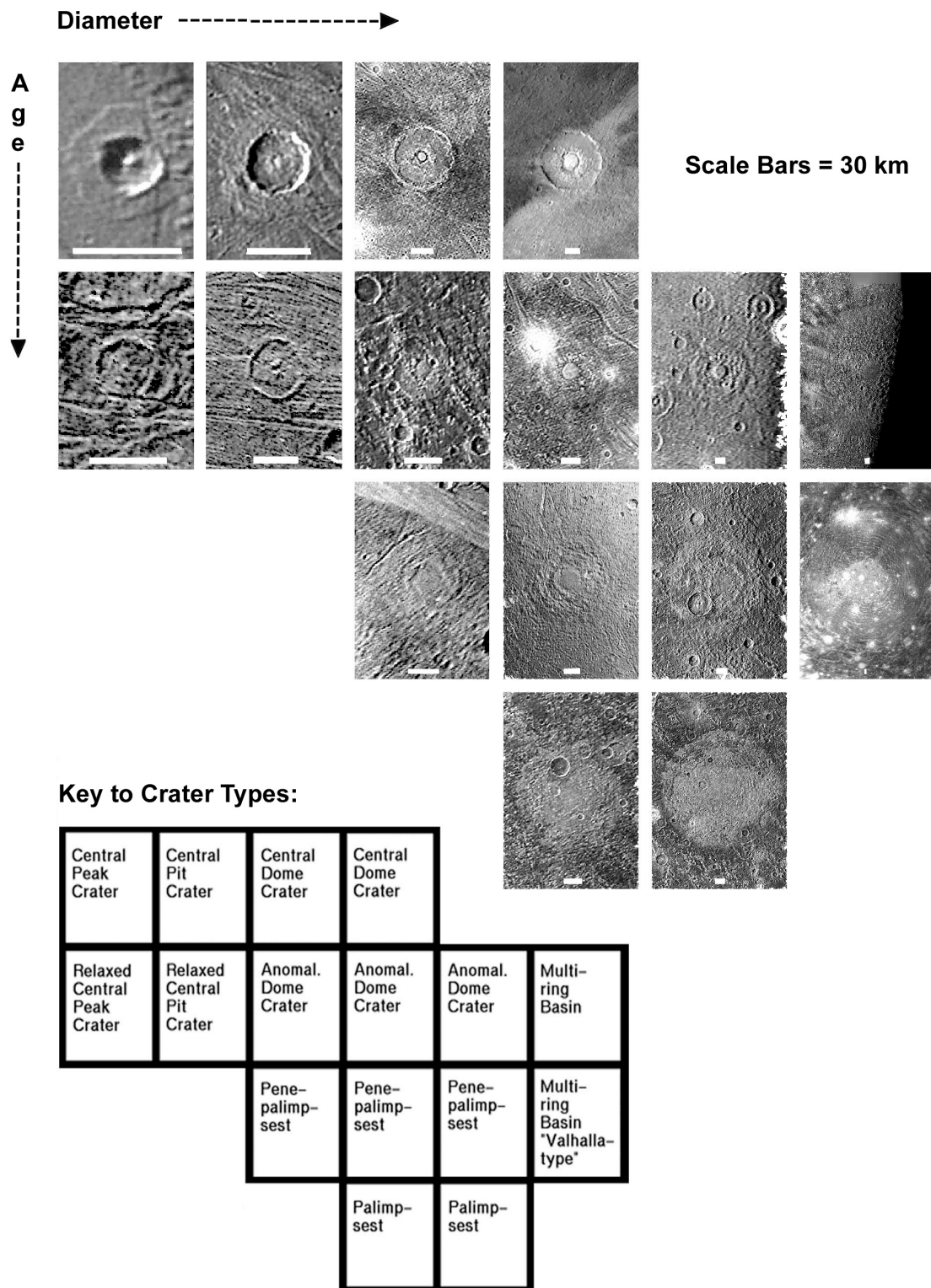


**Figure 1.9:** Mosaic showing the variety of complex crater morphologies observed on Ganymede (similar features are also observed on Callisto). These image tiles are arranged according to age and crater size. Scale bars are shown on each image and are 30 km long. A companion image gives names for each crater type. Images courtesy of Paul Schenk, LPI.

As younger craters of this diameter maintain topographically expressed central pit morphology it suggests that the ancient Ganymede crust was thinner than in more recent times. A thinner crust is likely to be associated with higher heat flow and higher rates of viscous relaxation (Section 1.2.4).

## **1.5. The Study of Impact Craters**

Reliable evaluation of impact craters and other features on solar system bodies requires two major elements: Firstly, sufficient observational data is needed so that crater morphology on different bodies may be studied in detail. This allows the formulation and development of formation theories. Secondly, it is necessary to have a means to study the impact process in its entirety. As no planetary impacts have been recorded in detail, computer models and gas-gun experiments provide the best means to do this; observational data will also provide a means to test model results. This section outlines some of the observational and experimental techniques used to study impact craters in the solar system. Of particular importance is the introduction of depth-diameter plots which will be used frequently for the presentation and analysis of results in this thesis.

### **1.5.1. Observational Data Analysis**

The most complete sets of structural data for impact craters exist for those found on Earth as observational data can be supplemented by field studies and remote sensing (Grieve, 2006). The structure of impact craters on Earth has been investigated using a range of surface observations and sub-surface geophysical techniques (e.g. Pilkington et al., 1994; Morgan and Warner, 1999). This has enabled better understanding of impact crater structure on Earth than on bodies for which such in-depth structural data is unavailable. However, as craters on Earth are heavily affected by weathering and tectonic processes, our ability to determine the original pristine crater morphology is limited. The efficient resurfacing of the Earth by these geological processes also results in relatively few craters to study, preventing accurate determination of size-morphology trends (for example). Instead, observational assessment of crater morphology is better done from the analysis of craters on less geologically active bodies, such as the Moon.

The Moon's proximity to Earth has allowed its surface to be studied for centuries, both remotely and more recently in situ. Its lack of recent geological activity means that significantly more impact craters remain on its surface than on other, more geologically active, bodies. This has allowed the collection of extensive data sets from which crater

scaling laws have been derived (e.g. Pike, 1977). Analysis of crater morphology combined with the structural and compositional data returned from the Apollo missions has led to impact cratering being reasonably well understood on the Moon.

The relative lack of structural and compositional information for the icy moons prevents such robust investigation of impact cratering in ice. Details of how ice behaves in the conditions prevalent during large impacts are yet to be reliably ascertained, further complicating our understanding of impact crater formation on icy bodies. Images returned from the Voyager and Galileo missions have allowed the analysis of crater morphology on the icy satellites (e.g. Passey and Shoemaker, 1982; Schenk, 1993). Images from these missions allow us to compare cratering trends on the rocky and icy bodies and to investigate how crater morphology is affected by target conditions. This comparison is particularly useful when comparing the cratering trends on Ganymede and the Moon as they have similar gravity. Resultantly, differences in crater morphology are likely to be primarily due to differences in their surface properties.

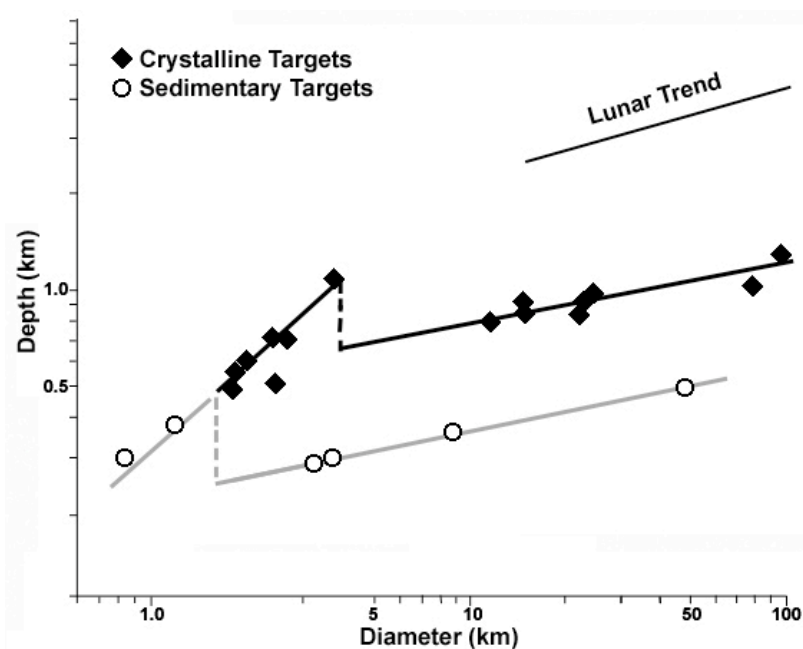


**Figure 1.10:** Depth-diameter relationship for impact craters on Earth. The simple-to-complex transition diameters are marked with dotted lines for both crystalline and sedimentary targets (Grieve, 1987). The s-c transition occurs at smaller diameters for sedimentary targets due to their lower material strength. A lunar trend line (from Pike, 1980) is included for comparison.

Close inspection of any planetary surface will reveal some craters that do not fit the size-morphology progression described in Section 1.1; however, it remains a useful tool in organising the fundamental forms of impact craters over a wide range of diameter scales. As the morphology and depth-diameter trends of craters on different surfaces of the same planetary body have been related to contrasts in local target composition (Grieve, 1987), graphical analysis of observational data can be used to infer approximate target properties (e.g. Figure 1.10). This section outlines how these graphs can be used, and how the trend line properties are linked to the processes involved during crater excavation and collapse.

### The Use of D-d Plots

Observational data for lunar craters has revealed a linear relationship between depth,  $d$ , and diameter,  $D$ , of final craters of the type  $d = \alpha D$  where  $\alpha$  is a constant of proportionality approximately equal to 0.2 (Pike, 1977; Melosh, 1989):

$$\log d = \log D + \log \alpha . \quad (1.10)$$

As the collapse of simple craters is primarily controlled by friction,  $\alpha$  is related to the target materials effective coefficient of friction. Figure 1.11 (Section A) shows that the formation of simple craters on the Moon and Ganymede are comparable due to the same trend line gradients. The similar  $\log \alpha$  values of simple craters on Ganymede and the Moon imply comparable near-surface strength.

The transition between simple and central peak craters (B on Figure 1.11) represents the change from simple crater collapse to the more dramatic collapse of larger transient cavities and is observed on all cratered bodies. The occurrence of this transition, combined with the similar trend line gradients in Section C of Figure 1.11 suggests a common underlying formation process for complex craters on silicate and ice targets. The trend lines for the largest lunar and Ganymede craters deviate in section E and complex craters on the icy satellites are up to 70% shallower than on the Moon (Schenk, 2002). As the gravity of the Moon and Ganymede are similar, this difference in crater depth is likely due to the weakness of ice relative to lunar rock and the additional weakening influence of Ganymede's sub-surface ocean.

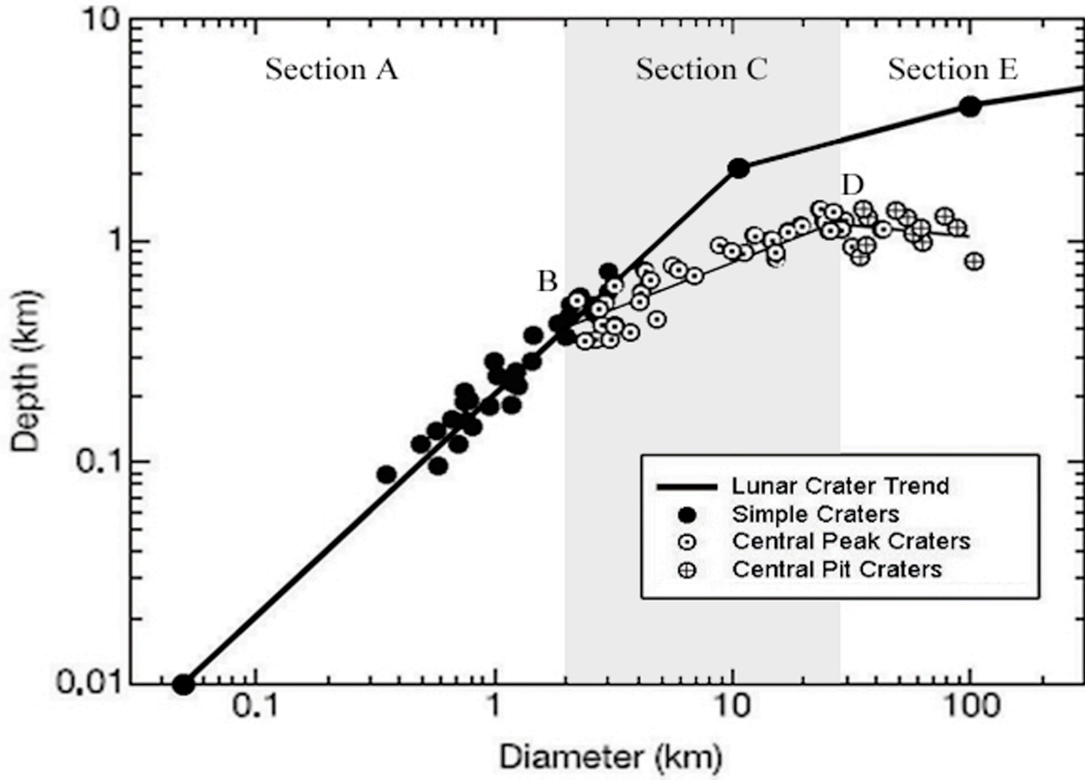


**Figure 1.11:** Depth-diameter plot for craters on Ganymede, modified from Schenk (2002). Different types of crater morphologies are noted and a lunar trend line included for comparison (Pike, 1977). Transition B is the simple-to-complex transition; transition D marks the transition from central peak to central pit morphology.

### The simple to complex transition

The abruptness of the transition between simple and complex crater collapse suggests that a strength threshold is exceeded beneath craters of sufficient depth (Melosh, 1989). If the target material is assumed to act plastically with constant strength  $Y = Y_0$ , the magnitude of  $Y_0$  can be estimated. At the s-c transition,  $Y_0$  is equal to the stresses trying to collapse the crater,  $\sigma$ . Melosh (1989) showed this to be very approximately equal to  $\sim \frac{1}{4} \rho g H_t$ , where  $\rho$  is the bulk density of the material,  $g$  is the target body's gravity and  $H_t$  is the depth of the transient crater. Therefore, at the s-c transition,

$$Y_0 \approx \frac{\rho g H_t}{4}. \quad (1.11)$$

The depth of the transient crater is empirically related to the final crater diameter via  $H_t \approx D/3.75$  (Melosh, 1989) which can be substituted into Equation 1.11 to find  $Y_0$ :

$$Y_0 \approx \frac{\rho g D}{15}. \quad (1.12)$$

For lunar craters, the transition diameter of  $D = 15$  km implies a mean resultant stress on the order of 5 MPa which is supported by modelling work (Wünnemann and Ivanov, 2003). In the case of Ganymede, an s-c transition diameter of  $1.9 \pm 0.5$  km (Schenk, 2002) suggests a target strength between 0.133 and 0.229 MPa. This relative weakness of ice is in agreement with the shallower complex craters. It is noted that both strength values are significantly lower than that expected for rock and ice on the basis of laboratory strength tests ( $\sim 50$  and 10 MPa for rock and ice respectively). This disparity is discussed further in Chapter 4.

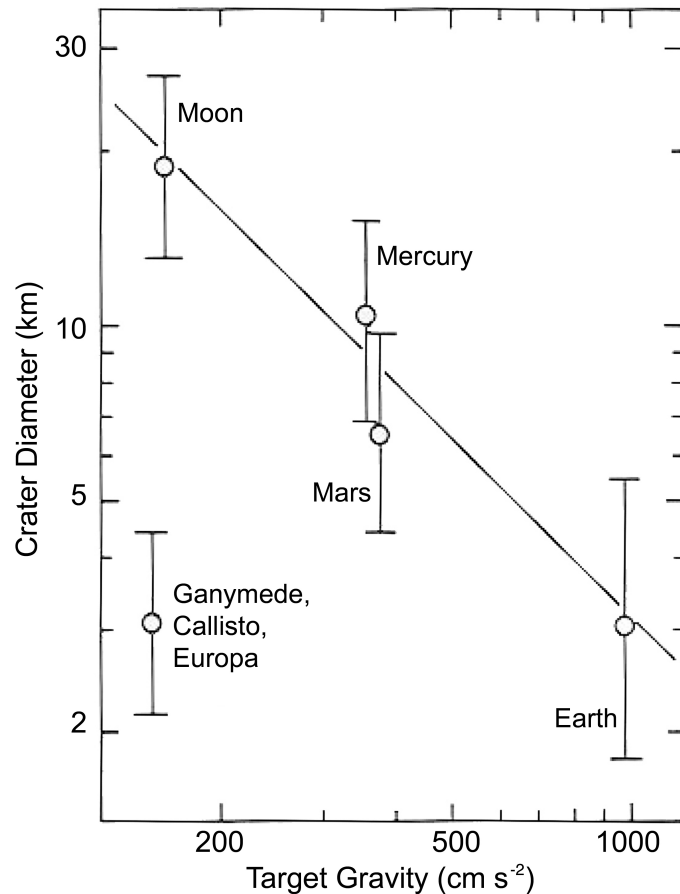


**Figure 1.12:** Crater diameter at the simple-to-complex transition on the Earth, Moon, Mercury and Mars based on data from Pike (1988). The figure has been updated after Melosh (1989) to include data for the Galilean satellites of Ganymede, Callisto and Europa from Schenk (2002). The trend line marks the  $D = 1/g$  line.

The strength relationship outlined by Equation 1.12 implies a  $1/g$  dependence for the diameter at which this critical strength is reached; this is confirmed by observational data. The crater diameter at which the simple-to-complex transition occurs is approximately inversely proportional to the target body's gravity (Pike, 1977). The inversely proportional relationship is clearly seen when comparing Earth, Mercury and the Moon in Figure 1.12. Variations in the s-c transition diameter on different terrains on the same body (e.g. Figure 1.10), and the lack of alignment of Mars and the icy Galilean satellites on Figure 1.12, implies that the position of the s-c transition is not solely dependent on gravity, but also varies subject to variations in material strength, target composition and heat flow (Melosh, 1989).

### 1.5.2. Experimental Data

Recreation of impact cratering under controlled conditions is important for developing our understanding of how different factors affect the impact process. This is possible with both computer and laboratory-based studies as specific parameters can be varied and the resultant changes in crater morphologies observed. Numerical modelling offers a means for examining various stages of the impact event that cannot be investigated by other methods, particularly for large planetary impacts. Conversely, experimental techniques, such as light gas gun impacts, are important to understand cratering processes and material response to impact at smaller scales. This makes both experimental and computational investigations important facets of impact cratering research.

#### Laboratory Impact Experiments

Laboratory experiments aim to produce small impact craters in materials of known composition using hypervelocity particles (those travelling faster than the speed of sound in the target material). There are several laboratory techniques used to accelerate particles of various sizes for hypervelocity experiments (e.g. Electrostatic Dust Accelerator, Plasma Gun, Light-Gas Gun (LGG)); these are outlined in Fechtig et al. (1972). Although the electrostatic acceleration of dust can produce particle speeds of up to  $90 \text{ km s}^{-1}$ , the projectile range is limited to particle masses below  $10^{-13} \text{ kg}$  (Burchell et al., 1999). In contrast, light-gas guns can accelerate larger projectiles ( $\sim 0.1 \text{ gram}$ ) to maximum velocities of  $\sim 10 \text{ km s}^{-1}$  (e.g. Fechtig et al., 1972; Shrine et al., 2002).

Light-gas guns fire spherical projectiles at vertical targets producing larger impact craters than those produced by plasma guns and electrostatic accelerators. As well as being able to study the produced crater morphology, LGG experiments allow the impact process to be observed via examination of high-speed video. Light-gas guns operate by releasing high-pressure gas behind a projectile which then accelerates into an evacuated mobile barrel en-

route to the target surface (see Asay and Shahinpoor (1993) for a more detailed review of light-gas gun design and operation).

The gases commonly used are hydrogen, helium and nitrogen (hence the name *light-gas gun*). The lighter the gas, the higher the achievable projectile velocity due to the lower molecular weight (Crozier and Hume, 1957). The preferred velocity can then be fine-tuned by selecting the appropriate type and amount of gunpowder to drive the gas, the barrel diameter, and the material and mass of the impactor. The targets used in LGG experiments are also well constrained as the material properties can be determined. As both the projectile and target properties can be changed to meet the needs of the experiment, LGG work allows for detailed investigation of small-scale impact involving different materials, impact angles and target structure.

### **Hydrocode/Numerical Simulation of Impact**

Although a valuable tool in the investigation of simple crater formation, results from small-scale LGG experiments cannot yet be reliably extrapolated to planetary scales. This has restricted understanding of processes like melting/vaporization and complex crater collapse (Pierazzo and Collins, 2004). The use of computer modelling has advanced the investigation of this gravity driven process, allowing complex crater collapse on planetary scales to be studied in its entirety. Hydrocodes simulate energetic events such as impact cratering by solving the differential equations of conservation of mass, momentum, and energy. They also incorporate strength models and equations of state to describe the material behaviour.

All variables can be defined by the programmer allowing for simulation of any size of impact event on any solar-system body. However, hydrocodes rely on the availability of accurate material models to describe the reaction of the target during impact. Resultantly, hydrocodes cannot yet simulate the range of materials available for testing by LGG experiments. Chapters 4 and 5 present this subject in detail, outlining the use of one such computer code for simulations of impact crater formation on the icy satellites.

### **1.5.3. Thesis Structure**

This work combines observational and numerical modelling data to develop a quantitative model for impact cratering in pure ice so that subsequent simulation into layered targets will be more reliable. Consequently, this thesis is presented in three parts: a) Acquisition of topographic profiles for analysis of cratering trends on Ganymede, and for testing numerical model results (Chapters 2 and 3). b) Determination of suitable strength model parameters necessary to accurately simulate impact into pure ice targets. Results are tested by

comparison with crater profiles from Ganymede (Chapters 5 and 6). c) Application of the refined strength model to modelling impact cratering in layered ice and water targets (Chapter 7). Simulation results are then matched to depth-diameter measurements of European craters to allow an estimation of Europa's crustal thickness.

### **a) Acquisition of 3D Observational Data (Chapters 2 and 3)**

As already mentioned, the current lack of topography data is restricting the investigation of craters on the icy moons. Fuller understanding of impact crater morphology requires the incorporation of topographic data so that a 3D view of the crater can be formed. This will allow a more detailed analysis of cratering trends with lunar data, and help us distinguish between competing proposals for the formation mechanism of large craters on the icy moons (e.g. Moore et al., 2004; Schenk and Moore, in prep.).

Chapter 2 presents analysis of crater morphology on Ganymede based on the combined study of Galileo images and topographic profiles created for a number of impact craters. Scaling trends derived from those data are compared with lunar cratering trends so that the surfaces of the Moon and Ganymede may be compared. The sensitivity of crater morphology to variances in crater size, relative age and terrain type is examined and the results presented in both qualitative and quantitative means.

### **b) Refinement of the Strength Model for Ice (Chapters 4, 5 and 6)**

Hydrocodes rely on accurate strength models and equations of state to recreate the appropriate material reactions to a high velocity impact. The equations of state and the static strength parameters employed in this work are presented in Chapter 4. Chapter 5 details the investigation of two different strength models, and assess the sensitivity of simulated crater morphology to the strength parameters. The most suitable strength model and its specific parameters are determined for the simulation of impact crater formation in unlayered ice based on the recreation of Ganymede cratering trends in Chapter 6. Chapters 5 and 6 also discuss the choice of Ganymede craters for validating numerical model results and provide comparisons between the simulation results and the topographic profiles presented in Chapter 2.

### **c) Application to Europa – How thick is Europa's Crust? (Chapter 7)**

Chapter 7 focuses on the study of Europa's crustal thickness. The optimal strength model defined in Chapter 6 is applied to a layered ice and water target; results from this numerical modelling are compared to observational data for European craters. Finally, an estimation of Europa's upper-crustal thickness is presented and compared to existing theories.

## Chapter 2

# Comparison of Craters on the Moon and Ganymede

Craters on the icy Galilean satellites of Europa, Callisto and Ganymede exhibit the same simple and central peak morphologies seen for craters below 150 km on the Moon, but do not evolve into the peak-ring basins, as do lunar craters above this diameter (McKinnon et al., 1991; Croft, 1985). Instead, large craters display characteristics with no obvious lunar analogues such as central pits (see Chapter 3). As these Galilean satellites have a similar gravity to the Earth's moon, these differences in their cratering trends are considered to be due to the mechanical properties of ice or the presence of shallow sub-surface liquid layers (Moore et al., 2001; Turtle and Pierazzo, 2001; Schenk, 2002).

Callisto is the most heavily cratered of the Galilean satellites, providing a rich collection of large impact craters for study. However, its surface has been found to be surprisingly crater-poor on smaller scales, suggesting that its small craters are being erased more efficiently by mass wasting processes and burial by impact ejecta (Pappalardo, 1999). Callisto is also thought to be less differentiated than Ganymede, leading to higher amounts of rocky material in its surface ice, which may affect its crustal strength properties in a way that would be difficult to predict. In contrast, the surfaces of Europa and Ganymede are approximated as pure water ice (Showman et al., 2004). As the ice crust of Ganymede is thicker than that of Europa, the morphologies of its smaller craters are expected to be relatively unaffected by the presence of its sub-surface ocean (Schenk, 2002; Schenk et al.,

2004). Ganymede therefore provides a suitable source for observations of craters that have formed in unlayered ice and thus a benchmark from which to understand craters on Europa (Bray et al., 2008). Ganymede also provides the opportunity to study craters in ice and ice-rock mixes as its surface is separated into distinct bright and dark terrains which are believed to consist of pure ice, and an ice-rock mix, respectively (Breneman and Belton, 1998).

Images returned from the Voyager mission have allowed the analysis of crater morphology on the icy satellites and the construction of both diameter and depth-related scaling laws (Passey and Shoemaker, 1982; Schenk, 1991). Higher resolution Galileo data has since been used to update the diameter-related scaling trends, and also crater depths on the basis of shadow measurements (Schenk, 2002). Other height data available from Galileo stereo and photoclinometry has not yet been utilised, and current depth-related scaling trends are based on the lower resolution Voyager data.

This chapter introduces the methodology for obtaining topographic profiles, and outlines the existing observational data for craters on the Moon and Ganymede. New profiles across complex craters on Ganymede, that utilize Galileo topographic data, are then presented and used to create scaling trends. The differences in lunar and Ganymede crater scaling are discussed and used to infer differences in the near-surface properties of these two bodies.

## **2.1. Introduction to Topographic Profiling Techniques**

In the absence of laser altimeter data, image-based methods must be used to extract local and regional topography of remote solar system bodies. The most basic method of obtaining height data is by measuring shadow lengths; knowledge of the sun angle at the time of image capture can then be used to calculate the height of the feature casting the shadow (e.g. Pike, 1980). Due to the relative simplicity of its derivation, feature heights from shadow measurements are generally more accurate than those produced by other image-based methods, and form the basis for current depth/diameter plots of Ganymede craters (Schenk, 2002). However, shadow measurement does not provide slope information and is generally restricted to rugged terrains that are reasonably close to the planetary terminator (the line between the illuminated and shadowed side of a planetary body) (Efford, 1991). As a result, shadow length measurement has since been superseded by two techniques that allow fuller topographic data to be collected.

Topographic mapping of planetary surfaces is now commonly based on the combination of photoclinometry (PC) and stereo image analysis. As each method resolves long and short wavelength topographic variations to differing degrees of accuracy, combination of the two allows reliable digital elevation models (DEMs) to be produced of large surface areas.

Topographic mapping using a combination of stereo and PC has been completed for the Galilean satellites (Schenk et al., 2001). A prominent problem, when considering the topographic profiling of Ganymede in particular, is that extreme variations in albedo reduce the reliability of PC DEMs over distances of 100s of pixels or more. As a result, combined Voyager-Galileo stereo provides the only long-wavelength (i.e. 100s of km) topographic data for Ganymede. Combined Voyager-Galileo stereo has been used to map the relative topography of geologic units on Ganymede and has proved important for supplementing measurements of crater depths using shadow length measurements (Schenk et al., 2001).

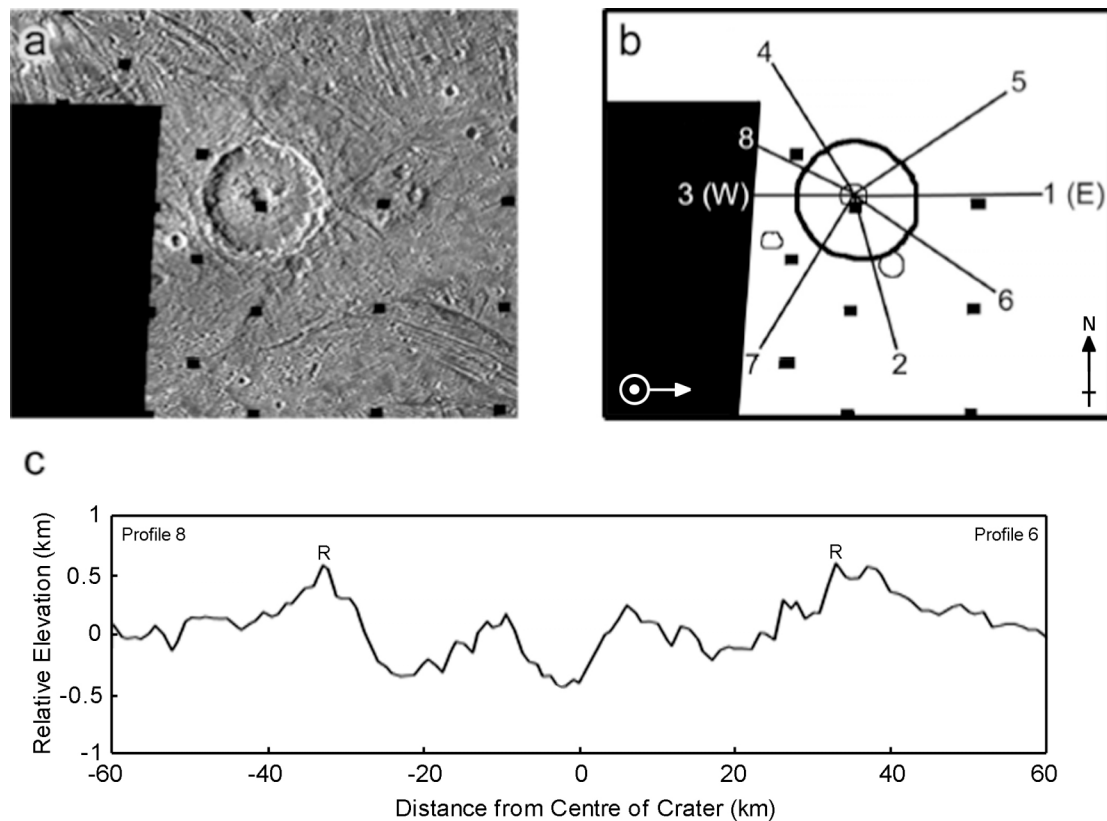


**Figure 2.1:** a) Galileo image of a central pit crater at 19S, 126W (See ZS19:126 in Appendix A). b) Sketch map of the image shown in ‘a’ marking the paths along which topographic profiles were collected. North, approximate illumination direction and regions of no data are marked with an arrow, a dotted circle and black areas respectively. Each radial profile is assigned a number from 1 to 8. Areas of no data, the cross-section at 90° to the illumination direction and features unrelated to the primary impact were avoided during profile collection. c) Topographic elevation along the profiles 6 and 8; vertical exaggeration is 60:1. As these two radial profiles form a complete cross section across the crater, they have been presented as a single DEM in this figure. Similar images, sketches and topographic profiles of all craters included in this work are attached as Appendix A.

### **2.1.1. Stereo Image Analysis ('Stereo Photogrammy')**

Stereo image analysis uses an automated pixel recognition program to derive topography from a 'stereo pair' – a pair of images taken of the same surface area under similar lighting conditions but from different viewing angles. Scene-recognition algorithms are used to identify the same feature on a stereo pair by matching albedo patterns within finite-sized patches in each of the two stereo images (Schenk et al., 1997; Schenk and Bulmer, 1998). The parallax shift between the two images then enables the height of that feature to be calculated. As the albedo patterns are matched in finite-sized patches (commonly 5×5 pixels), the DEMs created from stereo data have a resolution five times worse than that of the lowest-resolution image of the stereo pair.

The topographic profiles produced by stereo image analysis do not conform to a global topographic 'zero' level, preventing direct comparisons of different areas from being made. However, a single stereo DEM is controlled within/across the DEM itself, ensuring that the relative heights are accurate. Stereo topography can be affected by the radiation noise and data compression artefacts present in many Galileo images (Schenk et al., 2004); these produce spurious patterns and distort the shape of features present in the stereo pair. Such anomalies reduce the ability of the stereo matching routine to lock in on features and to accurately measure parallax shifts (Schenk et al., 2004).

### **2.1.2. Photoclinometry (PC)/shape-from-shading in 2 dimensions**

Whereas stereo matching compares finite areas to estimate heights no closer than every 3-5 pixels, photoclinometry can generate accurate relative heights at single pixel resolution. Another advantage of this technique is that it requires only one image, allowing for more extensive topographic coverage of a body than using stereo alone. As a result, most topography of remote solar system bodies is produced using this technique.

In photoclinometry topographic slope is assessed from surface brightness (Bonner and Schmall, 1973). This begins with the extraction of a linear reflectance scan of an image which allows an average brightness, and hence theoretical horizontal surface/reference level, to be calculated. Slope is then determined with the use of a 'photometric function', by calculating the ratio of the actual observed brightness at a given pixel to that of the theoretical smooth horizontal surface at that point (Squyres and Veverka, 1981; Davis and Soderblom, 1984). Integration of the calculated tilts along the profile trace then allows the elevation of each pixel to be calculated relative to the first pixel of the scan (Efford, 1991). Photoclinometric mapping of planetary surfaces is described in more detail in Jankowski and Squyres (1991).

As the integration of brightness (and thus slope) is performed for each pixel relative to the first scanned pixel, the errors involved increase with distance from the start of the scan. This makes PC unreliable for the topographic profiling of long wavelength features as the cumulative build up of errors over long distance scans will become significant. Photoclinometry depends upon a ‘photometric function’ that combines image and surface characteristics such as pixel brightness and surface albedo; see Efford (1991) for a detailed review of the different functions, including the Lunar-Lambert and Minnaert functions. The accuracy of the height measurements is also dependant on the use of an appropriate photoclinometric function (Efford, 1991) as the relative elevations derived using different functions vary by up to 15% (Wilson et al., 1983). As a result, it is preferential to supplement PC with stereo data when available, particularly in regions of large albedo variance as PC determines slope via image brightness and is therefore affected by surface albedo.

## **2.2. Method**

Profiles presented in this thesis have been created using a combination of Galileo stereo and photoclinometry. The freshest craters on Ganymede display highly variable bright and dark deposits on their floors and rims (Schenk and McKinnon, 1991). As the accuracy of DEMs derived via photoclinometry is affected by surface albedo variations, measurements were restricted to slightly more mature craters that have lost most of their extreme albedo deposits while remaining morphologically crisp. Terrain type was noted so that any differences in crater trends on bright and dark terrains could be documented. The photoclinometry of this work incorporated a lunar-Lambert photometric function (McEwen, 1991):

$$\frac{I}{F} \propto \frac{2L\mu_0^*}{\mu^* + \mu_0^*} + (1 - L)\mu_0^* \quad (2.1)$$

$I$  is the observed intensity of the pixel and  $F$  is the estimated solar flux at the time of image capture. The cosines of the emission and incidence angles of the tilted surface element are represented by  $\mu^*$  and  $\mu_0^*$  respectively.  $L$  is an empirical term that varies for different planetary bodies describing the relative Lambertian scattering character of their surface. The uncertainties in the ‘ $L$ ’ term for Ganymede are not considered to be a source of serious error (Efford, 1991). Photoclinometry using the Minnaert function is subject to large errors in slope estimates when dealing with high albedo substances such as ice (Howard et al., 1982). The lunar-Lambert function was therefore chosen over other options such as the Minnaert function because it provides a more reliable fit to observations of high albedo surfaces.

Stereo data was created from Galileo Solid State Imager (SSI) images, with the use of the scene-recognition algorithm developed by Schenk et al. (2004). Once each DEM of a crater was obtained, spurious patterns or shape distortions created by radiation noise or data compression artefacts were removed through the use of standard image noise filters, and manually by visual inspection of the DEM and original image(s). Data gaps, deep shadows and features superimposed after crater formation were also removed.

6 to 8 radial profiles were taken across each crater, pairing when possible to create 3 to 4 full cross-sectional profiles (Figure 2.1); crater diameters were determined from an average of the 3 to 4 rim-to-rim distances. Measurement of other crater dimensions and internal features were made from all radial profiles of each crater (see Figure 2.2); this gave a range of values for each crater characteristic, which have been used to determine error bars based on the full range of data (not the standard deviation). Errors stated in this work are inclusive of both natural variations in topography as a function of azimuth, and errors inherent to the photogrammetry/stereo process (see Schenk et al., 2004). Obvious outliers in these values were discarded and the maximum reasonable value adopted for each feature measurement; height and width values in this work should therefore be viewed as an upper bound; the error bars extend down to the minimum recorded measurement for that crater characteristic. This approach was favoured above taking the average of all radial profiles, as the most accurate depth measurements of Ganymede are based on shadow measurements and are themselves maximum values (Schenk, 2002).

In cases where the topographic data was created via stereo photogrammetry and the local terrain was not significantly disrupted by later impact or fracturing, the profile was extended up to 5 crater radii so that the pre-impact terrain surface could also be recorded, thus enabling

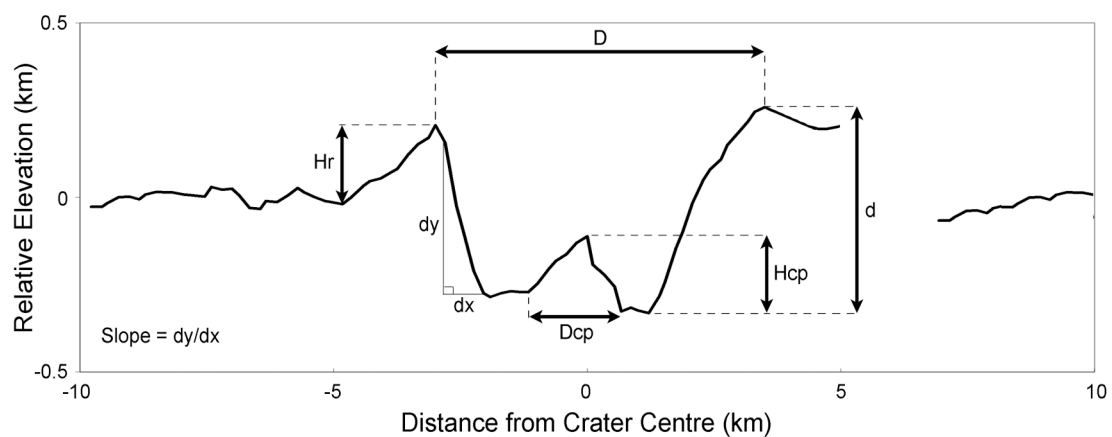


**Figure 2.2:** Annotated profile of a 7 km crater at 23N 194 W (see GN23:194 in Appendix A). Vertical exaggeration is 20:1.  $D$  is the rim-to-rim diameter;  $d$  is the rim to floor depth. Rim height and central peak height are noted with  $H_r$  and  $H_{cp}$  respectively.  $H_{cp}$  is central peak diameter. Wall slope calculation is also noted.

the pre-impact terrain slope to be removed from the profiles. This allowed easy comparison with computer simulation results, for which the pre-impact surface is represented by a smooth horizontal plain. In cases of extreme topographic tilt, craters with morphologic features deemed to be anomalous were not included in the dataset.

### **2.3. General Cratering Trends**

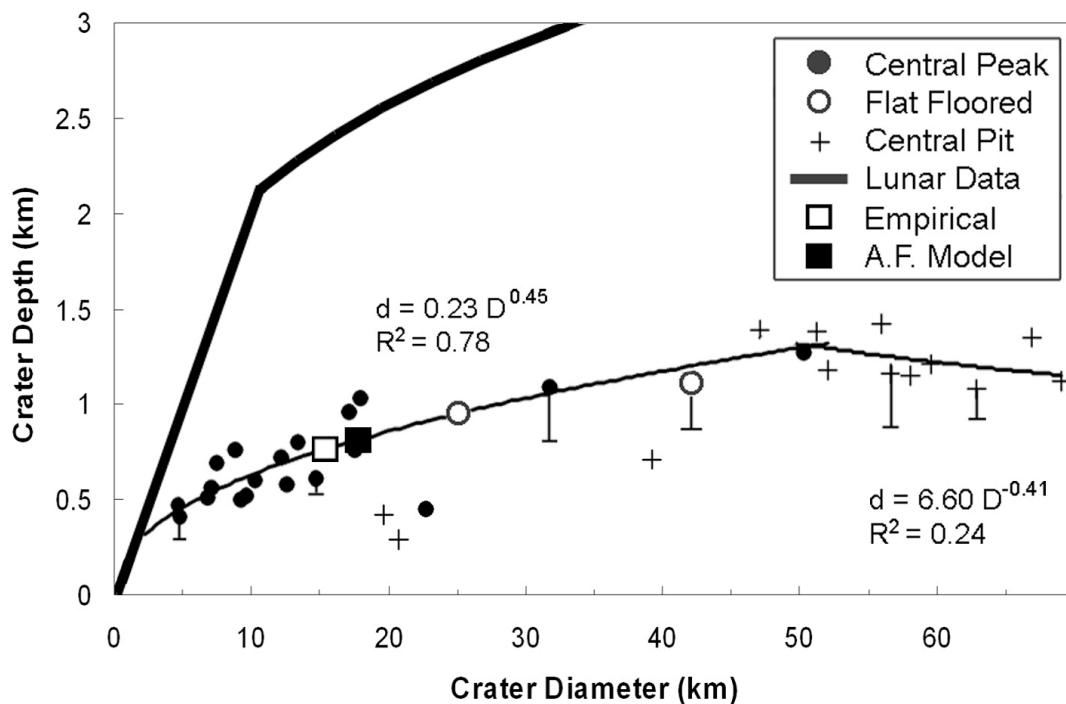
Topographic profiles were collected of 37 craters on Ganymede, ranging 1.6 to 102 km in diameter, and display a range of morphologies (Table 2.1). As profiles of simple craters ( $D < 2$  km) are rendered less reliable than larger craters due to their size relative to image resolution, analysis of simple craters on Ganymede was not attempted in this work. Likewise, as topographic profiles of a number of central dome craters on Ganymede have already been presented by Moore et al. (2004), Schenk and Moore (in prep.) and others, analysis of central dome morphologies is not included in this work. General depth-diameter ratios, rim heights and wall slope trends are created on the basis of the entire data set (Table 2.2) and are presented in this section prior to a separate analysis of the central peak (Section 2.4) and central pit crater trends (Chapter 3).

#### **2.3.1. Depth-Diameter ( $d/D$ ) Ratios**

The  $d/D$  relationship of fresh Ganymede craters has shown simple craters on Ganymede to have a similar  $d/D$  slope to that of lunar craters (Schenk, 1991). The depth of complex craters on Ganymede increases with increasing crater diameter to a similar degree as lunar craters. However, complex craters on Ganymede are inherently 60 – 70% shallower than pristine lunar craters of the same diameter (Croft, 1981). The simple-to-complex transition diameter for craters on Ganymede was first estimated at 3-5 km by Passey and Shoemaker (1982) and later refined by Schenk (1991) on the basis of Voyager data to  $5 \pm 1$  km. This value was updated after more accurate Galileo measurement to reveal an even smaller s-c transition diameter of  $1.9 \pm 0.5$  km (Schenk, 2002).

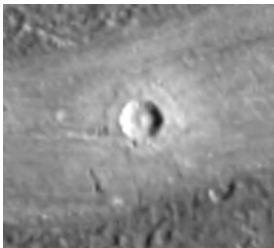
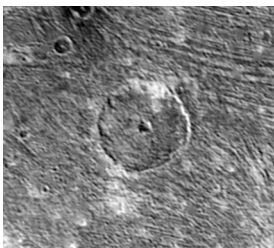
Schenk (2002) recorded a further two transitions in  $d/D$  ratio for larger crater sizes. The first occurs at  $\sim 26$  km and is associated with a subtle decrease in crater depths and the transition from central peak morphology to central pit and dome craters. Another, sharper reduction in crater depth occurs after  $\sim 60$  km and marks the development of anomalous crater morphologies. Both changes in  $d/D$  ratio are postulated to be due to temperature-induced transitions in rheology at depth (Schenk, 2002).

The  $d/D$  ratios of craters included in this work plot along the main  $d/D$  trend for fresh craters in Figure 1.11, and thus provide representative examples of fresh craters on Ganymede. As this work does not include simple craters, the simple to complex transition at  $1.9 \pm 0.5$  km is not included in Figure 2.3. There appear to be two further  $d/D$  transitions within these data at larger diameters of  $\sim 20$  and  $53$  km, although more depth measurements of craters in the  $20 - 50$  km diameter range are needed to confirm this. Craters up to diameters of  $\sim 53$  km can be fit by a general trend line of  $d = 0.23D^{0.45}$ , which includes central peak and smooth-floored craters (Figure 2.3). Above  $D \sim 53$  km, central pit morphology becomes prevalent and crater depths reduce further, producing a roll over in the  $d/D$  trend line. Central pits are observed in craters up to  $120$  km by Shoemaker and Passey (1982) and examples with diameters up to  $77$  km have been profiled in this work. The frequency of central pit occurrence is noted by Alzate and Barlow (2008) to peak between  $35$  and  $45$  km.



**Figure 2.3:** Depth-Diameter plot of craters on Ganymede that have been profiled for this work using Galileo data. The general  $d/D$  trend of unrelaxed central peak and central pit craters are included as thin black trend lines; the equations for these separate trends are marked next to the different line segments. A lunar trend line is included for comparison as a thick black line (Pike, 1977). Error bars are representative. Numerical modelling results from this work are included as squares and explained fully in Chapter 5.

**Table 2.1: Description of the crater types profiled in the course of this work\***

Crater Type	Diameter Range	Description	Example Image	Number Profiled
Simple	0 – 2 km	Bowl shaped depressions, no obvious internal features. Example to the right is 1 km in diameter.		1
Central Peak	2 – 50 km	Craters with a central uplift which is sometimes asymmetric or linear. Example to the right is 15 km in diameter		19
Smooth Floored	20 – 40 km	Craters without a clear central peak or pit, hummocky internal morphology. Example to the right is 35 km in diameter.		2
Central Pit	10 – 120 km	Craters with rimmed pits at or near their centre. Generally classified into 'floor pits' or 'summit pits'. Example to the right is 51 km in diameter.		14
Central Dome	60 – 180 km	Craters with depressed and flat floors, with an uplifted central pit that is partially filled by a smooth, high-albedo dome. Example to the right is 102 km in diameter.		1

\* The diameter ranges recorded for each crater type are approximate and based on Passey and Shoemaker (1982), Schenk (1993) and this work. A brief description of the crater morphology is included and the diameter of the imaged crater noted. More details about each crater type can be found in the main text. The far right column shows the number of each crater included in this work.

### 2.3.2. Rim Heights

The height of crater rims is thought to offer indirect evidence of the extent of rim-wall collapse (Melosh, 1989; Schenk, 1991). Rim heights ( $H_r$ ) of craters on the Moon have been documented by Hale and Grieve (1982) and found to be proportional to crater diameter ( $D$ ). A break in the  $H_r/D$  ratio occurs at a diameter of  $\sim 21$  km (Table 2.2) and indicates increased rim collapse in craters larger than this diameter.

Rims heights on Ganymede were measured by Schenk (1991) using a combination of Voyager photogrammetry and shadow measurements, and were found to increase with crater diameter, following a log-log slope of  $\sim 0.98$  up to diameters of 10 – 15 km. More obvious rim-wall slumping was observed in craters above this diameter; larger craters have a smaller  $H_r/D$  due to the relatively shorter rim heights and wider diameters produced by the additional rim collapse. Schenk (1991) found the break in  $H_r/D$  slope to occur at  $D = 14.2^{+9.6}_{-5.7}$  km.

The rim height measurements for craters below  $\sim 12$  km in diameter from Voyager photogrammetry (Schenk, 1991) are consistently  $\sim 20\%$  shorter than our new measurements from Galileo-based photogrammetry (Figure 2.4). This is likely due to Voyager's lower image resolution and has resulted in trend lines that differ for the smaller craters (Table 2.2); Voyager and Galileo-based rim height trends are consistent for the larger craters (Figure 2.4). The height of the crater rim above the pre-impact terrain level increases as crater size increases, as seen in lunar craters (Figure 2.4A); however, the relative rim height ( $H_r/D$ ) decreases (Figure 2.4B). Below  $11.85^{+2.25}_{-1.50}$  km diameter, the Ganymede (closed circles) and lunar trends are similar (Figure 2.4A). After this diameter the increase in rim height with increasing crater size is significantly less, and the lunar and Ganymede trend lines diverge. Ganymede crater rims become at least 50% shorter than lunar craters of the same size (Figure 2.4A). Both relations are included in Table 2.2. Above  $\sim 35$  km rim heights show a high variability. Trend lines 3 and 4 have been tentatively assigned for craters larger than this diameter in Figure 2.4A to mark suggested trends based on this and the Schenk (1991) datasets. The low number of data points for craters between 35 and 50 km, and the wide range of rim heights above crater diameters of  $\sim 50$  km suggest that trend lines 3 and 4 are unreliable without further supporting data.

### 2.3.3. Crater Wall Slopes

As slope angle is a proxy for the effective coefficient of friction ( $\mu_{\text{eff}}$ ), measurement of crater wall slope ( $S$ ) angles allows  $\mu_{\text{eff}}$  of the target material during impact crater formation to be estimated. The rim slopes of lunar craters above 15 km in diameter decrease as crater diameter increases from  $29^\circ$  to  $14^\circ$  for 10 - 60 km craters (Pike, 1976); this decrease in slope

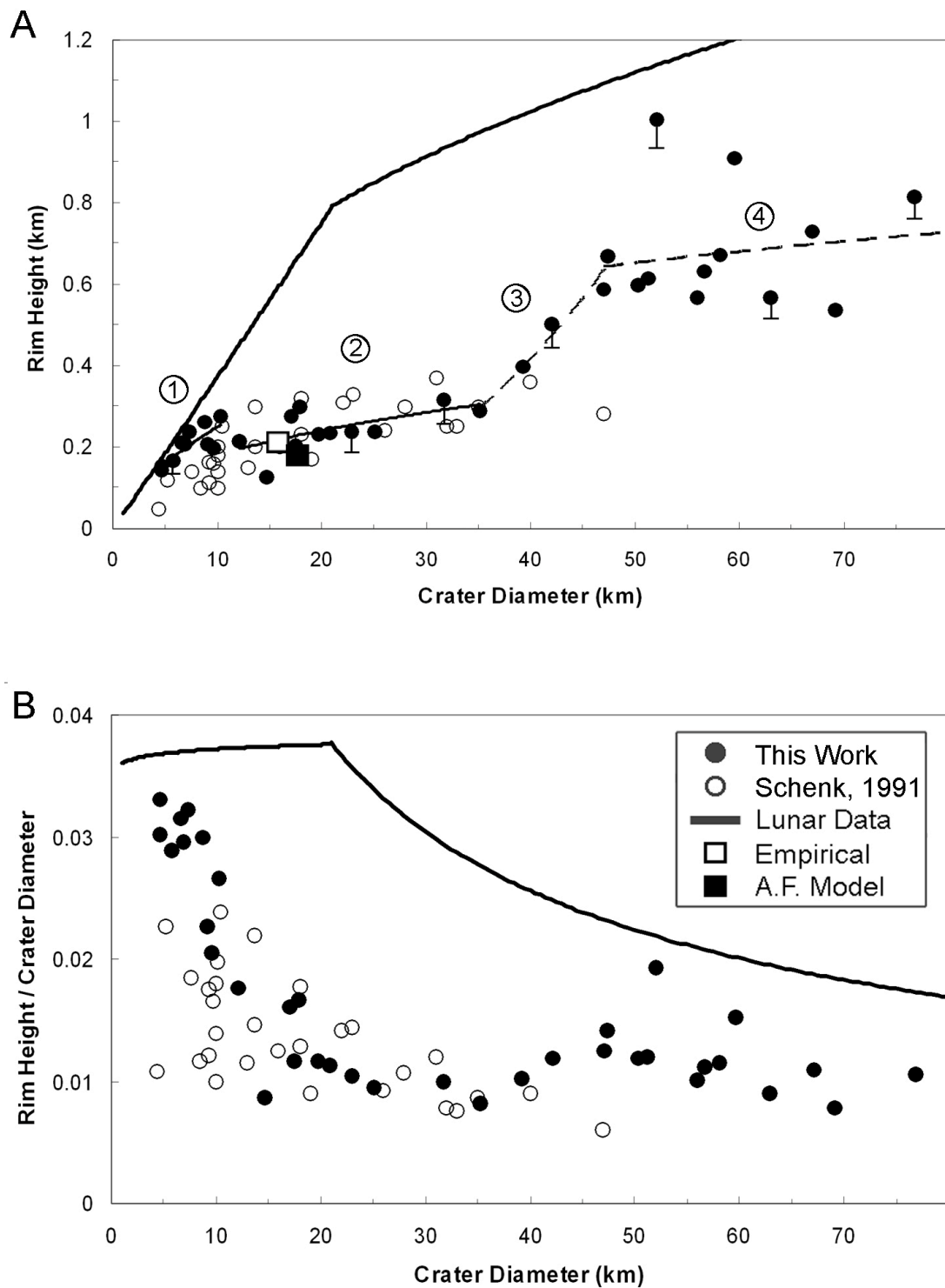


**Figure 2.4:** A) Rim height ( $H_r$ ) and Diameter ( $D$ ) measurements of craters on Ganymede. The trend line for rim heights of craters below  $\sim 12$  km in diameter was created based Galileo measurements only (1); the second trend line for craters between 12 and 35 km in diameter was constructed based on the combined Galileo and Voyager data set (2). Suggested trend lines for the crater rim heights of larger craters are marked with dashed lines (3 and 4). Representative error bars are included. B)  $H_r/D$  variation with crater diameter. A lunar trend line is included for comparison in both plots (Pike, 1977). The squares show the rim heights of the best-fit numerical model results (see Chapter 5); key applies to both plots.

angle demonstrates a weakening of the target material as crater size increases from  $\mu_{\text{eff}} = 0.55$  to 0.25. A kink in the slope of  $S/D$  plots is also observed (Pike, 1977), corresponding with the s-c transition. This is attributed to the additional amount of collapse from the rim of complex craters increasing diameter whilst decreasing the rim height (Pike, 1980).

A decrease in wall slope with crater size has also been observed for Ganymede (Wood, 1973), where a variation of wall slope between  $15^\circ$  and  $35^\circ$  has been noted (Schenk, 1991). A break in the  $S/D$  curve is recorded at a similar diameter to the change in the  $H/D$  ratio and correlates with the identification of slump features in Ganymede craters above  $15 \pm 5$  km (Schenk, 1991).

Average wall slopes ranging from  $5^\circ$  to  $25^\circ$  were recorded for craters in both bright and dark terrain; this is within the range of slump block and rim-wall scarp slopes measured by Schenk (1991) from Voyager photogrammetry ( $5^\circ - 10^\circ$  for slump blocks,  $15^\circ - 35^\circ$  for rim-wall scarps). These average crater wall slopes are consistently shallower than for similar sized craters on the Moon, by up to 50% (Figure 2.5). The wall slopes of Ganymede craters above 10 km in diameter decrease as crater diameter increases from  $24^\circ$  for a 10 km crater, to  $17^\circ$  for 50 - 60 km craters, a similar decrease to that observed in lunar craters.

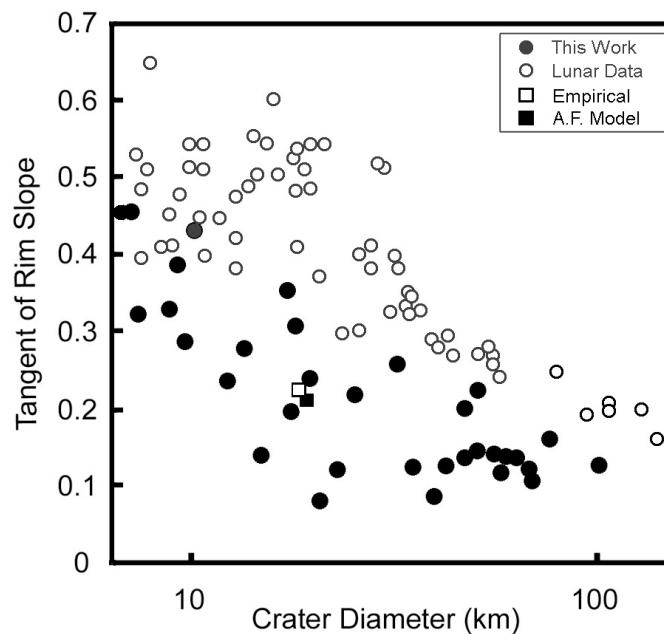


**Figure 2.5:** Wall slope and diameter measurements of craters on Ganymede (this work). Lunar and Ganymede wall slopes are shown with closed and open circles respectively. Lunar data is from Pike (1976). Errors in slope measurement are  $\sim 5\%$  and incorporated in the data point size. Best-fit simulation results are marked with squares (see Chapter 5).

## **2.4. Central Peak Craters**

Complex craters on Ganymede between 2 and 25 km generally have central peaks that protrude from their flat floors. They structurally resemble central peak craters on the terrestrial bodies except for their relatively shallow depths and the reduction in observed terraces on the crater wall (Schenk, 1991; 2002). The 19 central peak craters profiled in the course of this work have diameters which range from 4.7 km to 50.4 km in diameter.

Section 2.4.1 presents measurements and scaling trends for central peak dimensions relative to crater diameter. The size and shape of the peaks within these craters were found to be extremely variable. Figure 2.6 shows a typical central peak crater in dark terrain. Its peak is central and approximately symmetrical, and the peak dimensions are close to those expected on the basis of scaling trends in Table 2.2. Some craters profiled in this work were not included in the creation of these general scaling trends as they had morphologies deemed to be influenced by existing structures in the target or by post-impact modification (as explained in Chapter 1). Examples of these craters are presented in Section 2.4.2.

### **2.4.1. Central Peak Dimensions**

Central peaks are thought to form via the partial rebound of the transient crater floor during the modification phase of impact crater formation (e.g. Melosh, 1982). It is intuitive therefore that the larger the impact, the greater the amount of central uplift. This is reflected by the positive correlation of central peak dimensions with crater diameter (Table 2.2). On the Moon, peak diameter ( $D_{cp}$ ) is noted to be 0.2 to 0.25 of the crater diameter (e.g. Pike, 1985; Murray, 1979). The published trends for central peak heights ( $H_{cp}$ ) are more variable between different works, but also follow a positive trend (Figure 2.7B) (e.g. Wood, 1973; Wood and Anderson, 1978; Hale and Grieve 1982). Murray (1979) noted subtleties within these positive trends as both  $H_{cp}/D$  and  $D_{cp}/D$  ratios show an initial increase with crater diameter, until  $D \sim 40$  to 50 km, after which the ratios remain constant up to diameters of 80 km (Murray, 1979). Hale and Grieve (1982) did not note any such discontinuity in central peak width, although do note that peak height becomes irregular in craters of diameters between 51 and 80 km.

The apparent peak volumes ( $V_{cp}$ ) are also recorded to increase with crater size on the Moon (Figure 2.9). Different  $V_{cp}/D$  trends are observed for craters below 51 km and above 80 km (Hale and Grieve, 1982), (Table 2.2). The average slope of 22 central peak craters on the Moon was also measured by Hale and Grieve (1982); these data are included in Figure 2.10 and show no significant trend with crater size, nor any difference between large and small central peaks.

In previous work, a comparison of central peak widths ( $D_{cp}$ ) on Ganymede and the Moon revealed a similar positive correlation to crater diameter, except that central peaks on Ganymede were recorded as being  $\sim 25\%$  wider than central peaks in the same diameter lunar craters (Moore et al., 1985; Schenk, 1989). The heights of central peaks on Ganymede ( $H_{cp}$ ) increase rapidly with crater diameter for diameters  $< 15$  km (Passey and Shoemaker, 1982; Schenk, 1991). Above 15 km, there is a significant fall off in both  $H_{cp}/D$  and  $D_{cp}/D$  ratios; peaks become relatively narrower and less elevated with respect to crater diameters (Figure 2.8), and more closely resemble lunar trends (Schenk, 1991). Schenk (1991) suggested that more significant rim-wall collapse occurs in craters above 15 km in diameter on Ganymede decreasing the  $H_{cp}/D$  and  $D_{cp}/D$  ratios by either increasing apparent crater diameter or effectively burying the base of the central peak with debris from the rim collapse, decreasing its visible size.

The new measurements support previous observations that central peak diameters on Ganymede are typically  $1/3$  of the crater diameter (Table 2.2; Figure 2.7A). There is a positive trend in peak height for craters above 12 km in diameter which is similar to the lunar trend shown in Figure 2.7B. However, central peak heights in craters below this size do not follow published data. Instead, central peak height for craters below  $\sim 12$  km in diameter is highly variable and ranges from 50 to 550 m, with an average of  $\sim 200$  m. Both  $H_{cp}/D$  and  $D_{cp}/D$  ratios decrease with increasing crater size up to crater diameters of  $\sim 20$  km (Figure 2.8), after which they begin to increase, similar to lunar trends for craters of this size.

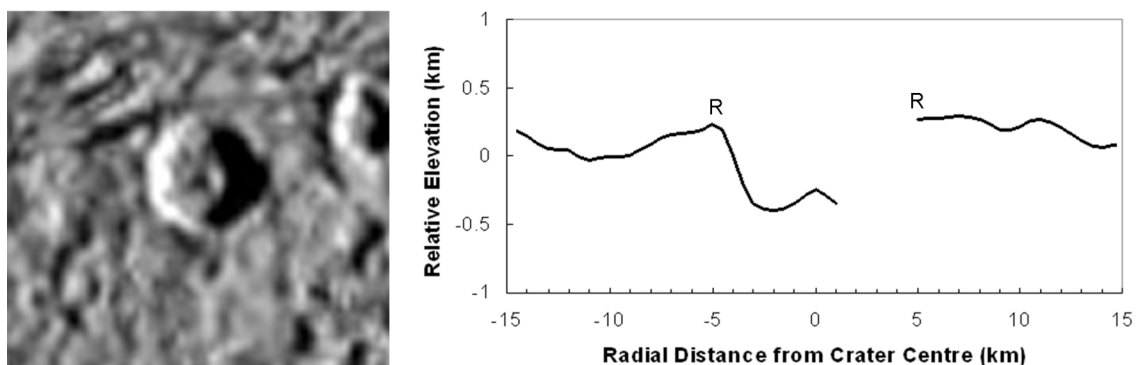


**Figure 2.6:** Example of a typical central peak crater. The crater is 9.6 km in diameter and located on an area of dark terrain at 1N 201W (see GN1:201 in Appendix A for more profiles and information). The topographic profile was taken along the east-west axis (North is up in the image). ‘R’ marks the location of the rims.

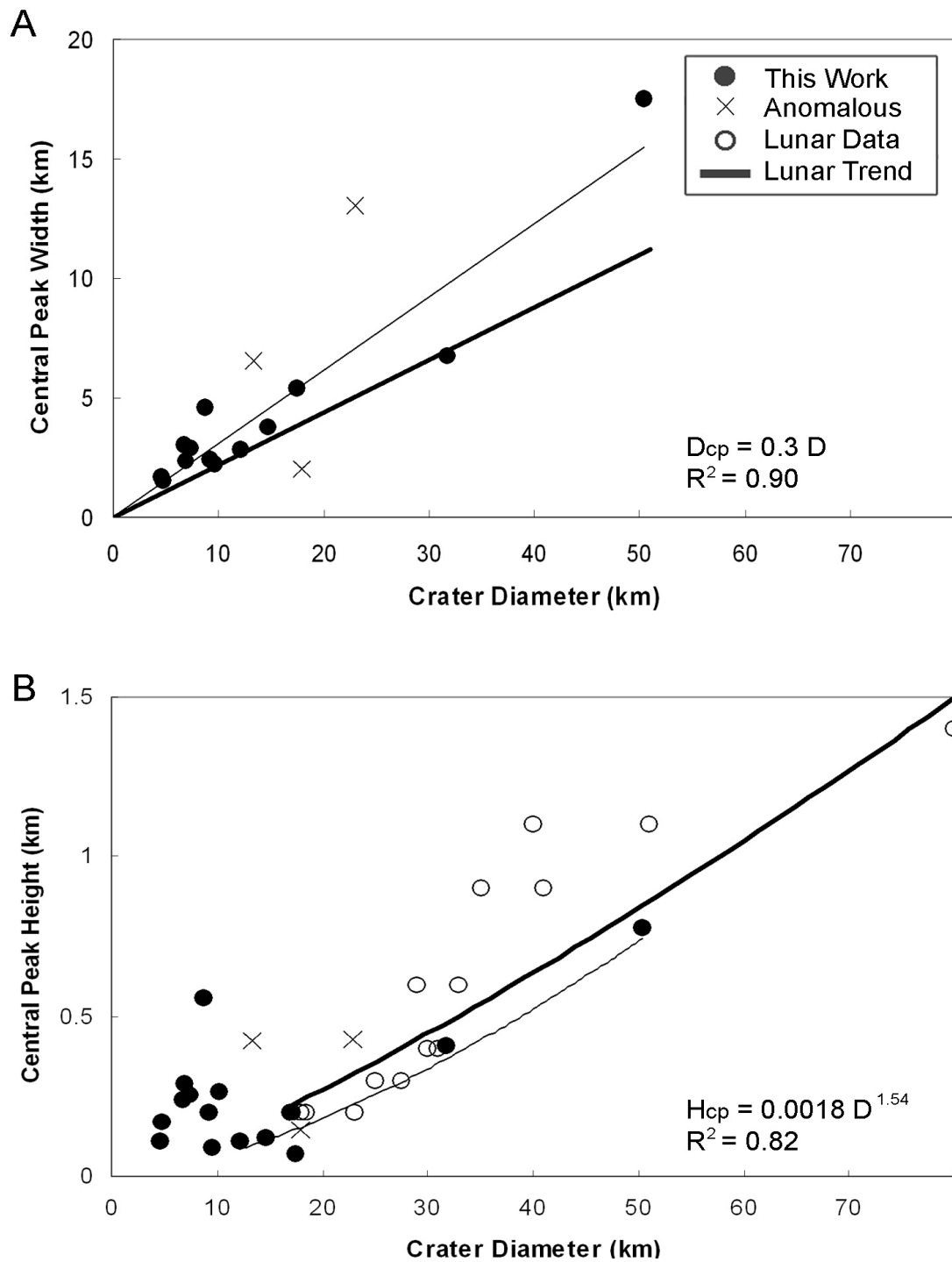


**Figure 2.7:** A) Central peak width ( $D_{cp}$ ) measurements. B) Central peak height ( $H_{cp}$ ) measurements. Legend applies to both plots. The Galileo-based trend line for central peak height is constructed from craters above 10 km only as peak heights below this crater size are highly variable. The measurements deemed anomalous for peak diameters are from craters that are obviously relaxed, leading to a wider central peak, or that have been affected by pre-existing structures in the Ganymede surface (see Section 2.4.2). The apparent disparity of the lunar data points (open circles) and trend line for lunar craters (Pike, 1985; Hale and Grieve, 1982) in Figure 2.7B is due to the trend line reflecting the peak heights of craters larger than 80 km in diameter in addition to those marked on the graph below this diameter.

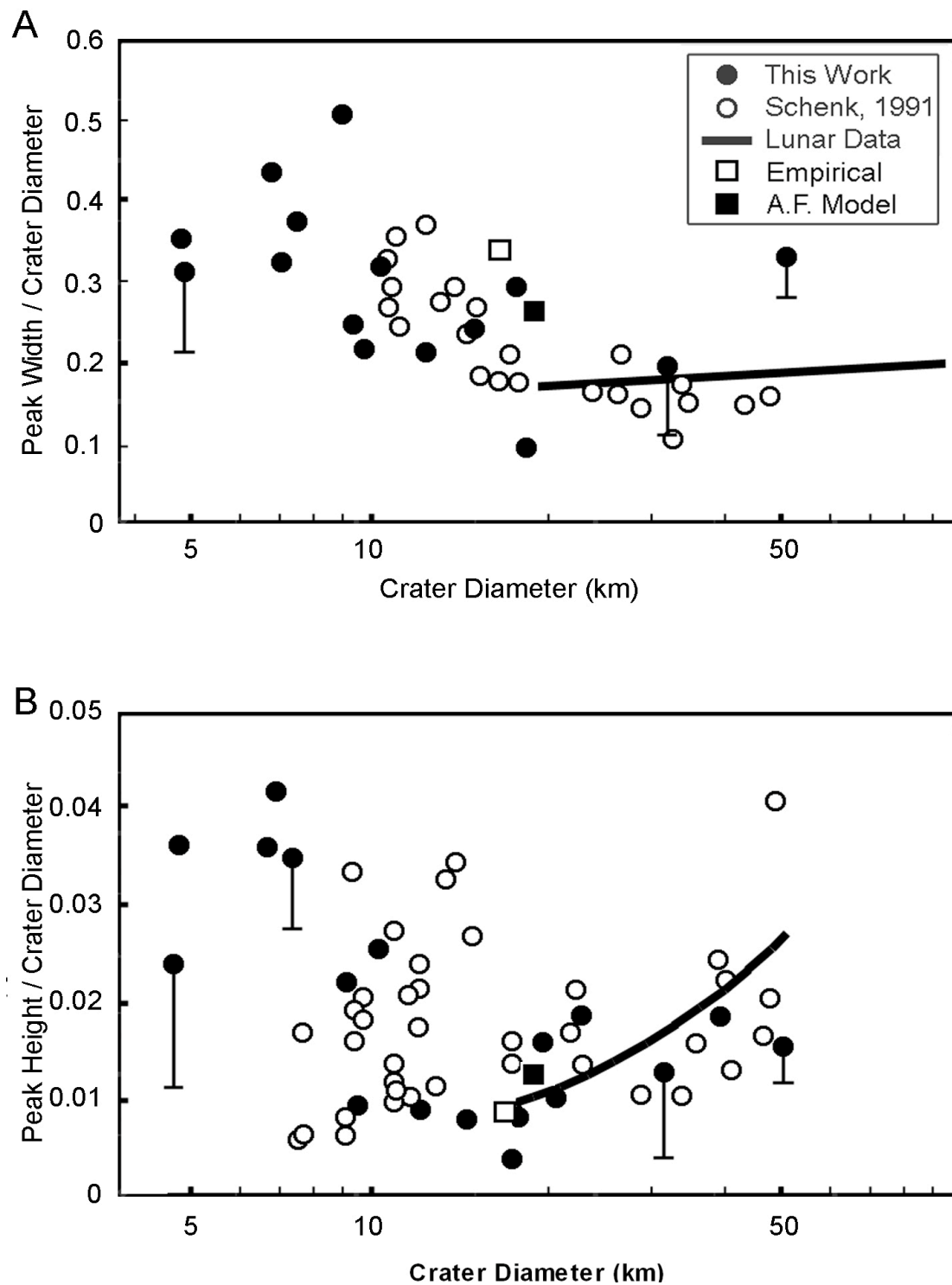


**Figure 2.8:** A) Relative central peak diameter ( $D_{cp}/D$ ) and crater diameter ( $D$ ) measurements of craters on Ganymede. B) Relative peak height ( $H_{cp}/D$ ) and diameter measurements. Measurement from Galileo and Voyager data are shown with closed and open circles respectively. The heavy lines correspond to the lunar peak width trends (Hale and Head, 1980) and peak height trends (Hale and Grieve, 1982). Best fit results from numerical modelling using an empirical strength model and one applying Acoustic Fluidization (A.F.) are marked with square data points (see Chapter 5).

As noted for central peak heights, the volume of central peak complexes is highly variable in craters below diameters of  $\sim 10$  km on Ganymede. After this crater diameter, peak volume increases with increasing crater size in a trend that appears to be similar to peak volumes on the Moon (Figure 2.9), although more data points for central peak craters on Ganymede between 10 and 50 km in diameter would be required to confirm this.

Central peak slopes on Ganymede decrease as crater size increases up to crater diameters of  $\sim 20$  km (Figure 2.10). After this diameter peak slopes may begin to increase, although there are too few data points between 20 and 50 km to confirm this at present. The slopes of central peaks on Ganymede are consistently shallower than the peaks in lunar craters of the same size.

**Table 2.2: Summary of scaling trends for the Moon and Ganymede**

	Moon		Ganymede - Voyager		Ganymede - Galileo	
Properties	Dependence on crater diameter, D	D range	Dependence on crater diameter, D	D range	Dependence on crater diameter, D	D range
Crater depth	$d = 0.196 D^{1.01} \dagger$ $d = 1.044 D^{0.301} \dagger$	< 11 km 11 - 400 km	$d = 0.088 D^{0.989} *$ $d = 0.22 D^{0.44} *$	0.4 - 1.4 km > 5 km	$d = D^{0.2} ***$ $d = 0.23 D^{0.45}$	< 1.9 ( $\pm 0.5$ ) km 5 - 53 km
Rim height	$H_r = 0.036 D^{1.014} \dagger$ $H_r = 0.236 D^{0.399} \dagger$	< 21 km 21 - 400 km	$H_r = D^{1.061} *$	< 14.2 km	$H_r = 0.045 D^{0.772}$ $H_r = 0.085 D^{0.365}$ $H_r = 0.00008 D^{2.326}$ $H_r = 0.048 D^{0.649}$	< 11.9 (+ 2.3, -1.5) km 12 - 35 km 35 - 50 km > 50 km
Peak diameter	$D_{cp} = 0.22D \dagger\dagger$	20 - 140 km	$0.3 D **$	< 14 km	$0.300 D$	5 - 50 km
Peak height	$H_{cp} = 0.032 D^{0.9} \ddagger \ddagger$ $H_{cp} = 0.0006 D^{1.969} \ddagger$	> 35 km 17 - 51 km	$H_{cp} = 0.0004 D^{2.557} *$ $H_{cp} = 0.09 D^{0.429} *$	< 15 km > 15 km	$H_{cp} = 0.0018 D^{1.54}$	12 - 50 km

$\dagger$  Pike, 1977

$\dagger\dagger$  Pike, 1985

$\ddagger\ddagger$  Wood and Andersson, 1978

$\ddagger$  Hale and Grieve, 1982

$*$  Schenk, 1991

$**$  Passey and Shoemaker, 1982

$***$  Schenk, 2002

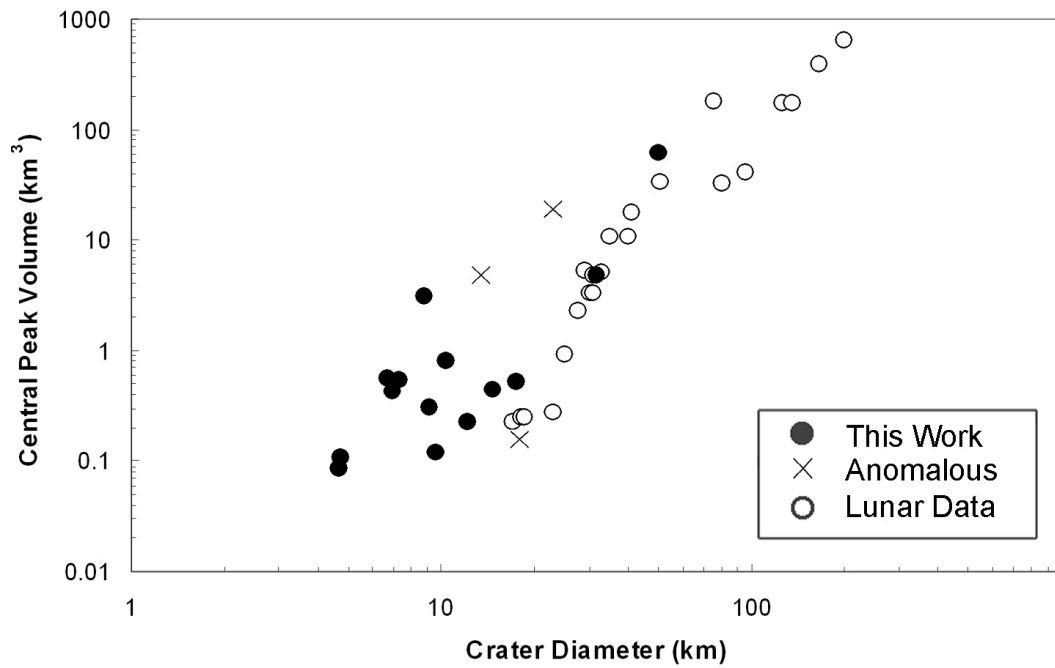


**Figure 2.9:** Approximate volumes of the central peaks in Ganymede craters (closed circles and crosses, this work), and lunar craters (Hale and Grieve, 1982). The ‘anomalous’ data points represent the peak volumes from the craters in Figure 2.11B, D and E.

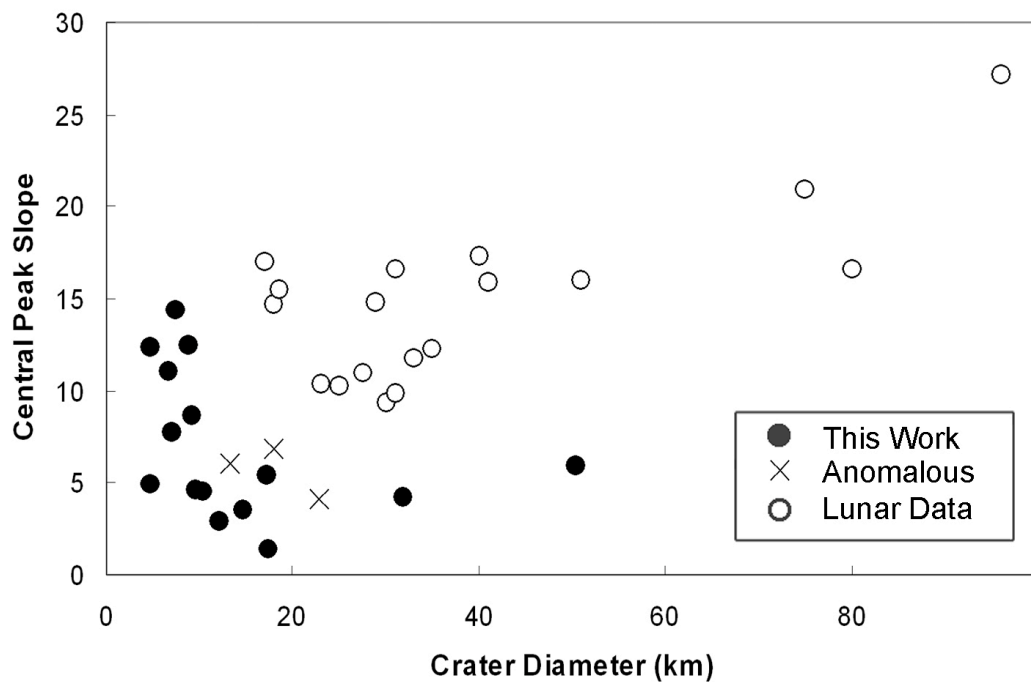


**Figure 2.10:** Average central peak slope values (in degrees) on Ganymede (closed circles and crosses, this work) and the Moon (Hale and Grieve, 1982). The ‘anomalous’ data points represent the peak volumes from the craters in Figure 2.11B, D and E.

### 2.4.2. All Peaks are Created Equal, but Some are More Equal Than Others

This section presents a selection of central peak craters to demonstrate the variation in central peak morphology. Measurements from some of the examples in Figure 2.11 were not included when creating the trends presented in Section 2.4.1. Each crater in Figure 2.11 is described and compared to the ‘typical’ central peak crater in Figure 2.6; reasons for exclusion from the main dataset are presented after each crater description where necessary.

The crater in Figure 2.11A has an overly large peak which is almost at the same elevation as the crater rim. This example has an average to high  $d/D$  ratio and is too small or young for relaxation to be the cause of the additional breadth and elevation of its peak. It is more likely that the local dark terrain is subject to a relatively high heat flow which has weakened the target material at depth, allowing for more significant central uplift. As the large central peak of this crater is not thought to be the result of post impact modification, dimensions of this crater and its central peak have been included in the main dataset in Section 2.4.1.

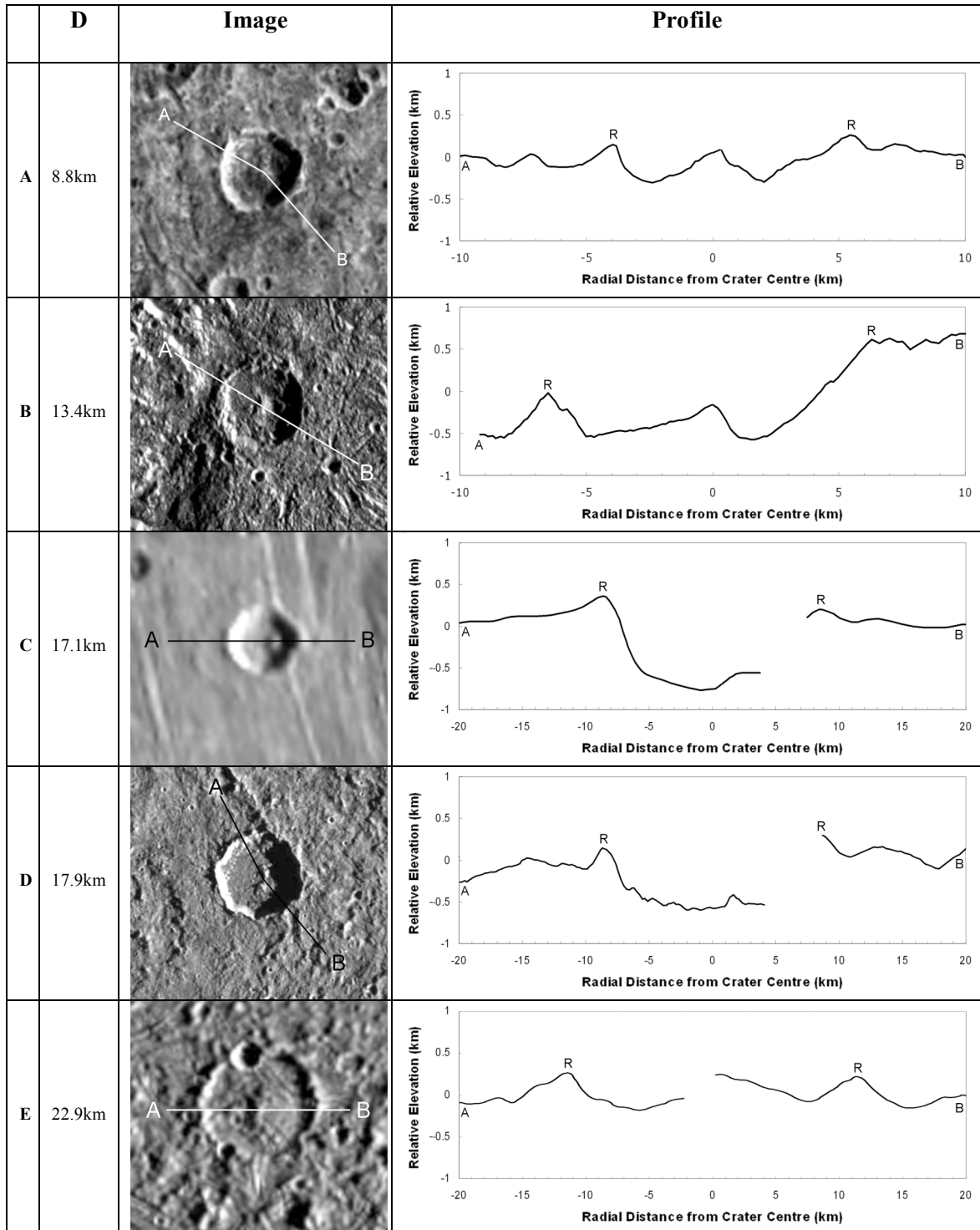
Figure 2.11B shows a crater that formed on the central dome of a pre-existing pene-dome crater, Neith. The north-western rim is significantly shallower than the rim section to the south-east; the central peak appears to be extended to the northwest. It is likely that this crater’s precarious placement on the edge of the dome has led to the partial collapse of its north-western edge, and led to its anomalous crater dimensions.

Figure 2.11C shows an example of an off-centre peak. The crater itself is also asymmetric and appears compacted on its eastern side. In this case, it is possible that ridges in the bright terrain to the East of the impact point retarded the excavation flow in that direction. The off-centre and partially shadowed peak of the crater in Figure 2.11C prevented width and volume measurements being collected.

The crater in Figure 2.11D is located on a pene-palimpsest, Buto Facula. It has a smaller than average central peak which is linear, rather than conical, in shape. The peak axis runs parallel to a ring section of Buto Facula to the East. It is possible that the pre-existing rings of Buto Facula have influenced the formation of this crater.

The crater shown in Figure 2.11E has a large central peak which is almost at the same elevation as the crater rim. It is located in a region of dark terrain that hosts a variety of anomalous and heavily relaxed craters with low  $d/D$  ratios. Unlike the crater in Figure 2.11A, this example is relatively old and relaxed, which typically leads to a low  $d/D$  ratio and larger central peak. The floors of relaxed craters tend to be uplifted and domed (Schenk, 1993); this elevates the level of central peaks and acts to broaden its apparent base.

As the craters in Figures 2.11B to E display morphologies deemed to be influenced by pre-existing structures or by post-impact modification, they were not included in the main data set used in the construction of scaling trends in Section 2.4.1.



**Figure 2.11:** Examples of central peak craters with anomalous central peaks. Rim-to-rim diameter of each crater is included and topographic profiles of the example craters are on the right, rims are marked with ‘R’. North is up in all images. Deep shadow produces regions of no data; this has been removed from the profiles where necessary. Each crater is described in the main text and detailed as part of Appendix A.

### 2.4.3. The Development of Central Peaks

A series of central peak crater profiles is presented in Figure 2.12, showing the general morphological trends as crater size increases. In craters below 30 km in diameter central peaks are mainly conical in shape (Figure 2.12A), although some off-centre and asymmetrical examples were recorded (Figure 2.11). Central peaks generally remain below the pre-impact surface level and below the crater rim height. However, some of the larger central peak craters that were profiled in this work show peak heights in excess of the pre-impact surface and the crater rim (Figure 2.12B). These large central peaks are also revealed to have a two-tiered morphology with a peak slope that is considerably shallower at its base. This morphology also occurs in the European summit-pit crater Cilix, and several central pit craters on Ganymede. In the largest central peak crater profiled in this work this wide peak base is replaced by a topographically expressed uplift between the central peak and the crater rim (Figure 2.12C). Such concentric internal features are also observed to surround the summits of central pit craters (Figure 2.12D) and increase in diameter with increasing crater size (see Chapter 3). These additional rings were not visible from previous images, reaffirming the usefulness of well resolved topographic data when assessing the morphology of geologic features on remote bodies.

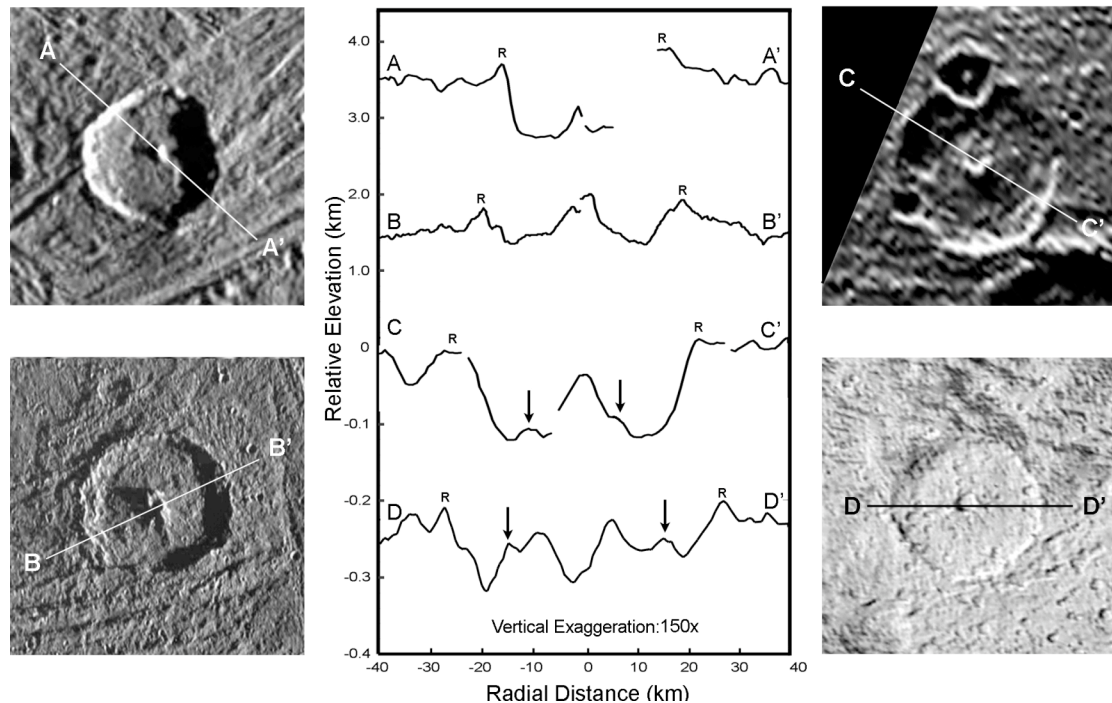


**Figure 2.12:** The paradigm of central peak collapse. Topographic profiles across a selection of craters on Ganymede. Profiles A and B are from Photoclinometry; C and D are from stereo photogrammetry. Crater rims are labelled with 'R', internal rings are highlighted with arrows. Artefacts and regions of high shadow have been removed. North is up in all images.

## **2.5. Transitional Crater Morphology**

This section introduces smooth-floored craters, a crater-type that is considered to be a transitional phase occurring at the simple-to-complex (s-c) transition and also between central peak and central pit morphologies. This chapter has specifically investigated the effect of target materials and structure on the morphology of central peak craters. However, as outlined earlier, the impact process is affected by other factors other than target properties including target gravity, impact velocity and angle and impactor composition. This section first introduces smooth-floored craters and then examines one example of a summit pit crater and smooth-floored crater with similar diameters on the same terrain to suggest that the morphologic differences between these craters are likely due to different impactor properties.

### **2.5.1. Smooth-Floored Craters**

Large craters that have flat floors and do not display a central peak or pit on Ganymede are designated ‘smooth-floored’ craters (Passey and Shoemaker, 1982). The terms ‘hummocky’ and ‘flat-floored’ have also been used to describe this crater type (Wood and Anderson, 1978). Smooth-floored craters on the Moon are generally seen as a transitional morphology between simple and central peak craters (e.g. Melosh, 1989). They have lower  $d/D$  ratios than simple craters and show progressively more rim collapse with increasing crater size (Wood and Anderson, 1978).

Smooth-floored craters like those seen on the Moon may also mark the transition from simple to complex morphology on Ganymede. However, as the s-c transition occurs at  $1.9 \pm 0.5$  km (Schenk, 2002), the relatively low image resolution prevents craters around the s-c transition diameter from being adequately resolved. Smooth-floored craters are also noted in

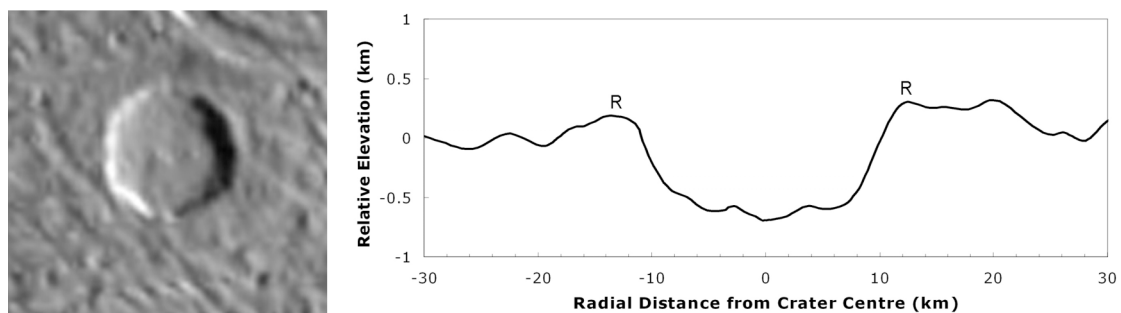


**Figure 2.13:** Image and topographic profile of a smooth-floored crater. The crater is 26 km in diameter and located on an area of dark terrain at 33N 192W. The topographic profile was taken along the east-west axis (north is up in the image); ‘R’ marks the crater rim (see GN33:192 in Appendix A for more profiles and information).

the transition range between central peak to central pit morphology.

Smooth-floored craters on Ganymede have diameters ranging from  $\sim 20$  to  $40$  km and have  $d/D$  ratios ranging from 1:6 to 1:20 in the bright terrain, and up to 1:80 in dark terrain (Passey and Shoemaker, 1982). They comprise  $\sim 20\%$  of the Ganymede craters of 20 to 30 km in diameter and 5% of the craters between 30 and 40 km (Passey and Shoemaker, 1982).

Only 2 smooth-floored craters were profiled in this work, preventing statistical analysis of this crater-type. The example in dark terrain (Figure 2.13) has a  $d/D$  ratio of 1:26 and a rim height of 240 m; both values are in line with those recorded by Passey and Shoemaker (1982). However, Achelous (Figure 2.14B) is deeper than expected for a smooth-floored crater in bright terrain with a  $d/D$  ratio of 1:37. Its rim height of 500 m is also larger than the expected value of 100 – 300m.

### 2.5.2. The Odd Couple – Gula and Achelous

Achelous is an example of a smooth-floored crater and is located  $\sim 130$  km south of the summit pit crater, Gula (Figure 2.14). Achelous and Gula are 35 km and 39 km in diameter respectively and both lie on the same swath of bright terrain. The similar size and terrain type suggest that the pair should be the same crater type. However, their internal morphologies differ dramatically. Gula has an extremely prominent central peak with a two-tiered slope and a small pit at the summit; Achelous has a hummocky floor with no obvious peak or pit structure predominating.

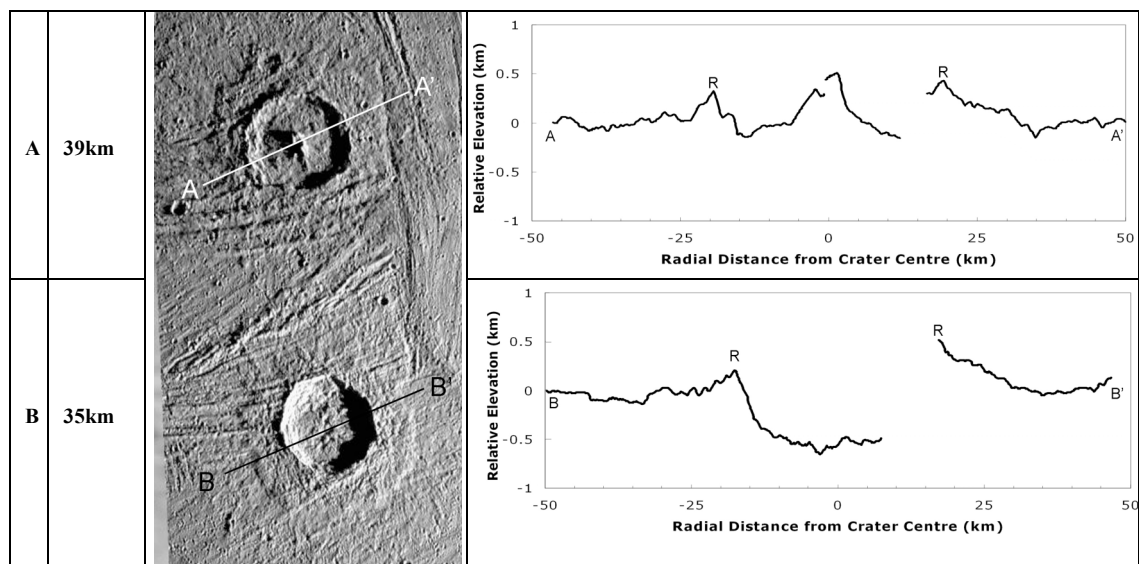


**Figure 2.14:** Galileo image showing the proximity of Gula (A) and Achelous (B), North is up. Approximate rim-to-rim diameters of the craters are noted on the left and the topographic profiles included on the right, 'R' marks the rims. Regions of deep shadow have been removed from the profiles.

On Ganymede the age of an impact crater can influence its morphology in two ways. Firstly, ancient impacts on the icy satellites are likely to have occurred into a warmer and thinner ice crust than exists in the current epoch (e.g. Passey and Shoemaker, 1982). Differences in target structure and heat flow may thus produce different crater morphologies. Secondly, older craters on Ganymede will have experienced more extreme amounts of viscous relaxation than younger craters of the same size, leading to shallower crater depths and up-domed crater floors.

The relative ages of Gula and Achelous can be approximated by comparing their ejecta morphology and cross-cutting relations with different episodes of bright terrain tectonism. A formation order can be tentatively assigned as lower numbers of craters on the ejecta blanket of Achelous hint at it being the youngest of the pair. However other evidence suggests that Gula and Achelous are not of significantly different ages. Both Gula and Achelous have polygonal rims (see Section 1.3.1). The orientation of the polygonal rim sections are similar for both craters, which could suggest their formation was influenced by the same ridges in the local terrain (Melosh, pers. comm., 2006). Both craters therefore formed after this episode of bright terrain tectonism. The ejecta blankets are still clearly visible for both craters, and are cut by ridges in bright terrain trending NEE-SWW. This suggests that the craters are relatively young, and that both formed prior to the same episode of bright terrain deformation which disturbed their ejecta blankets.

The similar size, terrain type, and apparent age of these two craters would suggest that the target properties were constant for both impacts. The craters therefore ought to have the same internal morphology. The striking difference in their morphology may be due instead to a difference in impactor properties (Melosh, pers. comm., 2006).

The same diameter of crater can be formed by small, high-velocity impactors and large, low-velocity impactors. Numerical modelling of impact crater formation in ice employing a range of impactor velocities is presented in Section 5.1.2. These simulations suggest that the impact of a small projectile travelling at a high velocity can result in more significant fluidization of the central crater region relative to the impact of a larger impactor travelling at a lower velocity. This additional fluidization facilitated the collapse of the central peaks in the simulated craters formed by the highest velocity impacts, producing summit pit morphology (Figure 5.3).

The lack of central feature in Achelous could be produced by the lack of central uplift, or by the complete collapse of an unstable fluid central peak. However, it was also noted from simulation results that craters in which central peaks had developed were consistently shallower than craters of the same diameter in which central uplift had not occurred. As Achelous is significantly deeper than Gula it is possible that central uplift did not occur in this

case. This suggests that the amount of fluidisation was less during the formation of Achelous than for Gula. It is thus likely that Gula was formed by the impact of a relatively small, but high velocity projectile, than that which formed Achelous. This led to a more fluidized central region producing its large two-tiered peak and shallow crater depth. Conversely, Achelous may be the result of a low velocity impact of a relatively large projectile. This will have formed a similar sized crater, but with a less fluid central region that did not uplift to form a central peak.

## **2.6. Observational Summary and Implications**

The selection of crater profiles provides a representative sample of fresh central peak crater morphology on Ganymede. The higher resolution of Galileo Solid State Imager (SSI) data has allowed the trends for smaller craters to be updated relative to Voyager measurements. This section summarises the results of this chapter and discusses the implications of differences in the lunar and Ganymede scaling trends.

The subtle changes in the  $d/D$  trends noted by Schenk (2002) at 26 and 60 km are apparent from this dataset, although this work records the transitions to occur at 20 and 53 km. As the measurements from Schenk (2002) are also based on Galileo data and included depth measurement of  $\sim 50$  complex craters, it is unlikely that the smaller transition diameters recorded by this work are the result of image resolution differences (as is certainly the case when comparing small crater dimensions recorded from Voyager and Galileo images). Instead, the relatively low number of fresh craters profiled in this work with diameters between 20 and 53 km have likely lead to slightly different trend line for this diameter range than that found by Schenk (2002).

### **2.6.1. Degree of Crater Collapse**

As Ganymede has a slightly lower gravity than that of the Moon ( $1.46 \text{ ms}^{-2}$  relative to  $1.63 \text{ ms}^{-2}$ ), rim heights might be expected to be slightly larger on Ganymede. For crater diameters below  $\sim 12$  km, the rim height trends of simple craters on the Moon and complex craters on Ganymede are similar, suggesting a common controlling factor in the rim collapse, despite the contrasting crater-types (Figure 2.4A). However, rims on Ganymede decrease in height relative to their lunar counterparts as crater size increases, demonstrating progressively more rim collapse in ice. Above  $\sim 35$  km, rim heights begin to increase relative to crater diameter, returning to a lunar-like  $H_r/D$  trend at  $\sim 45$  km. After this, rim heights on Ganymede are highly variable suggesting that the amount of collapse occurring in these craters is dependent

on a factor other than crater size. As larger transient craters reach greater depths within the target, large craters on Ganymede are more likely to be affected by any sub-surface layers. Variation in the amount of rim-wall collapse occurring in craters above 45 km in diameter may reflect impact into different thicknesses of Ganymede crust.

The separate rim height trend for craters above and below 11.9 (+2.3, -1.5) km suggests that a strength threshold is exceeded at this diameter which prompts more rigorous collapse in larger craters. This is separate from the simple-to-complex transition at  $1.9 \pm 0.5$  km (Schenk, 2002), and indicates that central floor uplift in complex craters occurs before the rim collapse and that they are not necessarily connected processes. This suggests that the earlier s-c transition on Ganymede relative to the Moon may be the result of more rapid floor rebound due to weaker material at depth, rather than weaker surface ice allowing the onset of rim collapse at smaller crater diameters.

### **2.6.2. Effective Strength of the Target**

Wall slopes on Ganymede are shallower than those in lunar craters of the same size (Figure 2.5). This shows the surface ice to have a lower effective coefficient of friction than lunar rock. Wall slope measurements of Ganymede craters suggest a maximum effective coefficient of friction for the surface ice during impact crater collapse of  $\sim 0.5$ , slightly below the maximum estimate of  $\sim 0.7$  inferred from Voyager slope data. There is no obvious difference between the wall slopes of craters in dark and bright terrain showing that the additional rock content of the dark terrain does not provide noticeable strengthening to the surface ice.

The average wall slope of Ganymede craters decreases as crater size increases, demonstrating an effective weakening of the target. This decrease in wall slope is similar on the Moon and Ganymede (Figure 2.5) indicating the same trend in material weakening with crater size on these two satellites. This suggests that the mechanism of material weakening during impact is similar in icy and rocky targets, and that existing lunar-style strength material models may also be appropriate for impact simulations on icy bodies.

### **2.6.3. Central Peak Development**

The height and width of central peaks on Ganymede increases with growing crater size (Table 2.2). The existence of Ganymede craters below  $\sim 15$  km in diameter relative to the same-sized lunar craters point towards more significant central uplift in icy targets. The Ganymede central peak trends in Figure 2.7 suggest peaks of craters larger than this diameter are slightly wider and shorter than their lunar counter parts. This results in shallower peak slopes, but similar peak volumes, for craters on Ganymede relative to the same sized craters on the Moon

(Figures 2.9 and 2.10). However, more measurements for Ganymede craters above 15 km are needed to ensure the estimated trend lines are appropriate.

The progression in central peak morphology, from a conical shape to a two-tiered slope with a wide base (Figure 2.12), suggests that large central peaks become gravitationally unstable and begin to collapse downwards and outwards. As peak collapse progresses further the basal sections may develop into the concentric ring morphology seen in Figures 2.12C and 2.12D. These rings are likely to be connected with internal crater development rather than purely the result of rim-wall collapse, as they occur inside the maximum distance from the crater rim expected for mega-terraces (Pearce and Melosh, 1986). The features could be produced as the result of outward moving peak material colliding with collapsing rim-wall debris, similar to a suggested mechanism for peak-ring formation (Morgan et al., 2000; Collins et al., 2002). Alternatively, such concentric topographic uplifts could be explained by multiple vertical oscillations of the crater's central region; this would provide support for the Bingham plastic model for peak-ring formation (Melosh, 1982; Alexopoulos and McKinnon, 1994).

#### **2.6.4. Implications for Numerical Modelling**

The similar trends in wall slopes between craters on the Moon and Ganymede suggest that the mechanism of material weakening during impact is similar in icy and rocky targets. This allows the application of existing lunar-style strength material models to impact simulations of cratering on icy bodies. As central peak formation does not appear to require significant rim collapse, numerical models must be able to produce central peak morphology by another means than material collapsing from the rim to the middle of the crater.

The wide spread of central peak morphologies shows that matching numerical modelling results to a specific crater profile may be inappropriate/unreliable as the morphology of that crater may not be typical, or may have been affected by local structures in the target or by post-impact modification. Also, the stark difference in the morphologies of Gula and Achelous, that appear to have formed under the same target conditions, acts as a reminder that even with constant target properties other factors also control final crater morphology. It is therefore considered advisable to test numerical modelling results by comparison with general trends, rather than by matching a specific crater profile, as the latter would only probe the impact conditions prevalent for that individual impact event.

Comparisons between craters on the Moon and Ganymede show that crater depth, wall slope and amount of central uplift are all affected by material properties. However no major differences were observed between similar-sized craters in the dark and bright terrain of Ganymede, and this suggests that dark terrain does not contain enough silicate material to

significantly increase the strength of the surface ice. Scaling trends based on measurements from craters in both bright and dark terrains are therefore suitable to compare to simulations of impact into pure ice.

## Chapter 3

# The Enigma of Central Pits

As crater diameter increases, central peak craters on rocky bodies are gradually replaced by peak-ring basins in which the central peak is replaced by a concentric ring of raised massifs. Although craters on the icy Galilean satellites exhibit simple and central peak morphologies, no peak-ring craters have been observed on these bodies (Chapman and McKinnon, 1986; McKinnon et al., 1991; Croft et al., 1995). Instead, with increasing crater size, central peak craters on Ganymede are gradually replaced by central pit craters (Figure 3.1).

As central pit craters are also observed on Mars, but rarely on less ice enriched crusts, most hypotheses for the origins of pits rely on the volatility or weakness of water ice. Consequently, if a mechanism for central pit formation can be determined, these craters may be used as a tool to investigate the relative water content of planetary crusts. Pit diameters on Ganymede have previously been measured and compared to Martian values (Passey and Shoemaker, 1982; Barlow, 2006; Alzate and Barlow, 2008). However, pit depth and volume information may also be important for testing between pit-forming mechanisms. This chapter introduces central pit craters, outlines the various formation theories, and presents new topographic profiles of central pit craters on Ganymede. Measurements from these data are used to construct scaling trends, which are then compared to available Martian data.

### **3.1. Introduction to Central Pit Craters**

Central pit craters on Ganymede range in diameter from 5 to 120 km (Passey and Shoemaker, 1982) and are abundant on both bright and dark terrains. Pit craters are characterised by a pit at or near the centre and a crater rim with terraced walls that extend for 1 – 7 km (Passey and Shoemaker, 1982). The central pits tend to have raised rims in the smallest central pit craters, but are usually rimless at larger crater diameters (Schenk and Moore, in Prep.); these two different morphologies are classified as ‘summit pit’ and ‘floor pit’ craters respectively. Many pit craters have floors that are domed rather than flat, although this is thought to be due to viscous relaxation subsequent to their formation, rather than being a morphological characteristic of the crater-type (Schenk, 1993).

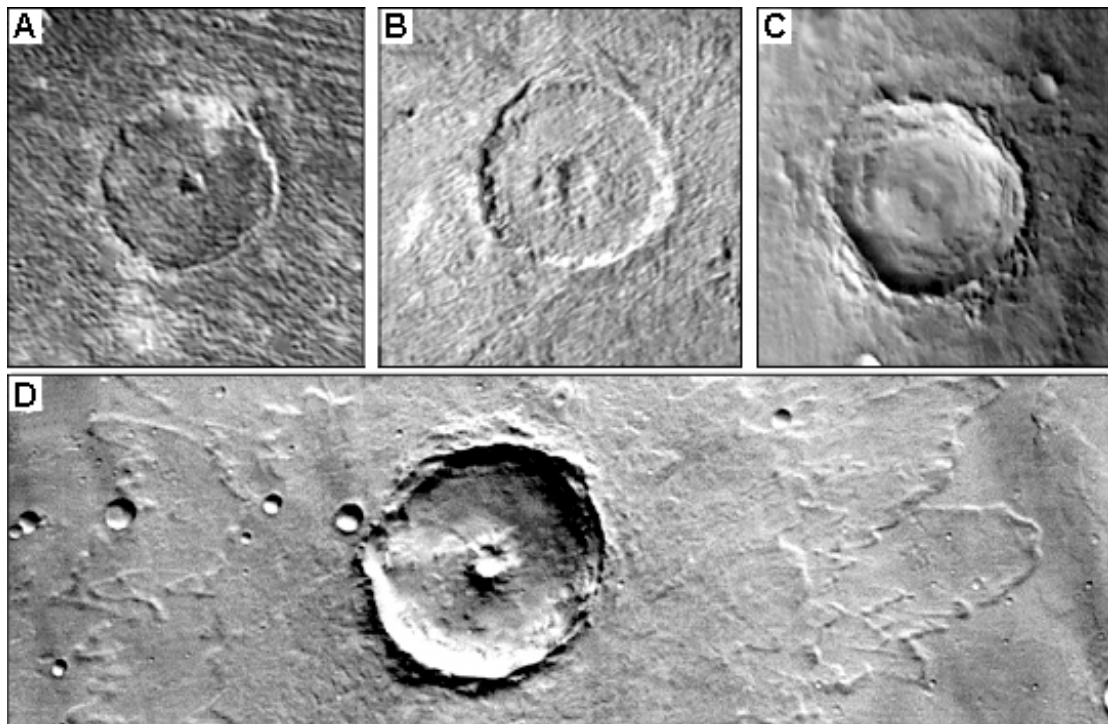


**Figure 3.1:** Examples of central pit craters on Ganymede and Mars: A) Galileo image of a 61 km diameter crater at 29S, 168W on Ganymede. B) Galileo image of Isis (67N, 201W), a 75 km diameter pit crater on Ganymede. C) The Martian ‘floor-pit’ crater, Shardi. This example is 17.4 km in diameter with a 2.8 km wide pit (THEMIS image I08526015). D) A 25 km ‘summit pit’ crater on Mars displaying a multiple layer ‘rampart’ ejecta blanket (THEMIS image I03218002).

### 3.1.1. Occurrence on Mars

Central pits are also observed on Mars (Figure 3.1C and D) in craters ranging from 5 to 57 km in diameter (Alzate and Barlow, 2008). They generally occur at larger crater diameters than central peaks, and in smaller craters than those with peak-rings. Wood et al. (1978) noted that pits in Martian craters occur most commonly between crater diameters of 25 – 45 km. This maximum frequency of central pit craters on Mars has since been revised and apparently occurs between  $D = 10 - 15$  km. This is smaller than that on Ganymede ( $D = 30 - 40$  km), and is thought to be a result of the different gravity of the two bodies (Alzate and Barlow, 2008).

Pits in Martian craters were first recognised by Smith (1976) and have been separated into three morphological types. 1) Small pits on relatively massive peaks, 2) larger pits with a summit surrounding them and 3) apparently rim-less pits. The first two types are commonly combined under the name of ‘summit pit’ craters as noted on Ganymede. Unlike the relatively small summit pit craters on Ganymede, summit pits on Mars span almost the same range of crater diameters as floor pit craters (Barlow, 2006).

### 3.1.2. Occurrence on Other Rocky Bodies

Apart from on Mars, central pit craters are notably rare on other silicate bodies. The only type of central pit crater observed on the Moon is that of a small pit on top of relatively large summit (Figure 3.2). Allen (1975) noted that 35 of the 123 craters included in his work with lunar craters possessed these pitted central peaks; larger central pits and floor pit craters are not observed. Figure 3.3A shows an image of the Serra da Cangalha structure in central Brazil, a possible Terrestrial example of a summit pit crater (Greeley et al., 1982). It has a rim-to-rim diameter of  $\sim 12$  km and a prominent 250 to 300 m high central ring structure of 3 – 5 km in diameter (Reinhold et al., 2004; De Cicco and Zucoloto, 2002).

The central morphology of the 22 km diameter Gosses Bluff structure in Australia (Figure 3.3B) has also been likened to a summit pit by Milton et al. (1972), who suggested that the annular peak shape was the result of less-resistant material at the core of the sandstone peak being excavated and ejected during floor rebound. At present, this unusual central morphology in Terrestrial craters is interpreted to be the result of differential erosion of a lithologically diverse central peak (McHone, 1986; Reinhold et al, 2004), rather than the original formation of a summit-pit complex.

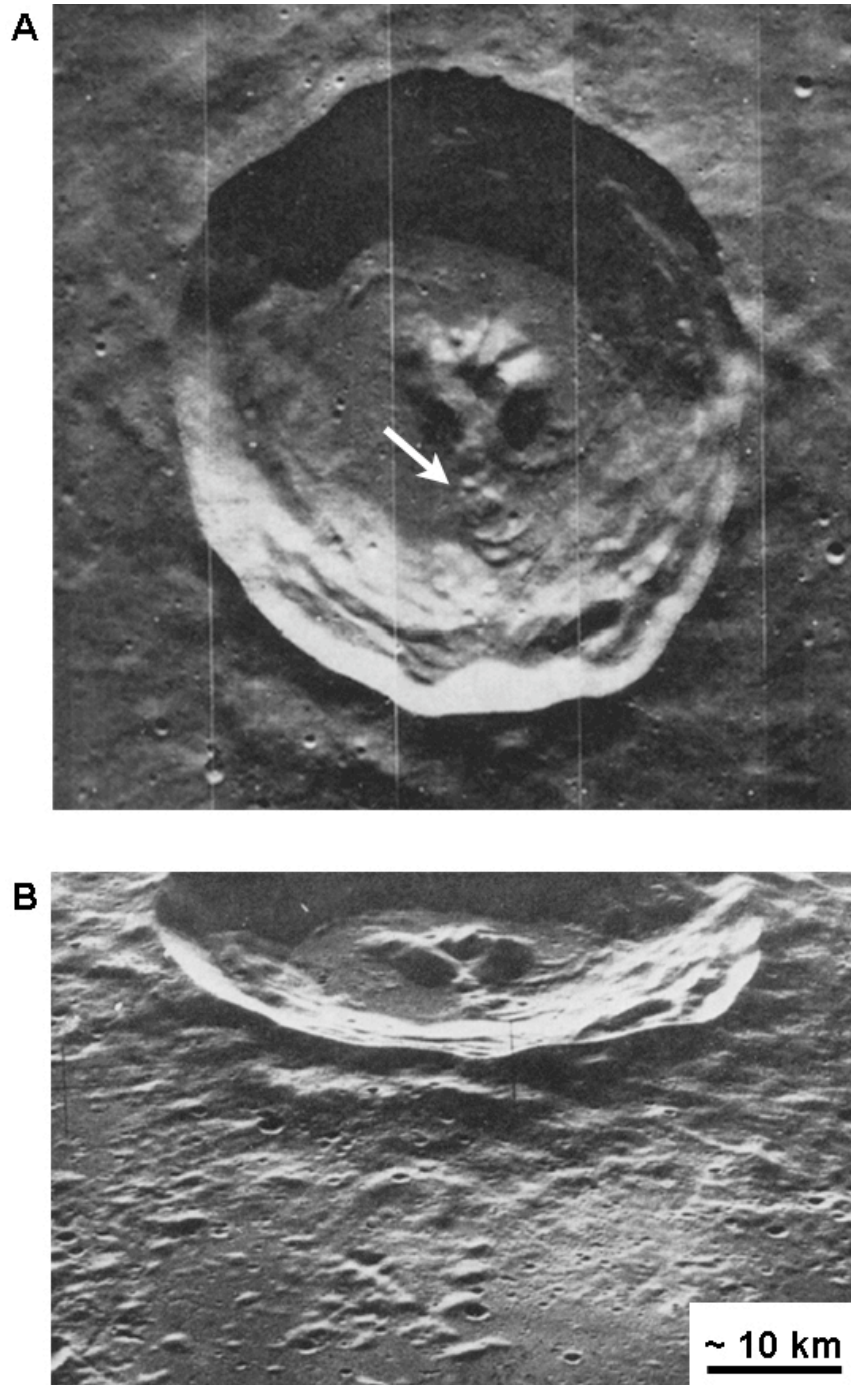


**Figure 3.2:** A) Lansberg – a 40 km crater in the lunar mare with a large central peak and small summit pit. Lunar Orbiter IV image (125-H3). A possible debris slide or flow deposit is marked with an arrow, as identified by Allen (1975). B) Oblique image of the same crater. Apollo 14 image (70 9825).

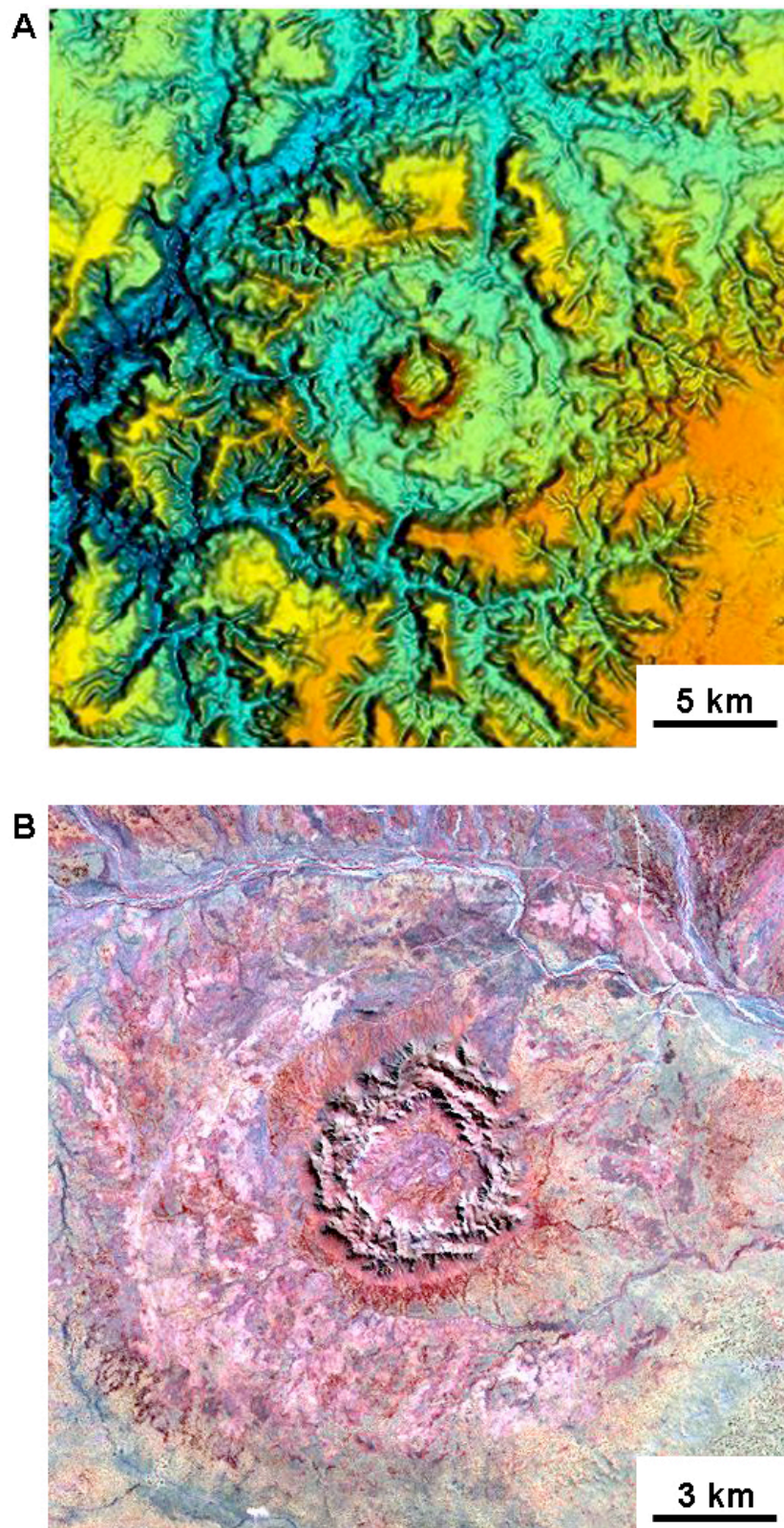


**Figure 3.3:** A) DEM image of the Serra da Cangalha structure in central Brazil ( $8^{\circ} 5'S$ ,  $46^{\circ} 52'W$ ), taken from the Earth Impact Database. The crater rim is estimated to have a diameter of 12 km. Image produced by Dr. Carlos Roberto de Souza Filho. B) Landsat image of the Gosses Bluff structure in Australia ( $23^{\circ} 49' 15'' S$ ,  $132^{\circ} 18' 28'' W$ ). Original rim-to-rim diameter is estimated to be 22km. North is up in both images.

## **3.2. Formation of Central Pits**

The formation of large central pits remains a mystery, despite several proposed mechanisms, the most plausible of which are outlined in the following section. Central pits are observed on the Jovian moons of Ganymede, Callisto and Europa, and the Uranian satellite Titania (Schenk, 1993). As central pit craters are not found consistently on all of the icy satellites, it suggests that the mechanism responsible for forming the central pit is not simply a result of the cratering process in ice. Central pit craters are also found in abundance on Mars showing that the mechanism of pit formation must be able to operate in both ice and ice-rock mixes.

Some laboratory-scale impact experiments have shown that rising central peaks in multi-layered targets can become detached at maximum elevation (Greeley et al., 1982). The debris from this disrupted peak then falls back into the original crater bowl creating a central secondary crater. A similar mechanism was proposed by Murray (1979) for the formation of peak-rings on the Moon. Greeley et al. (1982) note that the secondary impactor created by the disruption of the central peak was most likely held together by surface tension in their laboratory experiments. As this property cannot be expected to scale to larger impact events, this theoretical pit formation mechanism is already deemed unlikely to operate on planetary scales. As some earlier theories have been refuted on the basis of new data, the following sub-sections outline the most plausible and currently accepted theories only.

### **3.2.1 Impact into a Layered Target**

As already noted, the morphology of an impact crater depends upon not just the size, velocity and composition of the impacting body, but also the gravity, material properties and structure of the target. It is therefore expected that variation in upper crustal structure and composition will produce a range of impact morphologies, with some layering combinations plausibly resulting in the formation of central pits (Greeley et al., 1982). Laboratory impact cratering experiments have shown that the presence of layering within a target has a direct effect on crater morphology at laboratory scales. Greeley et al. (1982) performed a series of gas-gun experiments into differently layered targets, which produced some crater forms deemed analogous to central pit craters. In this study, pits and 'disturbed' central terrain were created by high velocity impact into layers of water, clay, sand and ice in a variety of different layering combinations.

Layering and crustal composition differences are thought to be a factor in central pit formation on Ganymede as the minimum size for central pit craters is 12 km in Ganymede dark terrain, compared to 25 km in bright terrain (Greeley et al., 1982). This variation has

been attributed to differences in the crustal structure at the time of formation (Passey and Shoemaker, 1982), or variation in the water ice content of the two terrains (Klaybor and Barlow, 2006). This could also be due to a higher heat flow at the time of impact into the older dark terrain. Prior to the formation of the younger bright terrain, Ganymede's near-surface would have been warmer, due to residual internal heat of Ganymede formation, radiogenic heating, etc (Passey and Shoemaker, 1982). This higher ancient heat flow could plausibly have maintained an ocean at a shallower depth than presently exists. Therefore, the older impacts will have occurred into a thinner warmer crust than younger impacts, and thus may explain why older central pit craters could be produced by smaller impact events. As Ganymede cooled, its crust will have thickened, requiring larger impacts to penetrate to the once shallower water layer. This crustal thickening with time may well be complicated by periodic changes in the tidal influence of Jupiter, causing the ice thickness to oscillate about a mean point (Sotin and Tobie, 2004).

### **3.2.2 Collapse of a Central Peak in Weak Ice**

Passey and Shoemaker (1982) suggested that a central peak whose weight becomes too great to be supported by the subjacent material would promptly collapse during/after crater formation, creating a pit. In this scenario, collapse occurs when stresses at the base of the central uplift exceed the effective material strength of the target. Schenk (1993) has investigated this by calculating the effective strength from the heights of the largest preserved central peaks on Ganymede. Strength estimates made by this method are similar to those based on simple-to-complex transition diameters. It is not clear why such collapse is proposed to form a pit rather than centralised broken massifs as in the lunar crater Copernicus. However, if combined with the multiple peak oscillation theory of Melosh (1982), the development of a central pit might be possible in a target material acting as a Bingham fluid during impact.

### **3.2.3 Explosive Release of Volatiles**

A sub-surface volatile layer has previously been suggested to explain unusual features of Martian impact ejecta blankets (Figure 3.1D) (Carr et al., 1977). Wood et al. (1978) proposed that central pit crater morphology on Mars may be due to the interaction of an expanding transient cavity with such a sub-surface layer or zone of ice. The near adiabatic compression and generation of heat during impact is hypothesised to result in the explosive decompression of sub-surface volatiles (Kieffer, 1977). The upper rock layers uplift to form a central peak, whilst the volatile material at the core of the peak is lost via vaporisation (Wood et al., 1978). The remaining crust is then suggested to collapse into the void left by the vented volatiles,

forming a pit (Hodges et al., 1980). Such a process could also explain the existence of small summit pits on the Moon (Figure 3.2) if impact occurs into a region with relatively high volatile content.

The High Resolution Imaging Science Experiment (HiRISE) has revealed morphological features of geologically young impact craters not visible in previous imagery. This includes the identification of ‘ponded pitted material’, interpreted to be volatile and clast-rich impact melt deposits (McEwen et al., 2007). This material has been noted on crater floors, terraces, ejecta blankets and occasionally on the flanks of central uplifts. It is commonly fractured or pitted (Figure 3.4), with pitted materials being by far the most abundant. These pits are sub-circular, rimless and without obvious surrounding ejecta which would indicate an explosive or impact origin. They are thought to be formed by the venting of volatiles and subsequent collapse of the surface material into the void (Tornabene pers. comm., 2007). These pits commonly occur in coalescing groups at the centre of the impact melt bodies; the floor beneath these pit concentrations is subsided. It is possible that a high enough concentration of these pits at the centre of Martian craters would produce, or contribute to the formation of central pits (Tornabene et al., 2007). Such a process would also be valid for the formation of Ganymede pit craters. However, the relatively low resolution images available of the Galilean satellites currently prevent identification of similar pitting in craters on Ganymede to test this hypothesis.

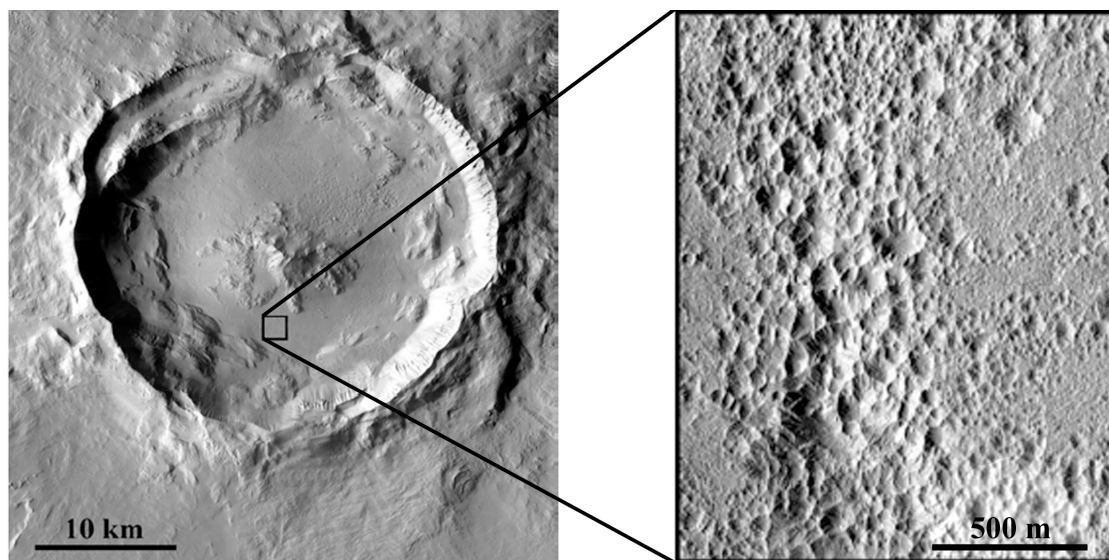


**Figure 3.4:** (left) THEMIS VIS mosaic of Tooting crater on Mars (23.4N, 207.5E), North is down (right) HiRISE view of a pitted section of the Tooting crater floor. The pits lack raised rims and are sub-circular; pits of this type are also noted on the lower flanks of the central uplift (Tornabene et al., 2007).

### 3.2.4. Draining of Impact Melt

Although the idea of a liquid central peak comprised of material derived from an excavated mantle (Croft, 1983) is probably untenable, the idea of a fluid central peak is still valid. The high shock temperatures produced on impact will vaporize and melt the target material closest to the impact point, leading to melt pools in central regions. The melt water produced during icy impacts, when not immediately vaporized or re-frozen, could sink into fractures where it would then refreeze. This could conceivably result in a central pit, rather than a central pool of impact melt, as would be the case for impact craters on silicate bodies (Melosh, pers. com., 2006). This process would similarly explain the observations of central peaks with pitted summits and allow for offset central pits. The Martian pitted material noted in Figure 3.4 may be also formed via this process, providing there is a sufficient amount of ground-ice (Tornabene and Melosh, pers. com., 2008).

## 3.3. Observational Data for Central Pits

The extraction of topographic profiles and the calculation of uncertainties in depth and slope measurements were performed following the same method outlined in Section 2.2. The additional measurements taken for central pit craters are shown in Figure 3.5. This section presents these measurements and, where possible, compares the Ganymede trend to Martian central pits.

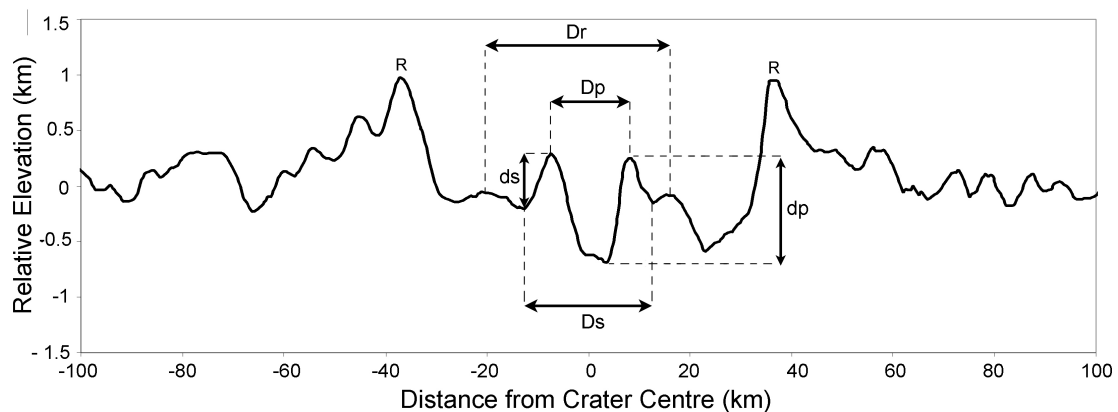


**Figure 3.5:** Annotated profile of the central pit crater, Isis, at 67.5S 201.5W. Depth, diameter and rim height measurements were recorded in the same way as shown on the central peak crater (Figure 2.2).  $D_p$ ,  $D_s$  and  $D_r$  are the diameters of the pit, summit and internal ring respectively.  $d_p$  is the pit depth and  $d_s$  is the summit height. Crater rims are marked with 'R', vertical exaggeration is 67x.

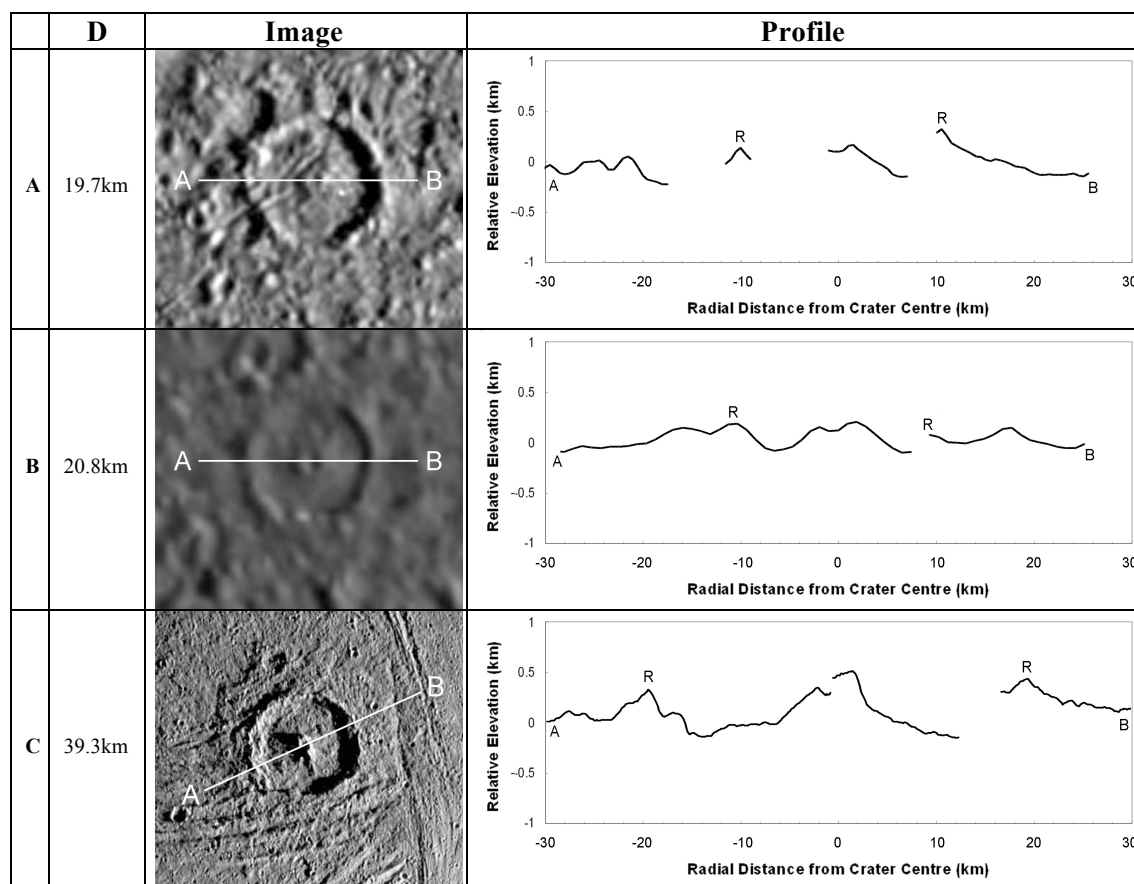


**Figure 3.6:** Summit pit craters on Ganymede included in this work. A and B are relaxed craters in dark terrain at 0.4N : 201.4W and 41N : 195.4W respectively. C shows the summit pit crater Gula (see discussion in 2.5.2). Topographic profiles of the craters are shown on the right; crater rims are marked with ‘R’.

Profiles of central pit craters were created using Galileo stereo only, as their large size renders the relative heights determined from photoclinometry inaccurate. Several central pit craters in this data set are covered in high-albedo deposits, which also prove a source of error in photoclinometry. Fourteen central pit craters were profiled, including 3 summit pits (Figure 3.6). All three summit pit craters have summit elevations that approach or exceed the crater rim height. The summit pit craters pictured in Figure 3.6A and B are older and more obviously relaxed compared to Gula in Figure 3.6C.

### 3.3.1 Pit Diameters

The relationship between pit diameter and crater size on Ganymede has already been investigated (e.g. Passey and Shoemaker, 1982; Schenk, 1993; Barlow, 2006). Summit and floor pits both increase in diameter as crater size increases, but with differing trends as summit pit craters have smaller  $D_p/D$  ratios than floor pit craters. The combined trend of pit

diameters with crater size produces an exponential relationship (Table 3.1, Figure 3.7A), recorded as  $D_p = 1.9e^{0.023D}$  by Passey and Shoemaker (1982) and supported by Schenk (1991).

An age-dependence has also been noted in which older pit craters have larger pits than younger examples. This is deemed due to the ice crust being warmer and thinner for ancient impacts due to a higher crustal heat flow earlier in Ganymede's history (Passey and Shoemaker, 1982). The effect of crustal properties on the occurrence and dimensions of central pits is also evident from the different concentrations of central pit craters on the dark and bright terrain of Ganymede. Klaybor and Barlow (2006) noted higher concentrations of central pits, and larger  $D_p/D$  ratios, on the dark terrain which is composed of older, more silicate-rich ice than the bright terrain. Barlow (2006) interpreted this to suggest that central pit formation is more effective in ice-rock mixtures than in pure ice. It could also be an effect of different target temperatures, as the dark terrain's albedo-related temperature is higher than that of the bright terrain.

The diameters of central pit craters on Mars have been recorded (e.g. Barlow, 2006) and are plotted alongside Ganymede pit data in Figure 3.7B. Both summit and floor pits, and relaxed and relatively fresh, craters on a variety of Martian terrains are presented in this figure. Barlow (2006) record a difference between the diameters of summit and floor pits: summit pits have  $D_p/D$  ratios between 0.05 and 0.19; this is smaller relative to floor pits, which have  $D_p/D$  ratios of 0.07 to 0.28. A difference has also been observed in the diameters of central pits in craters on 'cratered terrain' and the volcanic 'plains units' of Mars ('CT' and 'PU' in Table 3.1 respectively). Pits in craters on PU are up to 50% larger than in CT; this is interpreted as the result of shallower volatile depths and/or greater volatile concentrations in the plains units (Wood et al., 1978).

Data from this work supports existing Ganymede scaling trends, with pit diameters increasing exponentially with crater diameter (Table 3.1; Figure 3.7A). Both Voyager-based measurements (Schenk, 1993), and Galileo-based measurements from this work are plotted alongside data from Martian central pit craters in Figure 3.7B. Pits in Craters below  $\sim 40$  km in Diameter follow the same trend on both Mars and Ganymede ( $D_p = 1.89e^{0.03D}$ ). At larger crater diameters the Ganymede and Martian trends diverge and the Ganymede pit diameters increase relative to the majority of their Martian counterparts. This difference is most obvious at crater diameters larger than 70 km, in which pits in Ganymede craters are consistently larger than those in Martian craters.

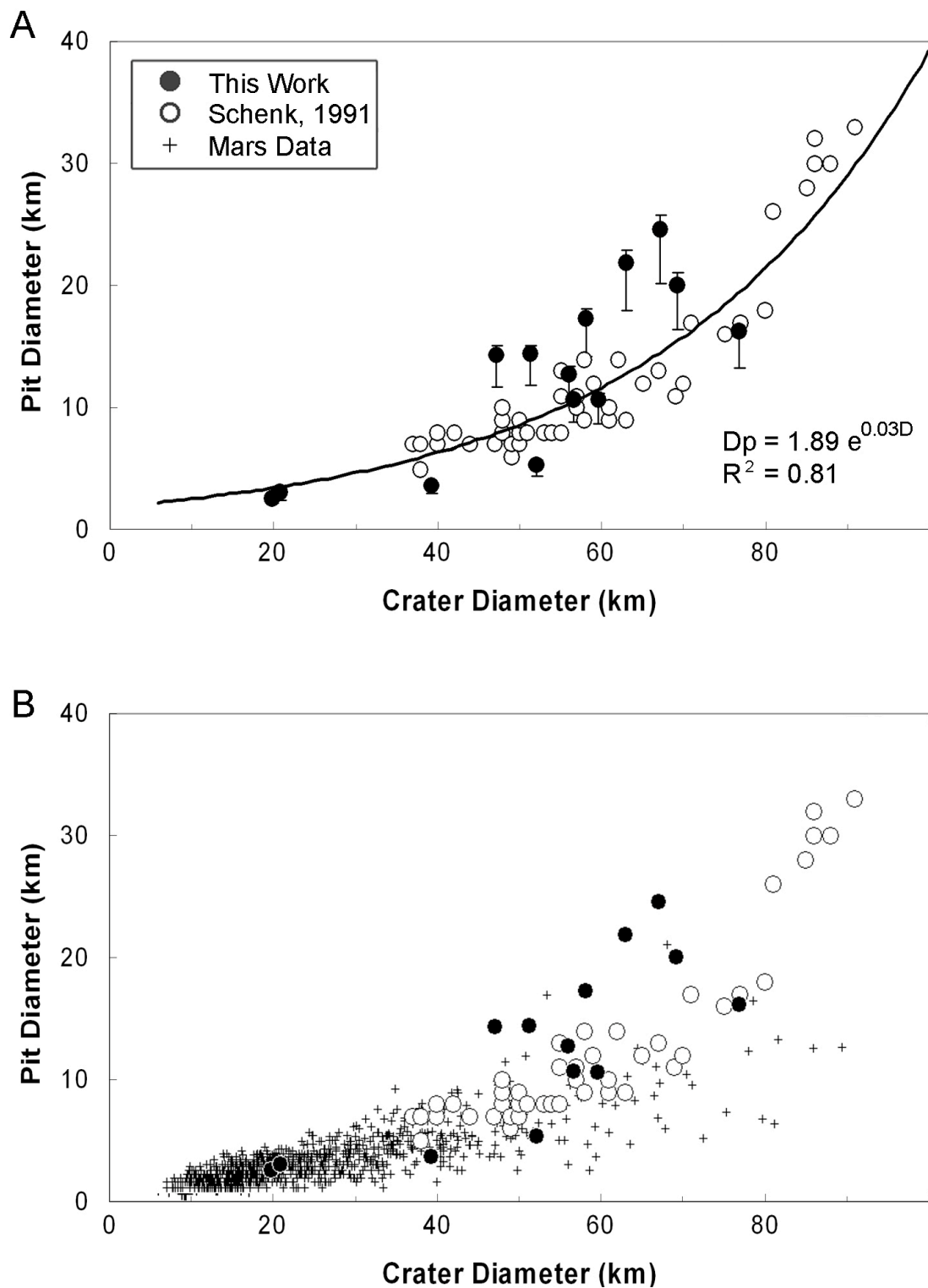


**Figure 3.7:** A) Measurements of central pit and crater diameter from Galileo (this work, filled circles) and Voyager data (Schenk (1993), open circles). The trend line shows the least squares fit to the combined dataset. B) As A, with Martian central pit data (as recorded in Barlow's catalogue of large Martian impact craters) included for comparison as crosses. Legend applies to both plots.

### 3.3.2. Pit Depth and Volume

Measurement of Martian and Ganymede pit depths have been made (e.g. Kagy and Barlow, 2008), but are not currently available, preventing calculation of approximate volumes from these sources. Knowledge of pit volume and internal shape is necessary to reveal the depth of pit influence, and can also be used to infer the quantities of material involved in the formation process. Such information will have important implications for the development and testing of pit formation theories; for example, variation of pit volume in craters formed on different terrain types may indicate a material property dependence of the pit formation mechanism.

The relation of pit depths with crater diameter is presented in Table 3.1 and in Figure 3.8. Pit depth increases with increasing crater size, following a power law (Table 3.1). No variation in pit dimensions with terrain type was found (e.g. Figure 3.9). The new measurement of pit depth has allowed a simplified estimate of pit volume to be made in which pit shape is approximated as conical. Pit volume increases as crater diameter increases, the estimated pit volumes are included in Table 3.1 and presented in Figure 3.9.

### 3.3.3. Pit Summit Relations

Although the central uplifts of floor pit craters are less pronounced than those observed in summit pit craters, the uplifts are still large enough to be studied from topographic profiles. The small summit pit craters on Ganymede tend to have raised rims around the central pits whereas larger floor pit craters have irregular broken pit-rims (Schenk, 1993). The dimensions of these summits have not yet been documented as their boundaries are poorly defined in images. The new topographic data acquired during the course of this work has allowed measurement of their dimensions. Scaling trends for the widths, heights and approximate volumes of these summits are presented in Figures 3.10 – 3.14.

The summits surrounding central pits on Ganymede increase in diameter as crater size increases (Figure 3.10). As pit size also increases with crater size, this produces a similarly positive correlation between pit and summit size. The size of the central pit relative to its summit does not vary between different terrain types on Ganymede (Figure 3.11). Height and volume relationships for the summits of pit craters relative to crater diameter are included in the next section to allow comparison with central peak trends.

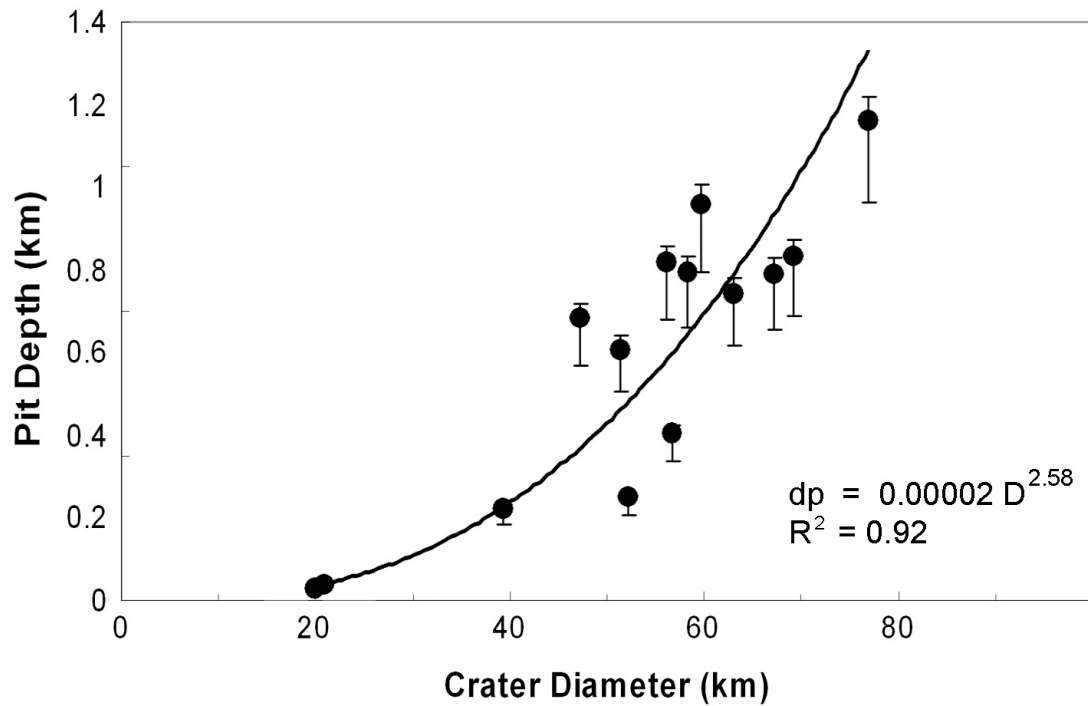


**Figure 3.8:** Measurements of central pit depth. Data from this work is noted by closed circles. A power-law trend line was assigned on the basis of a high  $R^2$  value.

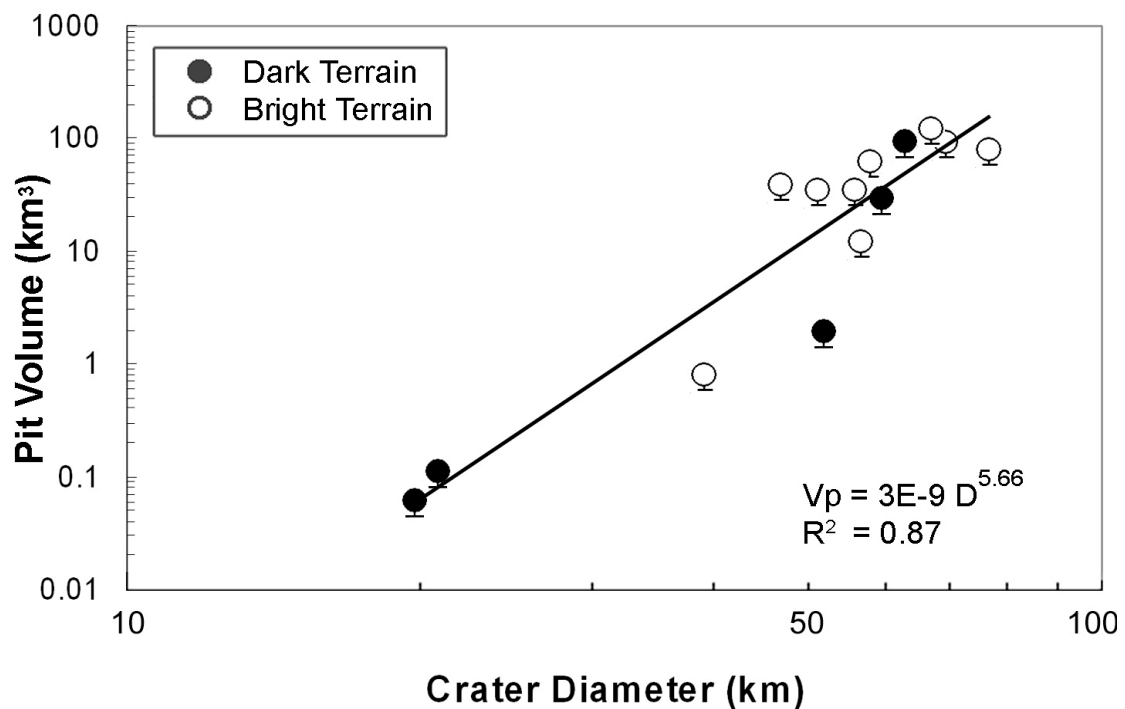


**Figure 3.9:** Ganymede central pit volumes. Volume estimates are based on the measurements shown in 3.7A and 3.8, assuming a conical pit; pits on bright terrain ( $\sim$  pure ice) are marked with open circles, those on dark terrain are marked with closed circles.

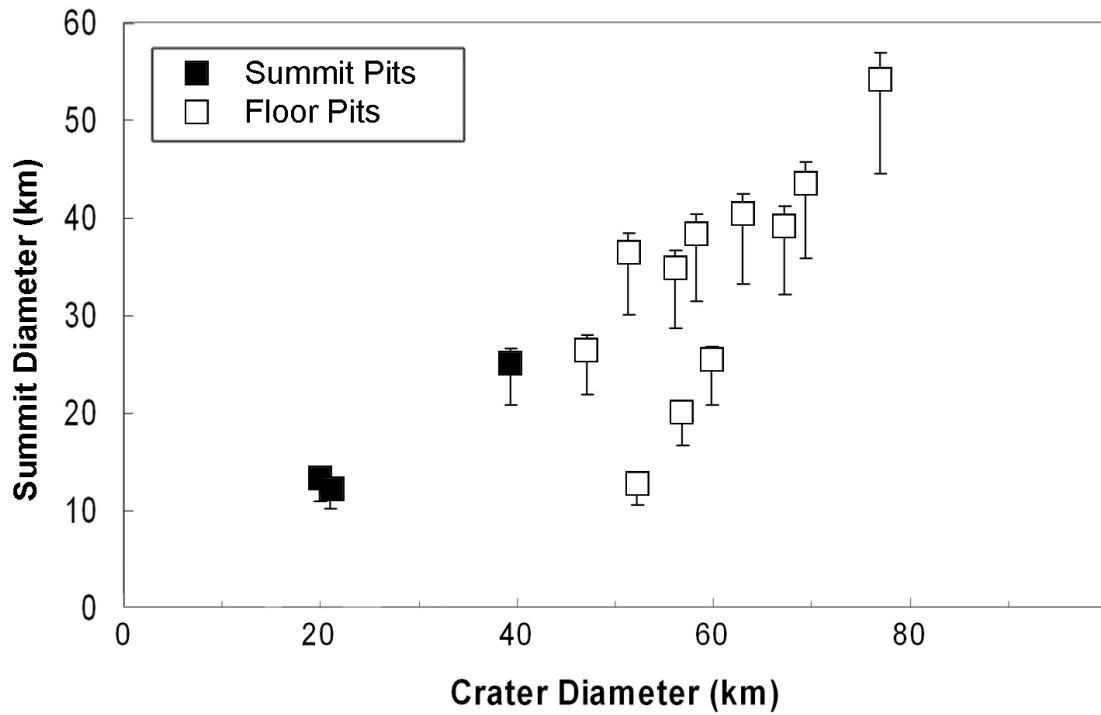


**Figure 3.10:** Width of summits relative to crater diameter. Summit pits and floor pits are noted with closed and open squares respectively.

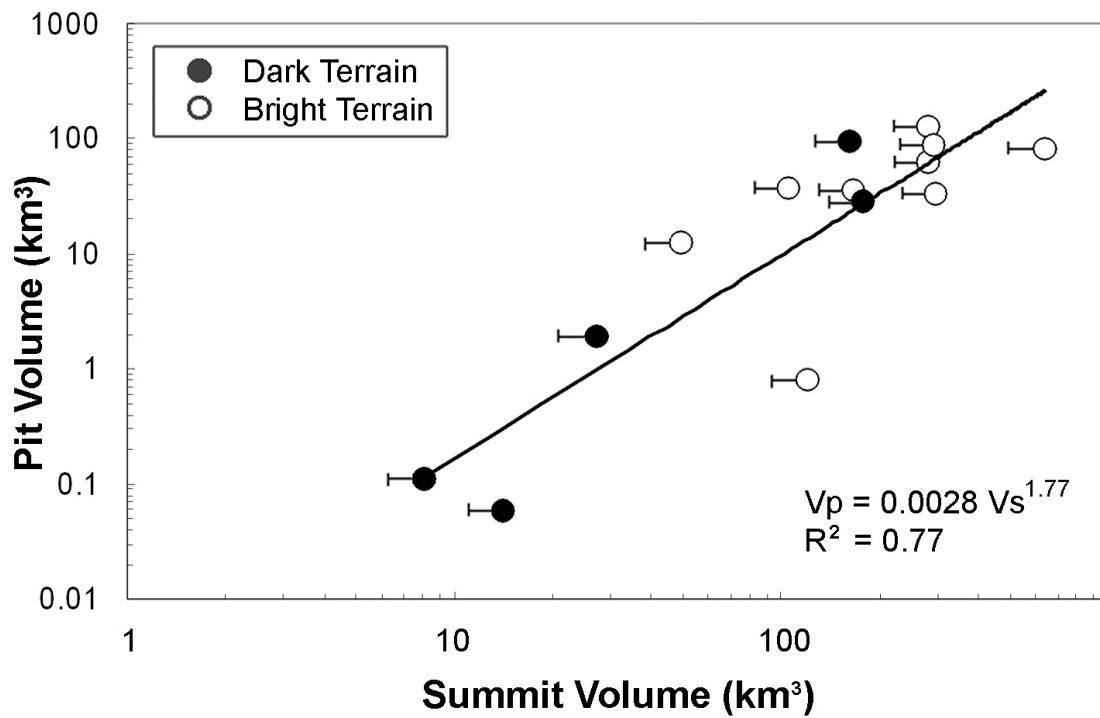


**Figure 3.11:** Pit volume relative to summit volume. Craters located in dark and bright terrain are marked by closed and open symbols respectively.

### **3.4. The Continuing Trends of Central features**

Comparison of the size-morphometry progressions of central peaks and peak-rings has added support to the hypothesis that peak-rings develop from central peak collapse (Alexopoulos and McKinnon, 1994). This development is discussed further in Sections 3.5 and 3.6.3. Similarly, any common trends in the central peak and pit summit size could reveal a link between the two morphologies. This section presents the remaining data for central pit summits and compares the measurements to central peak dimensions on Ganymede.

Figure 3.12 shows that the widths of central uplift continue to increase with crater size. The linear relationship defined in Chapter 2 for central peaks is included in Figure 3.12 as a dotted trend line with an equation of  $D_{cp} = 0.3 D$ . The summits of central pit craters also follow a positive trend but are larger for a given crater size than central peaks.

The height of the summits in the two smallest central pit craters ( $D \sim 20$  km) are similar to central peaks in craters of the same diameter (Figure 3.13). Unlike central peaks however, the height of pit summits in larger craters do not increase with increasing crater diameter. Instead, summit heights in craters between 40 and 80 km in diameter vary about an average value of  $\sim 700$  m, similar to the tallest central peaks.

The volume of central pit summits increases as crater diameter increases (Figure 3.14). The crater diameter and summit volume of central pit craters are generally larger than central peak volumes; as a result both central peak and pit summit volumes are fitted with a combined trend line in Figure 3.14.

**Table 3.1: Central Pit Scaling Trends for Mars and Ganymede**

Parameter	Mars	Ganymede (Voyager)	Ganymede (This Work)
Pit Diameter	$D_p(\text{PU}) = 0.17 D - 0.13$ † $D_p(\text{CT}) = 0.08 D - 0.44$ †	$D_p = 1.9e^{0.023D}$ * **	$D_p = 1.89e^{0.03D}$
Pit Depth			$d_p = 2 \times 10^{-5} D^{2.58}$
Pit Volume			$V_p = 3 \times 10^{-8} D^{5.66}$ $V_p = 0.028 V_s^{1.77}$
Summit Diameter			$D_s = 7.7 e^{0.024D}$
Summit Height			210 – 850 m
Summit Volume			$V_s = 38 V_p^{0.44}$

† Wood et al., 1978 ( $D < 40$  km)

\* Passey and Shoemaker, 1982

\*\* Schenk 1993

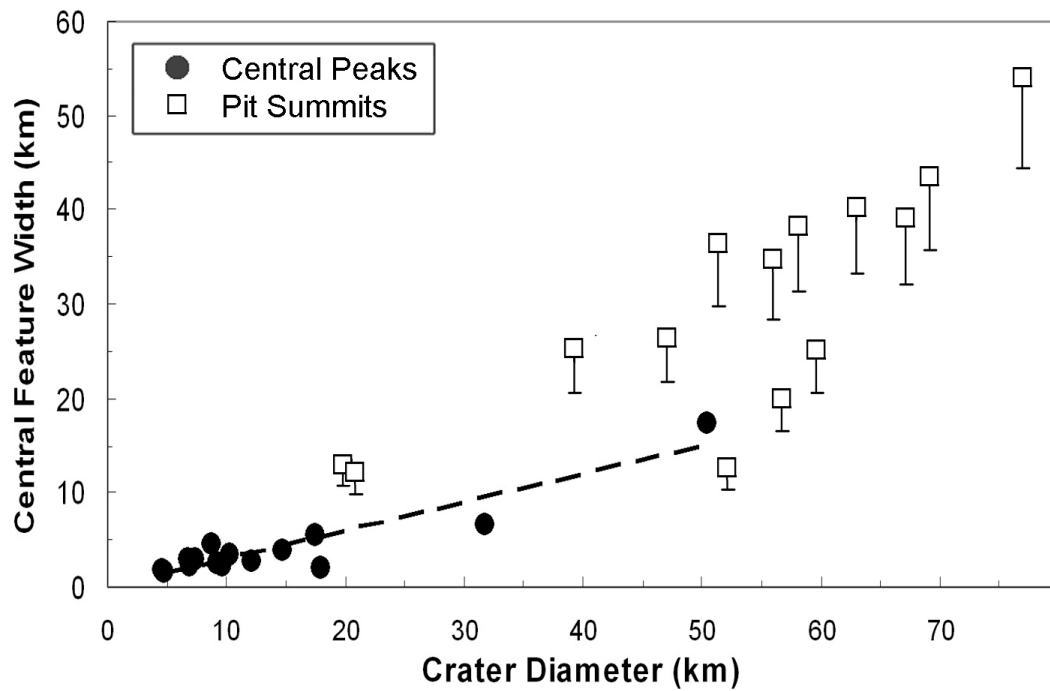


**Figure 3.12:** Measurements of crater diameter and the width of central peaks (closed circles) and the summits of central pit craters (open squares). The linear relationship defined in Chapter 2 for central peaks is included as a dotted trend line with an equation of  $D_{cp} = 0.3 D$ .

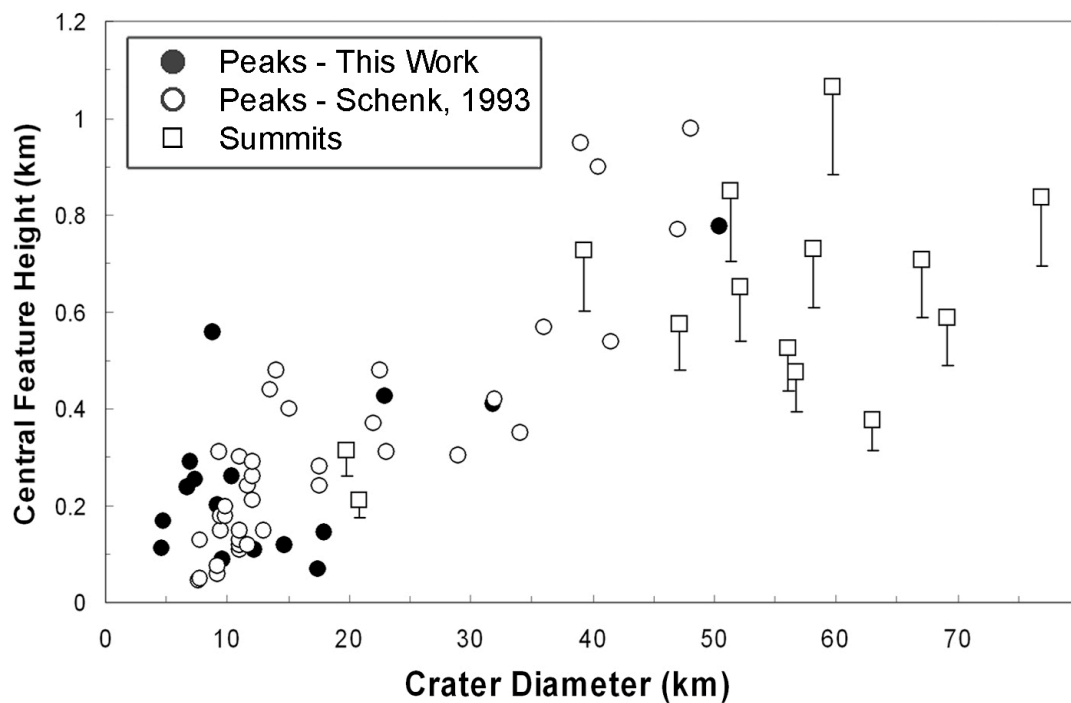


**Figure 3.13:** Central feature height and crater diameter measurement. Central peak craters from this work and Schenk (1993) are marked by closed and open circles respectively. Central pit summit heights are marked with crosses.

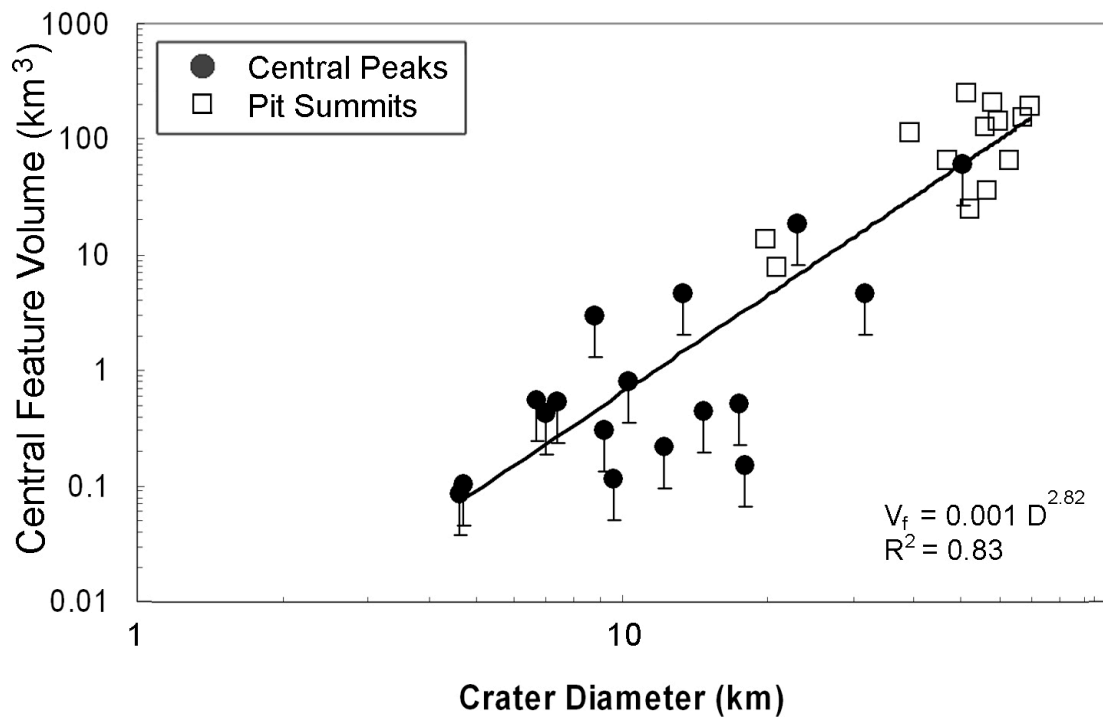


**Figure 3.14:** Approximate volume of central features. Central peaks are marked with closed circles. The summit volumes are calculated by estimating the volume of the equivalent peak volume and then subtracting the pit volume.

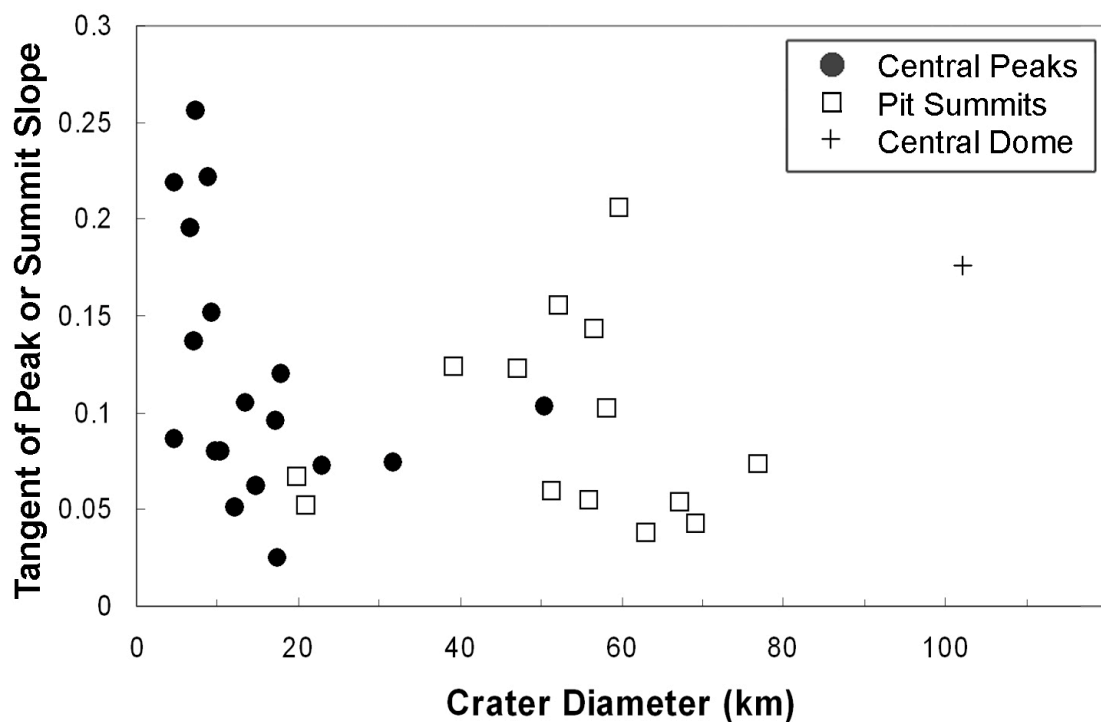


**Figure 3.15:** Peak and summit slopes for all craters. Central peak slopes are marked with closed circles, pit summits with open squares, and central dome crater marked with a cross; the 'summit' of the dome crater was the summit of the pit containing the dome.

Although central feature diameter and volume follow positive trends, a trend in central uplift slope is not easily identified. Figure 3.15 shows that there is no common trend linking the central feature slope with crater diameter for central peak and central pit craters. However, changes in the slope of peaks/summits could possibly correspond to changes in crater morphology. Central peak and crater wall slopes decrease as crater diameter increases to 20 km (see also Figure 2.5). The first central pit craters in this data set are observed at this diameter, after which central peak slope increases with growing crater size. The largest central peak crater in this dataset has a diameter of 51 km; pit summit slopes are variable in crater of diameters between 50 and 60 km. After this, the crater wall and summit slopes decrease. More data is necessary to investigate whether this correlation between changes in crater morphology and the slope of internal features is robust, and if the same trend occurs with central dome craters as only one data point is available from this data set (Figure 3.15).

### **3.5. Additional Features of Central Pit Craters**

Six of the summit pit craters profiled in this work included an extra topographic high between the pit summit and the crater rim (Figure 3.16). When present, this feature was identified in most of the radial profiles for each crater, showing it to approximate a concentric ring of hills within the crater. Such internal crater morphology is reminiscent of peak-rings in craters on rocky bodies (see Section 1.13). These features were only noted after inspection of the topographic profiles and had not been obvious from images alone.

The diameter of these apparent rings were measured as shown in Figure 3.5, and the measurements compared to published data for peak-ring craters on the terrestrial planets (Figure 3.17). Internal rings in Ganymede craters have ring diameter ( $D_r$ ) to crater diameter ( $D$ ) ratios between 0.45 and 0.49; this is similar to peak-ring  $D_r/D$  ratios on the terrestrial planets (Figure 3.17). The examples of central peak basins on the Moon shown in Figure 1.4 also have  $D_r/D$  ratios of 0.45 and 0.49.

Although this work presents only six  $D_r$  measurements over a limited range of crater diameters ( $D = 52$  to  $77$  km), a trend in  $D_r$  with increasing crater size is evident. The diameter of internal rings increase as crater diameter increases:

$$D_r = 0.53D . \quad (3.1)$$

This is a similar trend to that of peak-ring diameters on the terrestrial bodies, and Ganymede data in Figure 3.17 plot almost exactly on the general trend line prescribed by Equation 1.2.

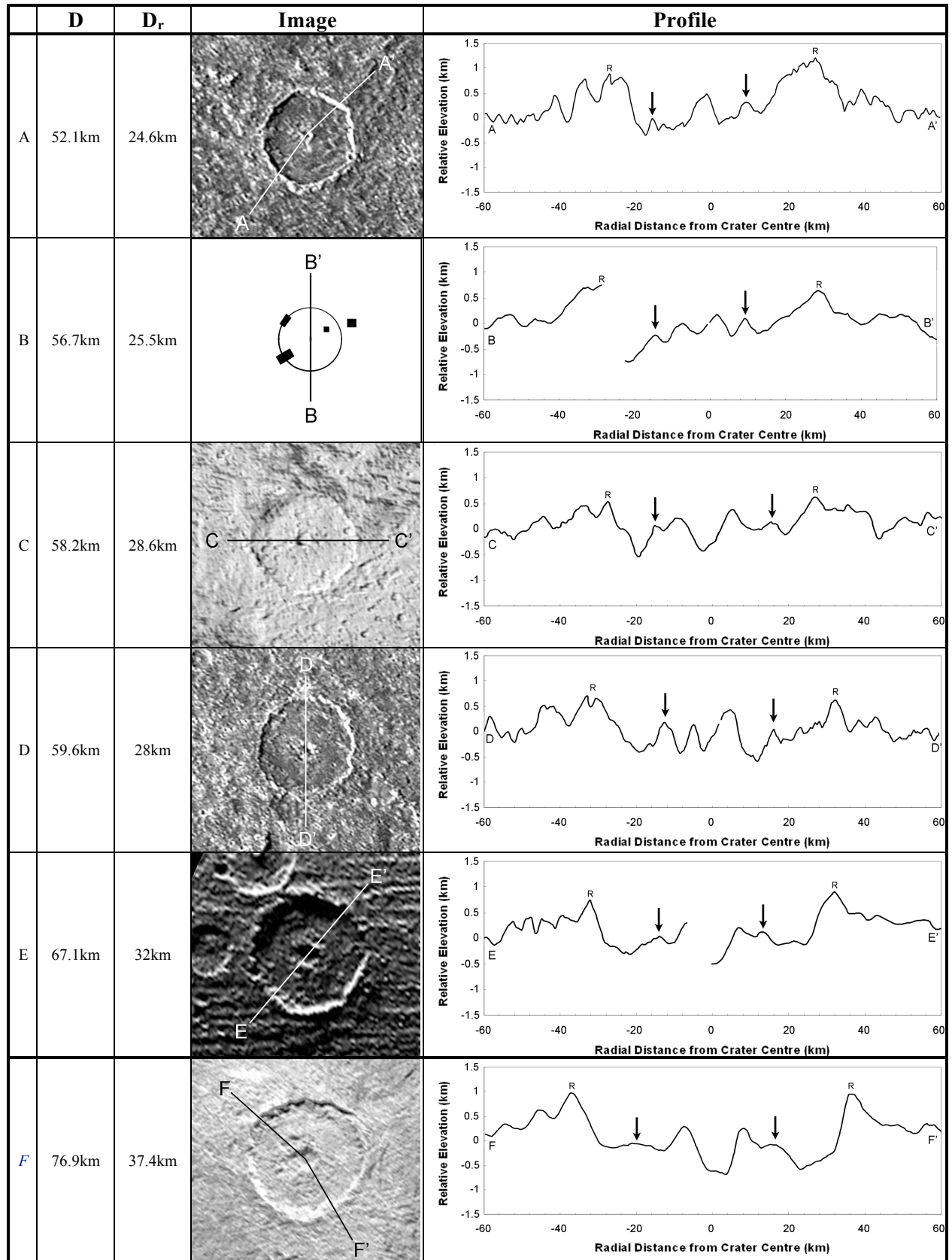


**Figure 3.16:** Images and topographic profiles of the central pit craters included in this work that have an internal ring. Crater rims are marked on the profiles with ‘R’, proposed ring position with arrows.

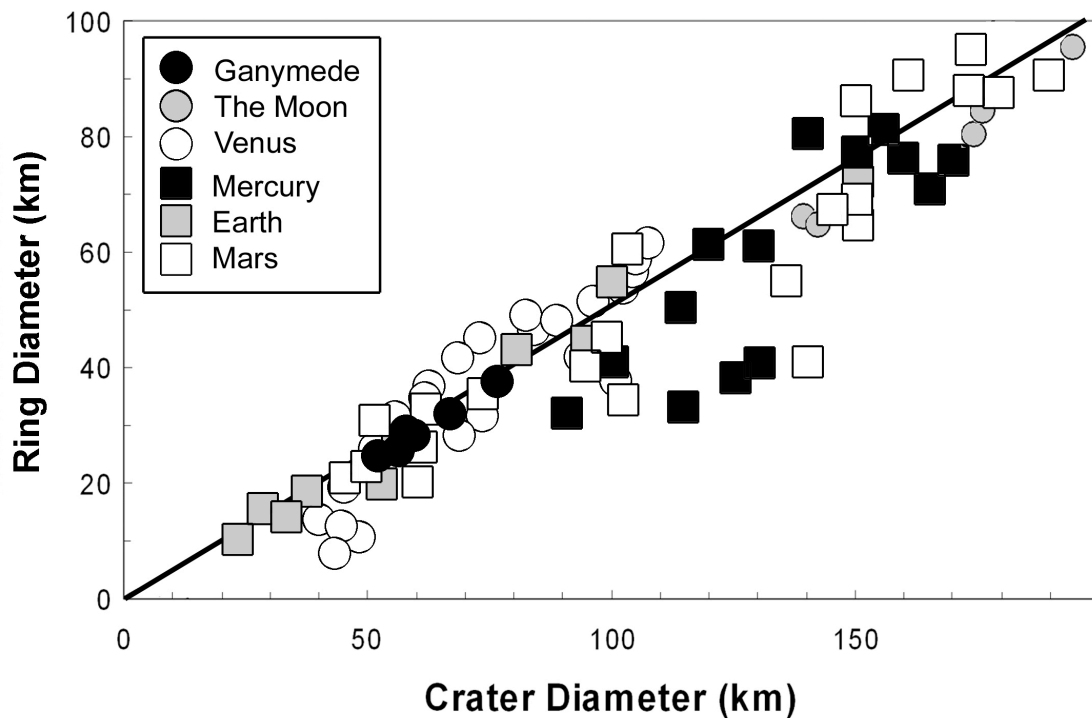


**Figure 3.17:** Measurement of internal ring diameter and crater diameter on Ganymede, the Moon and the terrestrial planets. Ganymede ring diameters are from this work, Martian data from Wood (1980), Lunar and Mercurian data from Wood and Head (1976), peak-ring measurements for Terrestrial craters are from Pike (1985) and the Venusian measurements were acquired from the online USGS Venus Crater Database (January, 2008). The trend line marks  $D_r = 0.5 D$ .

### **3.6. Summary and Implications**

#### **3.6.1. Pit Growth in Different Materials**

Pit diameter, depth and volume all increase with growing crater diameter on Ganymede, following power law trends (Figures 3.7 to 3.9). All formation theories presented in Section 3.2 can predict/explain this pit growth as larger impacts excavate to a greater depth in the target and produce higher shock pressures and temperatures, and thus produce greater melt and volatile volumes. Larger pits can be formed by the draining of more significant quantities of impact melt, the enhanced fluid-like movement of the central crater region, or by the release of additional volatiles produced as a result of the larger impact. No clear difference between the relative sizes of pits in different terrains was observed. This may be the result of low sample numbers in this work; terrain influence may be apparent with larger data sets and is still deemed likely as it has been noted previously (e.g. Schenk, 1993; Klaybor and Barlow, 2006; Barlow, 2006).

Pits in craters below  $\sim 40$  km in diameter appear to follow the same trend on both Mars and Ganymede. However, above crater diameters of  $\sim 40$  km, pit diameters on Ganymede become up to two times larger than pits in the same sized craters on Mars (Figure 3.7B). As the surface composition, target gravity and impact velocity differ between the two bodies, there are several possible explanations for this divergence in pit diameters. The association of central pits primarily with ice-rich crusts suggests that the formation mechanism of central pits may be more effective in pure ice targets, leading to the larger pits on Ganymede (contrary to Barlow, 2006). Alternatively the lower impact velocity on Mars ( $\sim 10$  kms<sup>-1</sup> compared to 21 kms<sup>-1</sup> on Ganymede) will result in lower post-shock temperatures relative to Ganymede, producing lesser melting and potential vaporization of target material (Pierazzo et al., 1997),

### 3.6.2. Pit and Summit Formation

The summits of central pit craters increase in diameter and volume with growing crater size, although the trend in summit dimensions is not as strong as for pits. Apparent widening of summit bases as a result of crater floor relaxation may lead to misinterpretation of the summit boundaries and lead to this wider spread of results. The summit surrounding the central pit increases in volume as pit volume increases (Table 3.1, Figure 3.11). This could suggest that their development is linked. The summits of central pit craters are wider, relative to the crater diameter, than central peaks would be for a similar crater size (Figure 3.12). This suggests that central pit craters are not simply large central peak craters with a hollowed summit and that some other process acts to further widen the central uplift of these large craters.

Figure 3.13 shows that the height of central features do not continue to increase after the transition from central peak to central pit morphology. Instead, summit heights vary about an average of  $\sim 700$  m. The lack of continued increase in summit height relative to central peak heights suggests that a maximum stable height for central uplifts has been reached prior to, or in conjunction with, the development of central pits. The maximum central feature height noted in this work is 1.1 km and occurs in a crater of  $\sim 60$  km in diameter. Central uplifts exceeding this theoretical limit may collapse, base-first as suggested in Chapter 2, distributing the additional volume of uplifted material at the base of the central peak/summit. This would maintain a constant summit height as crater diameter increases, while continuing to increase the summit width and volume (Figures 3.12 and 3.14). As the widening of the summits of pit craters relative to central peak craters can be explained simply by the fluid-like movement of the crater floor, the additional summit widths are not necessarily a consequence of pit formation.

### 3.6.3. Life After 30 (km)

Six of the fourteen central pit craters profiled in this work included an apparent ring between the central summit and crater rim (Figure 3.16). It is possible that this internal ring is a feature of most summit-pit craters, but has not been previously visible when evaluating the image alone.  $D_r/D$  ratios of 0.45 to 0.49 have been recorded for these internal rings, a comparable value to the average  $D_r/D = 0.5$  trend of peak-rings on the terrestrial planets (Figure 3.17).

The rings observed in the central pit craters of Ganymede are likely to be connected with internal crater development rather than rim-wall collapse as they occur inside the maximum distance from the crater rim expected for mega-terraces (Pearce and Melosh, 1986). The features could thus be produced as the result of outward moving peak material colliding with collapsing rim-wall debris, similar to a suggested mechanism for peak-ring formation (Morgan et al., 2000; Collins et al., 2002). Alternatively, such concentric topographic uplifts could be explained by multiple vertical oscillations of the crater's central region; this would provide support for the Bingham plastic model for peak-ring formation (Melosh, 1982; Alexopoulos and McKinnon, 1994).

Craters with a central peak and concentric ring have also been observed on the Moon (Figure 1.4), and occur at crater diameters intermediate to central peak and peak-ring craters. This suggests that this ringed peak morphology is an intermediate stage between central peak and peak-ring craters, and demonstrates that complete collapse of a central uplift is not necessary to produce topographically expressed rings.

The presence of 'central peak basins' on Ganymede, albeit with a pitted summit, suggests that the same process by which peak-rings are believed to form on terrestrial planets, also operates during the collapse of impact craters in ice. The similar  $D_r/D$  ratios on Ganymede and rocky bodies suggests that the mechanism of peak-ring formation operates independently of target gravity and material type, as an inherent part of the cratering process. However, peak-rings without a central peak are not observed on Ganymede. This could suggest that peak collapse to form peak-rings does not advance as far on the icy satellites, or that the development of peak-rings is overprinted by the growth of central pits (see Figure 3.19).

### 3.6.4. A Model of Pit Formation

A suitable mechanism for central pit formation has to be able to explain summit pit and floor pit craters on Mars and Ganymede. The peak collapse model (where the pit simply forms as a result of multiple oscillations of the crater centre being 'frozen in' at the appropriate stage) is difficult to envision from observational data alone as it is evident that central peaks in impact

craters collapse first at their base rather than the descent of the very peak centre (Sections 2.6.3 and 3.6.3).

Pit formation through peak collapse cannot be ruled out however as a number of the simulations performed in the course of this thesis did produce small summit depressions as the result of central peak collapse (e.g. Figure 5.3C). In these simulations the base of the peak collapsed first, as predicted. The continued downward collapse of the peak core then pushed this basal peak material further from the crater centre, whilst descending further, resulting in a shallow pit. This morphology was commonly the result of unusual impact conditions relative to the other simulations presented in Chapters 5 and 6, including higher impact velocities (20-25 km s<sup>-1</sup>), and/or weaker target material.

Although these simulations were the exceptions, it does demonstrate that central pits can theoretically form as a result of the fluid-like collapse of a central peak. However, as this process would be valid in all target materials, pits could be expected to be more common on rocky bodies. As this visualisation of the multiple oscillation model does not preclude pit formation on rocky bodies, it is not considered to be the sole mechanism forming central pits. It is however likely that the observed internal rings were created by such fluid movement of the target material.

The theory of pit formation involving the release of sub-surface volatiles is a valid idea. On Mars, the presence of a sub-surface cryosphere will allow differential melting and vaporisation of peak material, possibly producing a central pit. However, as the crust of Ganymede is entirely composed of volatile rich material, vaporisation will theoretically occur in all volatile-rich layers, and could therefore be expected to produce pits in craters of all sizes. As this is not the case, the occurrence of central pits only in the larger craters implies that significant vaporisation requires the production of large enough impact energy, or decompression volatilisation of ice from a great enough depth.

The melt-drainage model is also valid as a pit-formation mechanism, particularly for pure-ice surfaces as the impact melt will be denser than the surrounding solid target material. In densely fractured rocky materials, melt water would also percolate downwards into the fracture-space. Collapse of the overlying material into the created voids may explain the ponded pitted material recently observed in Martian impact craters (Figure 3.4). It is likely that volatile release and draining of melt-water are both active pit-forming processes which operate to different extents on Mars and Ganymede. Further testing of these possibilities is not attempted as part of this thesis, but is discussed in the final chapter.

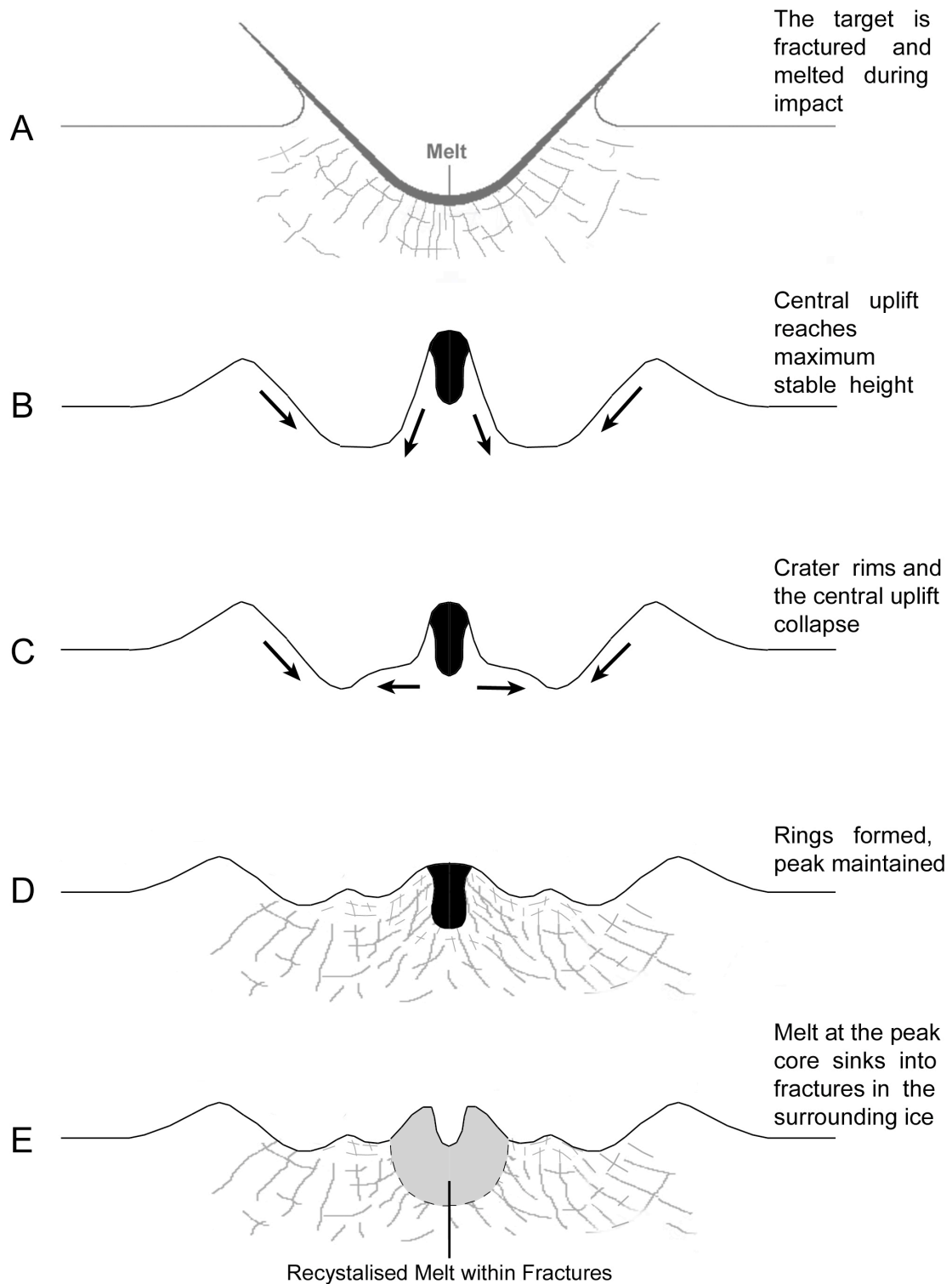


**Figure 3.18:** Series of diagrams illustrating the formation of a summit pit crater using the melt-drainage model. The series begins with the collapse of the transient crater. Rim and peak collapse form the internal rings noted in Section 3.5. The melt portion of the central peak sinks into the surrounding fractured rock and solidifies in the existing pore space.

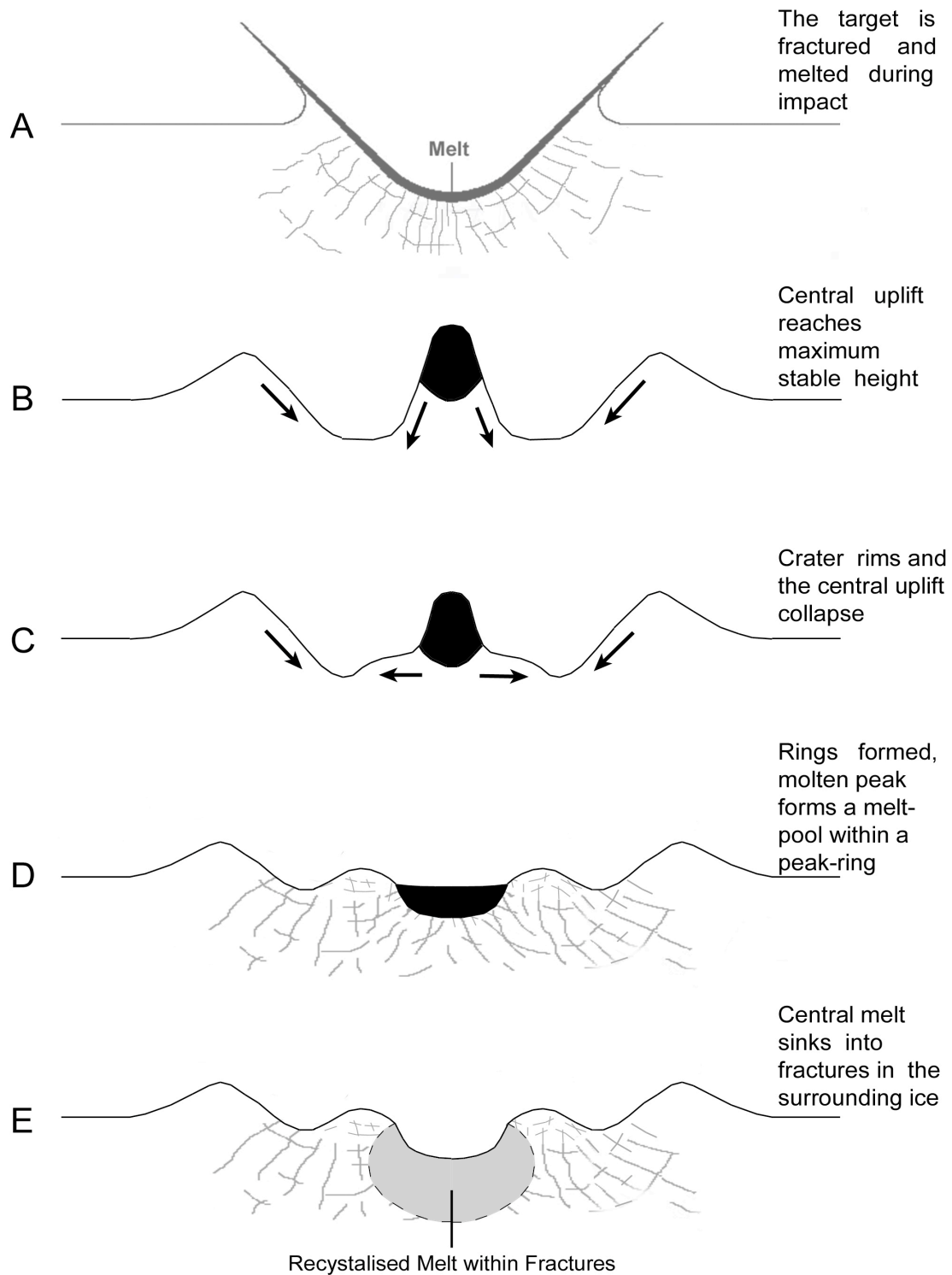


**Figure 3.19:** Series of diagrams illustrating the formation of a floor pit crater using the melt-drainage model. Floor pits are observed in craters with larger diameters than those with summit pits and so the crater presented in this figure is larger than that shown in Figure 3.18. The additional melt present in this larger impact prevents retention of the central peak and a melt pool is formed within a peak-ring structure. This melt then percolates into the surrounding fractured rock. The higher temperatures created by this larger impact produce a larger region of warm ice, allowing more melt to sink into the fractures, creating a larger pit than in the case of smaller impacts (Figure 3.18).

The creation of both summit and floor pits in craters on Ganymede via the melt drainage mechanism, including the formation of internal ring structures via the fluid-like movement of target material during crater collapse, is outlined schematically in Figures 3.18 and 3.19.

Figure 3.18 shows a suggested method of summit pit crater formation as a result of melt at the core of the central uplift percolating downward and outwards into the periphery of the peak/summit. In order for melt water to enter the fractures, the central peak ice must be warm enough to prevent the melt water instantly refreezing on contact. The melt water at the peak centre will continue to sink into the fractured material at the centre of the crater until this theoretical temperature barrier is reached at some distance from the point of impact, at which point further draining of melt water is prevented. The melt then recrystallises in the existing pore/fracture space within the central uplift. In the scenario depicted in Figure 3.18, the volume of warm fractured ice receptive to melt drainage is small relative to the larger crater of Figure 3.19. The melt is thus confined to the peak core and the internal rings remain topographically expressed.

The additional impact melt generated by larger impacts comprises more of the peak core hypothesised in Figure 3.19. The transient peak topography is therefore not maintained, instead forming a melt pool within a peak-ring (Figure 3.19D). The larger volume of warm ice at the crater centre allows the draining of a more significant quantity of melt into the surrounding fractured ice, producing a larger pit. The warm central region may extend far enough to encompass the peak-rings, perhaps leading to effective relaxation and rebound of the crater floor, masking the peak-ring uplifts.

As the melt water in this hypothesis fills already existing pore and fracture space at the crater centre, the 9% volume increase afforded by the expansion of water into ice Ih is not likely to produce significant volume change. However, it is possible that, in large impacts where sufficient melt is produced, recrystallisation of melt water in the fracture-space will cause some expansion and uplift of the central region. Peak-ring topography could be incorporated in, and thus apparently replaced by, the uplifted region surrounding the floor central pit.

Intense fracturing of the target during impact cratering results in a gravity low at the centre of craters (Hilderbrand et al., 1991). The recrystallisation of impact melt-water in fracture space will increase the density of the central region relative to the unfilled fractures further from the central pit. This mechanism of pit formation therefore predicts a concentric gravity low surrounding a relative gravity-high over the very centre of pit craters on Ganymede, and is thus a testable hypothesis.

## Chapter 4

# Introduction to the iSALE Hydrocode

High-velocity impact experiments have proved a valuable tool in the investigation of simple crater formation, and the collapse process for simple craters is reasonably understood (Grieve et al. 1977; Melosh, 1989). However, the lack of observed large-scale impact events, combined with the small-scale nature of laboratory experiments has restricted our understanding of processes like melting/vaporization and complex crater collapse (Pierazzo and Collins, 2004). The use of computer modelling has advanced the investigation of this gravity driven process, allowing complex crater collapse on planetary scales to be studied in its entirety. A hydrocode is a computer code used for modelling fluid flow at all speeds; hydrocodes can be adapted to consider different material strengths and rheologies, allowing them to be applied to many physical scenarios, including very energetic processes involving the passage of shock waves.

This work uses the iSALE hydrocode (Wünnemann et al., 2005), a multi-rheology, multi-material extension of the SALE hydrocode. SALE stands for Simplified Arbitrary Lagrangian Eulerian and was developed by Amsden et al. (1980) for simulating single-material Newtonian-fluid flow. This chapter begins by outlining the theory behind modelling impacts with iSALE and the code's development from the original SALE code by previous workers. The second part of this chapter describes the implementation in iSALE of new material models that were necessary to simulate the response of H<sub>2</sub>O ice to hypervelocity impact. These modifications are the work of the author and were based on high pressure, low temperature observational data for ice from a number of works.

## **4.1. Modelling Impact Cratering with iSALE**

During hydrocode simulations, the area under study is represented using a predefined ‘mesh’ of cells, of which the subject materials are either comprised, or are free to flow through. The material movement through/of the mesh is tracked over a series of short time intervals (‘time-steps’). To correctly describe the behaviour of material during impact, iSALE predicts a material’s response to internal and external forces on the basis of three pillars: Newton’s laws of motion, equations of state and constitutive models.

Firstly, the simulation of a material’s response to impact requires the solution of a set of differential equations which are established through the principles of conservation of momentum, mass and energy (Anderson, 1987):

$$\text{Conservation of Momentum} \quad \frac{Dv_i}{Dt} = f_i + \frac{1}{\rho} \frac{\partial \sigma_{ji}}{\partial x_j}, \quad (4.1)$$

$$\text{Conservation of Mass} \quad \frac{D\rho}{Dt} + \rho \frac{\partial v_i}{\partial x_i} = 0, \quad (4.2)$$

$$\text{Conservation of Energy} \quad \frac{DE}{Dt} = \frac{\Pi_{ij} \epsilon_{ij}}{\rho} - \frac{P}{\rho} \frac{\partial v_i}{\partial x_i}, \quad (4.3)$$

where  $v_i$  is the velocity,  $\rho$  is the material density,  $E$  is the specific internal energy (energy per unit mass) and  $x$  is the position.  $f_i$  denotes the external forces per unit mass,  $\epsilon_{ij}$  is the deviatoric strain rate and  $\sigma_{ji}$  is the stress tensor, which is composed of a hydrostatic component, the pressure  $P$  and the deviatoric stress,  $\Pi_{ij}$ . Subscripts  $i$  and  $j$  refer to the coordinate directions.

A complete representation of a material’s response to stress requires Equations 4.1 to 4.3 to be accompanied by an equation of state and a constitutive model as introduced in Sections 4.1.2 and 4.1.3. A number of SALE-related codes have been developed to incorporate different equations of state and a variety of constitutive models (Melosh et al., 1992; Ivanov et al., 1997); iSALE consolidates many aspects of these extensions. The different elements considered during the hydrocode simulation of impact are presented in this section and the development of each in iSALE is noted in the relevant sections.

### 4.1.1. Numerical Representation of Time and Space

Although computer modelling provides the only practical way of solving the differential equations 4.1 - 4.3, it is still limited by a finite memory allocation. To account for this, the continuous media under investigation is represented by mesh of discretised pieces known as cells. Each cell is usually defined by three or four vertices, connected by straight lines to form a triangle or quadrilateral respectively.

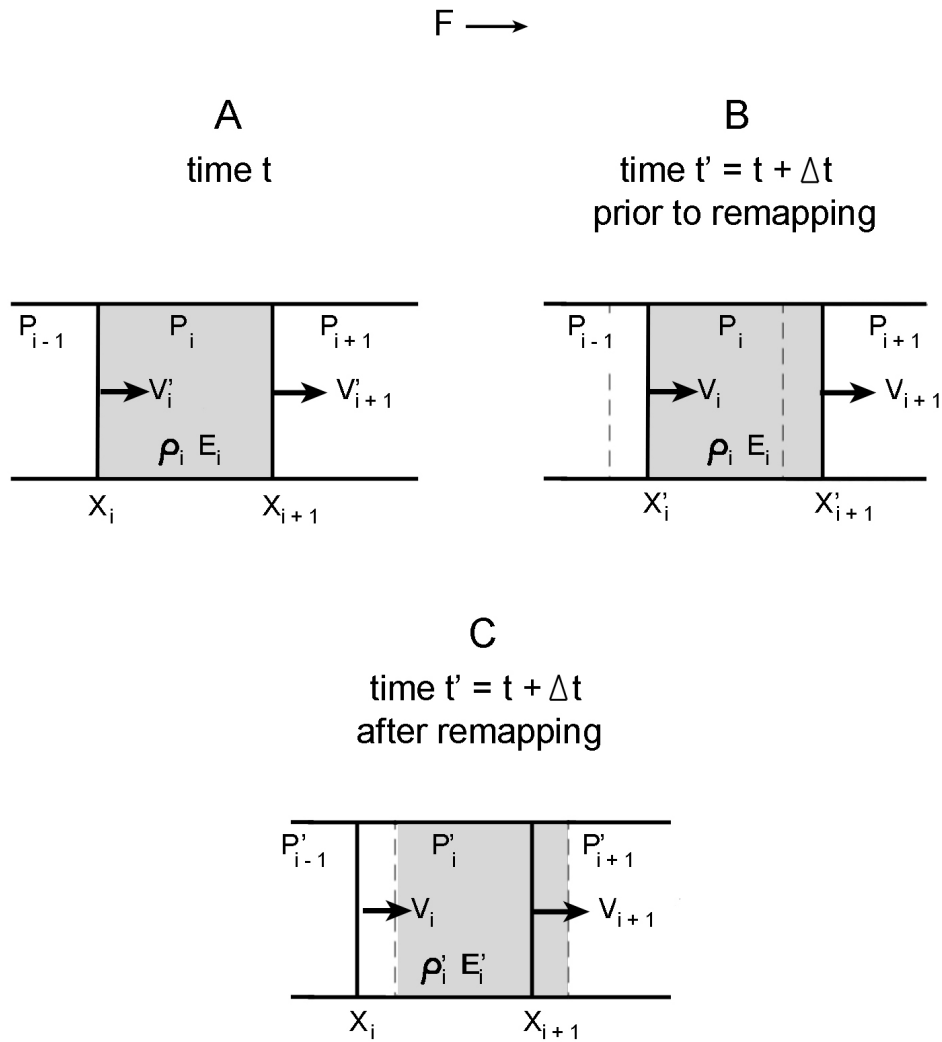
The cell vertices within iSALE's mesh are defined by either cylindrical or plane coordinates, restricting the code to the solution of two-dimensional or axis-symmetric scenarios and thus only applicable to impact angles of  $90^\circ$  to the target surface. A three-dimensional version of iSALE capable of simulating oblique impact has also been developed and is currently being tested and validated (Elbeshausen et al., 2007).

Figure 4.1A shows an example cell within an iSALE mesh at the beginning of a simulation ( $t = 0$ ). At the beginning of each simulation, scalar quantities such as mass, energy and density are assigned to each cell and remain constant within the cell; vector quantities such as velocity are assigned to the vertices ('nodes'). Velocities  $v$  and  $u$  are assigned separately in both  $x$  and  $y$  directions for a 2D simulation; another velocity component  $w$  can be assigned when considering 3D simulations.

The effects of forces acting on the vertices of this cell (gravity, pressure stress, etc) are then considered over a short interval of time (a time-step). The magnitude and direction of the acceleration applied to each node as a result of these forces are calculated. Figure 4.1B shows the cell of material after one theoretical time step in a Lagrangian description (the cell vertices remain fixed relative to the material). A purely Lagrangian description is achieved if this is the only step performed during the time cycle.

However, in cases of extreme deformation, continued change in the relative position of the cell vertices over advancing time-steps can lead to extreme cell distortion, which produces spurious results (such as negative volumes) and the simulation cannot be continued. To avoid these complications of a purely Lagrangian description, iSALE incorporates an optional second step in which the cell properties at the end of each time-step are remapped back to an undistorted mesh by *advecting* (effectively moving) the 'overlap' material into an adjacent cell (Figure 4.1C). The full advection routine is described by Amsden et al. (1980).

Although this approach allows extreme material deformation to be simulated, the additional process of remapping increases the run time of simulations. Also, when material interfaces occur within the confines of a single cell, the flux of the different materials into the adjacent cells during each time-step is approximated (Figure 4.2). This leads to a somewhat decreased accuracy in the placement of material boundaries relative to a purely Lagrangian description, but is necessary to achieve arbitrary levels of deformation.



**Figure 4.1:** Schematic illustration of a one-dimensional hydrocode computation.

A) A single cell of the computational mesh at initial time,  $t$ , is shaded. The cell boundaries are marked with solid lines;  $i$  denotes the cell number. Position ( $x$ ) and velocity ( $V$ ), are defined at the cell vertices. Scalar properties are assigned to the centre of each cell and include mass, internal energy ( $E$ ) and density ( $\rho$ ). Density is calculated from the mass within the cell as the volume of a cell is constant. The pressure is calculated from the density and internal energy using an equation of state of the form  $P(\rho, E)$ .

B) The code uses Newton's laws of motion to compute the acceleration of the vertices as a result of the net force ( $F$ ) on each vertex. The new velocity ( $V'$ ) is computed assuming this acceleration is constant over the time-step. The code advances from time  $t$  to  $t+\Delta t$  by first updating the vertex positions, assuming the new velocity is constant over the time-step ( $X_i \rightarrow X'_i$ ). The momentum at both vertices is averaged to calculate a cell-centred momentum.

C) To avoid accumulated cell distortion, the cell-centred, properties, including momentum, are remapped back to an undistorted mesh by transferring the 'overlap' material and its properties to the appropriate adjacent cell. The new mass, density ( $\rho'$ ), internal energy ( $E'$ ) and pressure ( $P'$ ) are calculated and assigned, ready for the beginning of the new time-step. The remapped vertex velocities are updated according to the new cell-centred momenta.

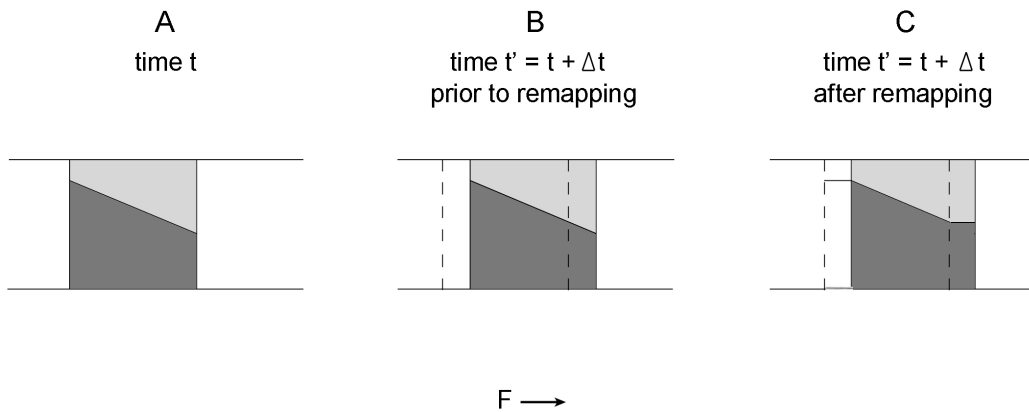


**Figure 4.2:** Schematic illustration of the same form as Figure 4.1 showing the treatment of mixed material cells by the iSALE hydrocode. Cell properties have not been included. A) A single cell containing two different materials at time  $t$ ; the different materials are marked with different shades. B) With progression to the next time-step,  $t + \Delta t$ , the cell properties are updated as outlined in the Figure 4.1 caption. C) The material boundaries ‘flowing’ out of the cell are approximated as the mesh is remapped. The incoming material from adjacent cells is also approximated, leading to disturbance of the material boundaries.

#### 4.1.2. The Equation of State (EoS)

Hydrocodes require the inclusion of an appropriate equation of state to describe the material’s response to changes in volume and the passage of the shock wave. The equation of state can be presented in several different forms relating different material properties. The conventional thermodynamic equation of state is an equation describing the state (solid, liquid or gas) of matter under given physical conditions by relating the pressure,  $P$ , to the temperature,  $T$ , and density,  $P = P(\rho, T)$ . Alternatively, a material’s equation of state may be defined as a relationship between shock velocity  $V$  and particle velocity  $v_p$ .

The equation of state used for impact modelling is presented in a slightly different form from the conventional EoS and relates pressure, density and internal energy,  $E$ . In iSALE the EoS is represented by a general equation of the form  $P = P(\rho, E)$ . Melosh et al. (1992) and Ivanov et al. (1997) implemented several equations of state for impact into the SALE-related codes. iSALE can now be used with the Tillotson (Tillotson, 1962) and the semi-analytical ANEOS (Thompson and Lauson, 1972); these are outlined in Melosh (1989).

The Tillotson EoS (Tillotson, 1962) is one of the most commonly used equations of state for impact modelling and was developed specifically for use in high-velocity impact simulations; it can be used over a wide range of pressures, densities and materials. The Tillotson EOS has two different forms depending upon whether the material under study is experiencing compression ( $\rho/\rho_0 \geq 1$ ) or expansion ( $\rho/\rho_0 \leq 1$ ).

### Dealing with Compression

The equation describing the state of a material undergoing compression is

$$P_C = \left[ a + \frac{b}{(E/(E_0\eta^2) + 1)} \right] \rho E + A\mu + B\mu^2. \quad (4.4)$$

$P$  denotes pressure,  $E$  the energy density of the material, and the initial and final densities are represented by  $\rho_0$  and  $\rho$  respectively.  $\eta = \rho/\rho_0$  and  $\mu = \eta - 1$ .  $a$ ,  $b$ ,  $A$ ,  $B$  and  $E_0$  are the Tillotson parameters, empirically derived constants which vary for each material (see Melosh, 1989) (e.g. Table 4.1).

### Dealing with Expansion

Rapid expansion causes partial vaporisation of the material if its internal energy exceeds the energy required for vaporisation to begin (the energy of incipient vaporisation,  $E_{iv}$ ). The extent of vaporisation depends on the internal energy,  $E$ , relative to the  $E_{iv}$  and the energy of complete vaporisation,  $E_{cv}$ . The expansion of ‘cold’ ( $E < E_{iv}$ ), partially vaporised ( $E_{iv} < E < E_{cv}$ ) and entirely vaporised ( $E > E_{iv}$ ) material is considered separately, using different Tillotson equations. For ‘cold’ expanded states when the energy density is less than that required for the material to begin to vaporise ( $E < E_{iv}$ ), Equation 4.4 is employed.

If the internal energy exceeds the energy of complete vaporisation ( $E_{cv}$ ), the material is treated as a gas. In cases of sudden adiabatic expansion, the vapour can be approximated to a perfect gas. The pressure in a perfect gas reduces to zero at zero temperature, so that it relies strongly on the internal energy:

$$P = \left( \frac{C_p}{C_v} - 1 \right) \rho E, \quad (4.5)$$

where  $C_p$  and  $C_v$  are the specific heat at constant pressure and constant volume respectively. However, expansion is accompanied by a change in temperature, preventing the direct application of Equation 4.5. The Tillotson equation of state instead describes the pressure in the expanded state ( $\rho/\rho_0 \leq 1$ ), when  $E > E_{cv}$ , with:

$$P_E = a\rho E + \left[ \frac{b\rho E}{(E/(E_0\eta^2) + 1)} + A\mu e^{-\beta(\rho_0/\rho-1)} \right] e^{-\alpha(\rho_0/\rho-1)^2}. \quad (4.6)$$

$\alpha$  and  $\beta$  are material dependent constants that control how closely the material approximates an ideal gas (Equation 4.5).

Equations 4.4 and 4.6 describe the pressure in an expanding material ( $\rho/\rho_0 \leq 1$ ) when unvaporised or fully vaporised ( $E_{iv} > E > E_{cv}$ ). The transition between these two regimes involves partial vaporisation of material for internal energies between  $E_{iv}$  and  $E_{cv}$ . The pressure in this transitional regime is best computed using Equation 4.7, which combines the pressures calculated from the compressed Tillotson EoS and the expanded Tillotson EoS (Equations 4.4 and 4.6 respectively).

$$P = \frac{(E - E_{iv})P_E + (E_{cv} - E)P_C}{E_{cv} - E_{iv}}. \quad (4.7)$$

The Tillotson EoS for ice is limited in its applicability for hypervelocity impact as it includes no liquid state, and is overly simplistic in its treatment of vapour (Pierazzo and Collins, 2004). Further considerations necessary when dealing with high pressure phases are outlined in Melosh (1989). However, the Tillotson EoS remains one of the most widely used equations of state for modelling impact crater formation because of its simplicity (which makes it efficient in complex hydrocode simulations) and because the accurate treatment of the vapour phase is not important for modelling impact crater formation.

### 4.1.3. Constitutive Model I – Static Strength

The equation of state is critical when modelling the early stages of impact when material strength is negligible compared to the pressures involved. Further into the impact process, when the pressures have dropped and the deviatoric stresses are more of the order of the target strength, the constitutive model becomes increasingly important (Pierazzo and Collins, 2004). The constitutive model describes the response of a material to differential stresses.

The constitutive model of the original SALE only enabled the code to simulate simple Newtonian fluid flow. This was initially improved upon by Melosh et al. (1992) with the addition of an elasto-plastic model for use with the existing viscous model. These rheological models allow elastic, plastic and viscous movement of material to be considered (see Jaeger and Cook (1969) for details of the different material models). More recent developments have produced a number of SALE-based codes incorporating the improvements of SALEB and other advances such as a wider range of possible rheological models and the ability to simulate up the three different target materials plus vacuum (e.g. SALE-2D, SALE-3MAT).

The stress at which geologic materials begin to fail (the yield strength) is a function of damage, confining pressure, temperature and strain rate (e.g. Jaeger and Cook, 1969). The

dependence of rock and ice strength on these factors and its implementation into iSALE is presented in the following sub-sections and in Section 4.2.3, and is described in Collins et al. (2004).

### The Effect of ‘Damage’ and Confining Pressure on Rock Strength

On impact, target material is fractured to form a mass of irregular debris blocks, which may be interlaced with melt veins or powder at the block interfaces (Spray and Thompson, 1995; Ahrens et al., 2002). The strength of a jointed rock mass depends upon the strength of the intact blocks and their freedom of movement (Hoek, 1983). The freedom of movement depends on the number, orientation, shear strength and spacing of the surfaces separating the blocks which may or may not be coated with weaker material (Hoek, 1983). It is intuitive therefore that fractured material is weaker relative to an intact sample of the same material as component debris blocks are able to move more freely in a highly fractured medium. The strength of intact and damaged materials is thus considered separately in iSALE.

The response of intact rock and ice strength ( $Y_i$ ) to variations in confining pressure is not linear (see Figure 4.9 for ice) and is described in iSALE using a smooth Lundborg (1968) approximation:

$$Y_i = Y_0 + \frac{\mu_i P}{1 + \mu_i P / (Y_m - Y_0)}, \quad (4.8)$$

where  $Y_m$  is the limiting strength at high pressure,  $Y_0$  is the shear strength at zero pressure and  $\mu_i$  is the coefficient of internal friction.

A theoretical fully fractured target is composed of completely disconnected material fragments with no cohesion between particles. The strength ( $Y_d$ ) of such a material is provided by frictional forces between the fragments and can therefore be described in iSALE using a simple Mohr Coulomb model (e.g. Collins et al., 2004):

$$Y_d = Y_{d0} + \mu_d P, \quad (4.9)$$

where  $Y_{d0}$  is the effective cohesion of the damaged material,  $\mu_d$  is the coefficient of friction at low pressure, and  $P$  is the ambient pressure.

The amount of target damage (the density of the fractures) caused by impact is highest close to the impact site and decreases with radial distance from the crater centre (e.g. Kenkmann, 2002). The strength of the target material therefore also varies radially, increasing from the fully damaged strength at the crater centre, to the intact strength at larger

distances. The degree of target fracturing is controlled in iSALE by varying the ‘damage’,  $D$ , between 0 and 1. Undamaged targets are represented by  $D$  values of 0; a value of 1 indicates that the target is fully fractured. A suitable target strength,  $Y$ , between the fully fractured and intact values is then calculated using Equation 4.10 (after Ivanov et al., 1997):

$$Y = (1 - D)Y_i + DY_d. \quad (4.10)$$

### Strain Rate Dependent Fracture

Strain rate is the rate of change in material strain over an interval of time. Numerical simulations show that during crater excavation and collapse the accumulated strain in the cratered material is of order 1 (Collins, et al., 2004). Impact crater formation, for km-scale craters on planets and satellites, typically lasts 10s to 100s of seconds, dependent on the transient crater size. Impact crater formation is thus generally associated with strain rates on the order of 1 to  $10^4 \text{ s}^{-1}$ . Crater formation time in laboratory scale cratering is of the order of milliseconds, implying that strain rates in this case are much larger than 1. In the case of viscous relaxation (Section 1.2.4), on the other hand, the same order of strain is accumulated over millions of years; thus, viscous relaxation of craters occurs at strain rates of  $\sim 10^{-15} \text{ s}^{-1}$ . Planetary-scale cratering thus operates at a strain rate regime between rapid laboratory-scale cratering and slow viscous relaxation.

For very high strain rates, between 1 and  $1000 \text{ s}^{-1}$ , the strength of some silicate rocks is observed to increase as strain rate increases (e.g. Lockner, 1995). However, for strain rates less than 1, the increase is so small that brittle rock strength is generally considered to be independent of strain rate (e.g. Lajtai et al., 1991). The effect of strain rate on rock strength is thus often neglected.

### Temperature Dependence

The strength of geologic materials decreases as their temperature approaches the melting point, losing all shear strength upon melting (e.g. Jaeger and Cook, 1969). As the strength of rock and ice is temperature dependant (see Section 4.2.3 for details specific to ice), the amount of heat generated by impact can theoretically be expected to produce localised weakening of the target material. The extent of this weakening is dependent on the ratio of the melting temperature of the material,  $T_m$ , and the ambient temperature,  $T$ . Consequently, the effect of this thermal softening is most extreme in materials with relatively low melting points, such as ice, as the ambient temperature is likely to be relatively close to the melting point. This trend is approximated in iSALE through Equation 4.11 (after Ohnaka, 1995):

$$Y_t = Y \tanh \left[ \xi \left( \frac{T_m}{T} - 1 \right) \right], \quad (4.11)$$

where  $Y$  is the material strength at low temperature and  $\xi$  is a material constant (see Table 4.2). As thermal softening is dependent on the material melt temperature, the dependencies of  $T_m$  are also incorporated in iSALE; this is outlined with specific reference to the melting point of ice in Section 4.2.3.

#### 4.1.4 Constitutive Model II - Additional Material Weakening During Impact

In addition to a material's standard response to applied stress as measured in a laboratory, it is generally accepted that a further weakening mechanism must be included in the constitutive model for impact events (e.g. Collins et al., 2004). As outlined in 1.5.1, the apparent strength of the Ganymede crust during complex crater formation is of the order of 0.2 MPa. This is well below the static strength values of ice (see Figure 4.9), suggesting that the target becomes weakened during impact.

The need for low material strength beneath craters to explain complex crater collapse is supported by recent modelling work (Wünnemann and Ivanov, 2003). This weakening may be achieved to some extent by the intensive fracturing of the target. However, the formation of central peaks and peak-rings also indicates a more fluid-like movement during complex crater collapse, similar to cratering in water (Worthington, 1963). In this case, the target material is better described as a Bingham fluid which responds elastically to stress until some strength limit is reached, after which it flows as a viscous fluid (Bingham, 1916).

As crater morphology is ultimately retained, this weakening process is required to be transient, lasting only as long as the crater takes to collapse (Melosh and Ivanov, 1999). The nature of this fluidization is poorly understood at present and several weakening mechanisms have been suggested. These are outlined by Melosh (1989) and include thermal softening (O'Keefe and Ahrens, 1993; 1999), interstitial fluid and melt fluidization (Spray and Thompson, 1995) and Acoustic Fluidization (Melosh, 1979).

For any one of these weakening mechanisms to facilitate complex crater collapse, the time taken for the collapse of a crater in a fluid of viscosity  $\mu$  must take place over a similar time scale to the purely gravitationally controlled free-fall collapse time,  $t_{\text{free}} = \sqrt{2H_r/g}$  where  $H_r$  is the transient crater depth and  $g$  is the gravitational acceleration of the target body. This has been defined by Melosh (1983):

$$t_{\text{visc}} = \frac{2\eta}{\sigma}, \quad (4.12)$$

For a driving stress of  $\sigma \sim \rho g H_t$ , Equation 4.12 suggests a critical viscosity of

$$\eta_{crit} \approx \frac{1}{\sqrt{2}} \rho g^{1/2} H_t^{3/2}. \quad (4.13)$$

In order for a suggested weakening mechanism to be the primary facilitator of crater collapse, the effective viscosity of the target material, when subject to the style of weakening, must therefore remain below  $\eta_{crit}$ .

iSALE already considers the effect of thermal softening with the implementation of Equation 4.11. O’Keefe and Ahrens (1999) assume that the critical temperature above which thermal softening will operate is 80% of the material’s melting temperature. Although temperatures shortly after impact can exceed this value, they are not thought to be prevalent over large enough volumes to account for such extreme material weakening during crater collapse (Ivanov, 2000). Another weakening mechanism is thus employed in iSALE. Of the suggested mechanisms, the most commonly used and well developed theory for use in the iSALE hydrocode is that of Acoustic Fluidization.

### Acoustic Fluidization

The basic concept of Acoustic Fluidization involves rock debris flowing fluidly when subject to strong vibrations and was first applied to impact crater collapse by Melosh (1979) as an extension of existing models of earthquake-induced landslides (Seed and Goodman, 1964). Impact and explosion events fracture the target material into debris blocks of varying size. The propagation of the impact/explosion shock wave through this fractured material produces a random seismic wave-field in its wake; the vibrations from which are transmitted as elastic (sound) waves via rock-to-rock contacts.

The stress fluctuations produced during explosion experiments have been noted to exceed the over-burden pressure near the crater in some locations (Gaffney and Melosh, 1982). In areas where the strength of the rarefaction waves does equal or exceed the overburden pressure, debris blocks are able to move relative to one another (Figure 4.3). These sporadic localised slips allow the rock mass to move in a fluid-like manner on a macroscopic scale with an effective viscosity,  $\eta_{eff}$ , dictated by the frequency and violence of the vibrations:

$$\eta_{eff} \approx \frac{\rho \lambda c}{2} \left( \frac{2}{erfc(\chi)} - 1 \right), \quad (4.14)$$

where  $\lambda$  is the wavelength of the acoustic vibrations,  $c$  is the bulk sound speed of the granular debris of bulk density  $\rho$ ,  $erfc$  is a complementary error function, and  $\chi$  is defined by:

$$\chi \approx \frac{1 - \Omega}{\Sigma}. \quad (4.15)$$

$\Omega$  is a dimensionless measure of the driving stress,  $v/\tau_{static}$ , where  $\tau_{static} = \mu P$  is the stress required to initiate failure when no vibrations are present.

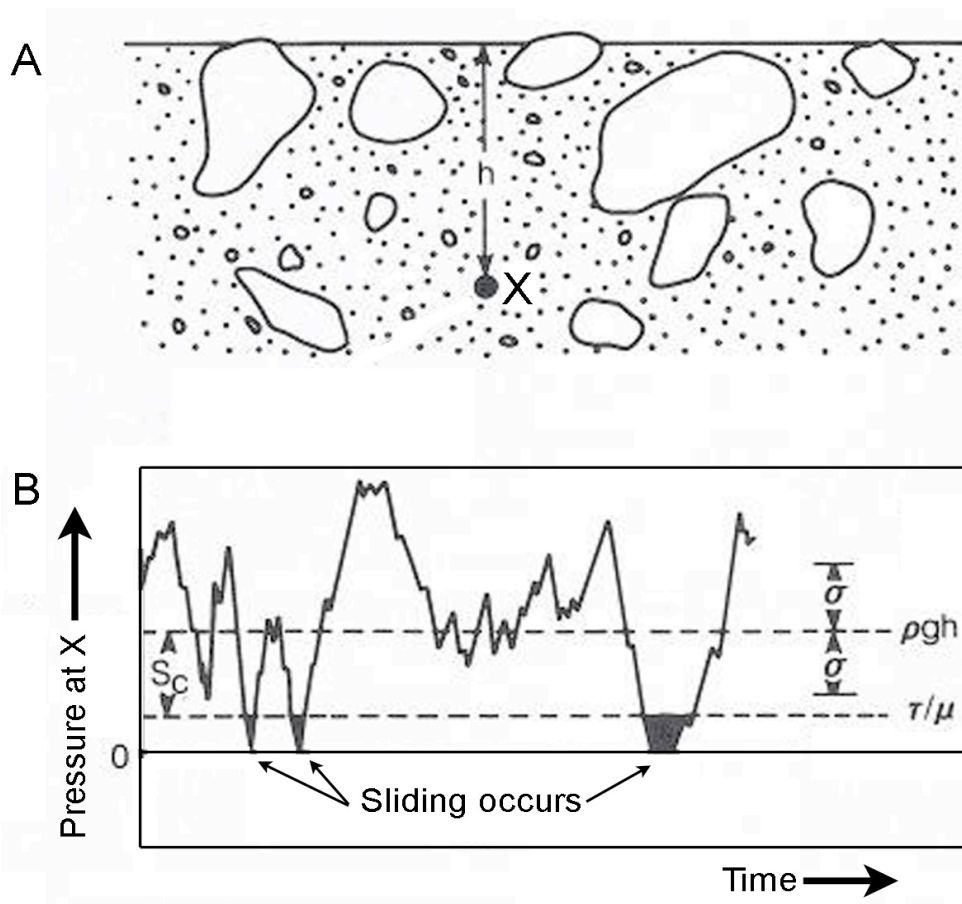


**Figure 4.3:** A) diagram of a fragmented rock mass. B) Schematic diagram showing the theoretical variance in net pressure with time at location X within a material. The net pressure oscillates about the overburden pressure ( $\rho gh$ ) at depth  $h$  in response to the acoustic pressure field.  $\mu$  is the coefficient of friction,  $\tau$  is the shear stress and the critical amplitude of the pressure vibrations ( $S_c$ ) is marked. When the net pressure drops below  $\tau/\mu$  slippage of the debris blocks can occur; these occasions are emphasised in black. Image taken from Melosh, 1979.

$$\Sigma \approx \frac{\sigma}{S_c}. \quad (4.16)$$

$\Sigma$  provides a dimensionless measure of the strength of the acoustic pressure field.  $S_c$  is the critical amplitude of the pressure vibrations above which slip between blocks can occur and is marked on Figure 4.3. This parameter is material dependent as it depends on density (via the overburden pressure,  $P = \rho g H_l$ ) and the coefficient of internal friction,  $\mu$ :

$$S_c \approx P - \frac{\tau}{\mu}. \quad (4.17)$$

For  $\Sigma \ll 1$  (Large  $S_c$ ), Equation 4.14 indicates very large effective viscosities. However, as the critical amplitude approaches the overburden pressure  $\Sigma$  tends to 1 and the bracketed section of Equation 4.14 tends to 1. This produces viscosities of the order of  $\rho \lambda c$ . The wavelength of the pressure vibrations,  $\lambda$ , must be much greater than the grain size,  $d$ , of the material for Acoustic Fluidization to operate (Melosh and Ivanov, 1999):  $\lambda \gg d$ . The viscosity of a fragmented sub-crater rock mass ( $\rho \sim 2700 \text{ kgm}^{-3}$  and  $c \sim 500 \text{ ms}^{-1}$ ) with a metre-scale grain size can therefore flow with a viscosity of the order  $10^8 \text{ Pa s}$ , for a  $\lambda = 10d$ .

As the vibrations dissipate, slip events become more localised and less frequent leading to a decrease in the size of the fluidized region, and a larger dynamic viscosity. Once a high enough viscosity is reached the target material ceases to act as a Bingham fluid and any remaining internal morphology is ‘frozen’ in place. The time taken for the acoustic vibrations to decay to this point depends upon the scattering, and also the regeneration, of acoustic energy during the flow (Melosh, 1996).

Observations of acoustic noise development during explosion tests suggest that the rate of decline in acoustic energy is primarily dependent on the volume of the acoustically fluidized area and on the efficiency of energy dissipation within the material (Gaffney and Melosh, 1982). Within a unit volume of fluidized material, the time taken for the acoustic energy  $E$  to decay to  $1/e$  times its initial value  $E_0$  is the ‘decay time’,  $\tau_v$ :

$$\tau_v = \frac{\lambda Q}{c}, \quad (4.18)$$

where  $Q$  is the ratio of the energy stored per oscillation to the energy dissipated per oscillation. In addition to producing suitably low effective viscosities to facilitate collapse

relative to the free-fall viscosity (Equation 4.19), the process of Acoustic Fluidization must also occur in a comparable time to free-fall collapse (Equation 4.20).

$$\eta \approx \rho\lambda c \leq \eta_{crit} \approx \frac{1}{\sqrt{2}} \rho g^{1/2} H_t^{3/2}, \quad (4.19)$$

$$\tau_v = \frac{\lambda Q}{c} \approx t_{free} = \sqrt{2H_t / g}. \quad (4.20)$$

Combination of these equations implies that the transient crater depth ( $H_t$ ) at which Acoustic Fluidization begins to operate is inversely proportional to the target body's gravity:

$$H_t \geq \frac{2c^2}{gQ}. \quad (4.21)$$

As the crater size at which Acoustic Fluidization can facilitate complex crater collapse scales with gravity, this weakening mechanism provides explanation of  $1/g$  dependence of the simple-to-complex transition diameter (Figure 1.12).

### Implementing Acoustic Fluidization

iSALE adopts a simple mathematical approximation of Acoustic Fluidization, known as the block model (Ivanov and Kostuchenko, 1998), in which the amount and longevity of Acoustic Fluidization can be controlled by two parameters: the kinematic viscosity of the fluidized region,  $\eta$ , and the decay time of the block vibrations,  $\tau_v$  (Wünnemann and Ivanov, 2003). This simplification is depicted in Figure 4.4. In the formal derivation of the block model Melosh and Ivanov (1999) relate  $\eta$  to the average block size of the fragmented sub-crater rock mass,  $B$ .

$$\eta = \frac{2\pi B^2}{T}. \quad (4.22)$$

The decay time of the block vibrations is related to the oscillation period via the quality factor,  $Q$ . Assuming that  $Q$  remains the same for all impact events into the same material,  $\tau_v$  is proportional to the period of block oscillations:

$$\tau_v = \frac{T}{Q}. \quad (4.23)$$

Ivanov and Artemieva (1999) argued that the block oscillations are dampened by soft, low density breccia surrounding individual blocks. Thus the oscillation period may be defined as:

$$T = \frac{2\pi\chi B}{c}. \quad (4.24)$$

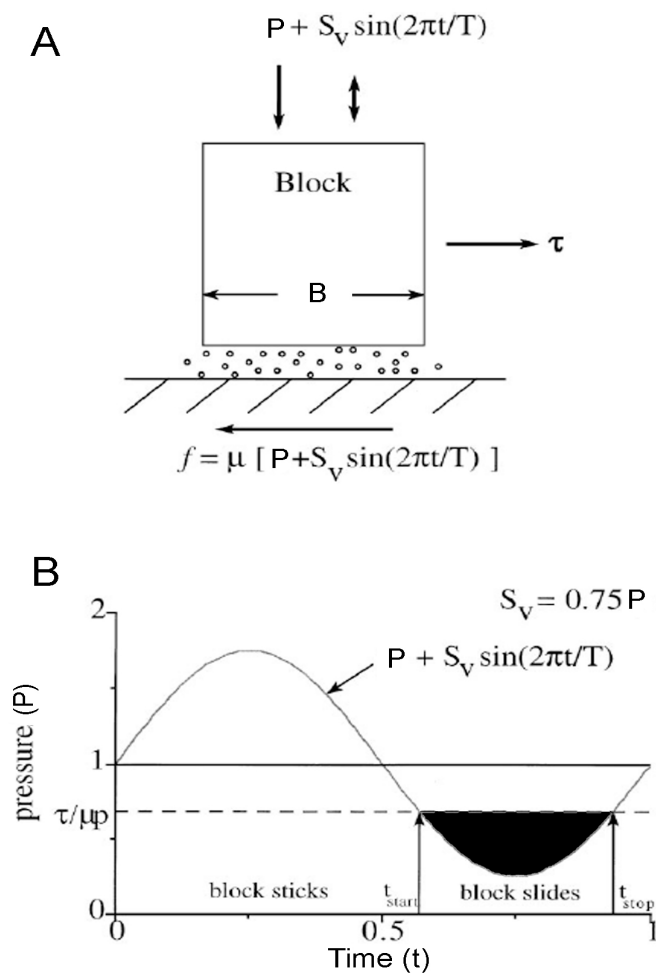


**Figure 4.4:** A) schematic model of a block sliding along an underlying surface. B) B denotes the block size, P the overburden pressure and  $\tau$  and  $f$  mark the directions of the traction stress and the friction stress respectively. The varying acoustic pressure is also indicated with a double ended arrow. B) Graph of the net pressure, relative to the overburden pressure, as the acoustic pressure field varies with time. The black filled areas in this figure and in Figure 4.3 are times at which the block is free to slide along the underlying surface. Figure taken from Melosh and Ivanov, 1999.

$\chi$  is a constant related to the relative size and density of blocks and the surrounding breccia, and  $c$  is the bulk speed of sound in the breccia material. Inserting this result into Equations 4.22 and 4.23 gives:

$$\eta = \frac{cB}{\chi}, \quad (4.25)$$

$$\tau_v = \frac{2\pi\chi B}{Qc}. \quad (4.26)$$

Thus both  $\tau_v$  and  $\eta$  are directly proportional to the block size and consequently directly proportional to each other, such that their ratio is constant for impacts into the same material ( $2\pi\chi/c = \text{constant}$ ).

$$\frac{\eta}{\tau_v} = \frac{c^2 Q}{2\pi\chi^2}. \quad (4.27)$$

To simulate a specific impact event, explicit values for  $\tau_v$  and  $\eta$  must be found such that the modelled crater morphology agrees with observational data. The determination of these Acoustic Fluidization parameters for ice is presented in the next chapter, and their scaling with crater size discussed in Chapter 6.

#### 4.1.5. Testing and Continuing Developments

Modelling results using SALE-related codes have been tested by comparison to terrestrial impact craters such as Sudbury (Ivanov and Deutsch, 1999), the Lake Bosumtwi Impact Structure (Artemieva et al., 2004), Chicxulub (Collins, 2000; Collins et al., 2002) and Ries (Wünnemann et al., 2005). iSALE is also being validated against experiments and compared against other impact hydrocodes as part of “The Hydrocode Benchmark and Validation Project,” led by Betty Pierazzo of the Planetary Science Institute, Tucson (see Pierazzo et al., 2008).

A three-dimensional version of iSALE, which can run on parallel processors, has also been developed and is currently being tested and validated (Elbeshausen et al., 2007). Both iSALE and iSALE3D are written in Fortran90 which has improved memory allocation, portability, readability and has reduced cycle completion time relative to the original SALE (written in Fortran77).

## **4.2. Updating iSALE for Modelling Impact into Ganymede**

### **4.2.1 Ice EoS for use in hydrocode modelling of impacts**

As discussed in Section 4.1.2 hydrocode modelling of impact involving a given material requires an equation of state (EoS) for the material, which defines the pressure in the material as a function of density and internal energy. In other words, a material's EoS describes the pressure that a sample of a given density and internal energy would exert on its surroundings. The pressure, density and internal energy variation during an impact is so extreme that the equation of state must cover an enormous range in density and internal energy. However, the behaviour of a material over such a range is impossible to determine entirely experimentally. Impact equations of state, like the Tillotson EoS, are therefore constrained in part by experimental measurements, and in part by extrapolation to extreme theoretical limiting cases.

For modelling impact crater formation the most important property of an equation of state is that it accurately describes the response of the material to shock compression—an instantaneous rise in pressure, density and internal energy. Consequently, equations of state suitable for use in impact hydrocodes are defined, in large part, by laboratory measurements of the shock response of materials. The compression experienced during the passage of a shock wave acts to raise the pressure, density, temperature and the internal energy of the material simultaneously and temporarily. The shock wave, which travels with a characteristic wave speed that depends on the strength of the shock and the material, also accelerates the material temporarily to a certain particle velocity. The locus of all possible shock states, in terms of shock velocity, particle velocity, pressure, density and internal energy are described by the Hugoniot equations (4.28 to 4.30). These represent the conservation of mass, momentum and energy across the shock wave, respectively:

$$\rho(V - v_p) = \rho_0 V, \quad (4.28)$$

$$P - P_0 = \rho_0 v_p V, \quad (4.29)$$

$$E - E_0 = \frac{1}{2}(P + P_0) \left( \frac{1}{\rho_0} - \frac{1}{\rho} \right). \quad (4.30)$$

In other words, these equations, which apply for all materials, allow the conditions (particle velocity  $v_p$ , density  $\rho$ , internal energy  $E$  and the pressure  $P$ ) after a shock wave of velocity  $V$  has passed to be defined relative to the initial conditions ( $\rho_0$ ,  $E_0$ ,  $P_0$ ). When combined with

the equation of state for a specific material, these three equations completely describe the response of that material to shock, which is referred to as the material's "Hugoniot." Conversely, to fit an analytical EoS, like the Tillotson EoS, to experimental shock data, the EoS must be solved simultaneously with the Hugoniot equations to produce the modelled Hugoniot for comparison.

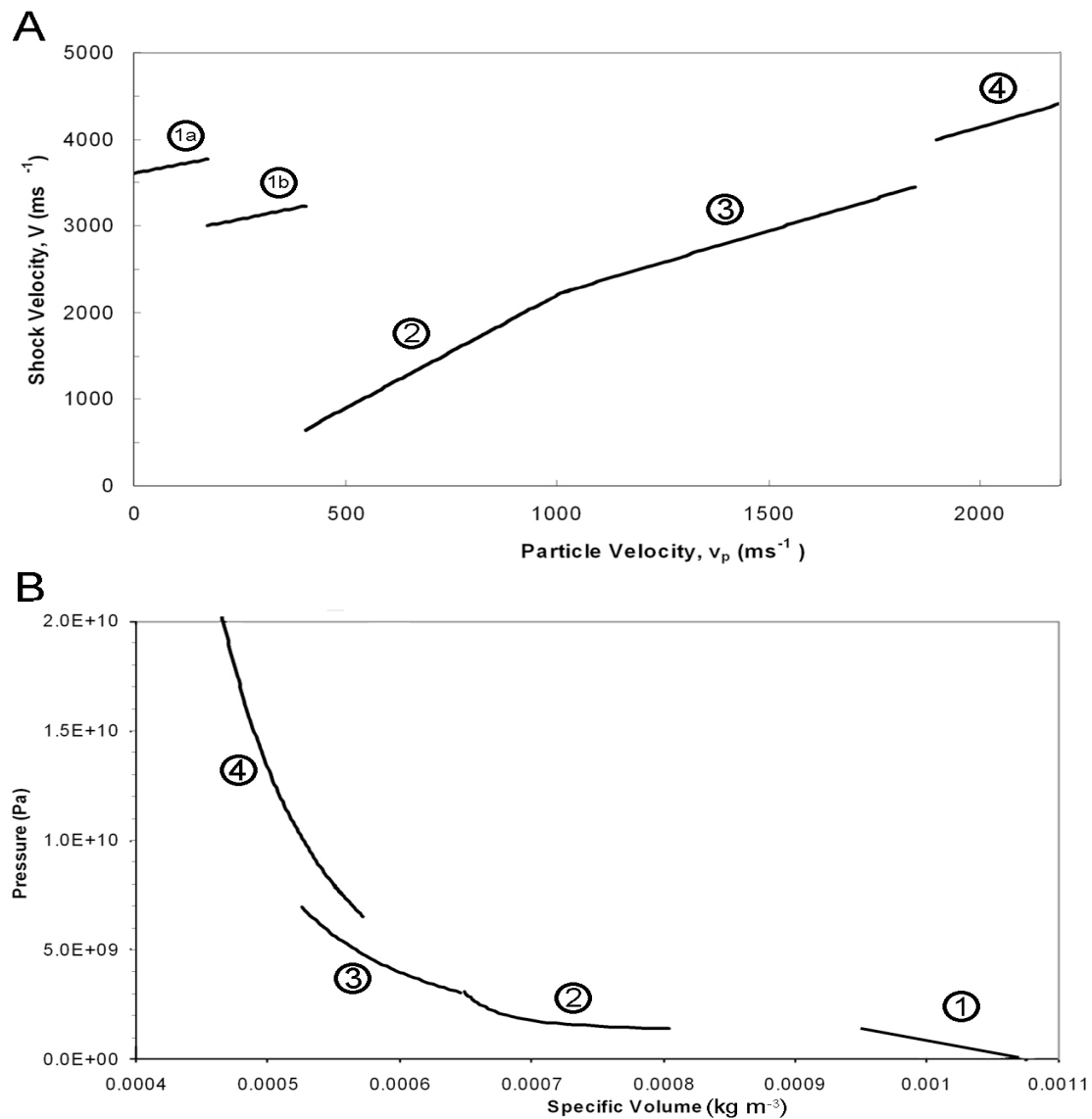


**Figure 4.5:** The observed shock Hugoniot curve for water ice, shown in different forms. A) The Hugoniot curve for water ice as derived from shock wave measurements in low temperature ice (100 K) by Stewart and Ahrens (2005). B) The same Hugoniot curve presented in terms of specific volume (1/density) and pressure. The observed Hugoniot displays four main regions (1) ice 1h (composed of elastic shocks (1a) and deformation shocks (1b)) and shock transformation to (2) ice VI, (3) ice VII and (4) liquid water.

Typical measurements made during a shock experiment are peak pressure versus particle velocity. These two variables can be used to calculate the other shock properties (e.g. internal energy, shock velocity, density) using the Hugoniot equations, so that the experimentally determined Hugoniot can be plotted in terms of any combination of the shock properties. At the same time, the Hugoniot equations can be solved simultaneously with the Tillotson EoS for compression (Equation 4.4 and 4.31), using a simple iteration, to construct a theoretical Hugoniot curve for the material, in terms of any combination of the shock properties. The Tillotson EoS parameters can then be adjusted, and the Hugoniot recomputed, to determine the best fit to the experimental Hugoniot curve.

### Current Fit of the Tillotson EoS to Observational Data

Figure 4.5A shows the Hugoniot curve for water ice as derived from shock wave measurements in low temperature ice (100 K) by Stewart and Ahrens (2005). This figure presents the shock data in terms of particle velocity ( $v_p$ ) and shock velocity ( $V$ ). These properties are related to pressure ( $P$ ) and specific volume ( $1/\rho$ ) via the Hugoniot Equations 4.28 and 4.29 and have been converted to construct Figure 4.5B.

The observed Hugoniot displays four main regions spanning pressures from 0 GPa to greater than 20 GPa: (1) ice 1h (composed of elastic shocks and deformation shocks) and shock transformation to (2) ice VI, (3) ice VII and (4) liquid water. Ice VI and ice VII are high density phases of water ice; their location relative to the more commonly known ice, Ih, is shown in the ice phase diagram shown in Figure 4.11B.

**Table 4.1: Tillotson Equation of State Parameters for Water and Ice Ih**

Material	$\rho_0$ ( $kg/m^3$ )	$a$	$b$	$A$ (GPa)	$B$ (GPa)	$C$ (GPa)	$E_0$ (MJ/kg)	$\alpha$	$\beta$	$E_{iv}$ (MJ/kg)	$E_{cv}$ (MJ/kg)
Water (0°C)	998	0.7	0.15	2.18	13.25	0	7	10	5	0.419	2.69
Ice Ih (-10°C)	1293	0.3	0.1	9.8	6.5	0	10	10	5	0.773	3.04
H <sub>2</sub> O	910*	0.3	0.1	12	-24	17	10	10	5	0.773	3.04

\*‘Water’ and ‘Ice Ih’ values are from O’Keefe and Ahrens (1982).

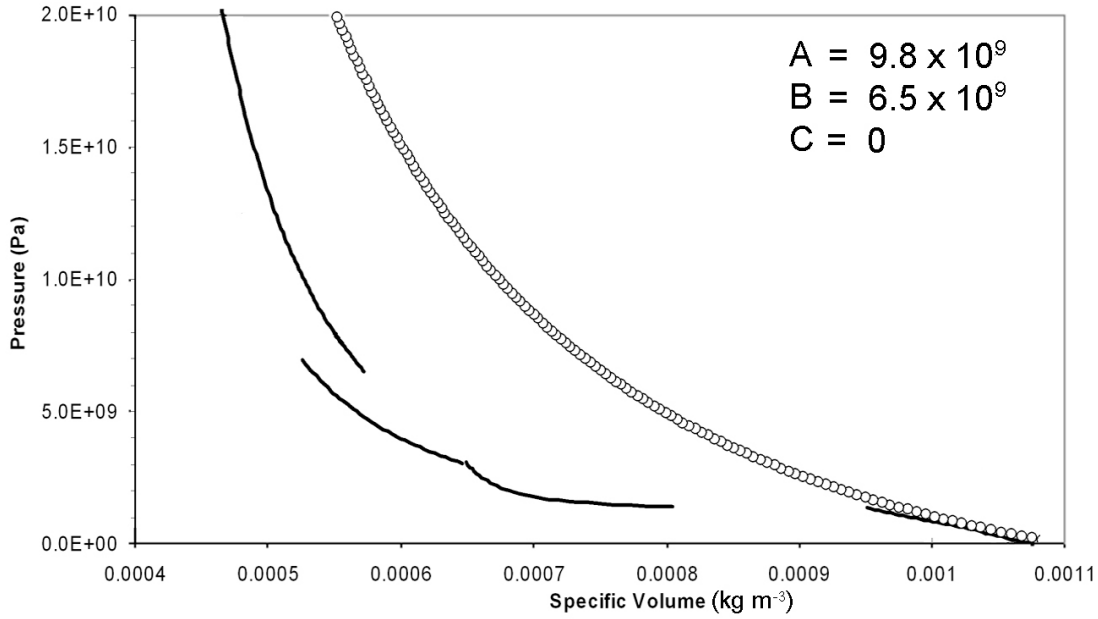


**Figure 4.6:** The Hugoniot curve produced using the Tillotson EoS (Equation 4.4) and the parameters for Ice Ih in Table 4.1 (open circles). The values used in Equations 4.4 for the parameters  $A$ ,  $B$  and  $C$  are shown on the figure; see Table 4.1 for the other parameter values. The observed Hugoniot for ice derived from Stewart and Ahrens (2005) data is shown with a black line.

Table 4.1 presents the Tillotson parameters for ice Ih and water, as defined by Anderson (1968), Larsen et al. (1973), and Gaffney and Ahrens (1980). The Hugoniot produced when using the Tillotson equation of state is included in Figure 4.6 and shows the fit to observational data to be imperfect; the thermodynamic behaviour of ice Ih is well matched, but the pressures are significantly over estimated for the ice VI and VII phases. The following section presents the development of an alternative equation of state to better recreate the Hugoniot curve of ice.

#### 4.2.2 Development of an Alternative EoS for Ice

This work assumed that a better approximation of the observed Hugoniot than that provided by the Tillotson EoS could be achieved by modifying the compression part of the Tillotson EoS (Equation 4.4) to include a cubic term:

$$P = \left[ a + \frac{b}{(E/(E_0\eta^2) + 1)} \right] \rho E + A\mu + B\mu^2 + C\mu^3. \quad (4.31)$$

$C$  is an additional material specific parameter.

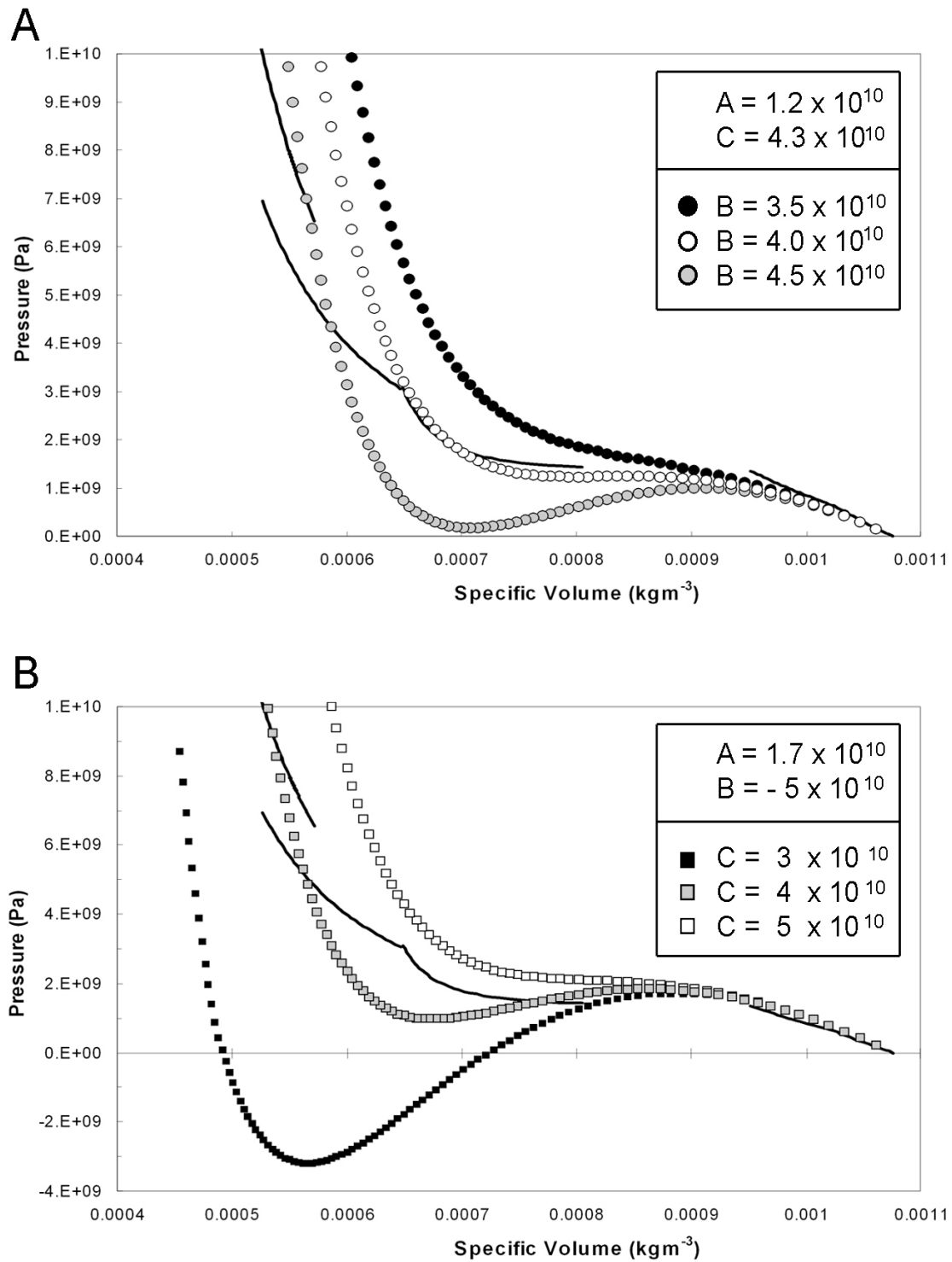


**Figure 4.7:** Example Hugoniot curves produced using different values for the  $A$ ,  $B$  and  $C$  parameters of Equation 4.31. These curves are marked by data points. The observed Hugoniot of Figure 4.5B is included for comparison as a black line. A) Constant  $A$  and  $C$  values, parameter  $B$  is varied. B)  $A$  and  $B$  values are constant,  $C$  is varied.

To determine the best-fit parameters  $A$ ,  $B$  and  $C$  for ice, a short Fortran script was written to solve Equations 4.30 and 4.31 simultaneously (see Appendix B). This program produced a series of corresponding density, pressure and internal energy values which were then plotted to create a series of possible Hugoniot curves (Figure 4.7). The Hugoniot curves produced with each set of  $A$ ,  $B$  and  $C$  values were then compared to the observational data (black lines in Figure 4.7) to determine the best fit, as presented in Figure 4.8.

The best fit parameter values for this new third-order Tillotson EoS are included with the established values for the Tillotson EoS for water and ice Ih in Table 4.1. The Hugoniot produced using the modified Tillotson EoS produces a fair approximation to the general trend shown by the observational data. There is a close approximation to ice Ih and, although still imperfect, the fit to the water, ice VII and ice VI curve sections is significantly improved relative to the Hugoniot created when using the original Tillotson EoS (Figure 4.6).

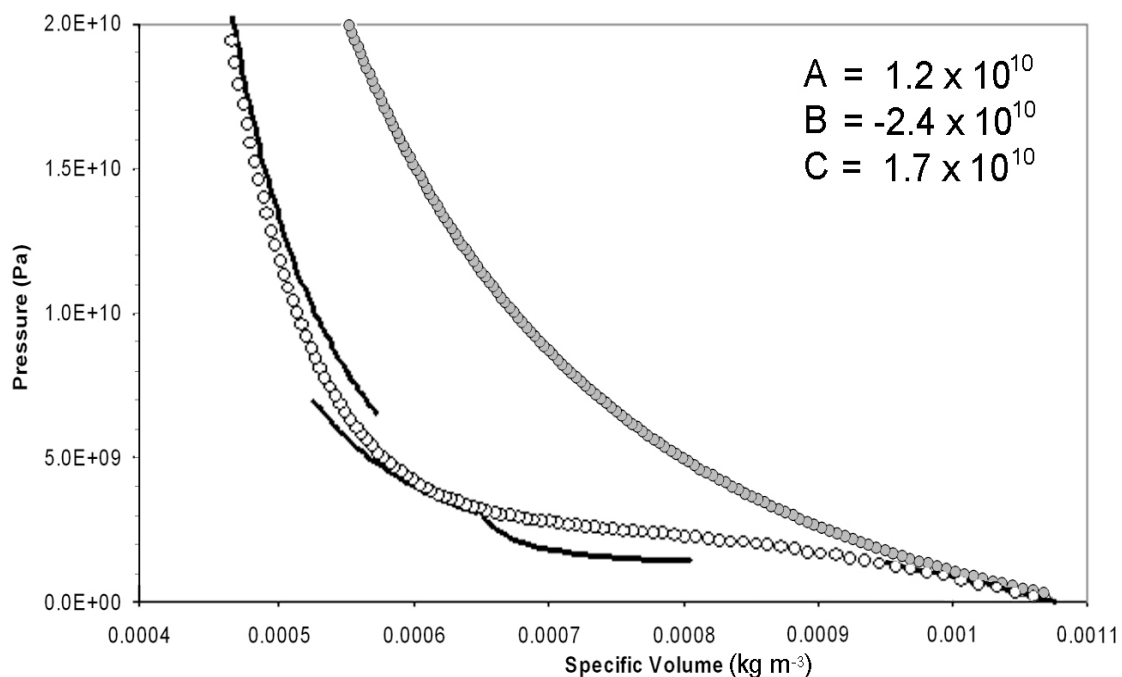


**Figure 4.8:** The third-order Tillotson EoS (Equation 4.31) developed during the course of this work using the parameters for ‘H<sub>2</sub>O’ in Table 4.1 is shown in open circles. The values used in Equation 4.31 for the parameters  $A$ ,  $B$  and  $C$  are shown; see Table 4.1 for the other parameter values. The observed Hugoniot for ice derived from Stewart and Ahrens (2005) data is shown with a black line. The Hugoniot curve produced using the Tillotson EoS (Equation 4.4) is included for comparison as grey circles.

### 4.2.3. The Constitutive Model for Ice

The constitutive behaviour of ice at low temperature is similar to that of rock as described in Section 4.1.3. In this section, published strength data for water ice is presented and modifications to iSALE for simulating the strength of water ice are explained.

#### Pressure and Damage Dependence of Ice Strength

The strength of intact and fractured water ice are included in Figure 4.5 (Durham et al., 1983; Beeman et al., 1988), which shows that the strength of fractured ice at a confining pressure of 100 MPa is one third of its intact value. The strength of fractured ice ( $Y_d$ ) increases with increasing confining pressure ( $P$ ), as noted for silicate rock. However, unlike damaged rock, fractured ice strength does not follow a linear dry-friction relationship (e.g. Equation 4.9). As a result, in this work the static strength of damaged ice was represented not by a simple Couloumb model, as was used by Collins et al., (2004), but rather using a Lundborg-like approximation:

$$Y_d = Y_{d0} + \frac{\mu_d P}{1 + \mu_d P / (Y_m - Y_{d0})} \quad (4.32)$$

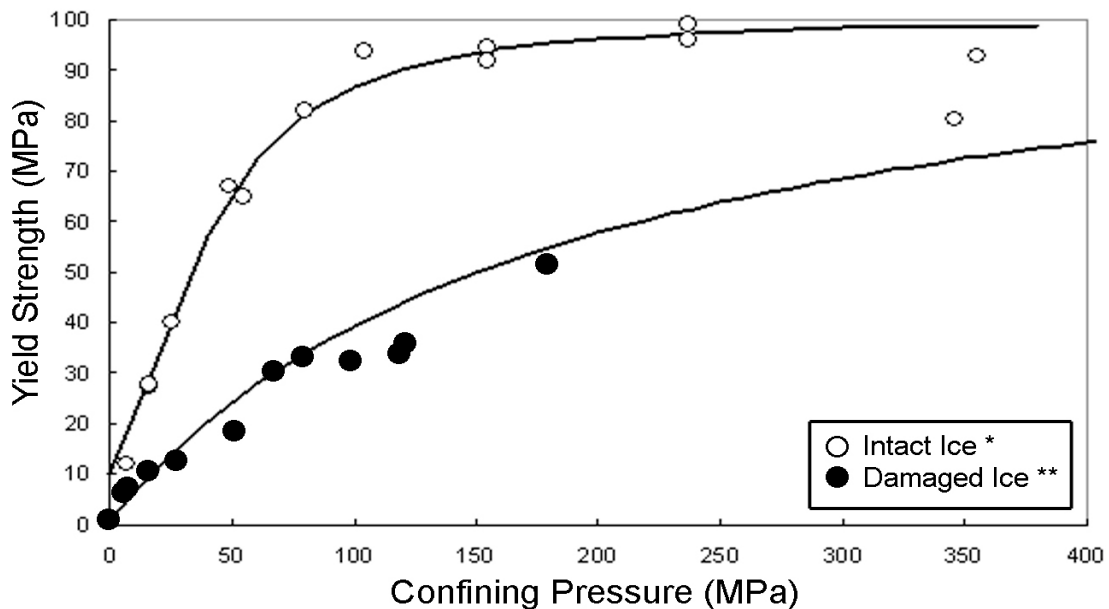


**Figure 4.9:** Ice strength as a function of pressure for fractured (\*\*Beeman et al., 1988) and intact ice (\* Durham et al., 1983). Trend lines were fitted to observational data using Lundberg approximations of the form in Equations 4.8 and 4.32 for intact and damaged ice respectively. The specific variables used to obtain these fits for ice are shown in Table 4.2.

$Y_{d0}$  is the effective cohesion of the damaged ice,  $\mu_d$  is the coefficient of friction at low pressure, and  $Y_m$  is the limiting strength at high pressure. Table 4.2 lists the static ice strength model parameters used in this work (see Collins et al. 2004; 2008, for further parameter descriptions).

### Strain Rate

The strength of ice shows a stronger dependence on strain rate than rock strength (Lajtai et al., 1991). However, as noted for rock, ice strength at strain rates appropriate for planetary-scale cratering is noted to remain approximately constant (Kim and Keune, 2007). The dependence of ice strength on strain rate is thus neglected in this work.

### Temperature Dependence

Laboratory data for ice at different temperatures is presented in Figure 4.10, illustrating the weakening of ice as ambient temperature increases. The temperature dependence of ice is approximated in iSALE through Equation 4.11 (after Ohnaka, 1995) and using the parameter values in Table 4.2, as noted for other materials in Section 4.1.3. As the extent of thermal weakening is a function of melt temperature, the variation in  $T_m$  with other factors is also considered.

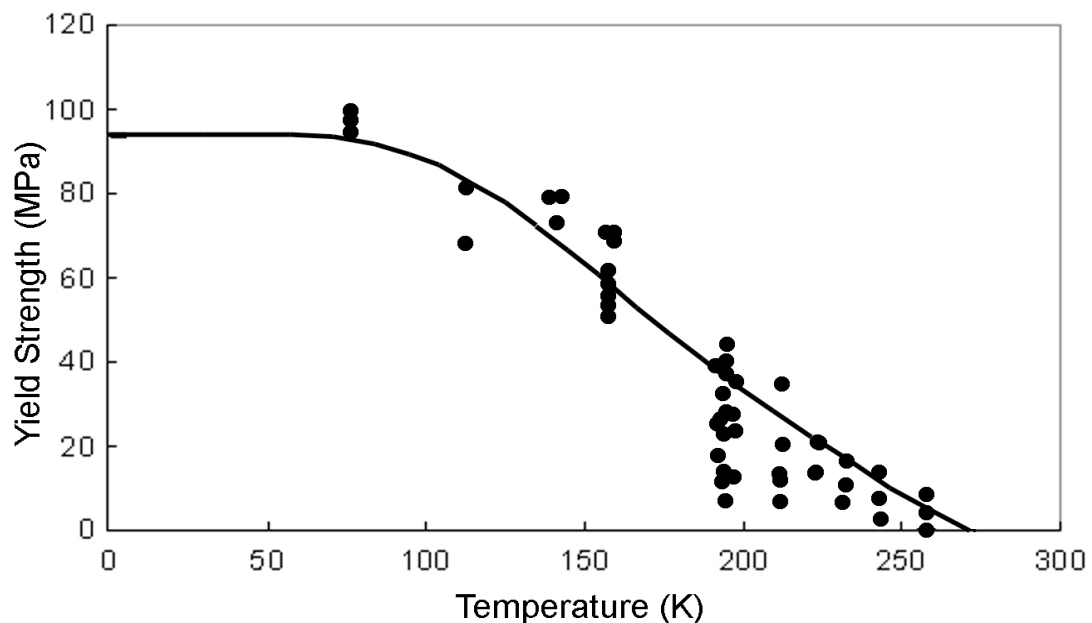


**Figure 4.10:** Variation of ice strength with ambient temperature. Data from Durham et al. (1983) is shown in closed circled and encompasses a range of pressures and strain rates. The black line marks the approximation of thermal softening algorithm employed in iSALE using Equation 4.11.

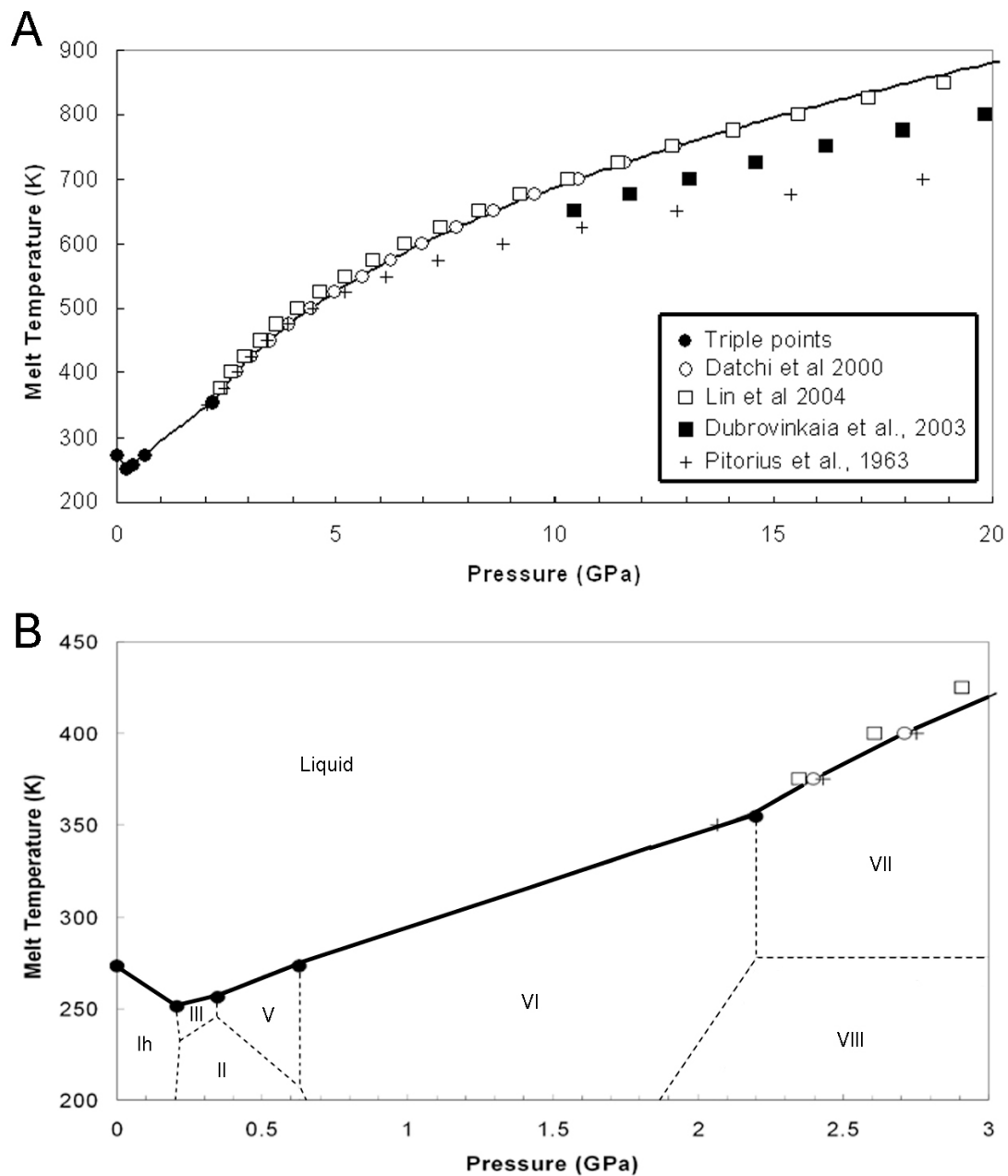


**Figure 4.11:** A) Melting temperature of ice at different pressures. Data from laboratory tests; references are noted in the figure key. B) Phase diagram of ice constructed from triple point data (Durham and Stern, 2001; Fletcher, 1970).

Figure 4.11 shows the melting point of ice recorded from a variety of high pressure laboratory tests (Pistorius et al., 1963; Datchi et al., 2000; Dubrovinkaia and Durovinsky, 2003; Lin et al., 2004). The black trend line in Figure 4.11A incorporates all data for pressures < 5 GPa and the similar results of Lin et al (2004) and Datchi et al. (2000) for the higher pressures. The melting temperature in the lowest pressure range was established on the basis of recorded triple points for water and its different ice phases (Durham and Stern,

2001; Fletcher, 1970) (Figure 4.11B). This complicated relationship is implemented in iSALE with a series of equations each applicable to a different pressure range (see Appendix C).

### **4.3 Summary**

Alongside laboratory experiments, remote observations and terrestrial field studies, numerical modelling provides a fundamental tool for investigating the dynamics of impact cratering. To simulate impact crater formation, hydrocodes employ a combination of classical continuum mechanics, equations of state and material strength models. Together, these are used to describe the dynamics of various materials and their response to shocks, which is governed by the specific material properties.

The iSALE hydrocode has undergone significant development from its original SALE form, specifically by Jay Melosh, Boris Ivanov, Kai Wünnemann and Gareth Collins. The code now incorporates a number of different equations of state, a range of possible rheological models and the ability to simulate multiple material targets. iSALE has been used to simulate a number of terrestrial impact structures, and the results tested by comparison with field and remote sensing data (e.g. Ivanov and Deutsch, 1999; Artemieva et al. 2004; Collins, 2000, Collins et al., 2002; Wünnemann et al., 2005). This work applies the iSALE hydrocode to simulating impact crater formation on Ganymede.

To simulate impacts in ice with iSALE it was necessary to adapt the existing material models used by iSALE. Both the constitutive model and the equation of state for ice have been updated on the basis of laboratory data (e.g. Beeman et al., 1988; Durham et al., 1983; Stewart and Ahrens, 2005). The material parameters are included in Table 4.2.

**Table 4.2: Material Properties Employed for the Simulations Presented in Chapter 5**

Parameter	Ganymede
Cohesion (yield strength at zero pressure), $Y_0$	10 MPa
Damaged cohesion, $Y_{d0}$	0.5 MPa
von Mises plastic limit (yield strength at infinite pressure), $Y_m$	0.11 GPa
Coefficient of internal friction, $\mu_i$	2
Damaged coefficient of friction, $\mu_{di}$	0.6
Melt temperature, $T_m$	273 K
Pre-impact surface temperature, $T$	100 K
Thermal softening parameter, $\xi$	1.2
Degree of Damage, $D$ (between 0 and 1)	1
Density at zero pressure, $\rho_0$	910 kg m <sup>-3</sup>
$\chi$	0.5
Sound speed, $c$	400 ms <sup>-1</sup>

Due to the complexity of the H<sub>2</sub>O phase diagram (Figure 4.11B), most available equations of state are tailored to specific ice phases, and can significantly decrease in accuracy of approximation in other regions of the phase diagram (e.g. fit to Hugoniot curve in Figure 4.6). The Tillotson EoS for ice Ih (Ivanov et al., 1997) is one example of an equation of state that is widely used for impact simulations which does not provide close fit to high pressure ice phases VI and VII and for liquid water. The third-order Tillotson EoS developed during the course of this work provides a better approximation of the Hugoniot curve for ice at these high pressures (Figure 4.8). The fit is still imperfect and may overestimate the pressures for the water-section of the ice Hugoniot curve, but provides a significantly better approximation of the observed Hugoniot for ice than the original Tillotson EoS.

High pressure, low temperature laboratory data for ice presented in this chapter has been utilised to create a static strength model for use in simulating impact into Ganymede, which is presented in the next chapter. The dependence of ice strength on temperature, pressure, damage and strain rate is incorporated into the constitutive model through implementation of the equations presented for these relations in this chapter (Equations 4.8, 4.10, 4.11 and 4.32). The material properties used for Ganymede ice are presented in Table 4.2.

Several mechanisms have been suggested to explain the additional target weakening that occurs during impact crater collapse. iSALE incorporates the weakening mechanisms of thermal softening and Acoustic Fluidization. Thermal softening is more effective in ice than rock due to its lower melting point; this is taken into account through the use of Equation 4.11. As thermal softening alone is not thought to account for such extreme material weakening during crater collapse (Ivanov, 2000), and the theory of Acoustic Fluidization is applicable to all granular materials, this work also applies this weakening mechanism to the icy Galilean Satellites. The extent of the fluidization during impact can be controlled in computer models by varying the Acoustic Fluidization ‘Block Model’ parameters  $\tau_v$  and  $\eta$ ; their identification for ice is considered in the next chapter.

## Chapter 5

# Modelling Crater Formation in Ice

Before using numerical modelling to investigate impact crater formation in layered ice, a strength model for pure, unlayered ice must first be established for use in the hydrocode. This involves determining the amount of apparent material weakening experienced by the target during impact, and using this alongside the ‘static’ strength model for ice (Section 4.2.3).

The lack of a definitive strength model for rock during impact implies that numerical modelling of complex crater formation is inherently non-unique - the same crater morphology can be produced with a range of strength models. Consequently, to construct a strength model for impacts in ice, initial investigations employed two methods of simulating material weakening during hydrocode modelling: one a purely empirical model in which the static strength parameters are altered, and a part-empirical, part-theory based model in which the mechanism of Acoustic Fluidization is implemented (see Section 4.1.4).

This chapter details the simulation of impact crater formation in pure ice using these two models. The first part of this chapter assesses the suitability of each model for recreating impact into ice. The most able model is then further investigated in the second part of this chapter and adopted for continued modelling of different sized craters on Ganymede in Chapter 6. Simulations employing the two equations of state for ice presented in Chapter 4 (Equations 4.4 and 4.31) are also compared to assess the influence of this vital component on modelled crater collapse.

## **5.1. Modelling Impact into Ganymede - Approach**

This work used the iSALE hydrocode and static strength properties for ice introduced in Chapter 4 to simulate impact crater formation on Ganymede. Model results were tested via comparison to the scaling trends presented in Chapter 2, and used to determine a set of target strength parameters that can produce a reasonable match between the modelled and observed data. The model set up, including mesh dimensions and impactor and target properties, is presented in this section.

### **5.1.1. Preparation: Reducing Errors and Run-time**

In addition to the material models used by hydrocodes, the resolution and size of mesh used to represent the target is a factor that affects the outcome of simulations. To allow assessment of the sensitivity of simulated crater morphology to changes in strength model parameters, all mesh variables must thus remain unchanged. As the best-fit simulation results were determined primarily on their fit to observed crater wall slope, depth and central peak width, the most suitable mesh size and resolution were selected so that processing time could be reduced while maintaining these simulated crater dimensions.

#### **Resolution**

The spherical projectile used for numerical simulation of impact is made up of a number of cells. The higher the resolution of the computational mesh (i.e. the smaller the cell size), the closer the modelled projectile comes to approximating a perfect sphere (Figure 5.1). Consequently, the projectile has slightly more mass in high resolution runs than for lower resolution runs. This additional mass can lead to different final crater morphologies as shown in Figure 5.1. All of the simulations in this work used a constant resolution of 10 cells per projectile radius, to prevent resolution differences affecting results.

A 10 cell resolution (Figure 5.1B) was chosen above lower resolution options (e.g. Figure 5.1A) as the smaller cell size allows better approximation of a perfectly spherical projectile. Additionally, the higher the resolution (the smaller the size of the cells), the more accurate the simulated spatial variation in target properties. This leads to more accurate results when resolution is high.

Although employing a 10 cell per projectile radius resolution will produce deviations in final crater dimensions relative to higher resolution results, a high resolution can significantly increase the processing time required for the simulation of hypervelocity impact; use of the 10

cell resolution mesh can be days or weeks quicker than simulations performed at higher resolution.

The effect of resolution on final crater morphology is greatest over the smaller features such as the central peak and the crater rim as they are comprised of fewer cells relative to the crater as a whole. This leads to the noticeable differences in the dimensions of the central peak and crater rim between the high and low resolution simulations shown in Figure 5.1. The depth-diameter ( $d/D$ ) ratio of the two simulation results also differs due to its dependence on the crater rim placement. To limit spurious results due to simulating impact at 10 cell resolution, simulation results were primarily assessed on their crater wall slope, as this property does not differ significantly between simulations of differing resolution.

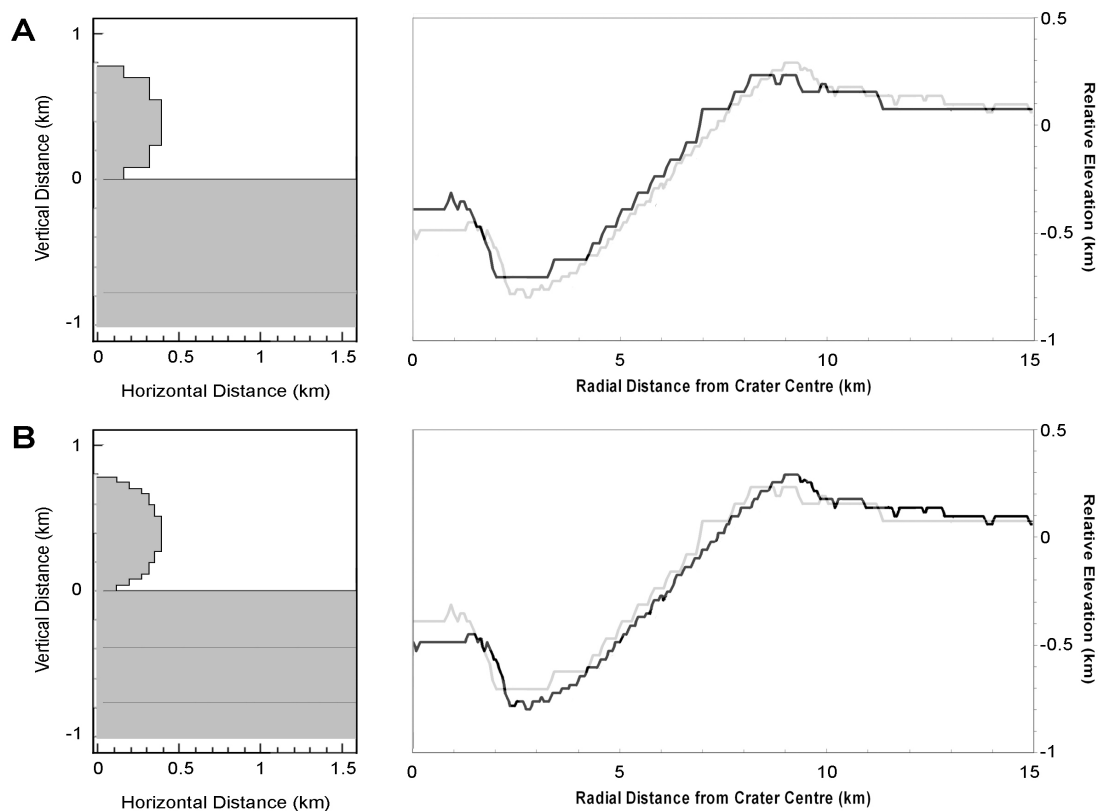


**Figure 5.1:** Effects of different resolution on simulated final crater morphology. A) Initial conditions (left) and final produced crater morphology (right) from a ‘low’ resolution simulation using 5 cells per projectile radius (1 cell width = 80 m). The projectile and intact target are shown on the left; lines within the target mark 10 cell depths, starting from the target surface. The crater profile produced is displayed as a black line on the graph on the right hand side. The grey line on this plot marks the higher resolution results. B) The same information is presented for a higher resolution run (10 cells per projectile radius, 1 cell width = 40 m). In this case, the black line on the right hand profile marks the 10 cell resolution result; the grey line marks the 5 cell result. Both simulations were designed to form a ~ 20 km crater employing an impact velocity of  $10 \text{ km s}^{-1}$  and a projectile radius of 400 m.

### **Mesh Size**

To reduce the time taken for simulations to complete, the mesh should ideally be as small as possible. However, if too small, reflections of the shockwave from the edges of the mesh will interfere with the damage regime in the target. To ascertain the minimum useable mesh size that does not cause strong reflected waves, a suite of simulations using varying mesh dimensions was performed; all other parameters were constant.

The smallest mesh used in this suite of simulations was equivalent to a radial distance from the centre of impact equal to 1 crater diameter ( $D$ ) (Figure 5.2A). This restricted area was chosen so that the effects of edge reflections would be present for assessment. A larger mesh with a radial extent of 2 crater diameters was run in conjunction with this (Figure 5.2B). As an upper bound, mesh dimensions of 5 by 5 times the final crater diameter were used to show an ideal simulation with limited edge reflections (Figure 5.2C). It is assumed that the crater morphology produced using the largest mesh represents the most accurate result of the three simulations.

The results of these simulations are shown in Figure 5.2. The simulation using the largest mesh ( $5D \times 5D$ ) produced a 30 km diameter crater with an 8 km wide central peak (Figure 5.2C). The intermediate mesh ( $2D \times 2D$ ) produces a nearly identical crater with the same dimensions as those of the 'ideal' result produced using the largest mesh, illustrating that reflections do not significantly affect the final crater morphology produced with this mesh size. The smallest mesh ( $D \times D$ ) simulation produces a crater with the correct  $d/D$  ratio and similar wall slope. However, the small mesh crater has a central pit and shows downwelling of material at the mesh axis (Figure 5.2A). The deviation of internal crater morphology produced using the small and large/intermediate meshes is due to reflections initiated at the edges of the small mesh. Consequently, all simulations presented in this work employ a mesh size no smaller than  $2D \times 2D$  to reduce edge reflections causing erroneous results, whilst decreasing run time relative to the larger mesh option.

#### **5.1.2. Impactor Properties**

Due to the 2D axis-symmetric nature of the iSALE hydrocode, the impact angle was restricted to  $90^\circ$  instead of more statistically likely  $45^\circ$  (Pierazzo and Melosh, 2000a). It is acknowledged that variation from this value will have an effect on the sub-crater stress regime (See Pierazzo and Melosh, 2000b). However, the  $90^\circ$  angle employed in iSALE is considered suitable as laboratory work by Gault and Wedekind (1978) has shown crater shape to remain circular for impact angles between  $90^\circ$  and  $30^\circ$ . Internal crater morphology is also noted to remain relatively consistent for impact angles larger than  $20^\circ$  to  $30^\circ$  (Schultz, 1992).

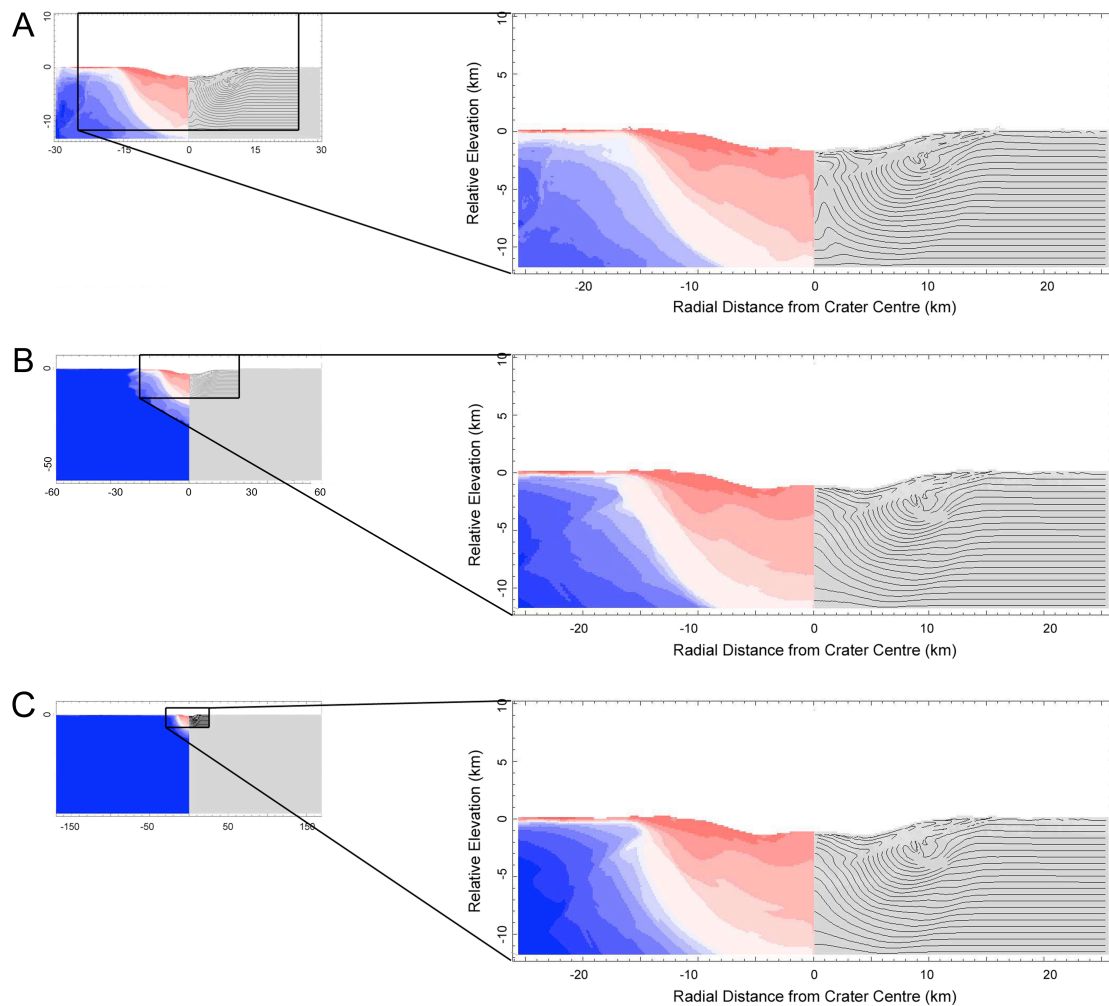


**Figure 5.2:** Effects of different mesh sizes on final crater morphology of a simulated 30 km diameter crater. The full mesh view is shown on the left hand side, and a close up of the final crater morphology shown on the right. Both simulations presented here used projectile with a radius of 500 m, with an impact velocity of  $15 \text{ km s}^{-1}$ , and a resolution of 10 cells per projectile radius. A) Results using mesh equivalent to 30 km by 30 km of modelled target area. B) Results using a mesh equivalent to 60 km by 60 km of modelled target area. C) Results using a mesh equivalent to 150 km by 150 km of modelled target area.

The structure and composition of the projectile used for all simulations presented in this thesis was simplified to spherical and homogeneous. The impactor was modelled as pure water ice with an impact velocity of  $15 \text{ km s}^{-1}$ . Pi-scaling relations were used to estimate the size the impactor required to produce a given sized transient crater (Schmidt and Housen, 1987).

The estimated average impact velocity for Ganymede is  $21 \text{ km s}^{-1}$  (Zahnle et al., 1998). Simulations involving such high impact velocity require computer processing times days longer than lower velocity impact simulations. It is thus advantageous to run simulations at a

lower impact velocity and use a larger projectile to produce the same size crater as it allows a faster turn around of results. However, although the same crater diameter can be produced using different combinations of impact velocity and impactor size, the resultant internal crater morphology may be different for impacts of different velocity (e.g. Gula and Achelous, Section 2.5.2).

To determine a suitable impact velocity that will reduce run time without significantly affecting internal crater morphology, a suite of simulations were performed employing different impact velocities and impactor masses; all other simulation variables were constant. Figure 5.3 compares the results of simulated impact into Ganymede employing impact velocities of 5, 10 and 15 km s<sup>-1</sup> to a simulation result using the more realistic Jovian system velocity of 21 km s<sup>-1</sup>. The impactor masses were scaled to produce the same final crater size using Pi-group scaling, a form of dimensional analysis in which the impactor properties can be related to crater morphology via a set of experimentally determined constants (Schmidt and Housen, 1987; Melosh, 1989).

The ‘ideal’ result from a 21 km s<sup>-1</sup> impact produced a ~ 17 km diameter summit pit crater. Note that the mesh size for these simulations was large enough to prevent spurious pit-formation as the result of reflected waves as was shown to occur with too-small meshes (Figure 5.2A). The formation of the subtle pit was, in the case of this simulation, the result of an over extended central peak collapsing to cause a pit at the centre of the peak summit.

The lower velocity simulations all produced slightly larger craters than the ‘ideal’ result. Although Pi-scaling is not infallible, this is more likely a resolution effect as noted in Figure 5.1. Although the cell size was kept constant for the different velocity simulations, the lower velocity runs used larger projectiles relative to the mesh cell size (i.e., more cells per projectile radius), enabling better approximation of the spherical shape of the projectile, increasing its mass.

The simulation employing an impact velocity of 5 km s<sup>-1</sup> produced a 19 km diameter crater with a prominent central peak. The difference in internal morphology between the 5 and 21 km s<sup>-1</sup> simulations was due to the target material at the crater centre behaving more fluidly as a result of the high velocity impact, leading to a large central uplift which underwent dramatic collapse. The 5 km s<sup>-1</sup> simulation produced a shorter, and consequently more stable, central uplift; this was retained as a central peak as its collapse could not progress far enough to form a central pit.

The crater produced using an impact velocity of 10 km s<sup>-1</sup> also has a central peak rather than a summit pit, although in this simulation, the peak dimensions are closer to those of the ‘ideal’ result. In addition to producing a wider crater with different central morphology, both the 5 and 10 km s<sup>-1</sup> simulations resulted in a crater 200 m (15%) shallower than the 21 km s<sup>-1</sup>

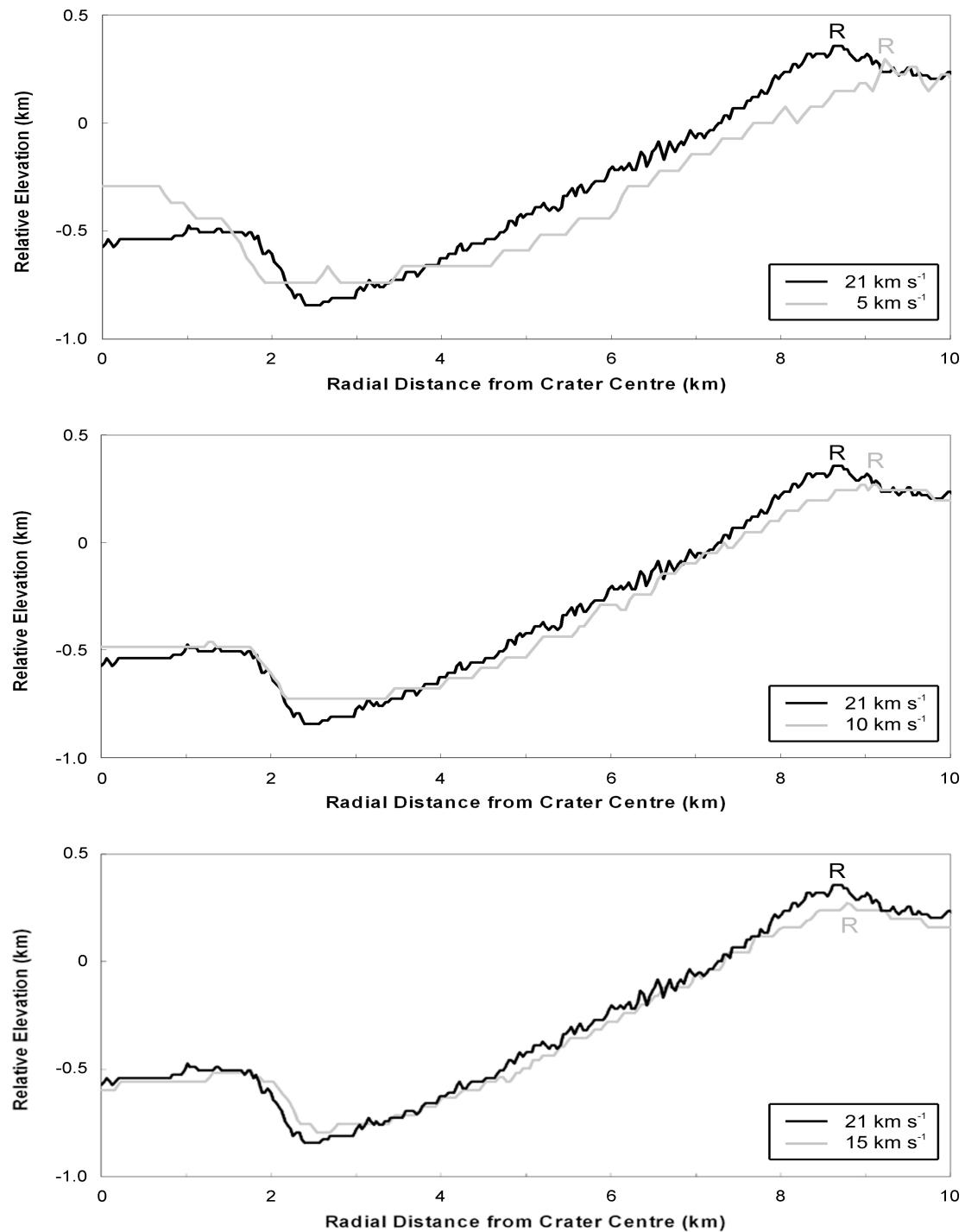


**Figure 5.3:** The effect of impact velocity on simulated crater morphology. Radial profiles of a simulated  $\sim 18$  km crater on Ganymede. A) Crater formed using an impact velocity of  $5 \text{ km s}^{-1}$  and a projectile radius of 75 m is marked as a grey line. B) Crater formed using an impact velocity of  $10 \text{ km s}^{-1}$  and a projectile radius of 50 m is marked as a grey line. C) Crater formed using an impact velocity of  $15 \text{ km s}^{-1}$  and a projectile radius of 40 m is marked as a grey line. The crater profile produced using an impact velocity of  $21 \text{ km s}^{-1}$  and a projectile radius of 33 m is included for comparison as a black line in each plot. Approximate location of the crater rim is marked with a black 'R' for the  $21 \text{ km s}^{-1}$  simulation and a grey 'R' for the lower velocity results.

result. Although there is still a 10% difference in simulated crater depth, the  $15 \text{ km s}^{-1}$  result provides a relatively close match to the ‘ideal’ result formed by the  $21 \text{ km s}^{-1}$  impact, reproducing similar crater diameter, wall slope and central morphology, but with a 40% shorter runtime.

### 5.1.3. Initial Target Conditions

The target structure was simplified to homogeneous and unlayered to prevent complexities arising from additional layering and multi-material effects. The static strength model for ice employed in iSALE was derived from low temperature ( $77 \text{ °K}$ ), high-pressure laboratory data (Durham et al., 1983; Beeman et al., 1988; Rist and Murrell, 1994; Weiss and Schulson, 1995) and takes account of the material strength dependence on pressure, damage and thermal softening (see Chapter 4).

The thermodynamic response of the Ganymede crust was approximated using an equation of state for pure  $\text{H}_2\text{O}$  ice, as the Ganymede crust is thought to be primarily water ice (Showman et al., 2004), and the thermodynamic properties of other compositional candidates remain undefined. As the third order Tillotson EoS presented in Chapter 4 was developed during the later stages of this thesis, the simulations presented in this chapter employed the Tillotson EoS for ice Ih (Ivanov et al., 2002). The effect of using the third order EoS is discussed in Section 5.3.2.

### 5.1.4. Weakening During Impact

Acoustic fluidization was implemented in iSALE through the incorporation of the block model (as explained in the previous chapter). To determine values for the acoustic fluidization parameters in ice different combinations of  $\eta$  and  $\tau$  were tested, controlling the relative amount of target weakening. A range of parameter values were used so that the sensitivity of crater morphology to the different parameters could be assessed (Section 5.3.1).

As the nature of target weakening during impact is still a matter of debate (Section 4.1.4), a purely empirical approach was also used to define the strength of the damaged target. The empirical model used a simple Mohr-Coulomb criterion in which the cohesion  $Y_{d0}$  and friction coefficient  $\mu_d$  in Equation 5.1 were varied to produce the correct morphology.

$$Y_d = Y_{d0} + \mu_d P. \quad (5.1)$$

### 5.1.5. Comparison to Observations

Hydrocode results must be tested by comparison to observational (ground-truth) data such as scaling trends and  $d/D$  plots. The best-fit model parameters for recreating impact cratering in pure ice were determined by comparing the modelled crater morphology with observations from Chapter 2.

Observations show the scaling trends of craters below  $\sim 12$  km on Ganymede to be subject to large variability, making the simulation of craters smaller than this size ambiguous when first determining the material properties of the surface. The upper bound for a suitable simulation size was set at a crater diameter of  $\sim 26$  km as the formation of craters above this diameter are thought to be affected by the presence of sub-surface rheological changes (Schenk, 2002). This chapter therefore concentrates on the simulation of a Ganymede crater between 12 and 26 km in diameter.

Model results were tested via comparison to scaling trends for craters on Ganymede, and used to determine the range of target strength parameters that can produce a reasonable match between the modelled and observed data. To produce a set of parameters most representative of the general trend, the simulations were not compared directly to single crater profiles and were instead compared to a representative crater profile created from the scaling trends in Table 2.2. As no significant difference in broad crater morphology was observed between bright and dark terrains, scaling trends were based on the mixed dataset.

Modelled craters were primarily assessed on their fit to wall slope as this crater property showed the least variation in response to changes in resolution and impact velocity. Central peak morphology and depth-diameter ratio also had to be reproduced, although a strict fit to peak dimensions was not critical as the central morphology of impact craters was observed to be particularly variable (Chapter 2).

## **5.2. Comparing Strength Models**

Both the empirical model and the Acoustic Fluidization (A.F.) model can be used to recreate impact crater morphology on Ganymede. Figures 5.4 show the best-fit simulation results produced for both models, using an impactor with a radius of 320 m and velocity of  $15 \text{ km s}^{-1}$ . Measurements from the simulated final crater profiles are included in Figures 2.3 – 2.5 and 2.8 to show the best-fit model crater dimensions relative to observational data. The target weakening parameters used to obtain the closest fit to observations of Ganymede craters are presented in Table 5.1.

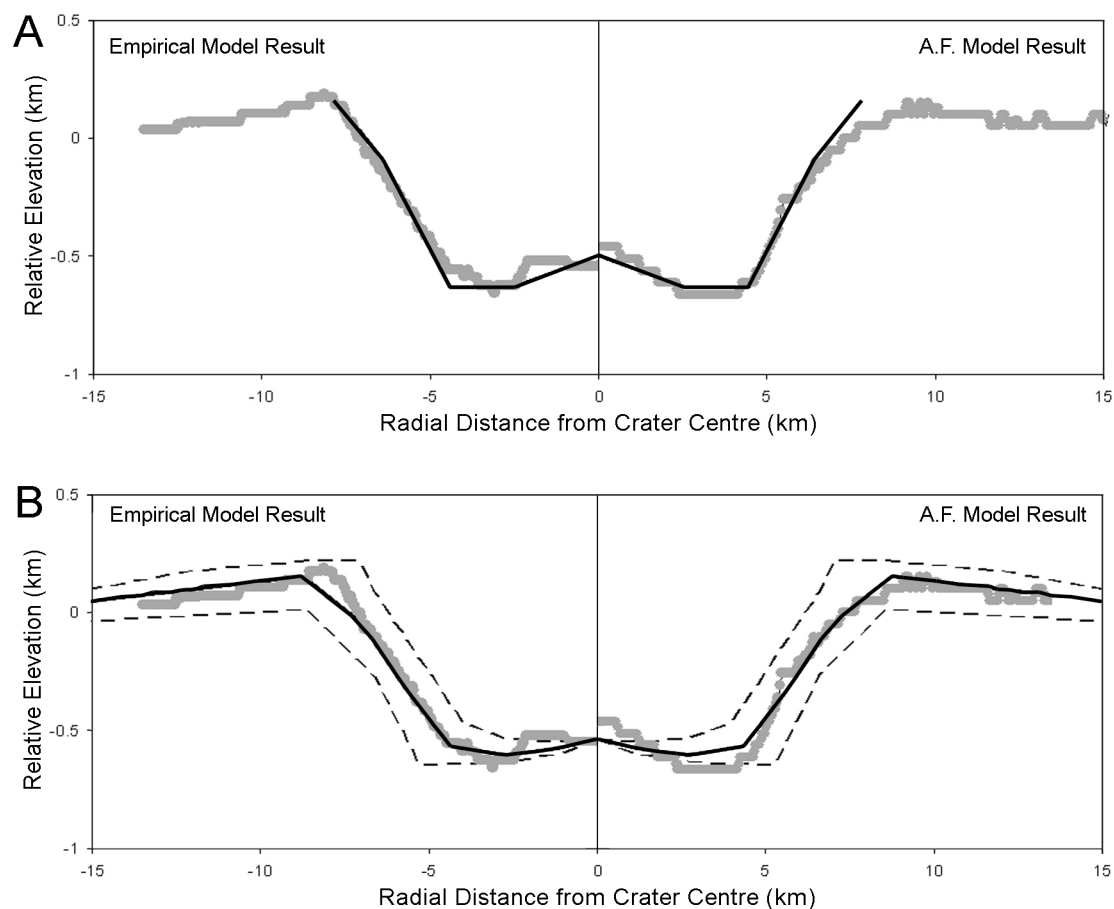


**Figure 5.4:** Final crater profiles produced using the Empirical (left) and A.F. Models (right). A) Relative to a representative crater profile for a 15 km crater constructed from the scaling trends established in Chapter 2 (black line). B) Relative to observational data for a 17 km diameter central peak crater at 38.4N, 194.9W. The solid black line represents the topographic profile of the crater, averaged from 8 radial profiles (see Appendix A for the individual radial profiles). The dotted lines delineate the extent of natural variation in crater topography with azimuth.

**Table 5.1: Impactor Properties and Best-fit Strength Model Parameters for a 15 km Crater**

Parameter	Ganymede
Impactor radius (km)	0.3 km
Impactor radius (cells)	10
Impact velocity	15 km s <sup>-1</sup>
<b>Empirical Model:</b>	
Cohesion, $Y_{d0}$	0.05 MPa
Coefficient of friction $\mu_d$	0.23
<b>Acoustic Fluidization Model:</b>	
Decay time	50 s
Kinematic viscosity	80,000 m <sup>2</sup> s <sup>-1</sup>

### 5.2.1. Empirical Model Results

A friction coefficient ( $\mu$ ) based on measurements of crater wall-slopes on Ganymede ( $\sim 0.2$ ) provided a reasonable estimate for this parameter, and the best-fit value was found to be 0.23. In conjunction with this value, a cohesion ( $Y_{coh}$ ) of 0.05 MPa most accurately recreated the morphology of a 15 km Ganymede central peak crater (Figure 5.4A). A fair fit to the observational data can be achieved using frictional coefficient values between 0.23 and 0.27; the error on cohesion value is larger as values can range from 0.04 to 0.06 MPa. These ‘acceptable’ ranges on parameter values were defined by fixing one parameter at its best-fit value and varying the other parameter until the simulated wall slope, central peak diameter or crater depth ceased to lie within observed values.

Figure 5.4A shows a good fit to the crater depth, average wall slope and peak size expected for a 15 km crater on Ganymede, although a subtle pit is present at the peak centre. This pitted summit morphology was present in all simulations in which the crater wall slope was correctly reproduced. Both the representative and actual crater profile show a break in wall slope close to the crater rim; craters produced using the empirical model display constant wall slopes and do not reproduce this, leading to an offset in the modelled and observed crater rim position in Figure 5.4B.

The final crater morphology of the empirical simulations was the result of rapid, large-scale inward collapse of crater wall material that collided to form a central peak. This collapse process can be followed in Figure 5.5. Maximum crater excavation depth is reached at  $\sim 30$  seconds after impact (Figure 5.5A). Material from the walls of the transient crater falls in towards the centre, shallowing and modifying the shape of the crater cavity (Figure 5.5B). Shortly after 100 s after impact, the collapsing wall material collides at the crater centre to create a large central uplift (Figure 5.5C). This uplift reaches maximum elevation at  $t = 180$  s, after which it collapses, beginning at the base (Figure 5.5D), to form a shorter, broader central peak (Figure 5.5E). Continued downward movement of the peak core resulted in a small pit at the centre of the peak.

This style of crater formation results in a deep bowl-shaped zone of highly deformed material beneath the crater that extends down to the maximum depth of the transient crater. This zone of heavily disrupted, inwardly collapsed material is delineated approximately in Figure 5.5E by the total plastic strain (TPS) contour of 1. Note that a large volume of this material experienced a total plastic strain in excess of 2, and that structural uplift beneath the centre of the crater extends to a depth of  $\sim 2$  km - beneath this, any net displacement of material is down.

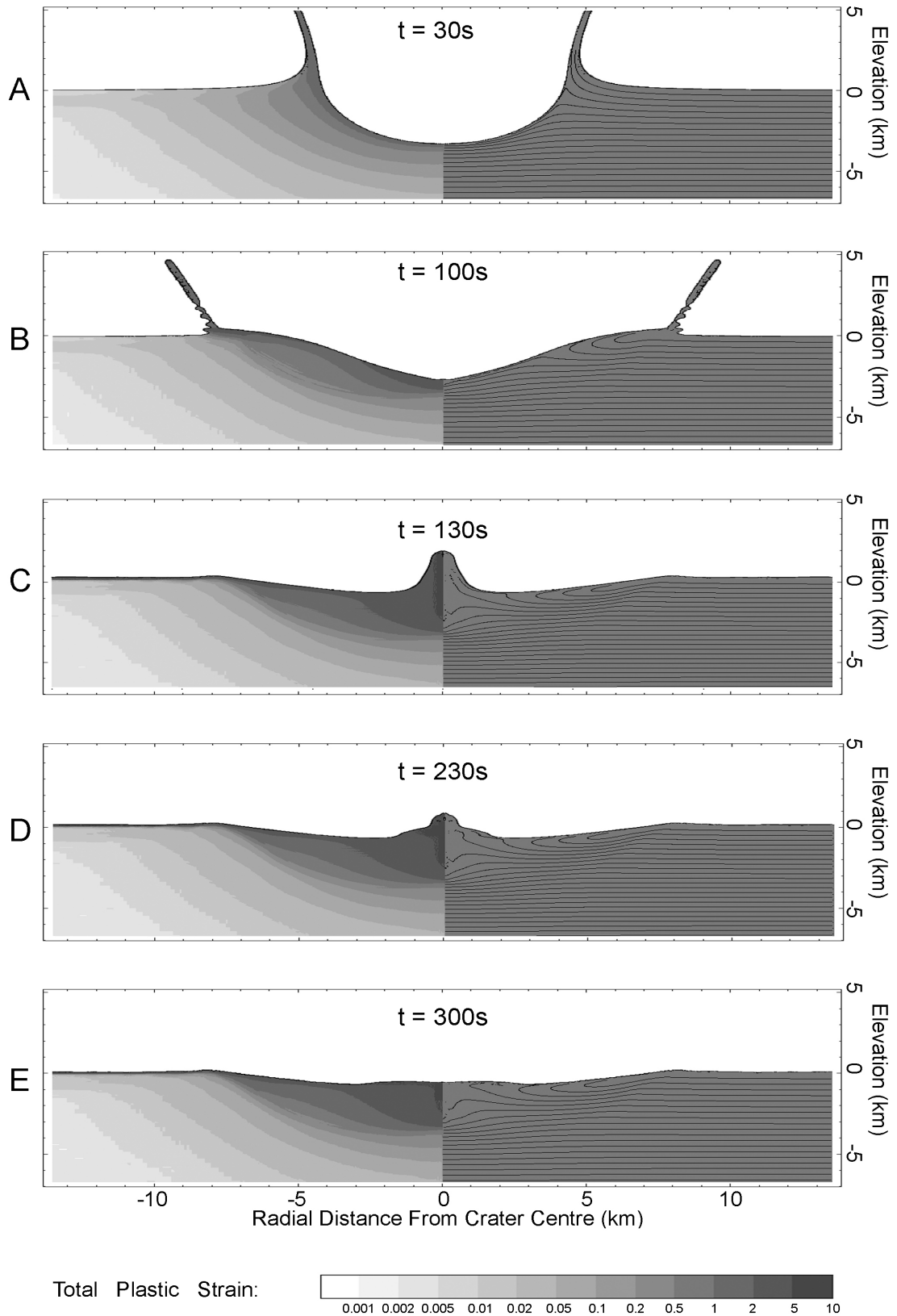


**Figure 5.5:** Empirical Model Results. Simulation stills of the best-fit crater created using the friction and cohesion values in Table 5.1, Total plastic strain experienced by the target is seen on the left; representative material layers are included on the right hand side to show deformation. The stages of crater formation (A to E) are outlined in the main text.

### 5.2.2. Acoustic Fluidization (A.F.) Model Results

After investigation of kinematic viscosities spanning the two orders of magnitude between  $5 \times 10^3 \text{ m}^2 \text{ s}^{-1}$  and  $5 \times 10^5 \text{ m}^2 \text{ s}^{-1}$ , the best match to observed crater morphology on Ganymede was achieved using a kinematic viscosity of  $80,000 \text{ m}^2 \text{ s}^{-1}$  and a decay time of 50 s. The final simulated crater shows good fit to crater depth, average wall slope and central peak diameter in Figure 5.4A. A reasonable fit to observations was obtained for decay times ( $\tau_v$ ) between 45 and 55 s when using a viscosity of  $80,000 \text{ m}^2 \text{ s}^{-1}$ . The acceptable variation in the kinematic viscosity was between  $70,000$  and  $90,000 \text{ m}^2 \text{ s}^{-1}$  for a decay time of 50 s (see Figure 5.10). As with the empirical model, these ‘acceptable’ ranges on parameter values were defined by varying the different parameters until the simulated wall slope, central peak diameter or crater depth ceased to lie within observed values (see Figure 5.7 and 5.9).

A non-uniqueness in the model was noted at this stage as a fair fit to crater morphology could also be achieved using a viscosity of  $110,000 \text{ m}^2 \text{ s}^{-1}$  and a decay time of 70 s. The simulated crater profile produced using these values had slightly broader rims resulting in a weaker fit to the representative profile. The profile of this alternative crater is presented later in Figure 6.2D.

The simulated crater depth, wall slope and central peak dimensions fit well to the representative profile of a  $\sim 15$  km crater (Figure 5.4A). However, the simulated crater has a broad rim, which reaches maximum elevation at a radius of  $\sim 8.5$  km (equating to a crater diameter of  $\sim 17$  km). The empirical and A.F. model results are thus also compared to a topographic profile of a crater on Ganymede with a diameter of  $\sim 17$  km in Figure 5.4B. The representative crater profiles used in this work do not incorporate the breadth of crater rims, preventing a close fit of A.F. model results to the rims of either a 15 km crater (fit for wall slope) or a 17 km crater (fit for rim position).

The final crater morphology in A.F. model simulations is the result of a combination of uplift of the crater floor to form the central peak, and inward collapse of the crater wall to broaden the crater. Figure 5.6 shows a series of simulation stills to illustrate this combined process. As with the empirical model, maximum excavation depth was reached approximately 30 seconds after impact (Figure 5.6A). Uplift of the crater floor begins immediately after this maximum penetration is reached. Both inward collapse of the crater walls and floor rebound have occurred by  $t = 100$  s (Figure 5.6B). No overshoot of the central uplift is experienced in this simulation, and the final crater morphology is produced within 200 seconds after impact (Figure 5.6C).

The structural uplift beneath the centre of the crater extends to a depth of  $\sim 6$  km. As the central peak in this simulation was created via uplift of this underlying material rather than rim debris, the deformation of the sub-crater target material is distributed over a larger

volume; this results in a smaller zone of high total plastic strain ( $> 2$ ) relative to the empirical model.

### 5.2.3. Summary and Discussion of Model Suitability

The crater depth, wall slope and central peak diameter were successfully recreated using both models, although the morphology of each final crater does differ slightly. The empirical simulation has produced a crater with smooth internal walls and a small pit at the centre of its (still correctly sized) central peak which provides a good fit to the representative crater profile

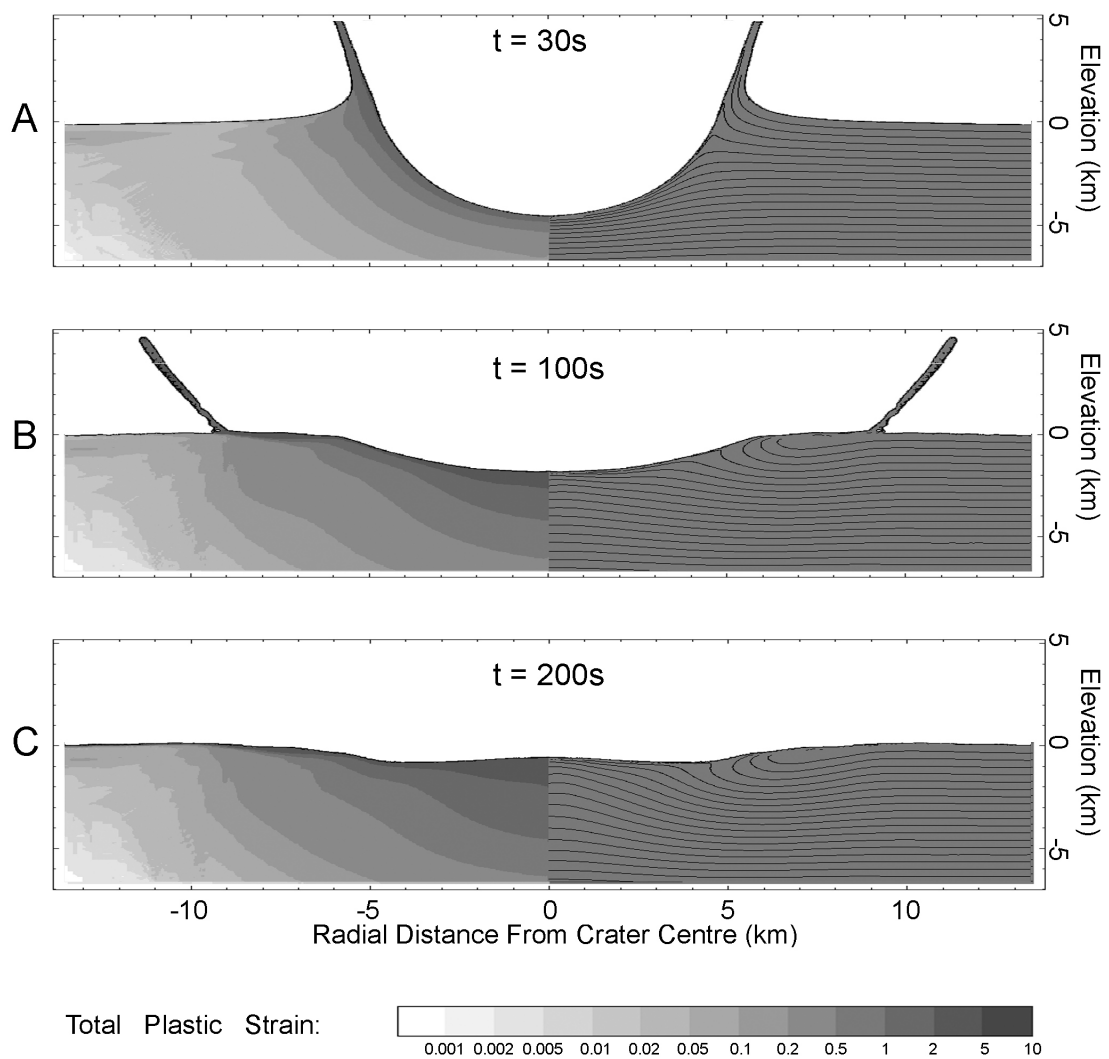


**Figure 5.6:** Acoustic Fluidization model results. Simulation stills of the best-fit crater created using the decay time and viscosity values in Table 5.1, Total plastic strain experienced by the target is seen on the left; representative material layers are included on the right hand side to show deformation. The stages of crater formation (A to C) are outlined in the main text.

(Figure 5.4A). The inner wall of the crater produced using the Acoustic Fluidization (A.F.) model displays a two-step morphology as a result of its broader crater rim; this results in a questionable fit to crater rim position (Figure 5.4A). Comparison to the representative crater profile alone suggests that the empirical model is the most suitable for simulating impact into Ganymede.

The subtle pit produced by the empirical model and the subdued crater rim of the A.F. model are flaws which can be explained by assessing the nature of target weakening used in each model. The empirical model utilised a whole-sale weakening of the target which did not decrease in magnitude with time after the impact. As the degree of weakening did not lessen over the course of crater collapse, the material comprising the central peak was too weak for the peak morphology to be maintained, and collapse continued to form a pit. As no suitable match to crater depth, wall slope and peak dimensions was found without the presence of such a summit pit, it is likely that the empirical model requires a means of lessening the amount of material weakening over time to better reproduce Ganymede crater morphology. This problem is not encountered when using the Acoustic Fluidization model as the weakening mechanism is transient.

The A.F. model assumes that the entire weakened portion of the target material acts in a fluid-like manner. This leads to the broader rim morphology seen in Figure 5.4, as the rim collapse occurs in a more fluid manner than compared to the dry-friction style of the empirical model. To better reproduce the style of rim collapse, a combination of empirical and A.F. model styles may be necessary to enable the transient fluid movement of the crater floor, and the dry-friction controlled collapse of the upper crater rim. This was not attempted in this thesis, but would be an interesting avenue for further research.

### **Differences in the Crater Collapse and Peak Formation Process**

As both models were developed to match observed crater morphology, comparison of final simulated crater morphology does not provide a suitable indicator of which model allows the most accurate recreation of impact crater formation in ice. Consequently, assessment of the most suitable strength model must also consider the process of crater collapse and differences in the formation mechanism of central peak morphology.

Maximum crater excavation depth is reached 30 seconds after impact in both models (Figure 5.5A and 5.6A) and very slight differences in the modelled crater morphology are already apparent at this stage: the empirical model reaches a maximum depth of 3.5 km below the pre-impact surface, shallower than the penetration produced by the impact into an Acoustically Fluidized target (4.1 km). The angle of the ejecta curtain also differs between models, and is steeper in the simulation using the empirical strength model.

Once the transient crater is formed the process of crater collapse is very different between the two models. Figures 5.5B and 5.6B show the developing craters 100 s after impact; at this point the rim wall material is already collapsing back towards the centre of the crater in both models. The model employing Acoustic Fluidization has already undergone noticeable floor uplift by this time and the crater cavity is 50% shallower than that of the empirical model. By 200 s after impact the crater simulated using the A.F. model has reached its final morphology. Due to the extended process of peak formation, the empirical model simulation completes later at  $\sim 300$  s.

The basal collapse of an over-extended central uplift, as seen during the best-fit empirical model simulation (Figures 5.5C and D), follows the model of large central peak development presented in Section 2.6.3 (also see Figure 3.18B and C). However, as the material weakening in the empirical model is not transient, this dramatic peak collapse progresses to create a small pit at the peak centre (Figure 5.5E). None of the  $Y_{coh}$  and  $\mu$  combinations employed during this work produced the correct central peak diameter without also creating a small central pit.

The best-fit A.F. simulation does not involve the over-extension and collapse of the central uplift, although the process was noted during A.F. models in which the amount of fluidisation was increased relative to the best fit value (e.g.  $\tau = 100$  s,  $\eta = 100,000$  m<sup>2</sup> s<sup>-1</sup>). This shows that, although not necessary for the simulation of a 15 km crater, the A.F. model has the capability to produce basal collapse of central peaks.

### Clues from Sub-Crater Structure

The two styles of peak formation presented in Figure 5.5 and 5.6 are most distinct in 3 ways: the size of the highly-deformed zone beneath the crater, the maximum strain beneath the crater, and the depth to the base of the structural uplift (see Figures 5.5E and 5.6C). Central uplifts formed using the A.F. model extend deeper, and experience lower total plastic strain than central uplifts formed using the empirical model. Observations of terrestrial and extra-terrestrial craters may therefore help to select the more appropriate strength model.

As discussed in Chapter 2, the observation that the transition from simple craters to those with central peaks occurs on Ganymede at a much smaller diameter than the transition in the magnitude of rim collapse suggests that central peaks are driven by floor uplift, rather than rim collapse. This is also supported by observational data from terrestrial impact sites which show central peak material to be uplifted from depth (e.g. Grieve and Pilkington, 1996; Therriault et al., 1997). Together, this suggests the model incorporating Acoustic Fluidization to be the more realistic of the two assessed in this work.

### 5.3. Model Sensitivity to Eos and Strength Parameters

#### 5.3.1 Sensitivity to Acoustic Fluidization Parameters

To assess the sensitivity of the modelled crater morphology to the Acoustic Fluidization parameters, a suite of simulations were performed in which each of the strength parameters were varied incrementally. The dimensions of the produced craters were then measured and compared. This section presents measurements from this suite of models and uses the results to facilitate the identification of the Acoustic Fluidization parameters for different crater sizes, as presented in Chapter 6.

Figures 5.7 to 5.10 show how crater morphology varies with change in the acoustic fluidization parameters,  $\tau_v$  and  $\eta$ . Figure 5.7B shows a clear dependence of crater depth-diameter ratio on the decay time  $\tau_v$  (Equation 5.2), which is almost independent of target

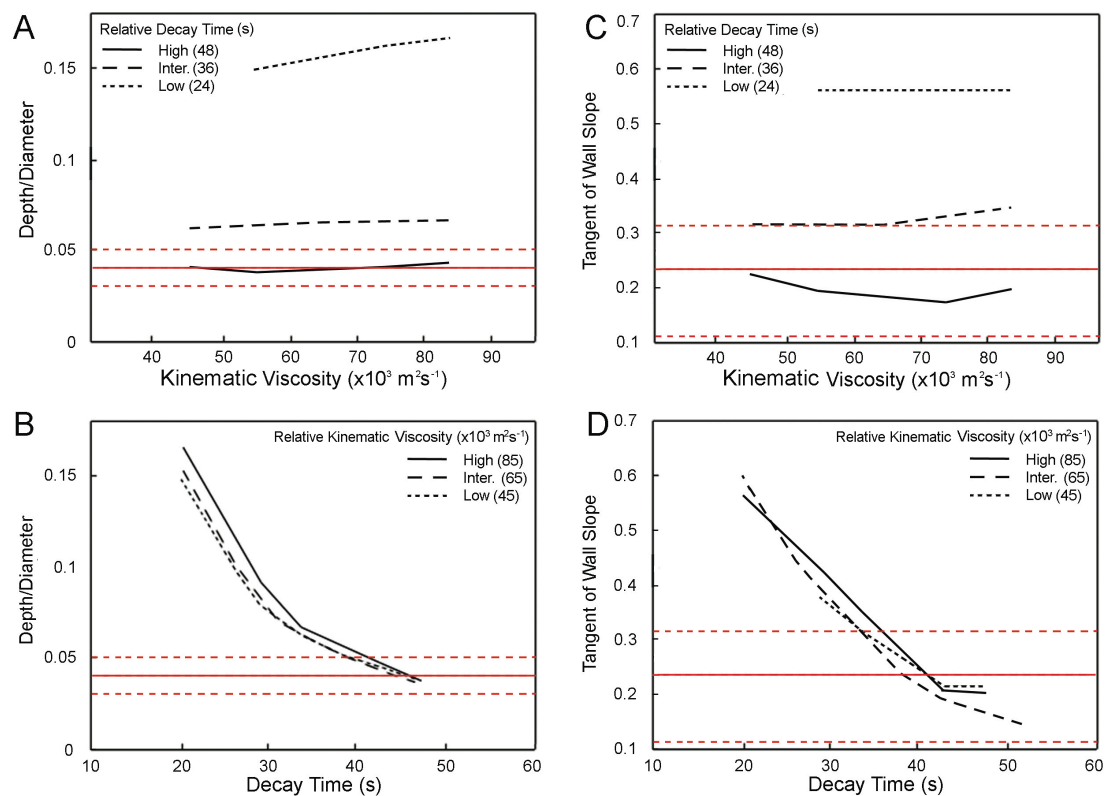


**Figure 5.7:** Depth-diameter and wall slope variation with change in the Acoustic Fluidization parameters. A) The influence of kinematic viscosity on simulated  $d/D$  for a range of decay times. B) The influence of decay time on simulated  $d/D$  for a range of kinematic viscosities. C) The influence of kinematic viscosity on simulated wall slope for a range of decay times. D) The influence of decay time on simulated wall slope for a range of kinematic viscosities. The ‘ideal’ depth and wall slope for a 20 km crater on Ganymede is included as a red line on each plot; the maximum and minimum observed values are noted as dotted red lines.

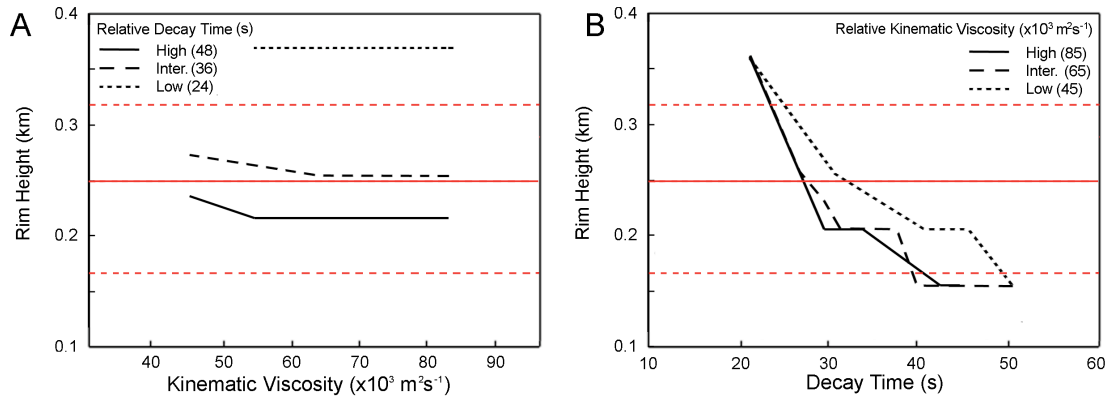


**Figure 5.8:** Crater rim height variation with change in the Acoustic Fluidization parameters. A) The influence of kinematic viscosity on simulated rim height for a range of decay times. B) The influence of decay time on simulated rim height for a range of kinematic viscosities. The ‘ideal’ rim height for a 20 km crater on Ganymede is included as a red line on each plot; the maximum and minimum observed values are noted as dotted red lines

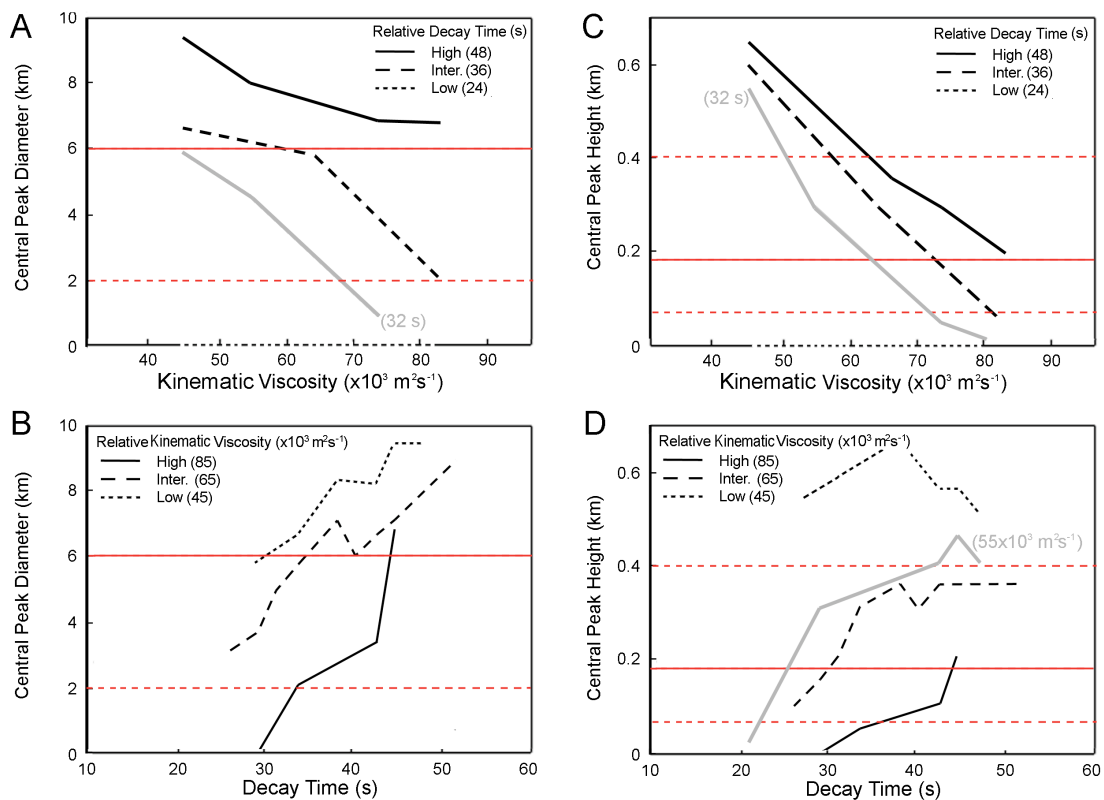


**Figure 5.9:** Central peak width and height variation with change in the Acoustic Fluidization parameters. A) The influence of kinematic viscosity on simulated peak width for a range of decay times. B) The influence of decay time on simulated peak width for a range of kinematic viscosities. As the decay time of 24 seconds does not produce a central peak, another intermediate decay time of 32 seconds has been included as a grey line. C) The influence of kinematic viscosity on simulated peak height for a range of decay times. D) The influence of decay time on simulated peak height for a range of kinematic viscosities. The ‘ideal’ central peak dimensions for a 20 km crater on Ganymede is included as a red line on each plot; the maximum and minimum observed values are noted as dotted red lines.

viscosity,  $\eta$ .  $d/D$  ratios decrease exponentially with increasing decay time for  $\eta$  values between  $45,000 \text{ m}^2 \text{ s}^{-1}$  and  $85,000 \text{ m}^2 \text{ s}^{-1}$ . Variation in viscosity only produces minor changes in  $d/D$  ratio of simulated craters when decay times are small.

$$\frac{d}{D} \approx 5230\tau_v^{-1.77}. \quad (5.2)$$

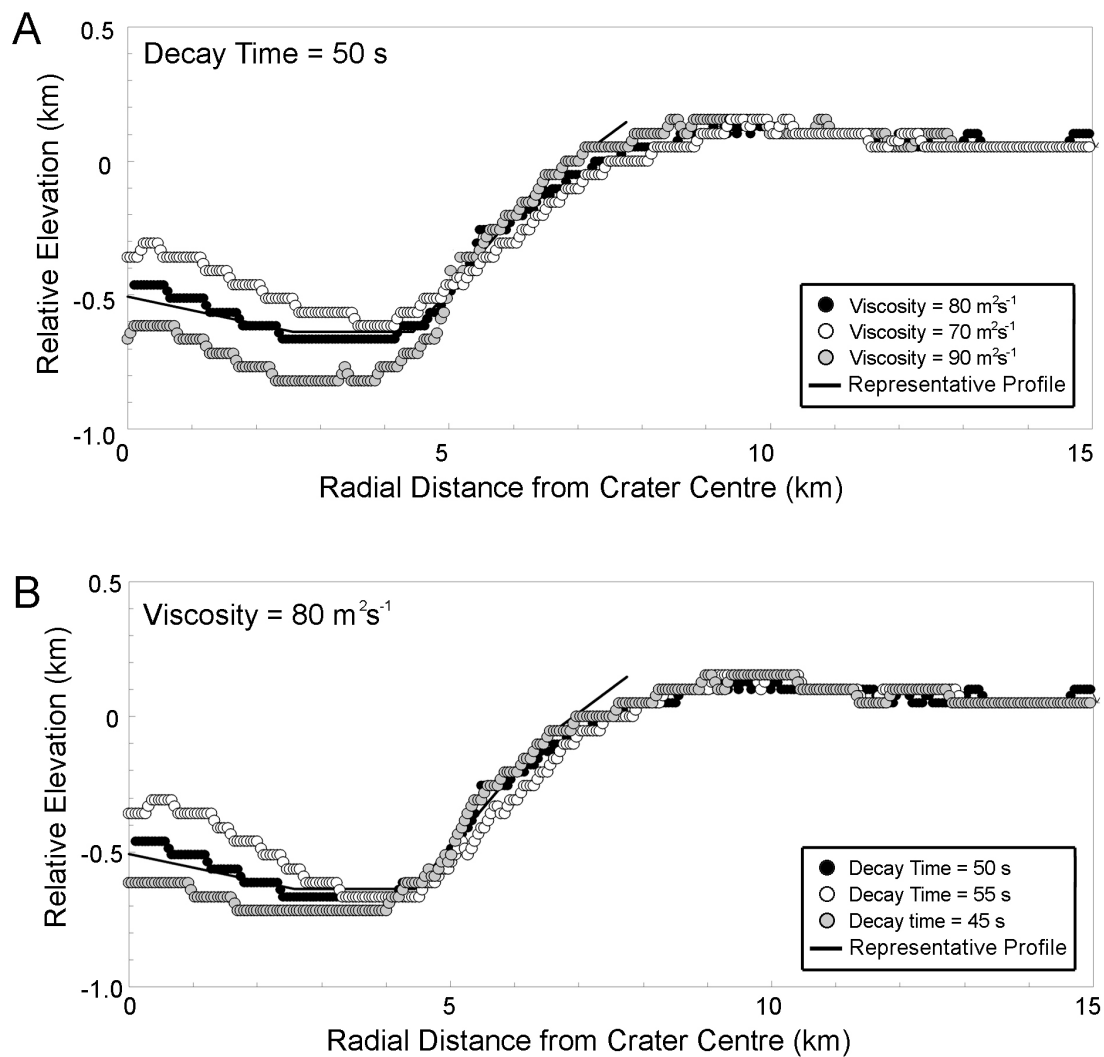


**Figure 5.10:** Sensitivity of final crater profile to changes in Acoustic Fluidization parameters. A) Best fit decay time of 50 s with best fit viscosity of  $80 \text{ m}^2 \text{ s}^{-1}$  (black circles). Slightly higher and lower viscosities are shown as white and grey circles. B) Best fit viscosity of  $80 \text{ m}^2 \text{ s}^{-1}$ , with a decay time of 50 s (black circles). Slightly higher and lower decay times are shown as white and grey circles. The representative crater profile constructed from scaling trends is included for comparison on both plots as a black line.

Crater wall slopes also decrease exponentially as decay time increases, with minimal influence from the viscosity (Figures 5.7C and D, Equation 5.3). Unlike the  $d/D$  ratio dependence, the influence of the target viscosity is greatest for long decay times.

$$\tan(S) \approx 4470\tau_v^{-1.51}. \quad (5.3)$$

Viscosity has more of an effect on crater rim height than either  $d/D$  or wall slope, and rim heights decrease as  $\tau_v$  and  $\eta$  increase (Figure 5.8). The rim height and the decay time possibly have an exponential relationship as shown by  $d/D$  and wall slope, however, this is complicated due to the influence of viscosity.

As is intuitive, a larger target viscosity and lower decay time decrease the amount of central uplift occurring in the target, producing smaller peaks. This is reflected in the trends of central peak height and width (Figure 5.9). A low enough decay time or high enough viscosity will prevent central uplift of the crater floor. This is shown in Figure 5.9 as central peak height or width trend lines intersect the x-axis. To better demonstrate the trend in central peak size above these critical values, other decay time and viscosity values have been included on the plots (grey trend lines). The clearest trend shown in these figures is that of central peak height and viscosity (Figure 5.9C).

### 5.3.2. Effect of the Equation of State (EoS)

The third order Tillotson EoS presented in Chapter 4 was developed during the later stages of this thesis work. As a result, the simulations presented in this chapter employed the Tillotson equation of state as outlined by Equation 4.4. As the focus of this study was late stage collapse, rather than early time phenomena where an accurate EoS is paramount, this simple thermodynamic description was deemed sufficient for the simulations presented in this work. To test this assumption, the best-fit simulation of the A.F. models was re-run using the alternative third order Tillotson EoS (Equation 4.31), with parameters listed in Table 4.1 for ‘H<sub>2</sub>O’; no other target or impactor properties were changed.

Figure 5.11 compares transient and final crater profiles simulated using the Tillotson and third order Tillotson equations of state. The third order Tillotson EoS produces a steeper ejecta curtain angle and a smaller transient crater diameter during the excavation of the crater (Figure 5.11), but does not significantly alter the depth of the transient crater relative to the original Tillotson EoS. Changes in the final crater morphology produced when using the different equations of state are also minimal and less than those produced by varying the Acoustic Fluidization parameters within their accepted range (Figure 5.10). Effects of the

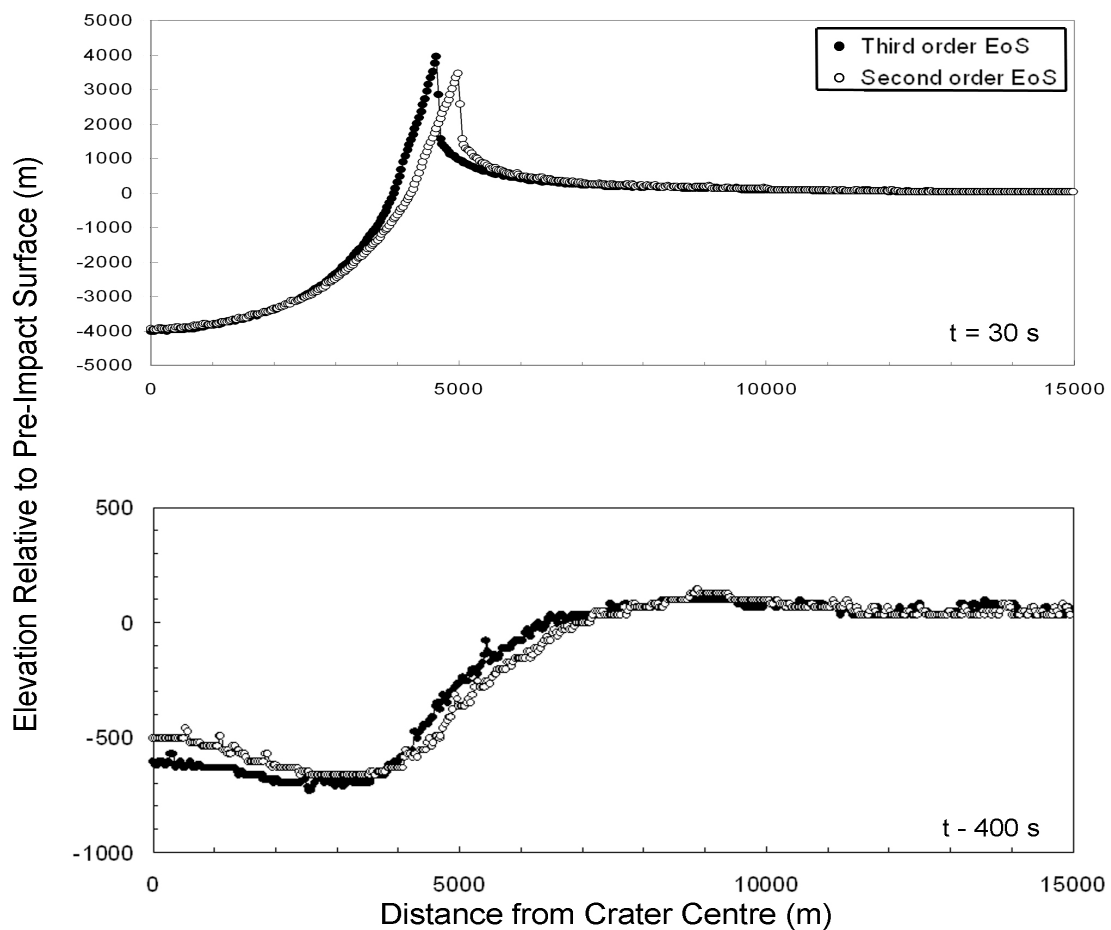


**Figure 5.11:** Comparison of the simulated crater profiles produced when using a second order Tillotson EoS (white circles) and a third-order Tillotson EoS (black circles). Top) Simulation results 30 seconds after projectile impact, roughly comparing to the transient cavity. Bottom) The final crater morphology; measurements from this profile are recorded in Table 5.2.

**Table 5.2: Final Crater Dimensions Simulated Using Different Equations of State**

Final Crater Dimension	Result from Tillotson EoS (Equation 4.4)	Result from third order EoS (Equation 4.31)	Percentage Difference in Measurement (2 s.f.)
Crater Diameter (km)	17.80	17.93	0.70
Crater Depth (km)	0.79	0.81	1.9
d/D	0.0446	0.0452	1.2
Wall Slope Gradient	0.198	0.197	0.76
Rim Height (km)	0.13	0.10	33
Central Peak Diameter (km)	5.28	5.15	2.5
Central Peak Height (km)	0.16	0.13	25

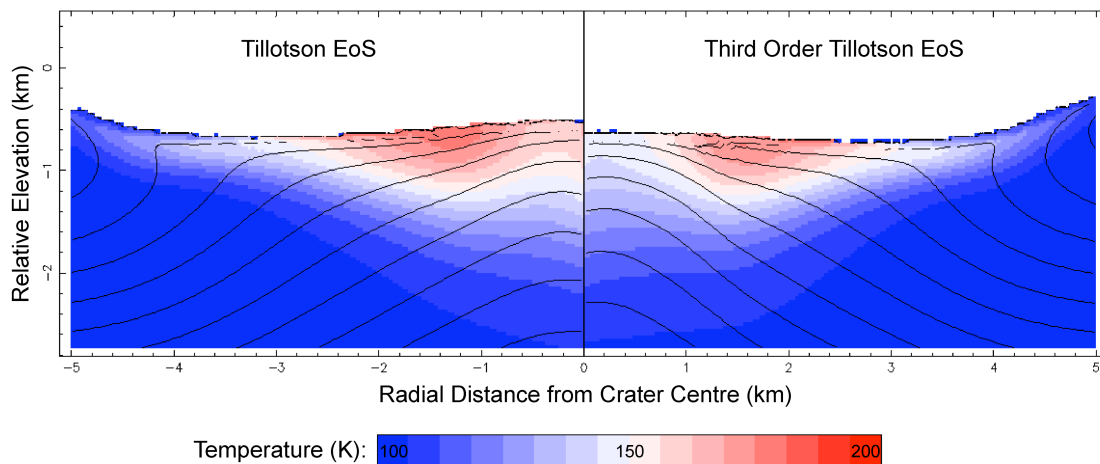


**Figure 5.12:** Post-impact target temperatures produced at the crater centre using the different equations of state. Results using the Tillotson EoS are on the left; third order Tillotson results are on the right. Black lines within the target mark representative material layers to show deformation. Surface temperature is 100 K. Time after impact is 400 s.

different EoS on produced crater morphology are most notable when comparing the height of simulated central peaks or crater rims, as these dimensions vary up to 33% between models (Table 5.2, Figure 5.11). Importantly, the depth-diameter ratio, wall slope and central peak diameter all vary less than 3% between the two models. As these are the crater dimensions deemed most suitable for testing crater simulation results (Bray et al., 2008), use of a different EoS is unlikely to significantly affect the results presented in Chapters 5 and 6.

Figure 5.12 compares the central peak complex of the craters created using the Tillotson EoS and the third order Tillotson EoS. Simulations using the different equations of state produce the same area of ‘warm’ ice (temperature > surface temperature), although the maximum temperatures after crater formation differ. The Tillotson EoS produces a larger region of  $T > 150$  K than that produced when using the Third Order Tillotson EoS.

## **5.4. Modelling Summary and Implications**

The morphology of a  $\sim 15$  km crater on Ganymede was recreated using both the empirical strength model and the Acoustic Fluidization (A.F.) model (Figure 5.4). An empirical model best-fit to a profile of a 15.5 km Ganymede crater was achieved using a cohesion ( $Y_{d0}$ ) of 0.05 MPa and a coefficient of friction ( $\mu_d$ ) of 0.23. These best fit values are 10% and 40% of the pre-impact cohesion and coefficient of friction values expected for damaged ice on the basis of laboratory tests (Table 4.2). As strength models suffer from non-uniqueness if the same effective strength can be produced with different combinations of model parameters, the

values presented here thus provide one example of the magnitude of material weakening experienced during impact crater formation.

The strength model incorporating A. F. also suffers from non-uniqueness and a good fit to observations was obtained using a viscosity of  $8 \times 10^4 \text{ m}^2 \text{ s}^{-1}$  and a decay time of 50 s, and also with the combination of  $11 \times 10^4 \text{ m}^2 \text{ s}^{-1}$  and a decay time of 70 s. This non-uniqueness will exist for each crater size simulated and as such may cause difficulties when determining a strength scaling with crater size.

### **Determining the Most Suitable Strength Model**

Both empirical and A.F. models were able to reproduce the final crater morphology observed for Ganymede craters. The empirical model produced the closer fit as the craters simulated using the A.F. model display overly broad rims that affected the measured diameter, depth and rim height.

The models predict very different styles of crater collapse and peak formation. In simulations using the A.F. model, central peaks were formed primarily by uplift of the target material from depth; in simulations using the empirical model central peaks are formed by the collision of material collapsing in from the transient crater rim. Although the empirical model gives a better match to the observed morphology, its predicted style of crater collapse is not supported by observations, as data suggests that peak formation occurs primarily as the result of crater floor uplift, rather than the collision of collapsing wall debris. This result suggests that morphology alone is perhaps not the best test of model success and that the A.F. model provides the most suitable model for recreating the cratering process.

However, it is noted that the A.F. model is not without flaw as it treats the entire target area as a viscous fluid, allowing rim collapse to occur smoothly relative to the empirical model, resulting in an overly-broad crater rim (Figure 5.4A). This suggests that modification of the model may be necessary to recreate less fluid collapse of the crater rim while still allowing fluid-like movement of the crater floor.

### **Sensitivity of Results**

Once the Acoustic Fluidization model was chosen for use in the continued modelling of impact crater formation on Ganymede (Chapter 6 and 7), the sensitivity of the produced crater morphology to changes in model parameters was assessed. Simulated crater morphology is highly sensitive to decay time: a 10% change in its value will alter the simulated crater depth by up to 20% (Figure 5.7B) for a viscosity of  $60,000 \text{ m}^2 \text{ s}^{-1}$ . For large decay times, crater morphology was not as sensitive to small viscosity variations. However, the effect of changing viscosity becomes more apparent for smaller decay times. A reasonable fit to the

observational data can be achieved using a decay time between 45 and 55 s (Figure 5.10B). As this is a relatively large decay time, there is a large tolerance on the best-fit viscosities ( $80,000 \pm 10,000 \text{ m}^2 \text{ s}^{-1}$ ); the difference in crater morphology created as a result of these variations are shown in Figure 5.10A.

The depth-diameter ratio of the simulated craters is clearly controlled by the decay time of the pressure vibrations and appears almost independent of target viscosity (within the explored range) (Figure 5.7A and B). This relationship can thus aid the identification of a suitable set of Acoustic Fluidization parameters for each different crater size – once a set of simulations using different decay times have been performed, the relationship between  $d/D$  ratio and decay time for that crater size can be found. The required  $d/D$  ratio for that crater diameter can then be used to estimate the best-fit decay time.

### **Influence of the Hydrocode Equation of State (EoS)**

Section 5.3.2 compares the best-fit A.F. model results obtained when using the Tillotson EoS (Equation 4.4) and the third order Tillotson EoS developed during the course of this work (Equation 4.31). Although the Hugoniot curve produced when using the third order Tillotson EoS recreates the observational data of Stewart and Ahrens (2005) better than when using a second order Tillotson equation of state (Figure 4.8), simulation results do not differ significantly (Figure 5.11; Table 5.2). This demonstrates that final simulated crater morphology was not overly sensitive to the EoS used for the test simulations.

The variation in crater morphology shown in Figure 5.11B is less than that caused by variation in A.F. parameters (Figure 5.10). This suggests that the use of the Tillotson EoS instead of the third order EoS will not have significantly affected results. Use of the Tillotson equation of state is thus continued for the simulations of different crater sizes presented in Chapter 6. However, the Tillotson EoS calculates higher post-impact target temperatures than the third order Tillotson EoS, leading to a warmer central peak core (Figure 5.12); this may have implications for the numerical modelling of central pit formation, as discussed in Chapter 8.

## Chapter 6

# Strength Model Scaling for Pure Ice

The observed shallowing of crater wall slopes as crater size increases indicates a progressive weakening of the target material as crater diameter increases (Section 2.6.2, Figure 2.5). Effective numerical modelling of the formation of different sized impact craters must therefore incorporate a means to scale the material weakening with event size.

Of the strength models evaluated in Chapter 5, the model incorporating Acoustic Fluidization is considered to better match observations (Bray et al., 2008). This model was therefore adopted for simulation of different sized craters on Ganymede as presented in this chapter. To recreate the Ganymede cratering trend using this strength model, the Acoustic Fluidization parameters must be scaled with event size in some way.

Wünnemann and Ivanov (2003) performed simulations of lunar impact, using the Block Model (Section 4.1.4) and found a good fit of simulation results to observed depth-diameter ratios by assuming that the parameters controlling the kinematic viscosity and the decay time were proportional to the projectile radius ( $R_p$ ). This chapter outlines the method used to determine a similar scaling relationship for impact into pure ice and presents numerical modelling results for a range of crater sizes on Ganymede. Simulation results for central peak craters are presented first, followed by application of the scaling trend to larger crater diameters.

## **6.1. Approach**

### **6.1.1. Determining the Scaling Trend for Pure Ice**

As discussed in Section 5.1.5, craters larger than  $\sim 26$  km in diameter on Ganymede are considered to be affected by rheological changes that occur with depth (Schenk, 2002). In order to determine the Acoustic Fluidization (A.F.) parameters for pure ice, only craters smaller than 26 km were included in the development of a scaling trend. As the simulation of smaller impacts requires substantial run times compared to larger simulated impacts (due to the relatively high resolution mesh), the scaling trend was first determined based on simulation of craters above 3.5 km in diameter. Craters at or closer to the simple-to-complex (s-c) transition on Ganymede ( $\sim 2$  km) were not attempted until the strength model had been provisionally developed (see Section 6.2.2).

The material properties and projectile velocity used for the simulation of a  $\sim 15$  km crater on Ganymede were again used for the simulation of different crater sizes (see Table 4.2 and 5.1). This ensures that the A.F. parameters are not influenced by changes in the projectile velocity. The size of the impact was controlled by varying the size of the projectile.

As both decay time ( $\tau_v$ ) and viscosity ( $\eta$ ) scale with block size (Equations 4.25 and 4.26) in the Block Model of A.F., their ratio is dependent on parameters that are expected to remain fixed for impacts into the same material (Equation 4.27). The most logical approach for simulating impacts of different sizes was therefore to fix the ratio of  $\eta$  and  $\tau_v$  as determined for a  $\sim 15$  km crater and vary the actual values of  $\eta$  and  $\tau_v$ .

All other approaches involved varying both  $\eta$  and  $\tau_v$  and their ratio. In cases where both  $\eta$  and  $\tau_v$  were varied for each crater size, the same process used to determine the best-fit parameters in Chapter 5 was employed. The relationships between A.F. parameters and simulated crater dimensions presented in Section 5.3 were used to expedite this identification of suitable parameters.

As the depth, diameter and wall slope of simulated craters were noted to be relatively unaffected by viscosity (Section 5.3.1), a suite of simulations with a fixed viscosity and variable decay time was performed, producing a range of crater sizes and morphologies. The wall slope and d/D ratio of the produced craters were measured and the relationships between  $\tau_v$ , crater wall slope and d/D ratio established (see equations in Figure 6.1).

As each simulation produced slightly different crater sizes, the expected d/D ratio and wall slope for 10 - 15 km diameter craters (as estimated from observations) were used to predict a maximum and minimum suitable decay time (grey arrows in Figure 6.1). Once these

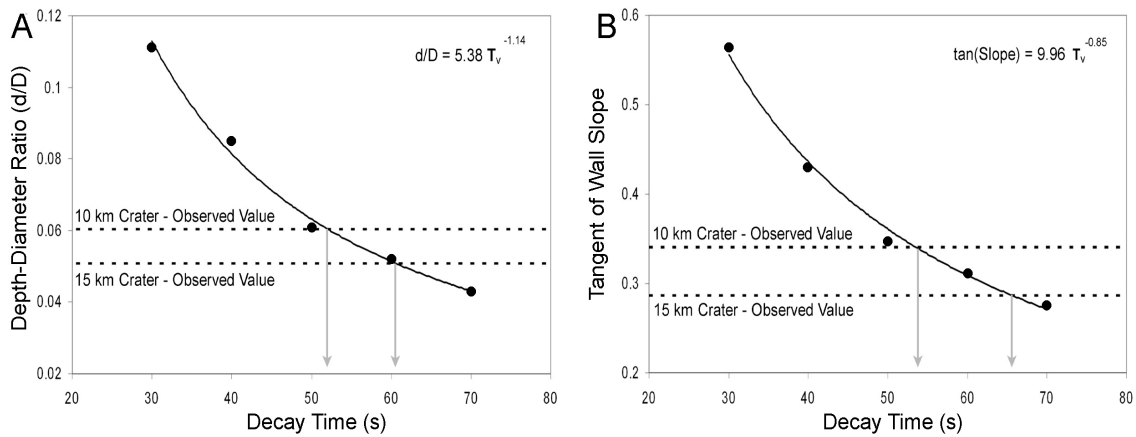


**Figure 6.1:** Finding suitable decay time for a 300 m projectile. Measurements taken from the simulated crater profiles are displayed as closed circles. The best-fit trend line is marked with a black line and its equation noted at the top right of each plot. A) Depth-diameter ratio variance with decay time. B) Effect of decay time on simulated crater wall slope. Kinematic viscosity was fixed at  $80,000 \text{ m}^2 \text{ s}^{-1}$  for all simulations in this figure. The range of expected values for depth-diameter ratio and wall slope are marked with dotted lines and the corresponding range of acceptable decay times indicated with grey arrows.

boundaries were established, the median decay time was calculated. This decay time was then held constant and the target viscosity varied.

To produce a set of parameters most representative of the general trend, the simulations were compared to representative profiles created from the scaling trends in Table 2.2. Best-fit A.F. parameters were determined primarily by fit to observed crater wall slope, as the position and dimension of the modelled crater rims is a noted weakness of the A.F. model (Section 5.2.3). This process was repeated for progressively smaller projectiles, each time adopting the best-fit viscosity determined for the previous (next largest) projectile size. Once these best-fit simulations were achieved, the relationship between decay time and viscosity with impactor radius was assessed and used to determine a scaling law for the A.F. parameters with event size (Figure 6.7 and Equations 6.1 to 6.3).

### 6.1.2. Testing the Scaling Trend

An important test of any proposed strength model for the numerical simulation of impact crater formation is the ability to recreate the s-c transition. As explained in Chapter 1, the s-c transition marks the change from the relatively small-scale collapse of small transient cavities to the more dramatic collapse of larger cavities. This produces a change in the d/D trend on each body as the additional collapse and uplift occurring during the modification of large transients produces relatively shallower craters. The change from simple to central peak

morphology on Ganymede occurs at  $2.1 \pm 0.2$  km; the corresponding change in gradient of the  $d/D$  trend line shown in Figure 6.9 is recorded at  $1.9 \pm 0.5$  km (Schenk, 2002).

Once the scaling trend for craters between 2 and 26 km in diameter was established, Equations 6.1 and 6.2 were used to estimate a suitable value for the decay time and kinematic viscosity needed to recreate the correct crater morphology and dimensions for a 1.5 km diameter crater on Ganymede (Table 6.3). These parameter values were then employed in the simulation of this crater sizes, using the method and material properties described in Chapter 5. As this thesis does not include analysis of simple crater morphology, simulation results were compared to established depth-diameter ratios from Schenk (2001) to assess model success.

A series of simulations for larger crater diameters were also performed using Acoustic Fluidization parameters calculated from the scaling trend (Table 6.3). The static strength properties and equation of state used for the simulation of 2 to 26 km craters were employed and the projectile size varied to create a range of crater sizes between 30 and 70 km in diameter. The produced crater profiles were measured and the results compared with observational data for central peak and central pit craters on Ganymede (Figures 6.3 to 6.6).

## **6.2 Strength Model Scaling for Pure Ice**

### **6.2.1. Development of the Strength Model Scaling**

The best-fit simulation results for a range of crater diameters between 2 and 26 km are presented in Figure 6.2. Each profile is shown relative to a representative crater profile created from the scaling trends in Table 2.2. The simulation crater depth, wall slope and peak width show a reasonable match to the actual crater dimensions in most cases (Figures 6.3, 6.5, and 6.6A). As peak height is noted to vary for craters up to  $\sim 12$  km in diameter (Figure 2.7B, Table 2.2), exact match to the representative profile was not deemed necessary, although the peak height was required to be within the observed range of 50 to 560 m for the profile to be considered a suitable fit.

The position and height of the simulated crater rim relative to the pre-impact surface level does not match observations. As the broad crater rims produced when employing A.F. are acknowledged to be a weakness of the model, the best-fit results are compared to a representative profile of appropriate wall slope rather than rim-to-rim diameter.

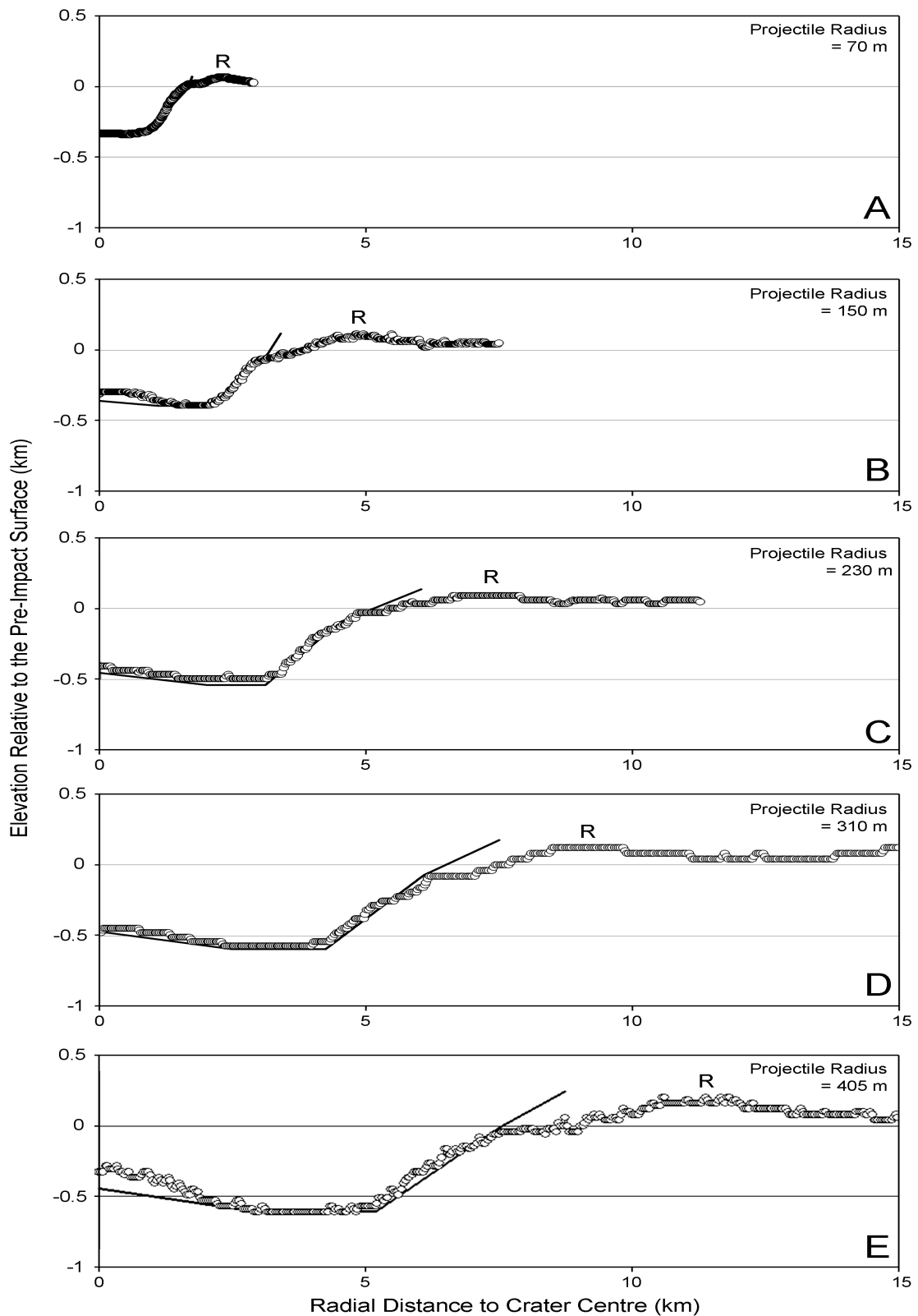


**Figure 6.2:** Best-fit simulation results of 3.5 to 17.5 km diameter craters (representative profile diameters). The simulation profiles (open circles) are compared to general crater profile generated from the scaling trends in Table 2.2 (black line). As explained in Chapter 5, the representative profile rim does not align with the simulation rim (marked with 'R')

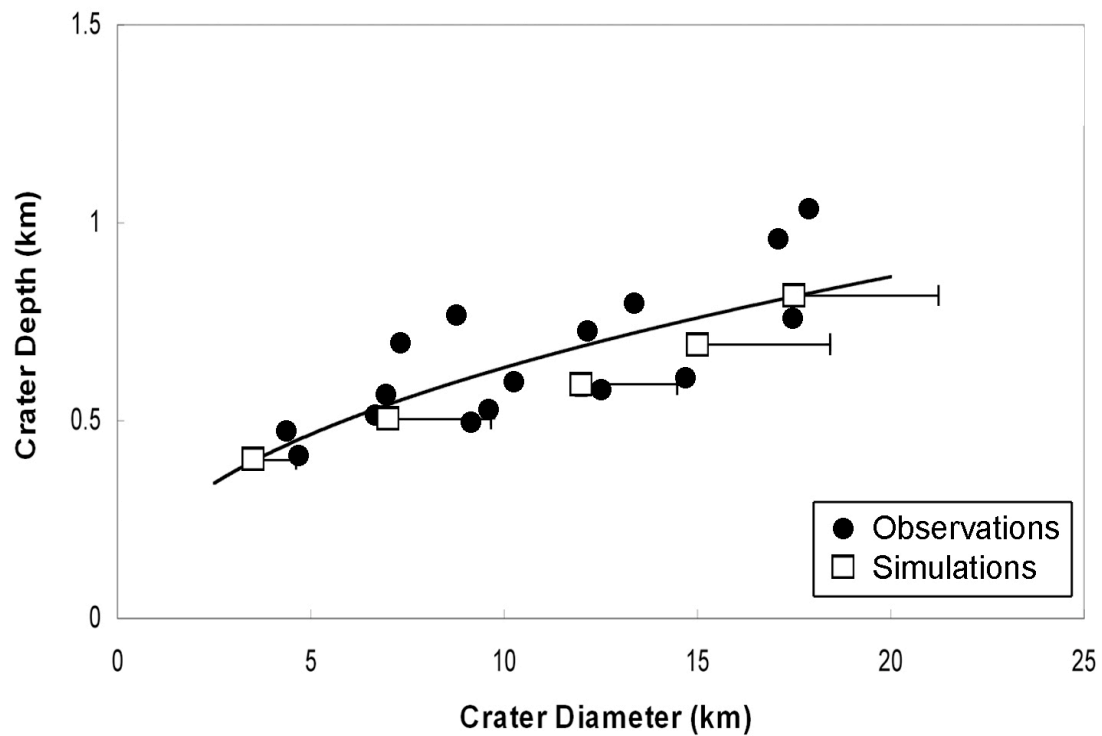


**Figure 6.3:** Depth-diameter ( $d/D$ ) plot of central peak craters on Ganymede between 0 and 25 km in diameter included in this work (closed circles). The  $d/D$  trend line established for these sized craters in Chapter 2 is included as a black line (see Table 2.2 for equation). Depth measurements of best-fit simulation results are shown as open squares with error bars; the squares mark the diameter of the representative profile used to fit the simulation results to, and the error bar limit shows the actual rim-to-rim diameter of the simulated crater. Depth and diameter of other simulation results are included on Figure 6.9.

**Table 6.1: Best-fit Simulated Crater Dimensions**

Projectile Radius, $R_p$ (km)	Diameter of Rep. Profile (km)	Diameter of Simulation (km)	Depth (km)	Tangent of Wall Slope	Rim Height (km)	Peak Diameter (km)	Peak Height (km)
0.07	3.5	4.68	0.40	0.44	0.06	0.89	0.01
0.15	7	9.65	0.51	0.30	0.11	3.07	0.09
0.23	12	14.53	0.58	0.30	0.09	3.20	0.09
0.31	15	18.44	0.69	0.25	0.12	4.77	0.13
0.405	17.5	22.76	0.81	0.22	0.21	5.83	0.32

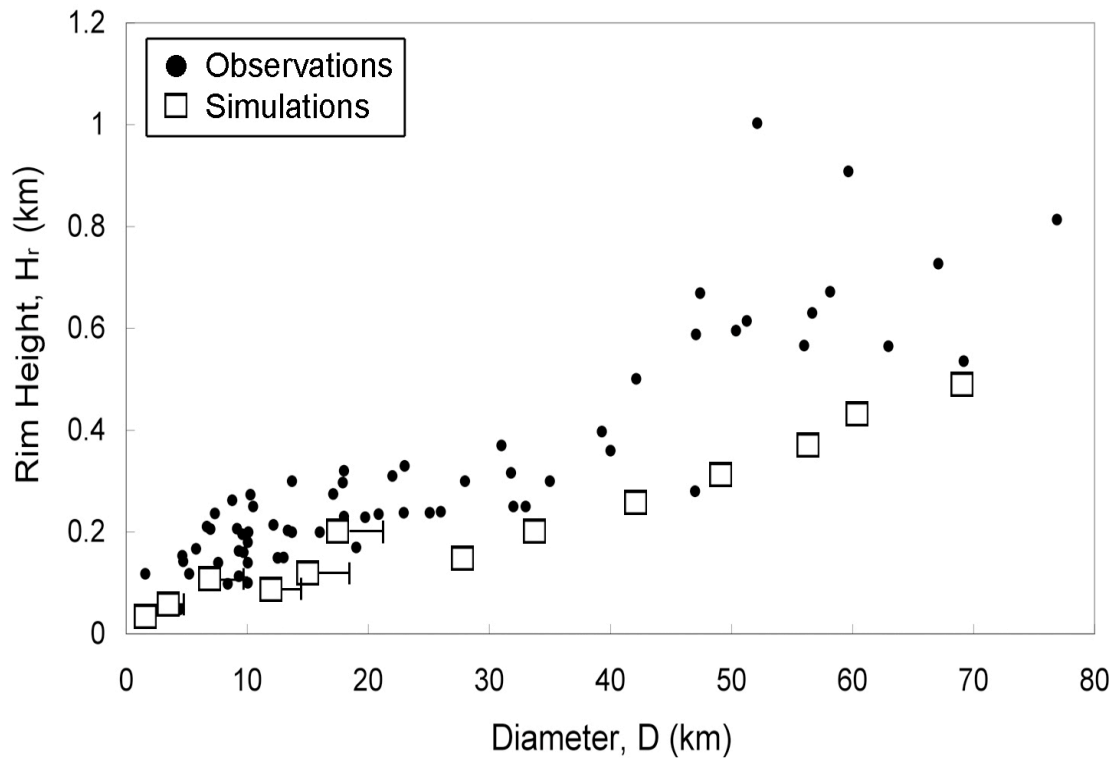


**Figure 6.4:** Comparison of observed and simulated crater rim heights. Observational measurements from this work and Schenk (1991) are shown with closed circles. Simulated rim heights are marked by open squares. Error bars are included on the simulations used to establish a scaling trend; in these cases the squares mark the diameter of the representative profile used to fit the simulation results to, and the error bar limit shows the actual rim-to-rim diameter of the simulated crater. For data points without error bars, the square marks the actual rim-to-rim diameter of the simulated crater.

The dimensions of the best-fit simulation profiles were measured (see Table 6.1) and are plotted alongside full observational data for Ganymede in Figures 6.3 to 6.6. The crater diameters marked with data points in these figures denote the rim-to-rim diameter of the representative profile each simulation was matched to, as the best fits were chosen based on the fit to this profile. The actual rim-to-rim distance of the simulated crater is noted as the maximum extent of the error bar for each data point.

The depths of the simulated craters are within the range recorded for craters on Ganymede (Figure 6.3), although are on the shallower end of the range. When comparing the crater depth to the rim-to-rim diameter measured from the crater simulated profile (rather than the representative profile), simulated crater depths are slightly too shallow relative to the main trend.

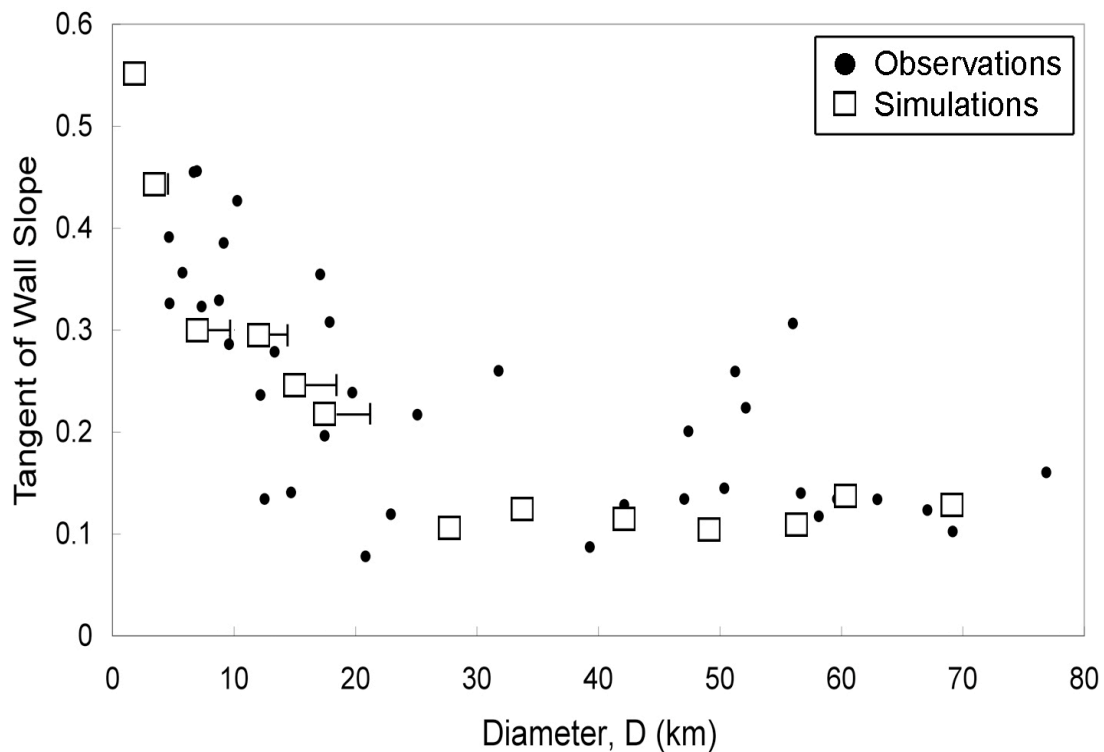


**Figure 6.5:** Comparison of observed and simulated crater wall slopes. Observational measurements from this work are shown with closed circles. Simulated rim heights are marked by open squares. Error bars are included on the simulations used to establish a scaling trend (see Figure 6.4 caption for further details).

The rim heights of the simulated craters are generally smaller than observed values (Figure 6.4). Rim heights closer to the observed values were produced during simulations using higher viscosities and lower decay times, but were not noted to occur concurrently with the correct internal crater morphology. The simulated crater wall slopes show a good fit to the observational data in most cases (Figure 6.5). The 7 km crater (Figure 6.2B) does not display the same good fit to observations as the 3.5, 12, 15 and 17.5 km craters, and has a wall slope on the shallower end of the observed range for this crater size

The central peak widths and heights of the best-fit simulated craters are presented in Figure 6.6A and B respectively. All simulations produce the correct central peak diameter; this fit to observations is reasonable when using both types of rim-to-rim diameters recorded in Table 6.1. As best-fit simulations were selected on their fit to central peak width, rather than height, the simulated peak heights plotted in Figure 6.6B do not provide as good a match to observations as the central peak width measurements. Although providing the closest fit to the representative crater profiles of the results displayed in Figure 6.2, the peaks of the 12 and 15 km craters are slightly shallower than the general trend of observed peak heights.

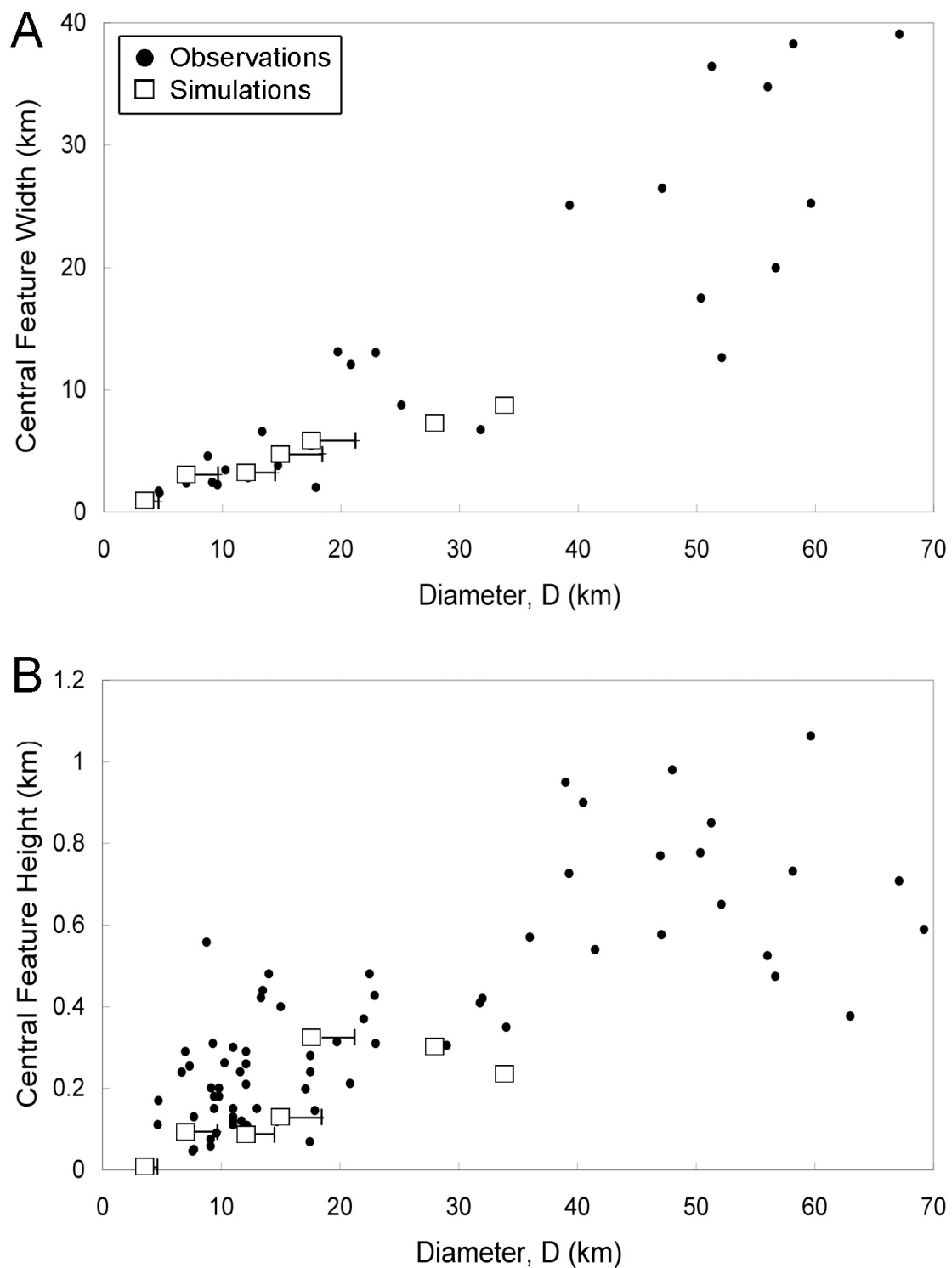


**Figure 6.6:** Comparison of observed central feature size and simulated central peak dimensions. A) Central feature width. Observed diameters of central peaks and pit summits are marked with closed circles; simulation results as open squares. B) central feature height. Observational data marked with closed circles and includes data for central peak and pit summit heights, as recorded by this work and Schenk (1991). Simulated rim heights are marked by open squares. Error bars are included on the simulations used to establish a scaling trend (see Figure 6.4 caption for further details).

Table 6.2 summarises the best-fit decay time ( $\tau_v$ ) and kinematic viscosity ( $\eta$ ) used to produce the crater profiles in Figure 6.2. Once best-fits were determined for 3.5 to 17.5 km diameter craters, it was apparent that the best-fit values of  $\tau_v = 50$  s and  $\eta = 80,000$  m<sup>2</sup> s<sup>-1</sup> for a 15 km crater did not fit the otherwise increasing trend in A.F. parameters with projectile size. However, the alternative best-fit parameters presented in Section 5.2.2 ( $\tau_v = 70$  s and  $\eta = 110,000$  m<sup>2</sup> s<sup>-1</sup>) provide a reasonable match to observational data (Figure 6.2D) and are consistent with the positive trend. The alternative A.F. parameters of  $\tau_v = 70$  s and  $\eta = 110,000$  m<sup>2</sup> s<sup>-1</sup> for a 15 km crater were thus chosen to construct a scaling trend.

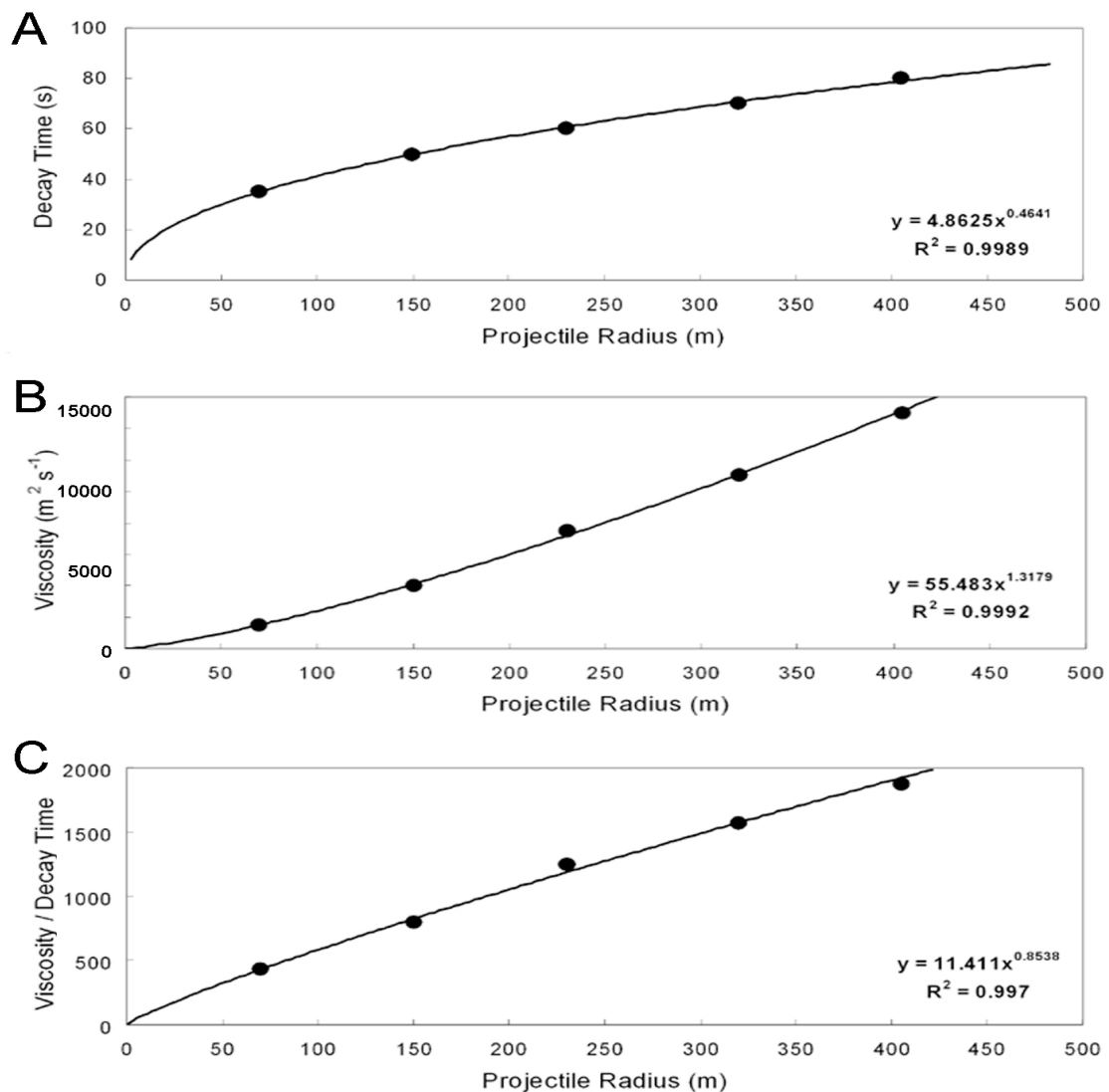


**Figure 6.7:** Trends in the best-fit Acoustic Fluidization parameters. The decay time and viscosity values employed for the simulation of the craters shown in Figure 6.2 are plotted against the projectile radius as closed circles in graphs A and B respectively. The ratio of these parameters also scales with projectile size; this relationship is shown in part C. The trend lines in parts A, B, and C are described by Equations 6.1, 6.2 and 6.3 respectively.

**Table 6.2: Best-fit Acoustic Fluidization Parameters**

Projectile Radius (m)	Decay Time (s)	Kinematic Viscosity ( $m^2 s^{-1}$ )	Viscosity/Decay Time
70	35	15,000	430
150	50	40,000	800
230	60	75,000	1250
310	70	110,000	1570
405	80	150,000	1875

**Table 6.3: Best-fit Acoustic Fluidization Parameters Predicted Using Scaling Trends**

Projectile Radius (m)	Decay Time (s)	Kinematic Viscosity ( $m^2 s^{-1}$ )	Viscosity/Decay Time
25	22	4,020	183
495	87	197,000	2280
675	100	297,000	2970
860	112	409,000	3650
1050	123	531,000	4330
1240	133	662,000	4990
1430	142	799,000	5640
1630	151	950,000	6310

This work shows that to recreate the observed crater morphology on Ganymede both the decay time and the kinematic viscosity must increase with projectile radius (see Figures 6.7A and B). Wünnemann and Ivanov's (2003) assumption that the A.F. parameters scale linearly with event size has been relaxed in this work, and the increase of  $\eta$  and  $\tau_v$  is instead described by two power laws (Equations 6.1 and 6.2):

$$\tau_v (s) = 4.86Rp^{0.46}, \quad (6.1)$$

$$\eta (m^2 s^{-1}) = 55.48Rp^{1.32}, \quad (6.2)$$

$$\eta/\tau_v = 11.41Rp^{0.85}. \quad (6.3)$$

### 6.2.2 Testing the Strength Model I - Recreating the Simple-to-Complex Transition

Equations 6.1 and 6.2 were used to estimate appropriate decay time and kinematic viscosity to model the formation of a crater smaller than 2 km on Ganymede. These calculated values are

included in the top section of Table 6.3. Figure 6.8 presents the crater simulated using the A.F. scaling trend derived in Section 6.2.1 using projectile radii of 25 m to produce a crater  $\sim 1.5$  km in diameter.

The depth and diameter of this crater was measured and compared to observational data for craters on Ganymede (Figure 6.9). Rim height and wall slope were also measured and are included in Figures 6.4 and 6.5 respectively. As only one simple crater was profiled in the course of this work, simulation results were compared to data from Schenk (2002) so that the simple-to-complex transition could be seen (Point 'B' on Figure 6.9). In addition to correctly recreating the simple morphology of craters below  $1.9 \pm 0.5$  km in diameter (Schenk, 2002), the change in depth-diameter ratio associated with the s-c transition was also achieved using the scaling trend presented in Section 6.1. However, the simulated crater is shallower than expected for simple craters on Ganymede (Figure 6.9).

Observations from terrestrial craters show that, in the case of simple craters, the shallowing of the final crater depth relative to the transient cavity is due to the presence of a breccia lens (Figure 1.1; e.g. Grieve, 1978) formed by collapse of material from the walls of the transient crater. Although some wall material has collected at the crater centre during the modification of the simulated crater in Figure 6.8, the main cause of this craters shallow depth is uplift of the sub-surface layers. Despite this noticeable uplift, the upward displacement of material layers beneath the crater is not expressed at the surface, maintaining simple crater morphology.

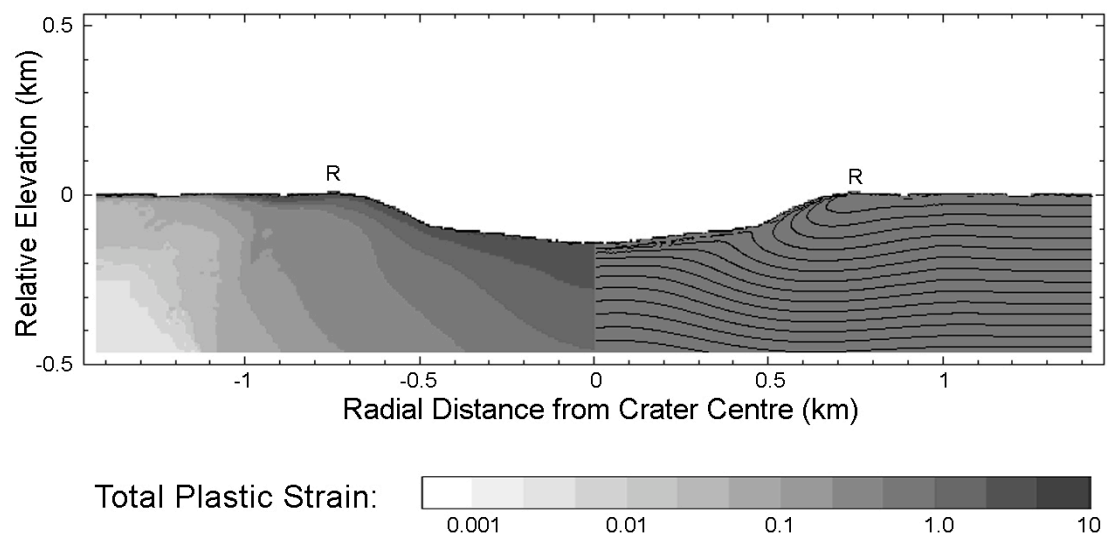


**Figure 6.8:** Simple crater formed by the simulated impact of a 50 m diameter projectile into pure ice using the Acoustic Fluidization parameters at the top of Table 6.3. Total plastic strain experienced by the target is seen on the left; representative material layers are included on the right to show deformation. Crater rims are marked with 'R'.

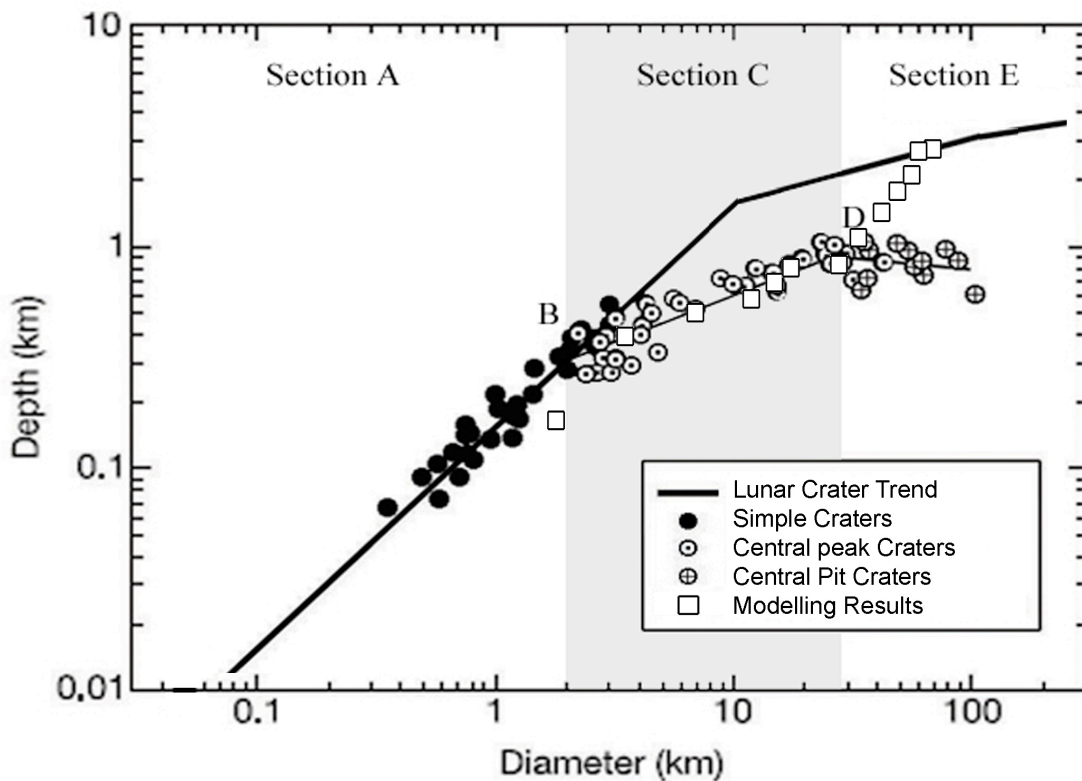


**Figure 6.9:** Depth-diameter plot for craters on Ganymede, modified from Schenk (2002) and updated from Figure 1.11. Different types of crater morphologies are noted and a lunar trend line included for comparison (Pike, 1977). The Ganymede trend is marked with a thinner black line. Transition B is the simple-to-complex transition; transition D marks the transition from central peak to central pit morphology. The depth and rim-to-rim diameter of the simulated craters are included as open squares.

### 6.2.3 Testing the Strength Model II - Extension to Larger Crater Sizes

Simulations using projectile sizes between 495 m and 1630 m were performed employing the A.F. parameters predicted from Equations 6.1 and 6.2 (as presented in the bottom half of Table 6.3). The produced crater profiles were measured and the results recorded in Table 6.4. These values are plotted alongside observational data in Figures 6.4 to 6.6 and Figure 6.9.

The correct crater depth is produced for craters up to  $\sim 34$  km in diameter ( $R_p = 1050$ m); above this diameter simulated craters are up to 150% deeper than expected for craters of this size on Ganymede (Figure 6.9). The difference between observed and simulated values increases with increasing impactor size.

The rim heights and wall slope of these larger craters continue the trends shown by the best-fit craters between 20 and 26 km diameter: simulated craters show a good fit to wall slope and a poor fit to rim height. The simulated craters above  $\sim 34$  km in diameter have wall slopes of  $\sim 0.12$ , consistent with observed wall slopes for craters of this size (Figure 6.5).

Simulated crater rim heights increase with increasing crater size, but remain consistently lower than observed rim heights (Figure 6.4).

### The Onset of Peak Instability ( $27 \text{ km} < D < 34 \text{ km}$ )

The 27 and 34 km diameter craters produced by the projectiles with radii of 495 and 675 respectively are both central peak craters (Black lines, Figure 6.10). The central peak dimensions were measured and included in Figures 6.6. The central peaks in the 27 and 34 km craters are 7 and 9.5 km in diameter respectively providing a good match to observational data (Figure 6.6A). The central peak height of the 27 km crater is also similar to peak heights observed on Ganymede (Figure 6.6B). The peak height for the 34 km crater is also consistent with observations, although the peak height is slightly smaller than would be expected for this crater size. These two craters have quite different collapse histories, leading to the difference in their central peaks.

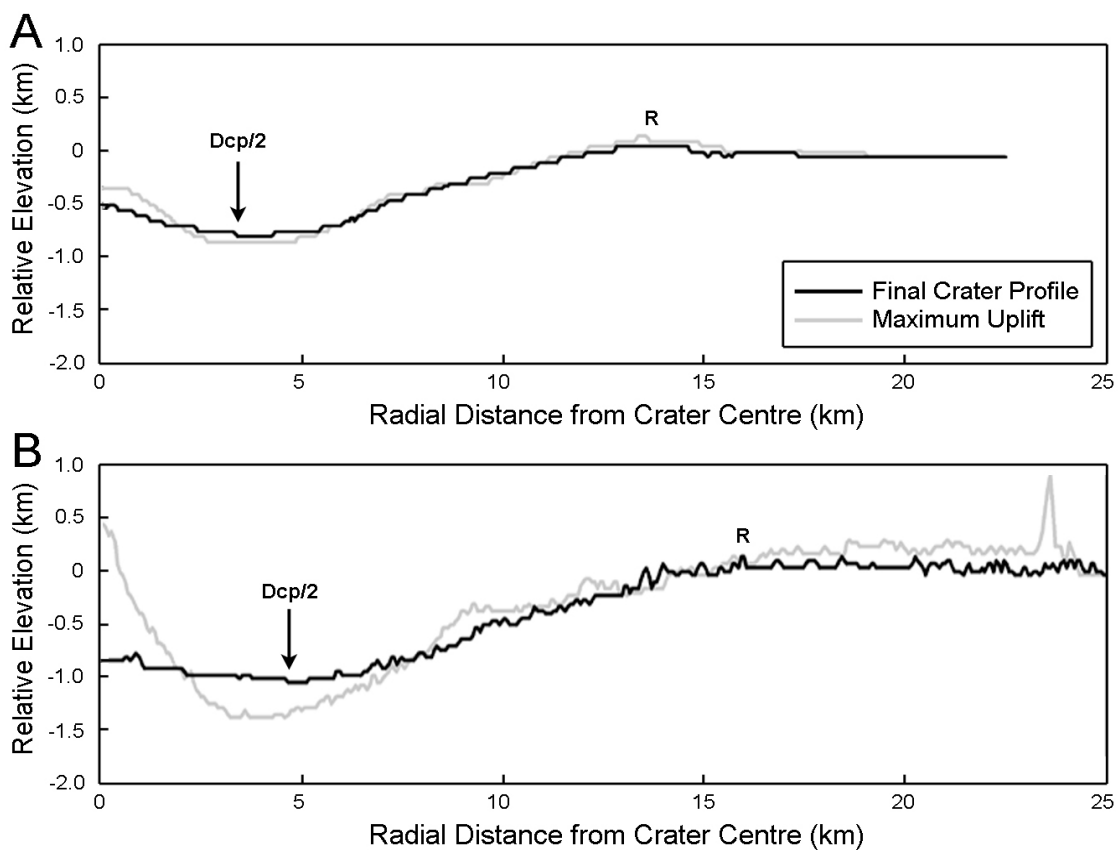


**Figure 6.10:** Comparison of the transient central uplift and the final central peak dimensions for A) 27 and B) 34 km diameter craters. Final crater profile is black; profile 200 seconds after impact in both simulations is marked in grey. Location of the final crater rims is marked with 'R' and the final central peak radius indicated with an arrow.

The final crater profiles of the 27 and 34 km crater are shown in Figure 6.10A and B respectively. The crater profile at the time of maximum central uplift is included in this figure so that the difference in central uplift between the two crater sizes can be compared. The central uplift in the 27 km crater reaches a maximum of 500 m, 200 seconds after impact. This uplift becomes more subdued over the rest of the simulation time, forming a 300 m tall central peak in the final crater ( $t = 600$  s). The central uplift in the 34 km crater extends higher than the crater rim level, reaching a maximum height at  $t = 200$  s of 1800 m. This extreme uplift is unstable and undergoes relatively significant collapse, spreading to form a shorter, wider central peak than that of the 27 km crater (Figure 6.10B).

### **Loss of Central Morphology in the Largest Simulations ( $D > 34$ km)**

For simulated impact of projectiles with radii larger than 860 m (leading to craters larger than 40 km in diameter), decay times were in excess of 112 s. Although the fluidised region reduced in size with time after these impacts (see Figure 6.11), the material at the centre of the crater remained weakened long enough to prevent the retention of internal crater topography. The larger quantity of melt produced during these larger impacts also contributed to loss of central topography.

A series of simulation stills are presented in Figure 6.11 to show the decay of the Acoustically Fluidised region and the loss of internal crater morphology for the impact of a 1050 m radius projectile; the depicted sequence is representative of that observed for simulated impact of all projectiles larger than 860 m in radius. The shaded regions of Figure 6.11 show the area in which the A.F. is operating. The darkest shades mark areas in which the acoustic vibrations are relatively strong, decreasing the target strength relative to its static value. The relative strength of the acoustic vibrations decrease with distance from the target surface as the overburden pressure (and hence the material strength in constant temperature targets) increases with depth.

The large central uplift in the larger simulations is comprised primarily of melt (coloured blue in Figure 6.11) and collapses, base first, to form a summit pit crater (Figures 6.11A to C). Still primarily composed of melt, this transient central morphology again collapses and the central melt body oscillates between peak and pit morphology until equilibrium is reached at  $\sim 600$  seconds after impact (Figures 6.11C to E). The melt pool produced by the simulated impact of a 1050 m projectile is approximately 10 km across and 4 – 5 km deep. This diameter is similar to the pit diameter expected for a 50 km crater ( $D_p = 8.5$  km, see Table 3.1). The depth of the melt pool is an order of magnitude larger than the pit depth observed for this size crater.

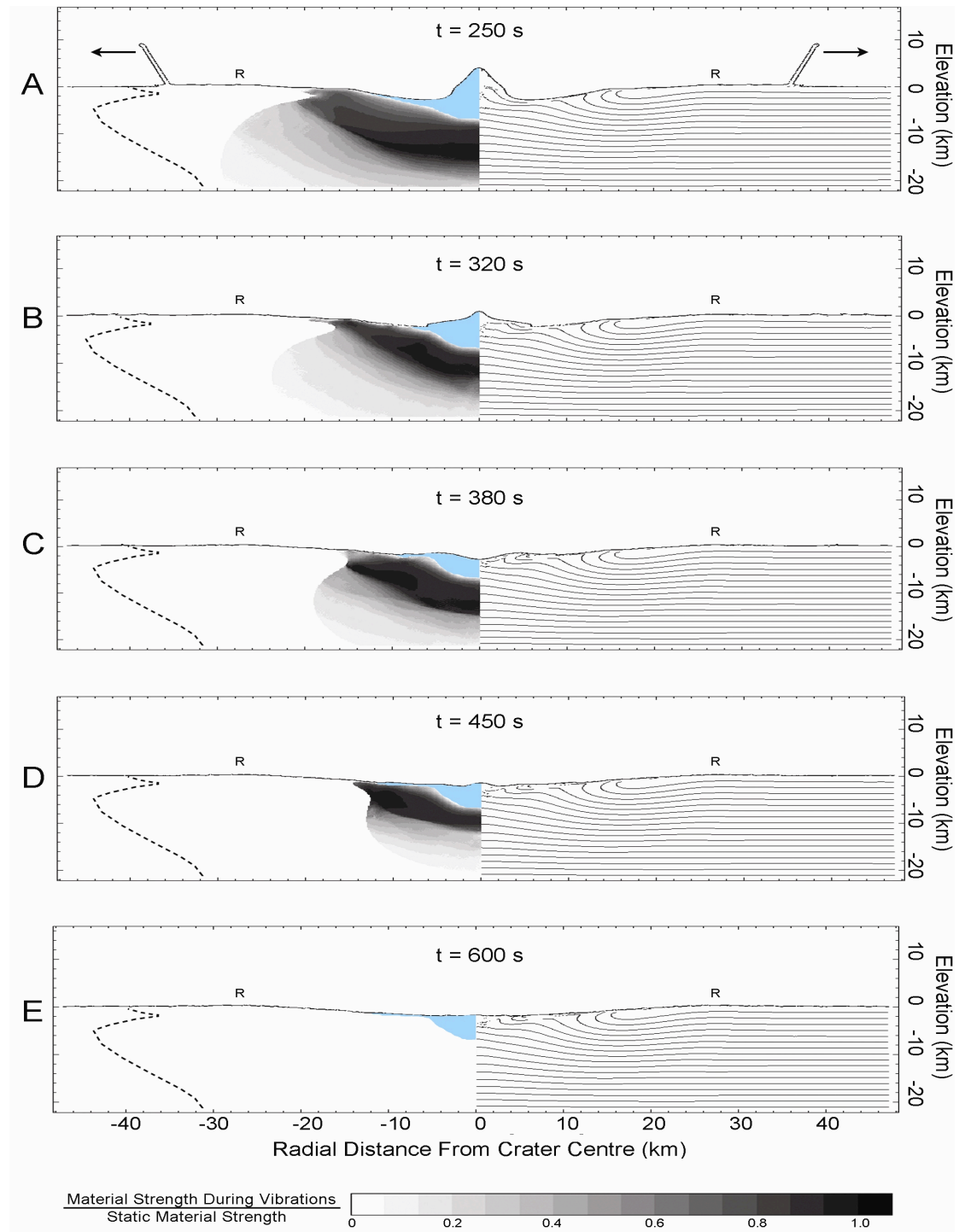


**Figure 6.11:** Series of simulation stills showing the decay of the Acoustically Fluidized region with time. The region of target material being affected by Acoustic Fluidization is shown as a shaded area on the left; the darkest shades mark the regions in which the influence of A.F. is strongest. The dotted line marks the maximum extent of the fluidised region, as it occurred  $\sim 20$  s after impact. Melt is coloured blue, location of the final crater rim is marked with ‘R’. The right hand side shows material layers. A) 250 s after impact, at the point of maximum central uplift; the ejecta has not been completely emplaced at this point. B) Basal collapse of the fluid peak. C) A transient morphology similar to that of a summit pit crater is formed 380 s after impact. D) Central region oscillates until equilibrium is reached (E).

### **6.3. Summary and Implications**

The large-scale morphology of Ganymede impact craters between 3.5 and 34 km can be recreated using the Block Model scaling trend for pure ice presented in this chapter (Equations 6.1 and 6.2). However, use of this scaling trend does not produce the correct morphology for craters above 40 km in diameter. The strengths and weaknesses of this strength model are discussed in this section.

#### **6.3.1 Parameter Scaling**

As predicted by the Block Model (Section 4.1.4), best-fits to observed crater morphology were achieved using a decay time,  $\tau_v$ , and kinematic viscosity,  $\eta$ , which increase for increasing projectile radius. However, the ratio of these parameters also increases with increasing projectile size (Equation 6.3). This is not an intuitive result as both decay time and viscosity are expected to scale with event size with a ratio that remains fixed for impacts into the same material (Equation 4.27).

The non-constant  $\eta/\tau_v$  required for the simulation of craters on Ganymede may suggest that the material ‘constants’ in Equation 4.27 vary with impact event size in some way. As the ratio of  $\eta$  and  $\tau$  increases with crater diameter it implies that the bulk sound speed in the target,  $c$ , or the quality factor,  $Q$  may be increasing with event size, or that the relative density of blocks and surrounding debris is changing in a manner which causes the constant  $\chi$  to decrease. Of these options the quality factor,  $Q$ , is most likely to be a function of event size.

$Q$  is the ratio of energy stored per cycle of vibrations to the energy lost over the same period and has previously been considered independent of event size (Section 4.1.4). A  $Q$  value that increases with event size could suggest that the dissipation of vibration energy is more efficient for shorter wavelengths (smaller block sizes).

The non-constant ratio of  $\eta$  and  $\tau_v$  may also be a result of model non-uniqueness as similar crater morphologies can be recreated using pairs of A.F. parameters with different ratios (e.g.  $\eta/\tau_v = 80,000/50$  and  $\eta/\tau_v = 110,000/70$  both allow recreation of 14 – 15 km crater morphology). It is therefore plausible that a constant ratio of  $\eta$  and  $\tau_v$  for all impacts into ice could be found with further investigation of different A.F. parameter combinations for different crater sizes.

#### **Implications for Block Size, B**

The amount and longevity of A.F. is dependent on the average block size of the fragmented sub-crater rock mass,  $B$ . The viscosity and decay time are related to  $B$  via equations 4.25 and

4.26 respectively. The A.F. parameter values determined during this work can therefore be used to estimate the size of the fracture blocks beneath each size of crater. As  $Q$  may vary with crater size in an as yet undetermined manner, the block size is most reliably calculated from the kinematic viscosity relation (Equation 4.25) as it is not dependent on  $Q$ .

Table 6.4 presents the block sizes predicted using Equation 4.25 and the best-fit parameters of Table 6.2, using  $c = 400 \text{ m s}^{-1}$  and  $\chi = 0.5$ . The estimated block sizes increases as projectile radius increases. The trend can be fitted by both a linear trend line and by a power law in which the rate of increase in block size increases as crater size increases; both have  $R^2$  values above 0.99. Both trend lines are presented in Figure 6.12 alongside the lunar Block Model of Ivanov and Arttimevia (2002) and Ganymede model of Bray et al (2006).

Based on physical constraints, the negative intercept of the linear Block Model trend line shown in Figure 6.12 is not considered a ‘real’ result. As discussed in Section 6.3.3, the kinematic viscosity employed for modelling the impact of small projectiles is possibly over-estimated. Reassessment of the best-fit parameters for a 3.5 km crater (for example) may reveal the kinematic viscosity to be larger than  $15,000 \text{ m}^2 \text{ s}^{-1}$ , leading to a trend intercept  $\geq 0$ .

Studies of terrestrial impact sites have provided information of the block size beneath several impact craters, allowing the validity of Block Model predictions to be assessed. Kenkmann et al. (2006) record a minimum block size of 50 m and an average block size of 170 m beneath the 10 km diameter Upheaval Dome crater on Earth. The Ganymede Block Model equations (both linear and power-law fit options) from this work shown in Figure 6.12 predict a block size of  $\sim 70$  m beneath a 10 km Ganymede crater, assuming a projectile diameter of  $\sim 360$  m. This is inline with the terrestrial observations, suggesting that the Ganymede Block Model produces realistic block sizes for craters of this size. However, the match is not so favourable for larger craters.

**Table 6.4: Block Sizes Predicted from Best-fit Viscosities**

Projectile Radius (m)	Representative Crater Diameter (km)	Kinematic Viscosity ( $\text{m}^2 \text{ s}^{-1}$ )	Block Size (m)
70	3.5	15,000	19
150	7	40,000	50
230	12	75,000	94
310	15	110,000	138
405	17.5	150,000	188

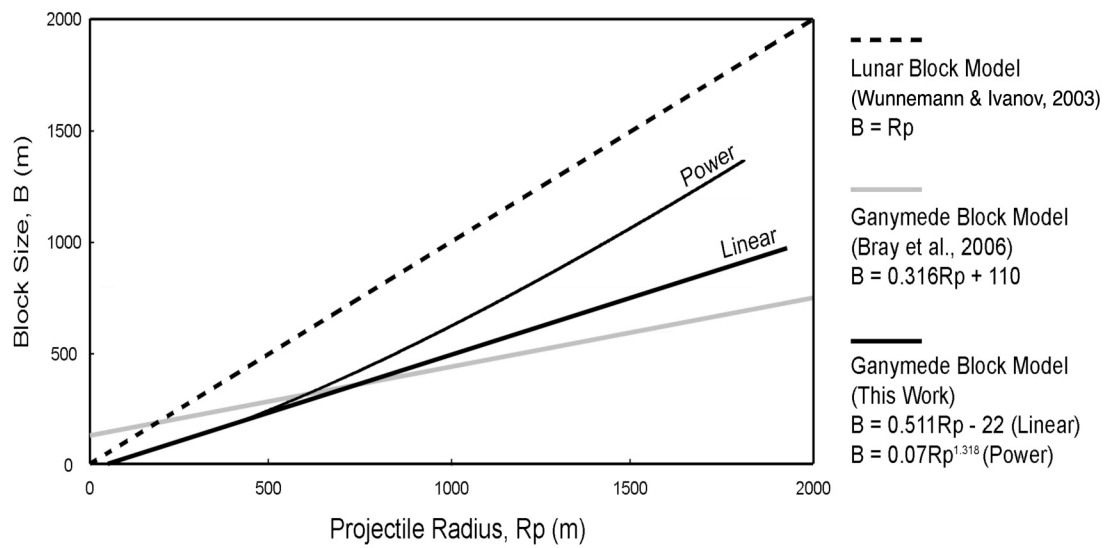


**Figure 6.12:** Block Model scaling for lunar craters (Ivanov and Artemieva, 2002) and Ganymede craters (Bray et al., 2006; this work). Equations for each trend line are included on the right.

Drilling of 40 km scale impact structures on Earth reveal block sizes ranging from 50 m to 200 m, with an average of 100 m (Ivanov et al., 1996). Observed blocks on the rims of lunar craters have also been used to estimate the block size of a lunar 40 km crater as 115 to 350 m (Moore, 1971). The linear Ganymede Block Model predicts a block size of  $\sim 950$  m beneath a 40 km Ganymede crater, assuming a projectile diameter of  $\sim 3.7$  km. Although the same order of magnitude, the Ganymede block size predicted is significantly larger than the block sizes predicted for terrestrial and lunar craters of 40 km diameter, suggesting that the Ganymede Block Model does not operate well at large crater diameters. This disparity is more extreme when employing the power-law equation of Figure 6.12, which predicts an average block size of  $\sim 1400$  m.

### 6.3.2 Recreating Observed Central Peak Crater Morphology

Central peak craters simulated using the A.F. parameters calculated with Equations 6.1 and 6.2 have depths, wall slopes and central peak diameters that match well to observations (Figures 6.3, 6.5 and 6.6A). Central peak height is variable among best-fit results (Figure 6.6B). This was deemed acceptable, as observational data for this dimension was also highly variable.

As more obvious trends in central peak height with crater size have been noted on bodies for which more peak measurements are available, it is possible that with continued collection

of Ganymede peak height data, that a stronger trend may emerge. Simulations results can then be tested by fit to another parameter, ideally reducing the occurrence of non-unique results and leading to the identification of a more robust A.F. parameter scaling.

As noted for the 15 km crater in Chapter 5, model match to rim height is poor. This may be due to the A.F. model treating the entire target area as a viscous fluid. This suggests that modification of the model may be necessary to recreate less fluid collapse of the crater rim while still allowing fluid-like movement of the crater floor.

### **6.3.3. Modelling Simple Craters and the S-C Transition**

The strength model presented in this work recreates the change in morphology from simple to central peak craters at a crater diameter between 1.5 and 3.5 km. This is consistent with the transition diameter of  $\sim 2$  km recorded for craters on Ganymede (Schenk, 2002; Figure 6.9). Further simulations are required to refine this transition diameter.

The depth of the simulated simple crater is too shallow compared to the main Ganymede trend in crater depths (Figure 6.9). This may be due in part to the difficulty modelling the crater rims with the A.F. model, as the simulated rim heights (and thus total crater depth) are  $\sim 100$  m smaller than observations (Figure 6.4). This disparity will have the most noticeable effect on small simulated craters, making them deviate from the observed depth-diameter trend.

The lack of significant breccia lense in the crater in Figure 6.8 is another problem for the model as breccia is expected to fill a large volume of simple crater cavities, shallowing the final crater relative to the transient cavity (Section 1.1.1). The shallow depth of this crater was instead formed by uplift of the crater floor.

It is intuitive that if central peaks are created from uplift of material from depth, upward displacement of material will be noticeable in the sub-surface layers of simple craters, prior to the development of topographically expressed central peaks in larger craters (Grieve, pers. com., 2008). The modelled uplift of the sub-surface layers evident in Figure 6.8 is thus not considered to be a flaw in the model. However, the overly shallow depth of the crater suggests that the extent of material uplift may be too extreme, indicating that the amount of Acoustic Fluidization employed for the simulation of this small crater is too large.

### **6.3.4. Central Peak Development – Basal Collapse Modelled**

Observational data suggests that at large crater sizes central uplifts become unstable, and collapse to form a two-tiered central peak (Section 2.4.3). This peak morphology has been noted in crater with diameters above 39 km (e.g. Gula, Figure 2.12B). As the next smallest central peak crater in this data set is 31.8 km in diameter and does not display a two-tiered

peak, the crater diameter at which the transition in peak formation style occurs is likely between 32 and 39 km. Profiles of more central peak craters in this size range and on different terrains would be necessary to refine this suggested value.

The 27 and 34 km craters simulated during this work have different peak formation histories, as shown in Figure 6.10. The peak in the 27 km diameter crater forms from uplift of the crater floor, similar to the central peaks in the smaller craters presented in this Chapter. The central uplift of the 34 km crater is much larger and collapses, base first, to form a broader central peak. The critical diameter for this style of peak collapse to occur in the models is thus between 27 and 34 km, similar to that suggested by observations.

Although capable of modelling this possible change in central peak formation, the morphologic progression of larger craters from central peak to central pit morphology was not produced using the strength model presented in this Chapter. Instead, the central regions of craters above 40 km in diameter remained fluid long enough to prevent the retention of internal features, producing a series of flat-floored craters.

### **6.3.5. The Need for Material Layering**

Craters above  $\sim 40$  km in diameter simulated in this work have depths up to 150% greater than the observed Ganymede trend (Figure 6.9). The inability of the pure ice strength model to recreate larger craters is an expected result as craters above 51 km in diameter on Ganymede are thought to be affected by the additional weakening influence of a sub-surface ocean at 100 to 200 km depth (Schenk, 2002).

The Block Model derived for pure ice in this work has not been proved reliable at crater diameters above 40 km, as it predicts larger block sizes than expected for craters of this size based on observations. Investigation of the effect of heat flow and sub-surface layering on simulated crater morphology using the current strength model is thus restricted to smaller crater sizes.

On the icy Galilean satellite of Europa, the sub-surface ocean is thought to persist at shallower depths leading to craters as small as 8 km in diameter being affected by its presence. As the strength model scaling for pure ice presented in this chapter can successfully recreate the main Ganymede cratering trend up to  $D \sim 40$  km, this work applies the strength model to the cratering trend of Europa in the next Chapter.

## Chapter 7

# Modelling Impact Cratering on Europa

A strength model for simulating the formation of craters in unlayered ice has been developed, and applied to Ganymede craters smaller than 40 km in diameter. This strength model can now be applied to layered targets to allow the further investigation of layered icy bodies. The Galilean satellites of Ganymede and Callisto are thought to have oceans at 100 to 200 km beneath the surface (Schenk, 2002). The third and smallest of the icy Galilean satellites, Europa, is also believed to have a subsurface ocean persisting at a much shallower depth.

The existence of a shallow sub-surface ocean at Europa makes the satellite of great scientific interest as its ocean could provide a valuable resource and/or a habitat for the development of extra-terrestrial life. As a result, one of the continuing debates of outer solar system research centres on the thickness of Europa's ice crust, as it affects both the habitability and accessibility of its sub-surface ocean (Gaidos et al., 1999; Chyba, 2000) and may subsequently have implications to human exploration of the solar system (Section 7.1.2).

A variety of methods have been used to estimate the thickness of Europa's ice crust; these are outlined in Section 7.2 and include the study of impact craters. As Ganymede and Europa have similar surface gravity and composition, comparison of craters on these bodies may be used to infer differences in crustal structure (Schenk, 2002; Schenk and Moore, 2004). This chapter presents results of simulated impact into layered water and ice targets, employing the strength model for pure ice established in Chapter 6; results are compared to observational data for European craters and used to produce an estimate of the thickness of Europa's ice

crust, and to assess the validity of applying a Ganymede-based strength model when simulating impact cratering on Europa.

## **7.1. Introduction to Europa**

### **7.1.1. Planetary Setting**

Europa is the smallest of the Galilean satellites and orbits second closest to Jupiter, outside the orbit of the volcanic moon of Io (Figure 7.1). The proximity of Io and Europa to Jupiter, and their part in the 1:2:4 orbital resonance with Ganymede, provides a sustained internal heat source despite their small size (Peale and Lee, 2002).

Galileo gravity measurements suggest that Europa is a differentiated body with an 80 to 170 km thick H<sub>2</sub>O shell above a rocky mantle and metallic core (Anderson et al., 1998). Although the exact state and thickness of the H<sub>2</sub>O layer is unknown, tidal heating within the moon is thought to be significant enough for the base of the H<sub>2</sub>O layer to melt (Greeley, 1999). Europa's water layer is thus commonly thought to consist of a solid ice layer above a liquid water ocean.

The Galileo spacecraft detected distortion of Jupiter's magnetic field during Europa's orbit, suggesting a local magnetic field at Europa. The highly non-dipolar nature of this field implies it is created via magnetic induction in a conducting layer (Pater and Lissauer, 2001). The strength and position of this conductor is consistent with a sub-surface brine ocean currently at 100 km depth (Khurana *et al.*, 1998). This result is of particular significance as it provides evidence for a sub-surface ocean being present in the current epoch.



**Figure 7.1:** Image of the four Galilean Satellites. From left to right, in order of increasing distance from Jupiter: Io, Europa, Ganymede, Callisto. Image from the JPL image database.

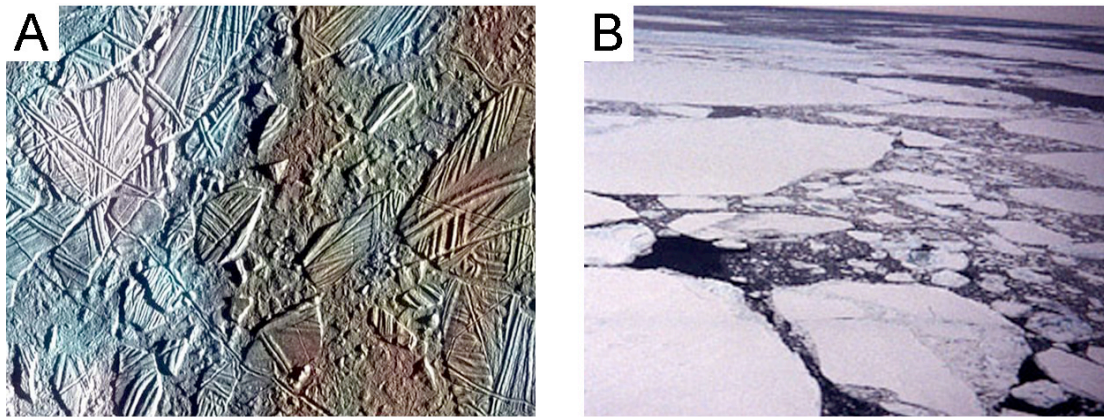


**Figure 7.2:** A) False-colour Galileo image of the Conamara Chaos region at 8°N, 274°W, Europa. The brown areas mark hydrated salts, the whitest/bluest areas represent purer ice. B) Image of Ice rafting on Earth.

The spectral properties of Europa's high-albedo regions indicate a surface of nearly pure water ice (Greeley, 1999). This white surface is interlaced by numerous low-albedo deposits (see Figure 7.2A). Near infra-red spectroscopy of these dark areas is consistent with the presence of hydrated salts such as Epsomite, plausibly formed from the evaporation of brines after "recent" extrusion at ridges and cryovolcanic domes (McCord *et al.*, 1998). These suspected brine deposits suggest that liquid from the sub-surface ocean or other brine-rich reservoir has reached the surface in the geologically recent past (McCord *et al.*, 1998).

Images from Voyager and Galileo revealed a low number of impact craters on Europa suggesting that the surface ice is geologically young (~ 30 Ma; Zahnle *et al.*, 1998) and subject to more efficient resurfacing than the other icy Galilean satellites. This resurfacing is expected to be ongoing, involving cryovolcanic and tectonic processes (Lucchitta and Soderblom, 1982).

### 7.1.2. The Importance of Ice Thickness - Implications for Astrobiology

Independent of background, most people hold an interest in the possibility of life elsewhere in the universe. While laymen anticipate the detection of 'advanced', humanoid life, it is unlikely compared to the discovery of lower forms (single prokaryotic cells, etc). After all, it took 4.4 billion years for the Earth to produce anything more complex than a jellyfish! Because of this, many argue that the synthesis of nucleic acids, the building-blocks of DNA, is a complicated and easily retarded process (Kutter, 1987). However, records of early life show its emergence as soon as conditions became receptive to its presence. This suggests to

some that single celled 'life' will spontaneously arise wherever three ingredients for life exist (Chyba *et al.*, 2000).

1. A source of raw materials (principally organic molecules)
2. A source of energy (to power its metabolism)
3. A liquid medium to facilitate chemical reactions (probably water)

Although other elements (silicon) and fluids have been researched, the combination of carbon-based life and H<sub>2</sub>O appears to be the most robust (Kutter, 1987). This reduces the Search for Life to the Search for 'Life as we know it'. This in turn can be simplified to the search for liquid water. The presence of a sub-surface liquid layer on Europa therefore makes the satellite of significant astrobiological interest.

In addition to the presence of liquid water, a nutrient and energy source is needed for life to have formed in Europa's ocean. Radiogenic heating and dissipation of Europa's tidal heat in its deep interior may result in ocean floor hydrothermal activity, providing theoretical indigenous life with a necessary source of energy and raw materials.

It is known from studies of ecosystems surrounding hydrothermal vents on Earth that vent communities are not entirely independent of the surface (Kutter, 1987). Nutrient and energy transfer over long time scales between the ocean surface and floor still plays a vital role, suggesting that a similar link might be necessary on Europa.

Intense radiation at the surface of the satellite produces oxygen via the dissociation of water ice (Cooper *et al.*, 2001). H<sub>2</sub> escapes, leaving the oxygen trapped in a thin (10<sup>-11</sup> bar) O<sub>2</sub> atmosphere, while some oxygen and related oxidants (OH, H<sub>2</sub>O<sub>2</sub>) may get trapped in the ice (Chyba, 2000). Moreover, irradiation of the surface may also produce organic molecules given that CO<sub>2</sub> is present. Once trapped in the ice, convective overturn could transport the oxidants and organics to the ocean below making them available for chemosynthetic redox reactions (Chyba, 2000). The development of indigenous life on Europa is therefore considered possible if Europa's upper-ice layer experiences convective overturn (Gaidos *et al.*, 1999).

Estimates by McKinnon (1999) have shown that an ice shell of < 10km would be susceptible to solid state convection and overturn, making the presence of life a possibility if the ice shell is thin. A thick, stagnant crust would conversely make transfer of nutrients unlikely and thus halt the development of any indigenous life (Gaidos *et al.*, 1999). The determination of Europa's crustal thickness is therefore an important exobiological issue and remains one of the controversial topics of planetary science.

## **7.2. How Thick is Europa's Crust?**

Many attempts have been made to estimate the thickness of Europa's crust using a variety of techniques including gravitational and magnetic anomalies, and study of the visco-elastic relaxation of topographic features. The estimates produced using the different methods are summarised in Table 7.1. The separate methods are outlined briefly in this section so that current estimates can later be compared to the estimate gained from this work

### **7.2.1. Estimates from Gravity and Magnetic Data**

The first "look" into Europa's interior was provided by Galileo gravity measurements, which were interpreted as indicating a differentiated body. Combined with cosmochemical models, an H<sub>2</sub>O crust of 80-170 km thick, overlying a silicate mantle and iron core was suggested (Anderson *et al.*, 1998). However, due to the similar densities of water and ice, the state of this H<sub>2</sub>O layer could not be determined using gravitational data alone. Magnetic anomaly data from the same mission was used to further constrain this value. The orbit of Europa was noted to cause perturbations in the Jovian magnetic field, indicating that the satellite had a magnetic field of its own. However, the observed field at Europa was noted to be highly non-dipolar in nature and vary with time, suggesting that the magnetic field was not created as a result of a constant process internal to the moon itself and was more likely the consequence of electromagnetic induction (Kivelson *et al.*, 1997). The passage of satellites through a planetary magnetic field during the course of an orbit causes electromagnetic induction to occur in any conductive materials within the satellite (Colburn and Reynolds, 1985). The strength of an induced magnetic field can be used to infer the properties of the conductive layer. The large-scale magnetic perturbations recorded by Galileo flybys were consistent with an induced field created by a perfectly conducting sphere (Kivelson *et al.*, 1997).

The Galileo magnetometer measurements recorded during Europa flybys were consistent with the magnitude, orientation and structure predicted for electrical currents flowing in a salty ocean by Kargel and Consolmagno (1996). As Jupiter's magnetic field is tilted with respect to its rotation axis, the satellites orbiting in the equatorial plane experience a magnetic field strength that varies periodically (Kivelson *et al.*, 1997). The strength of Europa's induced field could be investigated over a range of primary (Jupiter's) field strengths. Zimmer *et al.* (2000) refined this information to infer a high conductivity region (conductivity  $> 0.06 \text{ Sm}^{-1}$ ) at a depth of  $< 200 \text{ km}$ . The thickness of the brine ocean is estimated to be around 100 km deep (Kivelson *et al.*, 1997; Khurana *et al.*, 1998). If the ocean was thinner than a few tens of kilometres, or was less salty, it would not conduct enough current to explain the observed magnetic signature (Kargel *et al.*, 2000).

### 7.2.2. Estimates from Heat Flow Data and Visco-Elastic Deformation

The interiors of planetary bodies are heated by a variety of processes as outlined by Pater and Lissauer (2001). Internally generated heat is transported to the surface of Europa through the ice shell, perhaps melting it at depth. The thickness of the ice shell is therefore dependant on the crustal heat flow. As Europa cools and the number of impacts decrease, crustal heat flow will decrease (Pater and Lissauer, 2001), allowing the ice shell to thicken. However, the thermal gradient governing the depth of the European ocean is created primarily by tidal heating of the moon's interior. Hussmann *et al.* (2002) calculated the ice shell thickness and ocean depth for steady state models of tidal dissipation in Europa's ice shell. Their models have surface heat flows of  $\sim 20 \text{ mWm}^{-2}$ , corresponding to an ice thickness of  $\sim 30 \text{ km}$  above an ocean of at least 100 km depth.

As a result of the 1:2:4 Laplace resonance between Io, Europa and Ganymede, the tidal forces influencing each of these satellites changes periodically. This alters the amount of tidal heat dissipated in Europa's interior, affecting heat flow and thus the thickness of the ice shell, causing it to oscillate about a mean point (Sotin and Tobie, 2004). Hussmann and Spohn (2004) used thermal orbital evolution models to determine Europa's ice thickness as a function of time (Figure 7.3). Their results suggested that Europa's crust is currently 30 km thick and varies between 10 and 40 km on a period of approximately 200 Ma.

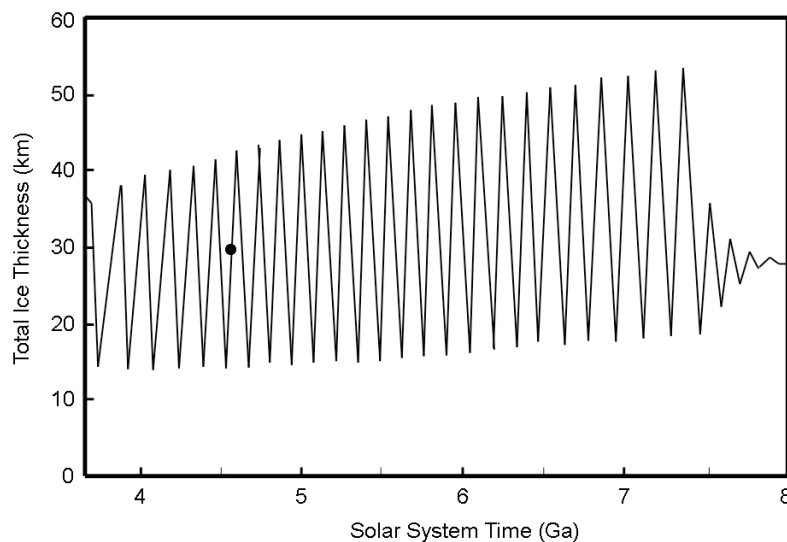


**Figure 7.3:** Ice thickness variation over time, since Europa's entrance into the orbital resonance with Io and Ganymede. Figure from Hussmann and Spohn (2004). The presented model takes account of primordial and radiogenic heat sources, and the tidal energy dissipation within Europa's ice layer. Current conditions are marked with a closed circle. The Laplace resonance is predicted to break down at  $\sim 7.5 \text{ Ga}$ , reducing the amount of tidally generated heat within Io, Europa and Ganymede.

**Table 7.1: Summary of Crustal Thickness Estimates**

Method of Estimation	Thickness Estimate
Gravity	H <sub>2</sub> O (liquid and ice) crust of 80-170 km
Magnetic anomaly data	< 200 km
Tidal dissipation and heat flow	30 ± 20 km
Visco-elastic relaxation of topography	25 ± 10 km
Impact Crater Morphology	3 to 25 km
Cycloidal ridges	~ 1 km
Diapirs	3 to 30 km

Estimates of ice thickness based on analysis of specific surface features apply only to the age of the diagnostic feature. For example, an impact crater of 10 Ma will reflect the crustal conditions at 10 Ma only. However, the role of tidal heating in maintaining Europa's ocean has been used to suggest that ice thickness estimates from the earliest geologic evidence may not deviate significantly from estimates based on more recent features (Sotin and Tobie, 2004).

In addition to controlling the crustal thickness, heat flow is the primary factor in Europa's efficient visco-elastic relaxation of surface features. This is a process by which vertical features return to isostatic equilibrium due to the relaxation of the topography; and is particularly effective on the icy satellites. This is reflected by Europa having one of the smoothest bodies in the solar system, with topographic maxima of ~ 900 m. As presented in Section 1.2.4, it was found by Parnetier and Head (1981) that relaxation time of topographic features on differentiated icy satellites is a function of their wavelength (height above the primary crust level), allowing the largest structures to relax fastest. By calculating an approximate time over which the topography of surface features has relaxed, assumptions can be made about heat flow and thus the crustal thickness. However, this approach can only produce thickness estimates for the elastic portion of the ice shell. Current estimates via this method predict an ocean at a depth of ~ 25 km, assuming a uniform global ice thickness.

### 7.2.3. Rafts, Diapirs and Cycloidal Patterns

The presence of ice rafts, domes and cycloids on Europa indicate a thinner crust than that estimated by the methods outlined above. Figure 7.2A shows a section of the Conamara Chaos region on Europa. The morphology of the surface ice in this and other 'chaos' regions is reminiscent of 'rafting' and cracking of ice blocks over a liquid substrate on Earth (Figure 7.2B). Terrestrial ice rafting occurs when a sheet of ice overlies a water layer. Movement in the water layer stresses the ice, eventually breaking it into discrete blocks. Comparable ice

morphology on Europa has been used to suggest that, during the formation of these chaos regions, a liquid reservoir may have persisted at less than 1 km depth (Geissler, 2004).

Cycloids (Figure 7.4) are long chains of curved ridges formed in response to stresses in the crust. Fractures propagate perpendicular to the local direction of stress (Hoppa et al., 1999). Because of the diurnal changes in tidal stress on Europa, fracture growth occurs across an ever-changing stress field creating a curving propagation path. Evidence of lateral motion, dilation, and strike-slip motion on these cracks suggests that they penetrate down to a low-viscosity layer (Pappalardo and Sullivan, 1996). Hoppa et al. (1999) used tidal stress and ice strength estimates to infer the maximum vertical penetration of the cycloid cracks, assuming their termination depth to correspond to a 'low viscosity layer' at a depth of  $\sim 1$  km.



**Figure 7.4:** Cycloidal double ridges viewed in the northern hemisphere of Europa. The impact crater central to the image is 'Maeve', a 21.6 km crater at 59.2N 77.5W. Image from Hoppa et al. (1999).

Domes formed by upwelling diapirs (warm, buoyant ice masses) in convecting ice also support the idea of a thin European crust. Domes were interpreted by Pappalardo *et al.* (1998) to have formed in a crust as thin as 3 km. However, uncertainty surrounds the formation of these features as Hussmann and Spohn (2004) predict their formation in an ice crust of 30 km.

#### 7.2.4. The Role of Impact Craters in Determining Ice Thickness

There are 28 confirmed primary impact structures on Europa between 4 and 50 km in diameter (Moore *et al.*, 2001). The depth and diameter of these and smaller European craters has been recorded by Schenk (2002) on the basis of Voyager and Galileo topography, and detailed analysis of crater morphology and secondary distribution undertaken by Moore *et al.* (2001), Moore *et al.* (1998).

The use of impact cratering to infer crustal structure on the icy moons is two-fold. The topography provided by the crater rim and any central feature can be considered in terms of viscous relaxation, as described in 7.2.2 (Nimmo *et al.*, 2003). The topography of the ‘Cilix’ crater is shown for example in Figure 7.5. The morphological trend of impact craters on a planetary body can also provide insight into its crustal structure and composition, as

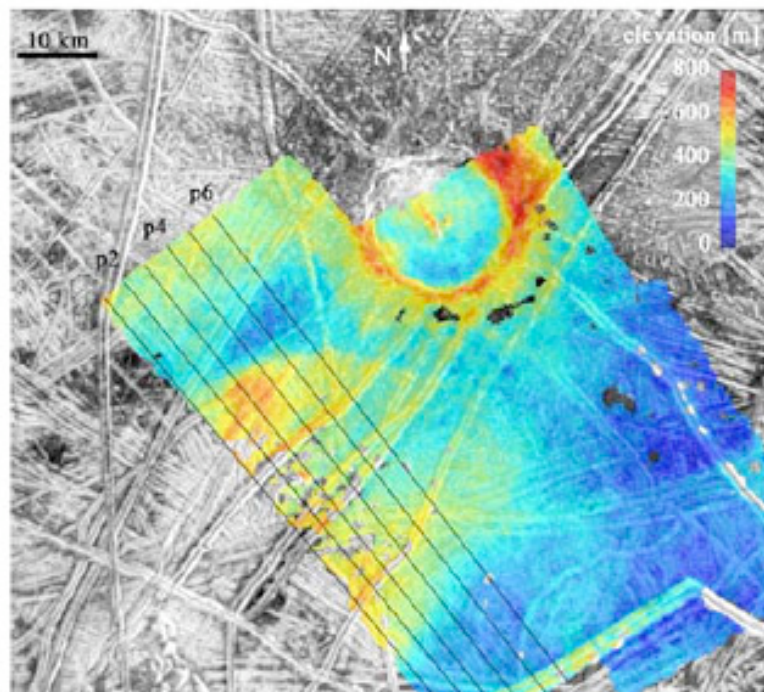


**Figure 7.5:** Galileo image of Cilix crater and surroundings, with superimposed stereo-derived topography (colour). Figure from Nimmo *et al.*, 2003. P2, P4 and P6 mark lines along which Nimmo *et al.* (2003) created topographic profiles.

explained in Chapter 2. The second method of estimating crustal thickness from impact craters uses this link to infer the local rheological conditions at the time of impact. This involves the computer simulation of impact into of different ice thicknesses, and comparison of the modelled and observed craters.

Previous investigations into the crustal structure of Europa using impact craters show mixed results, but all conclude an average ice thickness of less than 19 - 25 km (Schenk, 2002). A lower bound of 3 to 4 km was defined by Turtle and Pierazzo (2001) based on numerical modelling of central peak crater formation. As central peaks on the terrestrial planets are comprised of uplifted competent material uplifted from depth, the existence of central peaks on Europa requires the ice layer to be sufficiently thick that the impacts forming the craters do not fully penetrate it. Turtle and Pierazzo (2001) investigated the depths to which full melting of the target material occurred for a range of shock pressures and target heat flows and found that the melt region produced in the formation of Europa's largest central peak crater (Pwyll,  $D \sim 20$  km) can penetrate to 4 km depth.

Bray et al. (2006) performed numerical simulations of impact into layered ice and water targets, comparing the depth and diameter of the produced craters to the European cratering trend. A range of ice thicknesses were investigated using the same method outlined in Section 7.3, but utilising an earlier strength model for pure ice. Bray et al. (2006) found the most suitable ice depth to explain the general depth-diameter trend of craters on Europa to be 8 km.

### 7.2.5 The Nature of Europa's Upper Layers

The precise thickness of Europa's ice shell is a contentious issue, with estimates ranging from 1 to 30 km or more. The nature of heat transfer within the ice shell is another unknown in this debate, and can lead to different crustal thickness estimates based on whether a conductive or convective regime is assumed to predominate (Figure 7.6). Simple conductive models generally accompany estimates of a thick stagnant ice crust above a liquid water layer (Figure 7.6A). The heat flow,  $Q$ , in these scenarios can be estimated simply by considering the difference in surface temperature and melting temperature (assumed to be reached at the bottom of the ice crust),  $\Delta T$  over the theoretical crust thickness,  $d$ :

$$Q = \frac{k\Delta T}{d}, \quad (7.1)$$

where  $k$  is the thermal conductivity of ice. The thermal conductivity of ice varies with the inverse of temperature as defined by Klinger (1980):

$$k = \frac{567}{T}. \quad (7.2)$$

More complex structural models include a thinner conducting ice crust above a layer of convecting ‘slush’ (Figure 7.6C). Nimmo and Manga (2002) investigated the creation of lenticulae (dome-shaped uplift features) on Europa’s surface that are thought to be caused by temperature-dependent convection. They estimated that the strongly temperature-dependent convection necessary to form these < 4 km diameter domes on Europa requires a stagnant conductive ‘lid’ of < 5 km depth on top of an otherwise iso-viscous convecting ice layer. Such an upper lid thickness implies a minimum crustal heat flow of 90 mW m<sup>-2</sup>. The speed of convection, and hence the transferred heat flow and thickness of the upper conducting section of the crust, is controlled by the grain size and basal temperature of the convecting material among other factors (See Ruiz et al. (2007) for further information).

### **7.3 Approach to Modelling Impact into Europa**

Europa and Ganymede have bulk densities of 3.0 g cm<sup>-3</sup> and 1.9 g cm<sup>-3</sup> respectively, but their gravitational attractions are similar at 1.33 m s<sup>-2</sup> and 1.43 m s<sup>-2</sup>, as Europa is smaller (Johnson, 1999). As the high albedo and spectral properties of Europa and Ganymede suggest surface

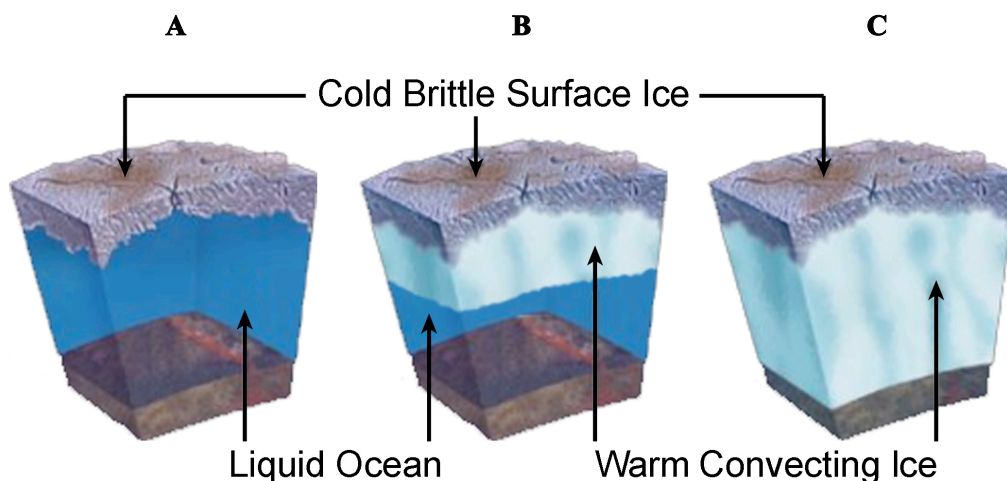


**Figure 7.6:** Simplified illustrations of the theoretical structure and state of Europa’s H<sub>2</sub>O layer above a silicate mantle. A) Brittle conducting ice shell above water. B) Conductive ice shell above warmer convecting ice, ice melts entirely at depth to transition into a liquid water ocean. C) Warm convecting ice beneath a conducting brittle ice lid.; the ice never reaches melting point.

compositions of nearly pure water ice (Greeley, 1999), comparison of craters on these bodies may be used specifically to infer differences in crustal structure (Schenk, 2002). It is also reasonable that the same strength model for pure ice, as derived for Ganymede, can be applied when modelling smaller crater sizes on Europa which have not been affected by the proximity of the sub-surface ocean.

The strength model for ice derived in Chapter 6 has been used to recreate the amount of target weakening caused by impacts of different sizes in pure unlayered ice, using Ganymede as a test case. This strength model was applied to layered ice and water targets and used to produce an estimate of Europa's crustal thickness that is more reliable than previous values (e.g. Bray et al., 2006). As presented in the previous chapters, this work used the iSALE hydrocode (introduced in Chapter 4) to simulate impact crater formation in H<sub>2</sub>O ice.

### 7.3.1. Target Set-Up - Introduction of a Material Layer

The structure of the target was approximated with an ice sheet of uniform thickness above a liquid water substrate to maintain simplicity and avoid the non-uniqueness introduced by the inclusion of more material layers. Figure 7.7 shows a typical mesh used in this suite of simulations including an ice thickness of 5 km.

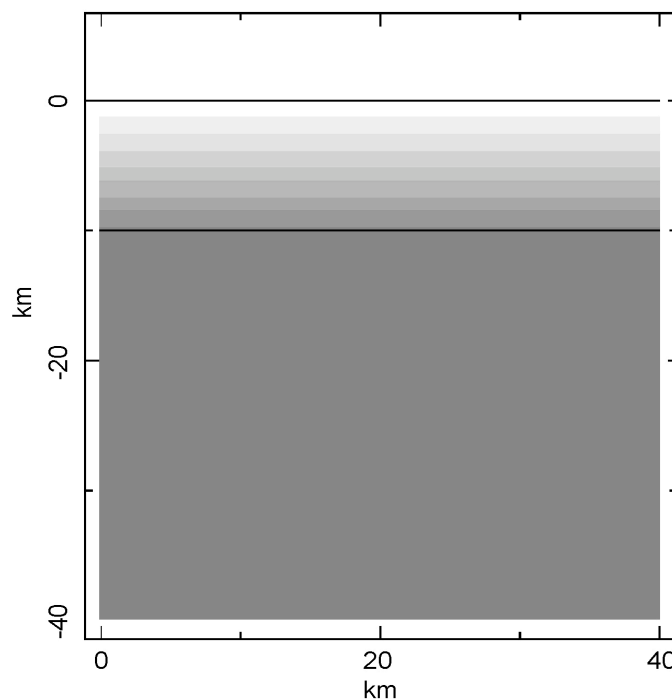


**Figure 7.7:** Example mesh used for the simulations presented in this chapter; the ice-water boundary is set to 10 km depth. The shaded contours within the upper layer (ice) show the gradual decrease in yield strength to 0MPa at the ice-water boundary.

A sharp discontinuity between solid ice and liquid water is considered to be unrealistic, as we would expect the target ice to become weaker with increasing depth as temperature increases. For each ice thickness a heat flow ( $Q$ ) was calculated assuming a constant density of  $910 \text{ kg m}^{-3}$  and thermal conductivity ( $k$ ) of  $3 \text{ J m}^{-1} \text{ s}^{-2}$ . This value of  $k$  was determined by using Equation 7.2 and averaging the surface temperature ( $T_s = 100$  to  $120 \text{ K}$ ) and melting temperature ( $T_m = 255$  to  $273 \text{ K}$  for pressures less than  $200 \text{ MPa}$ ) to obtain a simplistic average temperature for Europa's ice shell of  $\sim 180 \text{ K}$ . For the larger ice crust depths it was also necessary to incorporate the change in melting temperature with pressure beneath the ice layer. These values are included in Table 8.1.

Initial simulations employed ice thicknesses from  $5$  to  $40 \text{ km}$  in  $5 \text{ km}$  intervals and the results were compared to observational data as outlined in Section 7.3.3. The most suitable ice thickness from these simulations was selected and additional simulations performed varying the ice thickness by smaller increments to further refine the value.

**Table 7.2: Calculation of Target Heat Flow for Different Crustal Thicknesses**

Ice Depth, $d$ (km)	Pressure at Ice Base, $P$ (MPa) *	Melting Temperature of Ice at Pressure $P$ (K) **	Heat Flow ( $\text{mW m}^{-2}$ ) ***
1	1.21	272.9	519
2	2.42	272.7	259
3	3.63	272.6	173
4	4.84	272.5	129
5	6.051	272.4	103
6	7.26	272.2	86.1
7	8.47	272.1	73.8
8	9.68	272.0	64.5
9	10.89	271.9	57.3
10	12.10	271.7	51.5
15	18.15	271.1	34.2
20	24.21	270.5	25.6
25	30.26	269.8	20.4
30	36.31	269.2	16.9
35	42.36	268.6	14.5
40	48.41	267.9	12.6

\*  $P = \rho g d$  (Assuming  $\rho = 910 \text{ kg m}^{-3}$  and  $g = 1.33 \text{ ms}^{-2}$ )

\*\*  $T_m = 273 + (252 - 273)(P/200,000,000)$  for pressures greater less than  $200 \text{ MPa}$

\*\*\* From Equation 7.1

### 7.3.2 Material Properties for Impactor and Target

To allow the direct application of the strength model scaling derived in Chapter 6, the projectile used for simulations of impact into Europa was modelled as a pure water-ice sphere with an impact velocity of  $15 \text{ km s}^{-1}$ . The upper target layer was also modelled as pure water ice and its thermodynamic response approximated using the Tillotson EOS for ice Ih (Ivanov et al., 2002).

The static strength model for ice employed in iSALE was derived from low temperature ( $77 \text{ °K}$ ), high-pressure laboratory data (Durham et al., 1983; Beeman et al., 1988; Rist and Murrell, 1994; Weiss and Schulson, 1995) as presented in Chapter 4. Acoustic fluidization was implemented through the incorporation of the block model to recreate the additional material weakening during impact. The block model parameters ( $\eta$  and  $\tau_v$ ) controlling the amount and longevity of target weakening for each simulated crater size were calculated according to the strength model scaling derived in Chapter 6 (see Equations 6.1 and 6.2).

The material properties for water used by Turtle and Pierazzo (2001) were employed for the simulations involving water in this work. The Tillotson equation of state (EoS) characterises material with a condensed regime and a vapour regime, but does not include a true liquid state, making it unsuitable for simulation of water. The ANEOS equation of state tables from Thompson and Lauson (1972) provide a more reliable approximation of the thermodynamic response of water. However, as ANEOS cannot handle the solid-liquid transition of  $\text{H}_2\text{O}$  (Turtle and Pierazzo, 2001), application of the ANEOS was limited to the water layer, while use of the Tillotson EoS was continued for thermodynamic representation of the ice. This was also necessary to enable the same strength model for ice to be applied as variation in EoS was shown to influence central crater morphology (Section 5.3.2).

### 7.3.3. Comparison to Observations

The simulations presented in Chapter 5 produced craters between 3.5 and 17.5 km on Ganymede. Craters of these diameters are deemed small enough to be relatively unaffected by the additional weakening influence of the satellite's sub-surface ocean (c.f. Schenk, 2002), thus approximating impact into pure, unlayered ice. On Europa, the sub-surface ocean is closer to the satellite's surface than Ganymede; the crater diameter above which crater morphology is likely to be affected by the presence of the ocean is smaller ( $D \sim 8 \text{ km}$ ). A suite of simulations modelling the impact of a 310 m projectile into ice layers of different thickness above liquid water layer were performed, creating a series of  $\sim 14 \text{ km}$  diameter craters with various depths and internal morphologies. The results from this suite of simulations were compared to observational data for European craters so that the most suitable range of ice depths could be determined.

The heat flow and upper crustal thickness of Europa is hypothesised to vary with time and latitude (e.g. Hussmann and Spohn, 2004). The different impact craters on its surface may thus have formed in a range of crustal conditions. Modelling the morphology of an individual impact crater can only provide insight into the possible crustal conditions prevalent at the time of that specific impact. Consequently, modelled craters were compared to depth-diameter measurements of European craters from Schenk (2002) to produce an estimate of mean crustal thickness, averaged over the satellite's global area and recorded geological history. Once the best-fit ice depth was established for a ~ 14 km crater, impacts of different sizes were simulated and the depth-diameter ( $d/D$ ) of the created craters compared to the  $d/D$  trend for Europa.

## **7.4 Results**

### **7.4.1 Simulation of a ~ 14 km Crater on Europa**

The impact of a 620 m diameter projectile was simulated into ices of different thickness from 1 to 40 km. The profiles of impacts into 3 to 8 km ice thicknesses are presented in Figure 7.8. The depth and diameter of these and other profiles were measured and plotted alongside observational data for Europa from Schenk (2002) in Figure 7.9.

An impact of this size into ice thicknesses of 1 and 2 km resulted in full crustal breach, and the crater cavity was filled in completely. Consequently the results from these simulations were not included in Figures 7.8 and 7.9. For ice thicknesses greater than 2 km, crater morphology was maintained (Figure 7.8). The craters formed in ice depths of 3 and 4 km are shown in Figure 7.8A and B respectively. In both cases, the transient cavity intersected the sub-surface ocean allowing water to well up at the crater centre. The ice thickness in these simulations was sufficient for crater rims and some internal topography to be maintained 700 seconds after impact. The morphology shown in Figure 7.8A and B includes internal features reminiscent of peak-rings; this type of morphology is not expected for this diameter of crater on Europa. Figure 7.9 shows that both these craters are shallower than expected for a 14 km crater on Europa.

Simulated impact of a 620 m projectile into an ice thickness of 5 km produces a central peak crater with a suitable depth-diameter ratio for a crater of this size on Europa (Figure 7.9). The central peak has a diameter of ~ 5 km, approximately one third of the crater diameter. Impact into ice thicknesses above 5 km produces simple craters that are up to 200% deeper than expected for European craters of the same diameter (Figures 7.8D, E, F and

7.9). The morphology and the depth of craters formed by impact into ice thicknesses above 6 km does not vary significantly and can be represented by one data point in Figure 7.9.

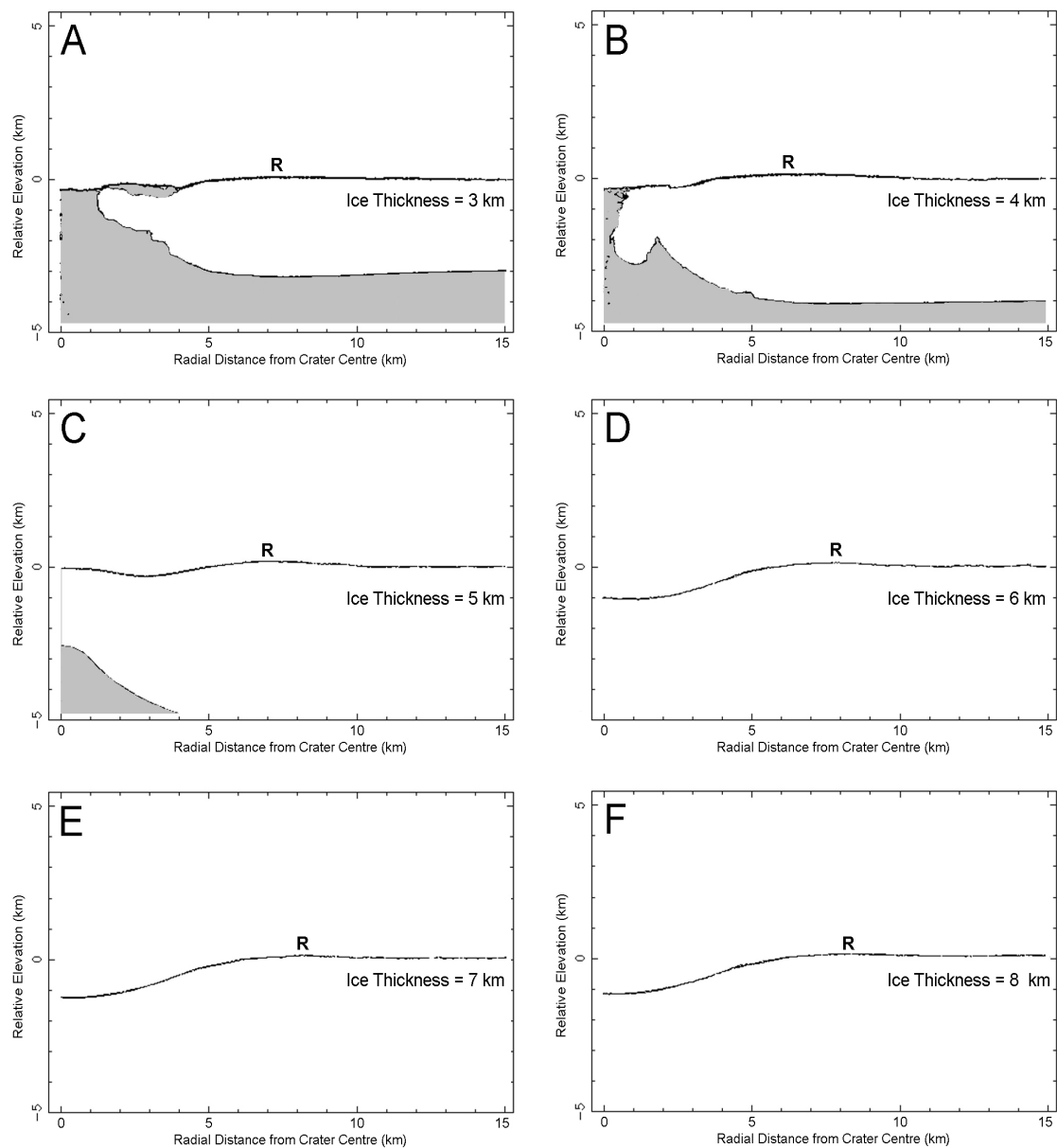


**Figure 7.8:** Radial profiles of craters produced by simulated impact into ice layers of various depths. Ice thickness is noted in each case and the approximate location of the crater rims marked with 'R'. Water is shaded grey. A similar progression in crater morphology with increasing ice thickness is shown in Turtle and Pierazzo (2001).

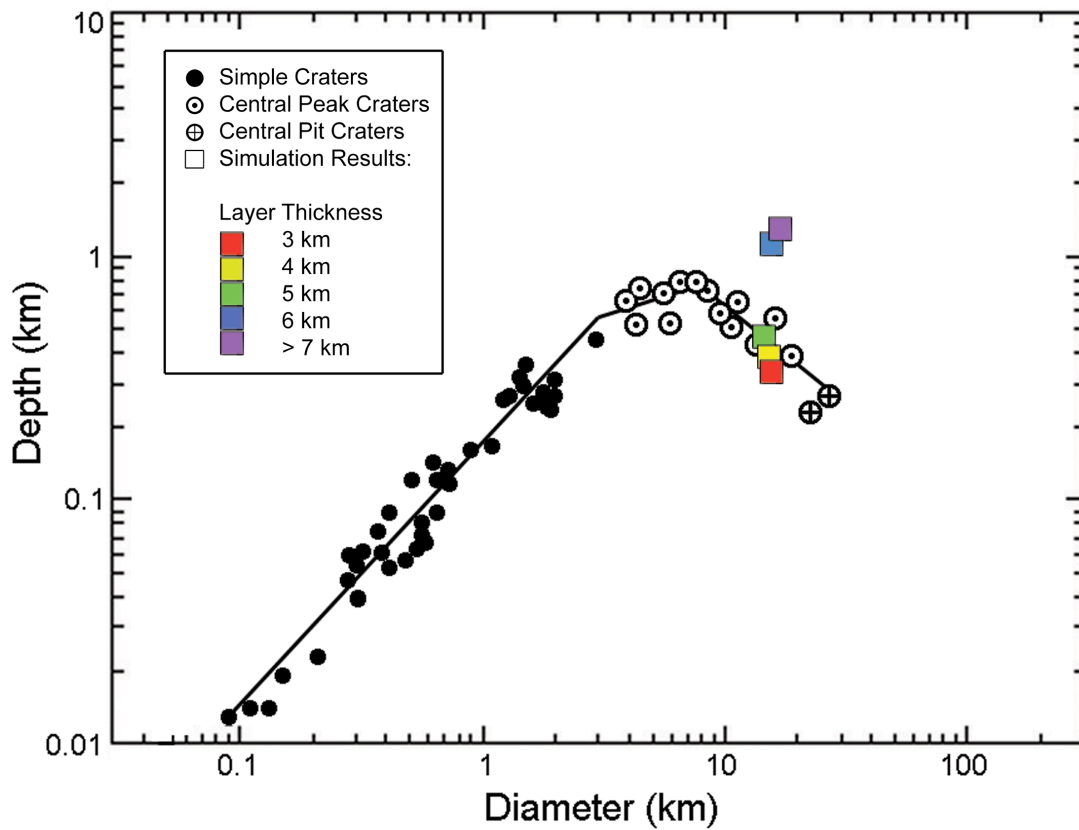


**Figure 7.9:** Depth and diameter of modelled craters, compared to observed  $d/D$  trend for Europa. The depth and diameter of simple and complex craters on Europa are marked with different data points and the general trends, as assigned by Schenk (2002), marked with black lines. Simulation results are marked with squares. As the same crater depth and morphology was produced by impact into ice thickness of 7 to 40 km, these results are marked with a single data point.

#### 7.4.2 Comparison to the European Cratering Trend

As the only suitable morphology and depth of crater was produced using a layer thickness of 5 km, this value was also used when simulating craters of different diameter on Europa between 1 and 40 km. A summary of this suite of simulations is presented in Table 7.3. The depth and diameter of the simulated craters were measured and compared to the  $d/D$  trend of Europa in Figure 7.10.

The simple-to-complex transition was recreated using the Ganymede-based strength model, although the simple crater was shallower than the main trend for simple craters on Europa. The impact of a 70 m and 150 m diameter projectile produced two central peak craters with diameters of 3.7 and 7.1 km respectively. Both craters have depths within the observed range for craters of this size on Europa. Although these central peak craters are slightly shallower than the main trend line in Figure 7.10, the increase in depth with increasing crater diameter is comparable to the observed trend.

**Table 7.3: Depth-Diameter Measurement of Simulated Craters**

Projectile Radius (km)	Final Crater Diameter (km)	Final Crater Depth (km)	Comments
0.025	1.8	0.2	Simple crater. Approximately the same $d/D$ ratio as Ganymede simulations of this size.
0.07	3.7	0.5	Central peak. Same peak formation mechanism as Ganymede simulations. Shallower than Ganymede simulated crater.
0.15	7.1	0.61	As above
0.3	14.3	0.48	Central peak. Same peak formation mechanism as Ganymede simulations. Significantly shallower than Ganymede simulated craters of this diameter.
0.495	--	--	Crustal breach. Multiple oscillations of a completely fluid central region produce several 'ejecta' layers. Crater cavity and internal morphology not maintained.
0.675	--	--	As above.

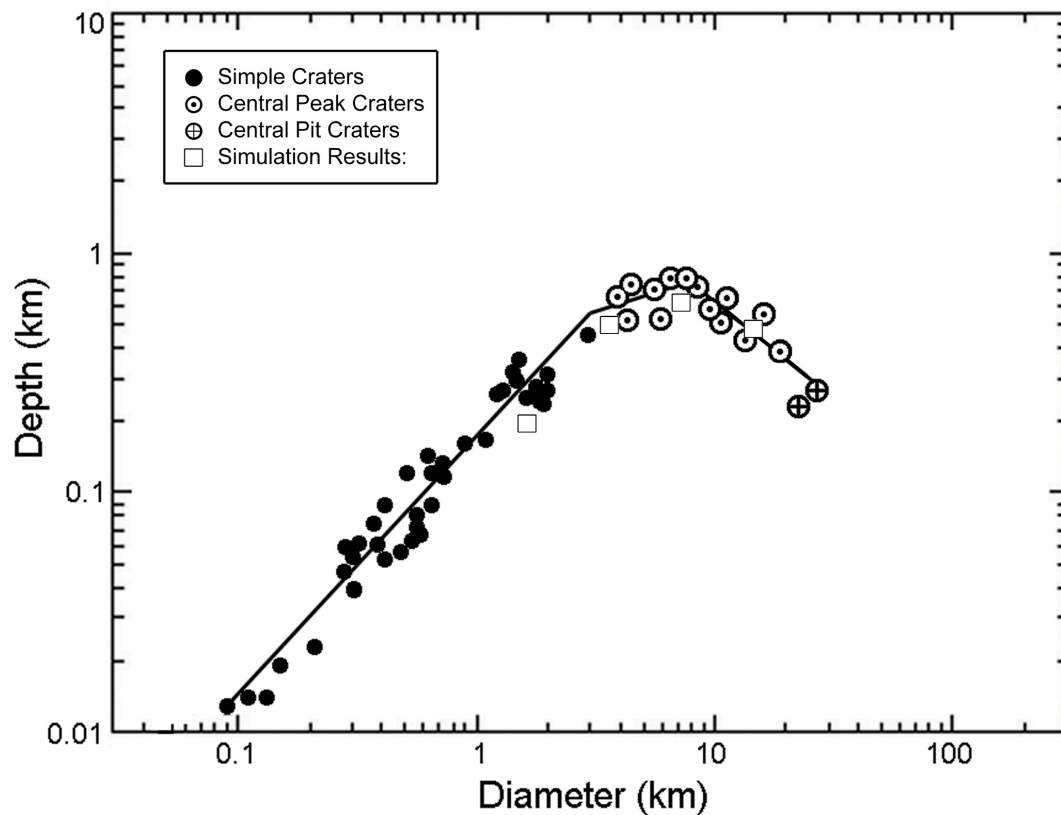


**Figure 7.10:** Depth and diameter measurement of simulation results compared to Schenk's 2002 observations. Simulation results for the largest impacts are not included on the plot as these crater cavities were infilled, preventing a depth and diameter from being obtained.

The  $\sim 14$  km central peak crater produced using this ice thickness is 20% shallower than the 7 km crater, recreating the observed change in  $d/D$  trend at crater diameters of  $\sim 8$  km. Simulated craters larger than 14 km in diameter were not included in Figure 7.10 as the cavities were filled in by upwelling water from the exposed sub-surface oceans.

## **7.5 Summary and Implications**

### **7.5.1 How Thick is Europa's Crust?**

After simulating impact into different thicknesses of ice above a liquid water substrate, the morphology of a 14 km crater on Europa was only successfully reproduced using an ice thickness of 5 km and a corresponding heat flow of  $\sim 100$  mW m<sup>-2</sup> (Figure 7.9). Impact into smaller ice thicknesses resulted in overly shallow craters with an internal morphology reminiscent of peak-rings or central pits (Figure 7.8A and B). This is an understandable result when considering craters with diameters larger than  $\sim 26$  km on Ganymede. Both the low depth-diameter ratios relative to smaller craters, and the presence of central pits in these large craters, have previously been explained by impact into a layered ice crust (e.g. Greeley et al., 1982). As the thickness of the ice crust increases, the minimum size of crater affected by the presence of a sub-surface ocean increases. The produced morphologies in Figure 7.8A and B demonstrate that (at least within the computer models) impact into a thin enough crust can produce a relatively shallow crater with a central pit morphology.

Formation of a 14 km crater in ice thicknesses above 5 km (up to and including 40 km thickness) produced a series of simple craters with a depth-diameter ratio that remains near constant after ice thickness exceeds 7 km (Figure 7.8D-F, 7.9). It is reasonable that the depth of these craters remain constant as, once the ice becomes thick enough for crater morphology to be unaffected by the weakening influence of a sub-surface ocean, both the depth and the morphology should remain unchanged and approximate the results of the same simulated impact into unlayered ice.

However, the lack of central peaks in these simulated craters is not an intuitive result as craters of this size simulated in unlayered ice (Chapter 6) maintained their central peak morphology. If the Ganymede-based strength model derived in Chapter 6 can be directly applied to cratering on Europa, 14 km diameter craters produced in the thickest ice depth (40 km) are expected to form similar craters to those produced in unlayered ice. As this is not the case it suggests that the target properties required to produce a 14 km crater on Ganymede may differ from those necessary to recreate the same crater size on Europa. This may suggest the need for different static strength, Acoustic Fluidization parameters for Europa and

Ganymede surface ice, or may indicate the incorrect application of heat flow and target layering in the final suite of simulations.

### 7.5.2 ...5km ...Really?

The  $d/D$  trend of European craters between 1.8 and 14.3 km in diameter can be simulated using the Ganymede-based Block Model scaling trend for ice strength presented in Chapter 6, combined with an additional target heat flow of  $103 \text{ mW m}^{-2}$  and a water layer at 5 km depth. The simple-to-complex transition and the 'roll over' in  $d/D$  values noted to occur at crater diameters of  $\sim 8$  km (Schenk, 2002) have been reproduced (Figure 7.10).

Although craters simulated using an ice thickness of 5 km display the correct morphology, the craters with diameters smaller than 14 km are consistently shallower than the main trend line for European craters. This suggests that the target material in these simulations may be too weak. As the 14.3 km crater has the correct  $d/D$  ratio and the 1.8, 3.7 and 7.1 km diameter craters are all shallower than the main trend, it suggests that the relatively shallow depths are not due to the weakening influence of the sub-surface ocean. To better recreate the observed trend in crater depths, the amount of Acoustic Fluidization could be reduced, or the static strength of the surface ice increased.

### 7.5.3. Comparison to Other Thickness Estimates

Estimates of ice layer thickness from the various techniques outlined in section 7.2 range from 1 km to 50 km. An estimate from this work of  $\sim 5$  km is within this range and similar to the minimum estimate of Turtle and Pierazzo (2001) which was also derived on the basis of numerical modelling. Ice thickness estimates below 10 km in depth fall into the category of 'thin-shelled' and suggest that convective overturn of the surface ice may be occur or have occurred on Europa, making the development of indigenous life a possibility.

However, comparison of this work and that of Bray et al. (2006) demonstrates that different strength models for water ice can change crustal thickness estimates by 3 km (5 km relative to 8 km estimate from Bray et al., 2006), limiting confidence in the accuracy of these results at this stage. Furthermore, it is apparent from this work that the strength model for Ganymede derived in Chapter 6 requires alteration before it can be reliably applied to cratering on Europa. This is discussed in the final chapter.

# Chapter 8

## Conclusions

The possible existence of liquid water beneath the ice crusts of Ganymede and Europa greatly increases the scientific interest in these bodies as the accessibility of these oceans has implications for astrobiology and future human exploration of the solar system. Study of the cratering trends on these bodies provides one means of assessing the depth of the ice layer above the sub-surface oceans.

The motivation behind this thesis was to develop a better understanding of crater mechanics in ice via observational analysis, and to further develop a strength model for pure H<sub>2</sub>O ice for use in the hydrocode simulation of impact on the icy satellites. This chapter will argue that the observational data presented in Chapters 2 and 3 of this thesis has allowed fuller investigation of the cratering process on Ganymede than was possible prior to the acquisition of topographic data. The implications of the observational work for pit and peak-ring formation are discussed and several avenues for future work explored.

The second component of this thesis utilised the observed cratering trends to better refine a strength model for ice (Chapters 4 to 6). This strength model was developed for pure, unlayered ice and employed in the hydrocode simulation of impact on Ganymede and then applied to Europa (Chapter 7). The success and limitations of this hydrocode strength model are summarised in this chapter, and its application for modelling impacts into Ganymede and Europa discussed.

## **8.1 Ganymede Observations**

Topographic profiles of 38 craters on Ganymede were collected using Galileo SSI data (Appendix A), providing information on feature height and slopes not previously available at Galileo resolution. This allowed the Ganymede crater scaling trends established on the basis of lower resolution Voyager data to be updated, and additional trends to be identified (Tables 2.2 and 3.1). The Ganymede trends were compared with data from other solar system bodies to examine the difference in cratering on rocky and icy surfaces. Conclusions drawn from this work are presented in this section.

### **8.1.1. Central Peaks Form Via Floor Uplift, Not Rim Collapse**

In addition to topographically expressed central features, complex craters also show more extensive rim-wall terraces than simple craters, attesting to the higher degree of rim collapse occurring in complex craters. Due to the lack of simple craters profiled in this work, the simple-to-complex (s-c) transition on Ganymede was not specifically investigated. However, trends in the crater rim height and central peak dimensions have allowed the difference in the onset of complex crater collapse on the Moon and Ganymede to be considered.

Similar rim heights of craters below  $\approx 12$  km in diameter on the Moon and Ganymede suggest that the collapse process in small craters is similar in rock and ice, despite the different crater types. Above this crater diameter rim heights on Ganymede decrease relative to lunar values, indicating progressively more collapse in larger Ganymede craters. The change of rim height trend at crater diameters of  $\approx 12$  km suggests that a strength threshold has been exceeded at this crater size which prompts more rigorous collapse of transient cavities.

The transition in rim heights at crater diameters of  $\approx 12$  km is separate from the s-c transition at crater diameters ( $D$ ) of  $\approx 2$  km. As the emergence of central peaks occurs before the inferred increase in rim collapse it suggests that the earlier s-c transition on Ganymede relative to the Moon may be the result of more pronounced floor rebound due to weaker material at depth, rather than weaker surface ice allowing the onset of rim collapse.

However, measurements of the rim heights of craters below 2 km in diameter are required before the order of this progression can be confirmed. Simple craters on other bodies can display significant terraces in the absence of central peaks, demonstrating that floor rebound does not necessarily occur prior to rim collapse in all target materials. Inclusion of rim height data for smaller craters on Ganymede may reveal an additional change in rim height trends in craters below 2 km in diameter.

Analysis of rim height trends for larger craters on Ganymede suggests a spatial and temporal control on the amount of crater rim collapse. The rim heights in larger Ganymede craters are highly variable, suggesting that the amount of collapse occurring in the formation of these different craters is dependent upon a factor other than transient cavity size. This could reflect a difference in crustal conditions at the time of impact.

### 8.1.2. Central Peaks Collapse to Form Peak-Rings, Even on the Icy Satellites

As crater diameter ( $D$ ) increases on the Moon, the diameter of central peaks ( $D_{cp}$ ) increases linearly ( $D_{cp} = 0.22 \left( \begin{smallmatrix} +0.03 \\ -0.02 \end{smallmatrix} \right) D$ ; Pike, 1985). As crater diameter continues to increase, central peak craters develop into peak-ring craters via the downward and outward collapse of unstable central uplifts, and possible collision with inwardly collapsing rim material (Alexopoulos and McKinnon, 1994; Morgan et al., 2000).

Central peaks on Ganymede are subtly wider than those on the Moon, ranging from 21% to 52% of the crater diameter, but also follow a linear relationship with crater diameter ( $D_{cp} = 0.3D$ ). The largest central peak craters profiled in this work display two-tiered central peaks which may have formed as a result of basal collapse of a large central uplift. Peak-ring craters are not observed as they are replaced in the morphologic progression by central pit craters. However, six of the central pit craters included in this work display topographically expressed rings between the central pit and the crater rim (Figure 3.16), with ring diameters ( $D_r$ ) which increase as crater diameter increases, following the common relationship for peak-rings on terrestrial bodies ( $D_r = 0.5D$ ).

The presence of internal crater rings in large Ganymede craters, coupled with the similar  $D_r/D$  ratio on rocky bodies suggests that the mechanism of peak-ring formation operates, independently of target gravity and material type as an inherent part of the cratering process. The absence of typical peak-ring craters on Ganymede may suggest that the would-be peak-ring morphology is overprinted by the development of central pits.

### 8.1.3. Central Pits – The Enigma Remains...

Although the author favours the melt-drainage model of pit formation presented in Figures 3.19 and 3.20, the observational data collected for central pits as part of this work does not reliably support or refute a particular formation theory. It does however suggest that the mechanism of pit formation is more effective on Ganymede than Mars, as pits are wider at large crater diameters on Ganymede (Figure 3.7). This may be due to the higher impact velocity on Ganymede creating more melt or initiating the release of a larger volume of volatiles; it could also indicate that the pit formation mechanism is most effective in targets

with higher ice content. If the latter is true, then analysis of pit volumes on Mars may provide a means to compare relative water-ice abundance on different terrains.

Although unable to assist in the identification of a suitable pit formation theory, the observational data does include topographic profiles and measurements of 15 central pit craters. The new depth and slope information provided by this work can thus be used to test pit formation models in much the same way as central peak dimensions were used to test the modelling of central peak crater formation. This topic is the focus of current research, details of which are outlined in Section 8.4.3.

## **8.2 Bridging the Gap - A Message to Modellers**

The interdisciplinary nature of impact studies requires good communication between geologists, modellers and experimentalists. The implications of observational results for modelling and experimental work (and vice versa) is an important area of discussion and has prompted recent 'Bridging the Gap' conferences. This section is composed from an observational point of view, with the knowledge that in order to test numerical modelling results it is necessary to compare the produced craters to observational data.

The wide variation in crater morphology and dimensions shown in this and other works strongly suggests that a single crater profile will not provide a suitable representation of all craters of that size. Modellers who are not seeking to recreate the conditions of a specific impact should therefore preferentially test model results via comparison to averaged cratering trends. This short section comments on the variability of the different crater dimensions measured in this work, and suggests to which crater dimensions it is most beneficial to match simulation results.

### **8.2.1. Match Model Results to Fresh Crater Depths and Average Wall Slope Trends**

As expected, the weakness of ice relative to rock has been apparent in the shallower depths and wall slopes of Ganymede craters (Figures 2.3 and 2.5). The crater depth and wall slope are thus important parameters to recreate with simulations. However, both crater depth and wall slope vary between different craters of the same rim-to-rim diameter. In the case of depth, this variation is often caused by post-impact modification through infill or viscous relaxation; such alteration is identifiable from examination of images and so has not detrimentally affected the published depth-diameter trends, as these are created using

relatively fresh craters only (e.g. Schenk, 2002). These depth-diameter plots are suitable for model testing as the simulation results approximate fresh craters.

Crater wall slope is an important dimension with which to match simulation results as it is related to the effective coefficient of friction of the target material. The trend in wall slope with crater diameter is also vital for models to reproduce as it marks the decline in apparent target strength during the formation of progressively larger craters. This decrease in wall slope is similar on the Moon and Ganymede thus suggesting that the mechanism of material weakening during impact is similar on icy and rocky bodies. This suggests that the same style of strength model can be applied to modelling impact into ice and rock. Unfortunately the spread of observed wall slopes for a single crater diameter (e.g. for a 15 km crater on Ganymede  $\tan(\beta) = 0.1$  to 0.35) provides a wide range of wall slopes within which model results may be considered correct. It is thus advisable that the average wall slope trend be matched also, so that the correct relative decrease in wall slope, and thus decrease in target strength, with crater size can be recreated.

### 8.2.2. Recreate the Correct Style of Peak Formation

The simple-to complex transition at  $D = 1.9 (\pm 0.5)$  km and the clear change in crater rim heights at  $D = 11.9 \left( \begin{smallmatrix} +2.3 \\ -1.5 \end{smallmatrix} \right)$  km provide two important strength-related transitions that numerical models should be able to recreate at the correct crater diameter; the error on both transition values allows an amount of leeway. As peak formation appears to rely upon uplift of the crater floor rather than as a result of rim collapse, numerical models must also be able to form central peaks by another means than material collapsing from the rim to the middle of the crater.

The peak dimensions measured in this work were subject to high variability and a number of the central peaks were excluded from the dataset on the basis of abnormality. This resulted in a relatively small dataset and prevented reliable trends being formed on the basis of this data alone. However, in combination with the Voyager-based work of Schenk (1991) this provides scaling trends that simulation results may be tested with until Galileo-based trends can be formulated. Models should aim to produce central peak heights and diameters within the observed range, preferably conforming to the scaling trends of Schenk (1991) when attempting to reproduce a range of crater sizes. Crater rim height trends are relatively reliable for crater diameters below  $\approx 40$  km and provide a suitable test of model success. Above this diameter, rim height is more variable and modelled craters should ideally maintain rim heights within the observed range.

### **8.2.3. Model Peak and Peak-Ring Development Separately From Pit Formation**

The presence of internal ring structures on Ganymede has been used to suggest that peak-ring formation occurs on both rocky and icy bodies via collapse and outward movement of an unstable central uplift. This process is considered intrinsic to the cratering process and should be recreated by a successful numerical model. However, despite the presence of central pits and the absence of typical peak-rings on Ganymede, numerical modelling which produces peak-ring structures in icy targets should not immediately be assumed incorrect. It appears likely that the pit formation mechanism occurs in addition to the cratering process, as a result of target ice melting or vaporisation, and will not be modelled by most hydrocodes. Modelling of pit formation should be considered separately, adopting the final simulated crater conditions (temperature, etc., as well as final crater shape), after the hydrocode modelling of crater formation.

## **8.3. Numerical Modelling of Impact into Ice**

The morphology of a 15 km diameter crater on Ganymede was simulated using 2 different strength models (Chapter 5): A purely empirical model in which the static strength of the simulated ice was varied, and a part-empirical model incorporating the theory-based weakening mechanism of Acoustic Fluidization. The strengths, weaknesses and physical implications of the most able strength model are presented in this section.

### **8.3.1. The A.F. Model Recreates the Correct Morphology, Block Size and Peak Formation Mechanism**

The empirical model provided the closest fit to observed crater dimensions as the craters simulated using the A.F. model display overly broad and short rims. Although providing the best fit to observations, central peaks produced when using the empirical model were formed by the collision of collapsing rim-wall material at the crater centre. However, this is not in line with the expected peak formation mechanism and so suggests that recreation of crater morphology is not the most suitable test of model success.

The strength model incorporating Acoustic Fluidization recreates the expected process of peak formation via uplift of the crater floor and thus presents a more suitable style of strength model for the simulation of impact crater formation. A non-uniqueness in the model was noted and a similarly suitable fit to the dimensions of a 15 km crater was reproduced using

two different sets of A. F. parameters: Decay time ( $\tau_v$ ) = 50 s and kinematic viscosity ( $\eta$ ) = 80,000 m<sup>2</sup> s<sup>-1</sup>, and  $\tau_v$  = 70 s and  $\eta$  = 110,000 m<sup>2</sup> s<sup>-1</sup>. In the context of the Block Model these viscosities correspond to average sub-crater fracture block sizes (B) of 100 and 140 m respectively. These values are in line with currently accepted estimates of B for terrestrial craters with diameters in the order of kilometers to tens of kilometers, suggesting that ice at 100 K is fractured to a similar extent as terrestrial rock during impacts of this size.

After modelling craters with diameters between 3.5 and 17.5 km, a scaling trend in A.F. parameters with impactor radius ( $R_p$ ) was established in which the viscosity and decay time both increased as  $R_p$  increased (Equations 6.1 and 6.2). In terms of the Block Model this relates to a block size increase from 20 m beneath 3.5 km craters, to 190 m beneath 17.5 km craters. The Block Model scaling recreates the appropriate amount of target weakening to reproduce the morphology of craters between 3.5 and 34 km in diameter on Ganymede, this reproduces the s-c transition at approximately the correct crater diameter, and also models basal collapse of unstable central uplifts in the largest simulated craters.

### 8.3.2. Model Improvement is Still Required

#### **Heraclitus: “Everything Flows” ...Unfortunately This Includes Rim Material!**

The strength model presented in Chapter 6 predicts too much fluidization at small crater diameters, resulting in an overly shallow simple crater (Figure 6.8). Its handling of rim collapse is also too fluid resulting in broad and shallow crater rims. This excessive fluidisation in simple craters can be easily remedied by altering the strength scaling slightly, as suggested in Section 8.4.1. However, overly broad crater rims were a noted feature in simulations of all sizes, indicating that treating the entire target area as a viscous fluid is an inherent flaw of the current A.F. model employed in iSALE. This suggests that modification of the model may be necessary to recreate a less fluid collapse of the crater rim whilst still allowing fluid-like movement of the crater floor.

The current Block Model scaling shows the ratio of A. F. parameters to increase with crater size. Implications of this are discussed in Section 6.3.1 and include the possibility that the ratio of energy stored per cycle of vibrations to the energy lost over the same period may increase with event size. Although it is possible that the dissipation of vibration energy is more efficient for shorter wavelengths (smaller block sizes), such a conclusion cannot be reliably supported until the non-constant ratio of A.F. parameters can be attributed to a cause other than the non-uniqueness of model results

### **8.3.3. Europa's Crustal Ice Thickness is Estimated to be $\approx 5$ km**

The Ganymede-based strength model for unlayered ice was employed for simulations of impacts into layered ice and water targets and results compared to depth-diameter measurements for craters on Europa.

The depth-diameter trend of craters below 14 km in diameter on Europa was only successfully reproduced using an ice thickness of 5 km and a corresponding heat flow of  $\approx 100 \text{ mW m}^{-2}$  (Figure 7.9). As this ice thickness is below  $\approx 10$  km, results from this work suggest that convective overturn of the surface ice may occur, or have occurred, on Europa making the development of indigenous life a possibility.

However, comparison of this work and that of Bray et al. (2006) demonstrates that different strength models for water ice can change crustal thickness estimates by up to 3 km (5 km relative to 8 km estimate from Bray et al., 2006). Furthermore, it is apparent from this work that the current strength model for Ganymede derived in Chapter 6 requires alteration before it can be reliably applied to cratering on Europa.

## **8.4. Future Work**

The study of impact cratering on the icy satellites will benefit from larger observational datasets and better material models for use in hydrocode simulations. Two obvious avenues for further work are thus the acquisition of more topographic data and the construction of scaling trends of crater dimensions, and of course, the continued refinement of the strength model and EoS for ice. Particular foci within these broad topics have been identified during the course of this work, and are suggested in this section.

### **8.4.1. Advancing the Reliability of Hydrocode Modelling of Icy Impacts**

#### **Development of a More Accurate EoS for Ice**

Although the different Tillotson equations used in this work did not significantly affect the final produced crater morphology, the post-impact target temperatures were affected. Development of a more accurate EoS for ice is thus necessary before the iSALE code can be reliably used for investigating impact processes in ice which involve melt and vapour movements, such as pit formation.

### **Refinement of the Existing A. F. Strength Model for Ice**

A larger number of small crater ( $D < 2$  km) simulations should be performed to more precisely define the crater diameter (between 1.5 and 3.5 km) for which the A. F. model recreates the emergence of central peaks. However, prior to this, the strength model presented for unlayered ice in Chapter 6 will require some modification so that less fluidisation occurs at smaller crater diameters. This will allow a more accurate recreation of the simple-to-complex transition, and also modify the Block Model scaling to remove the negative trend line intercept of Figure 6.12. This modification is relatively simple and requires identification of alternative best-fit parameters for the different crater sizes simulated in Chapter 6.

### **Development of a Hybrid Strength Model**

Although able to recreate the general morphology of central peak craters on Ganymede, the A.F. model's treatment of the entire target as a viscous fluid prevents accurate recreation of crater rim collapse. Closer approximation of observed rim heights was provided by the empirical model, suggesting that a combination of the A. F. model and a variant of the empirical strength model may be necessary to recreate less fluid collapse of the crater rim while still allowing fluid-like movement of the crater floor.

## **8.4.2. Continued Acquisition of Observational Data**

### **Establish the Order of Rim Collapse and Floor Rebound**

Further understanding of what processes occur at the simple-to-complex transition is necessary before the success of any hydrocode strength model can be assessed in detail (i.e. can the hydrocode recreate the correct processes in the correct order). The lack of simple craters profiled in this work prevented such an analysis as part of this thesis. Continued collection of simple crater profiles on Ganymede and measurement of crater dimensions, specifically rim height and peak size, is necessary to investigate whether floor rebound or rim collapse occurs first in the size-morphology progression of craters on Ganymede.

Such investigations are already underway for Martian craters with the use of high resolution images from HiRISE, and is also the intended focus of lunar work once higher resolution imagery becomes available for the Moon. Comparison of the interplay between uplift and rim collapse of craters in rock, ice and layered rock and ice targets ( $\sim$  the Moon, Ganymede and Mars respectively) may allow the relative rheology of the targets at different depths to be assessed.

### **Measurement/Profiling of Relaxed Craters**

Viscous relaxation of crater topography is an important process on the icy satellites. Modelling of the relaxation process is already being performed and the limited examples of relaxed craters included in this dataset used to supplement the assessment of viscous relaxation of crater topography (e.g. Dombard and McKinnon, 2006). Such studies will benefit from the collection of more profiles of relaxed craters so that model results can be tested.

### **Establishing a Peak Height Trend**

A trend in central peak height has not been obvious from this work, possibly due to a number of central peak measurements being rejected on the basis of having ‘abnormal’ morphology. Continued topographic profiling of central peak craters on Ganymede will fill this data gap and may allow identification of a trend in central peak height with crater size, as suggested by Schenk (1991). This would provide an additional parameter with which to test modeling results and may reduce the opportunity for non-uniqueness.

### **8.4.3. Combined Modeling and Observational Projects**

#### **Continued Investigation of Central Pits**

Comparison of Martian and Ganymede central pits suggests a dependence of pit size on surface ice content. An understanding of pit formation may thus provide a means with which to assess the water-ice content of planetary surfaces. Evaluation of the different hypotheses of central pit formation is the focus of a current multifaceted research project that combines a range of observational and computer based techniques. The project includes continued collection and analysis of central pit crater profiles, modification of the hydrocode strength model and equation of state for ice, plus the design of specific tests for each established pit formation theory.

#### **Further Investigation of European Craters**

Future investigation of cratering on Europa requires the collection of topographic profiles of European craters. This will allow comparison of crater morphology on Ganymede and Europa, allowing the difference between craters in unlayered and layered ice to be assessed in the same way as the difference between rock and ice was investigated in Chapter 2, by comparing lunar and Ganymede craters. Once observational data exists with which to test numerical models, there are many avenues for further modeling of European crater formation. Firstly, a strength model developed by matching simulation results to European craters below 8 km in

diameter will provide a more suitable base from which to model larger crater sizes and material layering interactions on Europa, compared to a Ganymede-based strength model.

This work only considered the simplified structural model of an ice layer over water. Once the strength model scaling for pure ice is more confidently established, different structural scenarios can be investigated, including the introduction of slush layers and convective ice regimes.

In addition to improving the strength model for H<sub>2</sub>O ice, construction of material models for other compositional candidates for Ganymede and European surfaces, such as hydrates, should be considered. This will ultimately produce more accurate results and estimates of crustal thickness, but is only possible once adequate strength properties are established for these materials.

### **8.5. Statement of Achievement/Contribution**

This thesis has presented topographic profiles of impact craters on Ganymede, based on the highest resolution data available today. This has enabled the collection of previously unavailable height and slope data, and the subsequent formulation of new scaling trends for central peak and central pit crater dimensions (Bray et al., 2008; Bray et al., 2009). The profiles have also revealed two-tiered central peaks and possible peak-ring structures in some craters, supporting the idea that large central peaks collapse downward and outwards to form peak-rings, even on icy bodies.

The scaling trends produced were used to test hydrocode results, helping to establish a working Acoustic Fluidization based strength model for the simulation of impact crater formation in ice; a third-order Tillotson-style equation of state for H<sub>2</sub>O ice was also developed during the course of this work. The strength scaling presented in this thesis allowed successful hydrocode simulation of craters between 3.5 and 34 km in diameter on Ganymede, including recreation of the trends in central peak size, crater depth, wall slope and rim height, with event size. Although collapse of a large central peak was simulated to occur at approximately the same crater diameter as suggested by observations, the development of peak-ring or central pit morphology was not recreated using the current strength model and may suggest that pit formation must be studied via a separate means.

The strength model established for pure ice was applied to the simulation of impact into layered ice and water targets and results tested by comparison to the depth-diameter trend of craters on Europa. Results of this work suggest that Europa's ocean has been positioned beneath an ice crust of ~ 5 km depth, averaged over the satellite's recorded geological history.

This adds support to the 'thin-shelled' view of Europa and suggest that convective overturn of the surface ice may be occurring or have occurred on Europa, making the development of indigenous life a possibility.

## Appendix A

# Database of Ganymede Crater Profiles

The following pages contain information and topographic profiles of all craters in this work preceded by a contents page that lists the craters included in the database. Craters already recorded in the online Ganymede Crater Database have assigned names or location indicators (e.g. ZS34:140 denotes a crater at 34°S, 140°W). Craters profiled in this work which were not already noted in the online database were assigned a title composed of its latitude and longitude coordinates (e.g. GN38:195 refers to a crater at 38°N, 195°W).

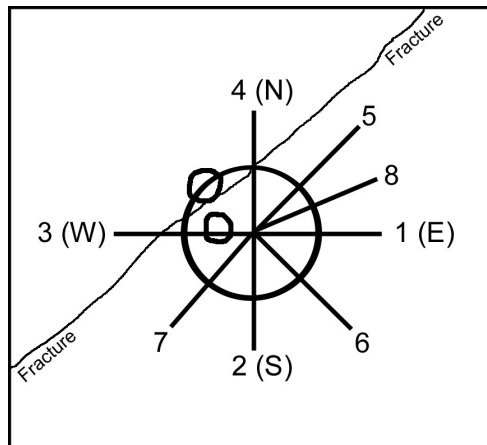
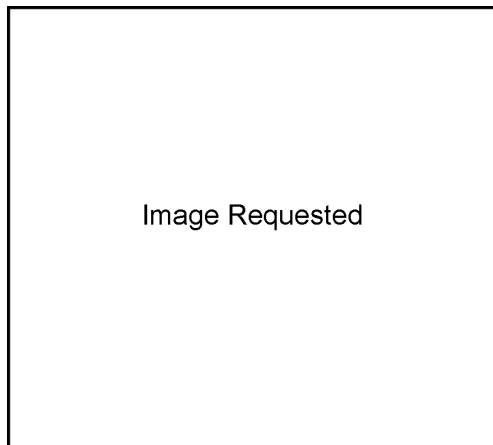
Galileo images of each crater are included alongside a sketch map of the image marking the paths along which topographic profiles were collected. North, approximate illumination direction and regions of no data are marked with an arrow, a dotted circle, and black areas respectively. Each radial profile is assigned a number from 1 to 8. Areas of no data, the cross-section at 90° to the illumination direction and features unrelated to the primary impact were avoided during profile collection.

Comments recorded during profile collection are included alongside crater type and approximate diameter. All profile axes are stated in kilometres.

# Contents

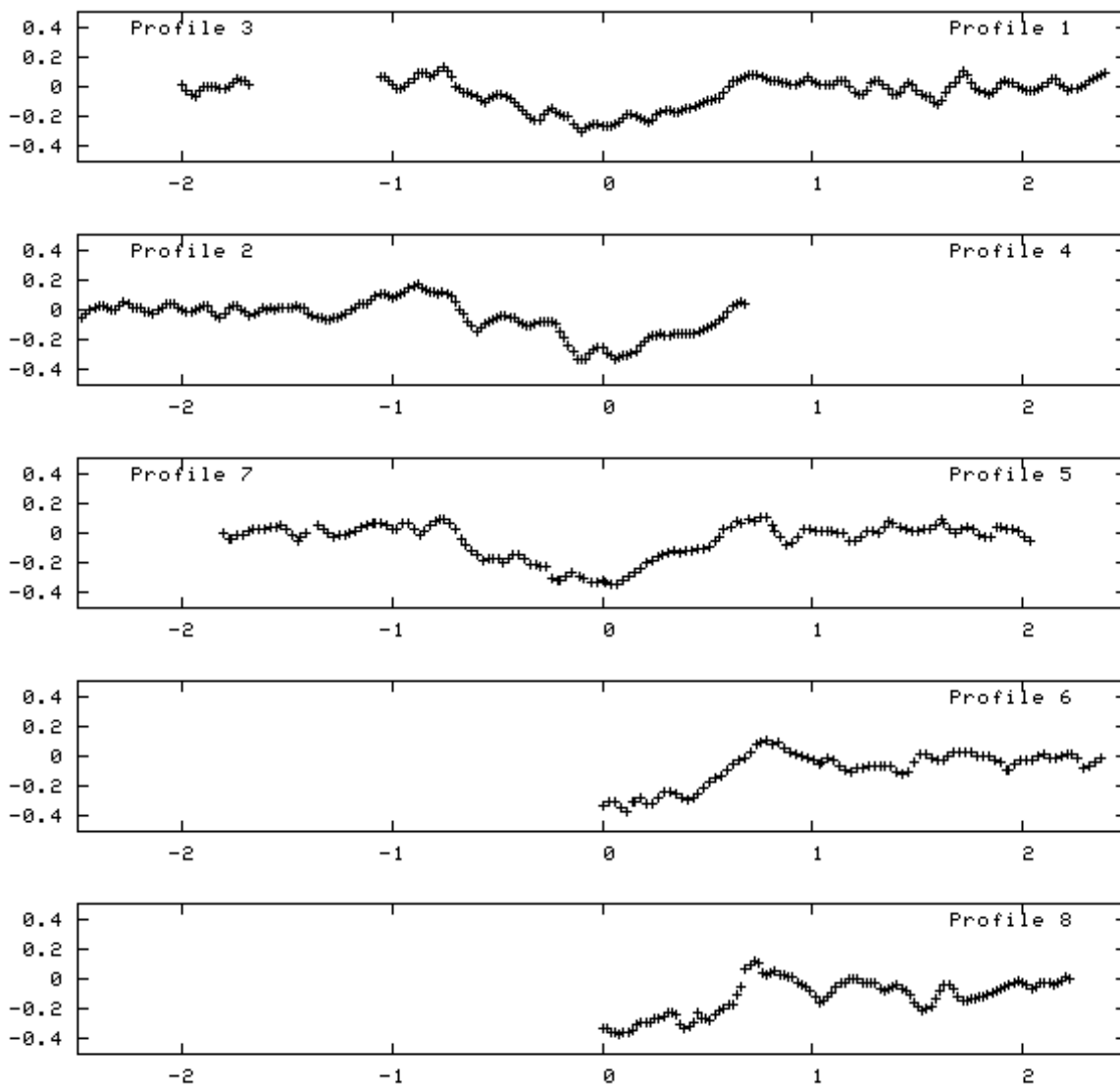
GS15:319 . . . . .	2
GN11:192 . . . . .	3
GN13:189 . . . . .	4
GN13:190 . . . . .	5
GN24:194 . . . . .	6
GN23:194 . . . . .	7
GN13:193 . . . . .	8
GN11:189 . . . . .	9
GN1:201 . . . . .	10
GN13:200 . . . . .	11
GN2:202 . . . . .	12
GS15:337 . . . . .	13
GN39:193 . . . . .	14
GN30:8 . . . . .	15
GN50:192 . . . . .	16
GN39:192 . . . . .	17
GN14:202 . . . . .	18
GN38:195 . . . . .	19
GN0:201 . . . . .	20
GN41:195 . . . . .	21
GN0:202 . . . . .	22
GN33:192 . . . . .	23
GN1:204 . . . . .	24
GN49:184 . . . . .	25
Achelous . . . . .	26
Gula . . . . .	27
ZS37:139 . . . . .	28
GS69:231 . . . . .	29
GS31:170 . . . . .	30
GS83:198 . . . . .	31
ZS34:140 . . . . .	32
ZS29:167 . . . . .	33
ZS30:163 . . . . .	34
GS74:152 . . . . .	35
ZS35:162 . . . . .	36
Lugalmeslam . . . . .	37
ZS19:126 . . . . .	38
Isis . . . . .	39
Eshmun . . . . .	40
ZS84:170 . . . . .	41

# GS15:319

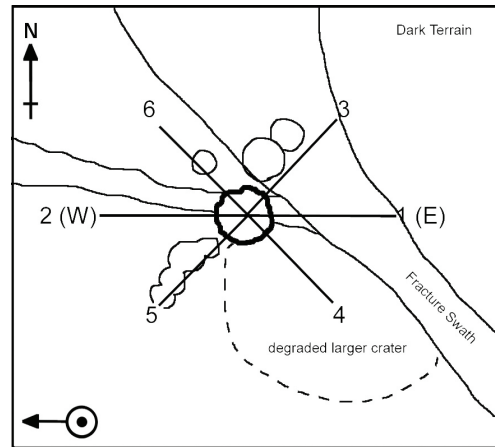
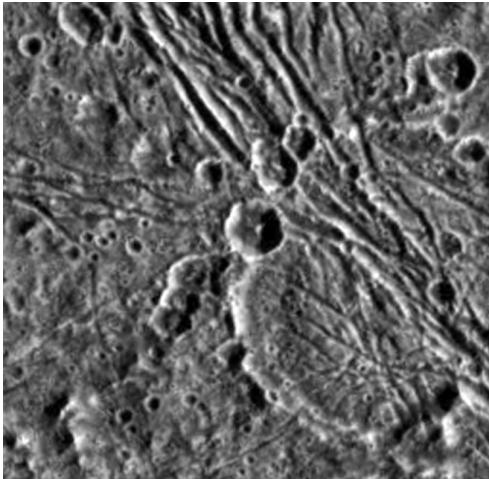


Poor resolution due to low parallax. Lack of image means profiles may still contain artefacts. The original Galileo image had an obvious mosaic line running E-W through the centre of the crater and may have affected profiles 1 and 3. ((Topography from Stereo))

Crater type	Simple
Approx. Diameter	1.6 km
Location:	14.5S, 318.7W
Terrain:	Dark Terrain
Excel file name	BD

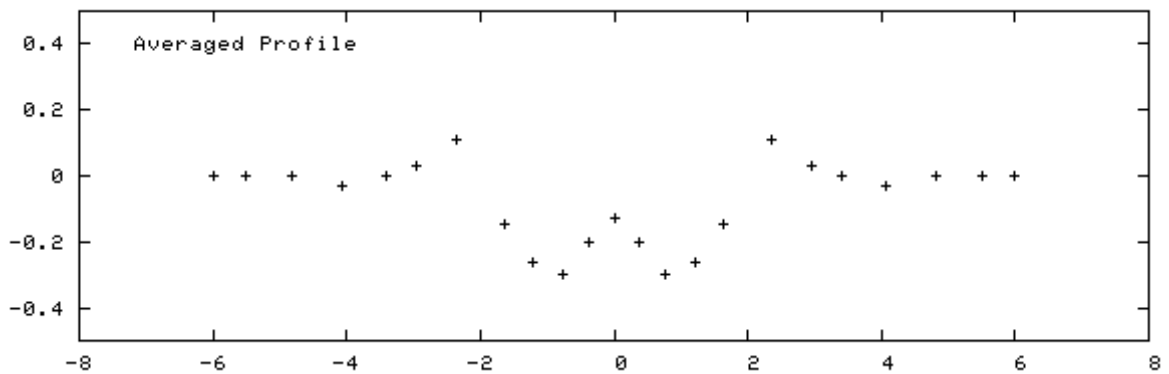
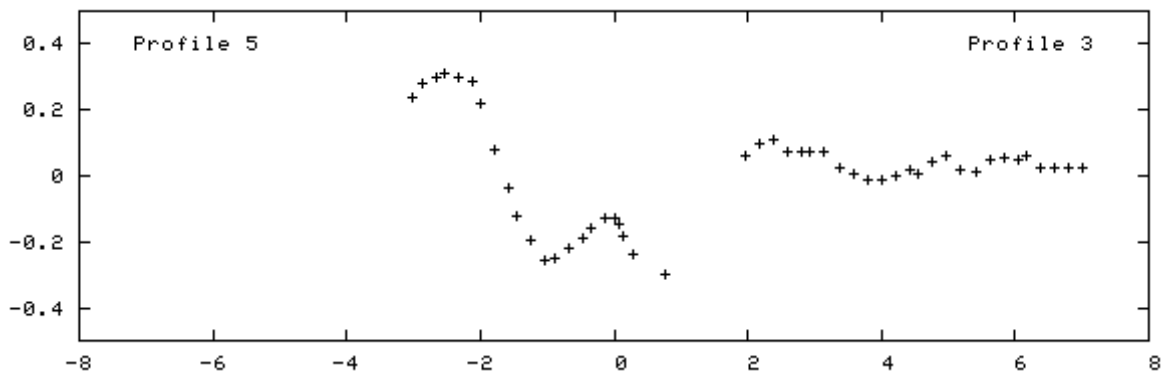
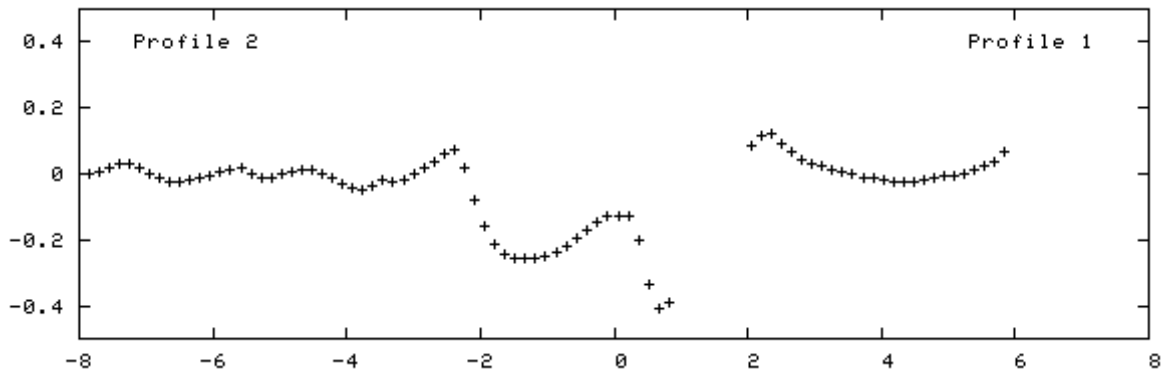


GN11:192

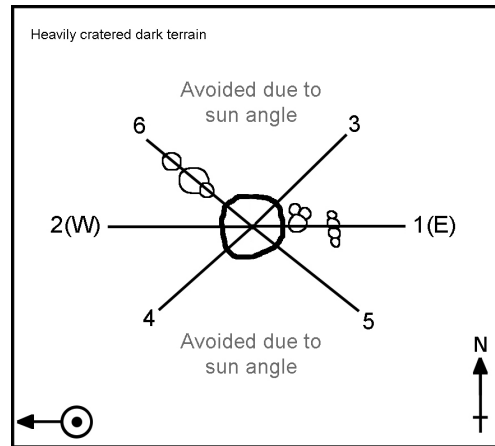
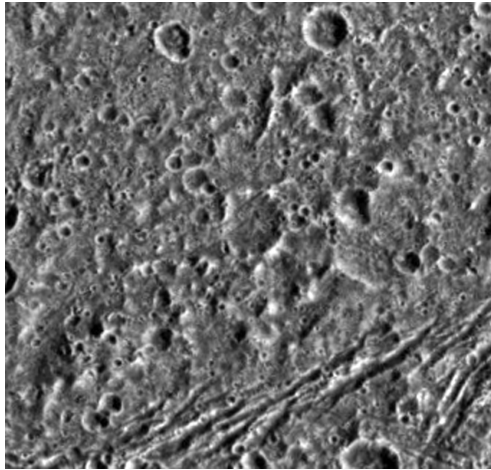


High sun angle, albedo variations and low resolution may influence the profile. ((Topography from Photoclinometry?))

Crater type	Central Peak
Approx. Diameter	4.7 km
Location:	11.41N : 191.52W
Terrain:	Dark Terrain
Excel file name	ans5

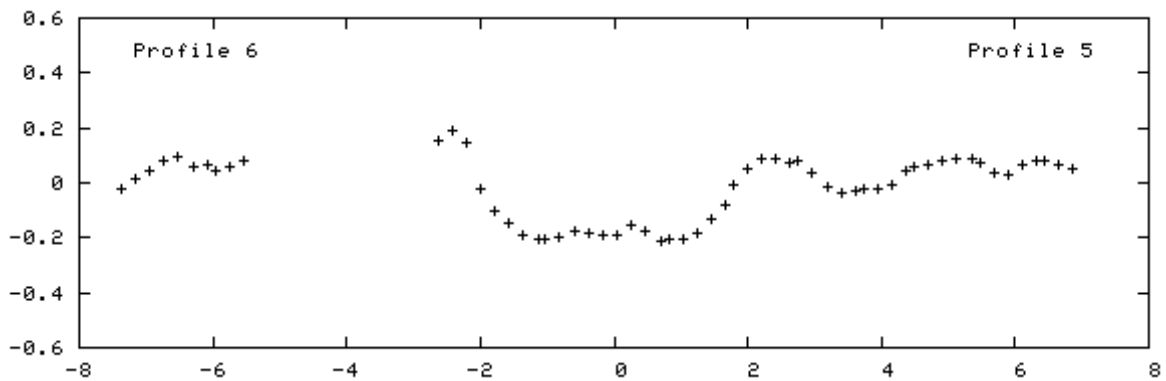
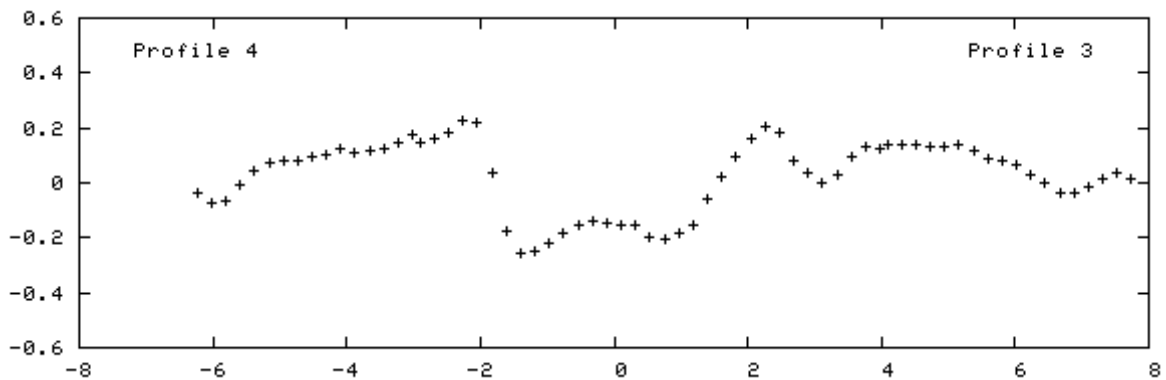
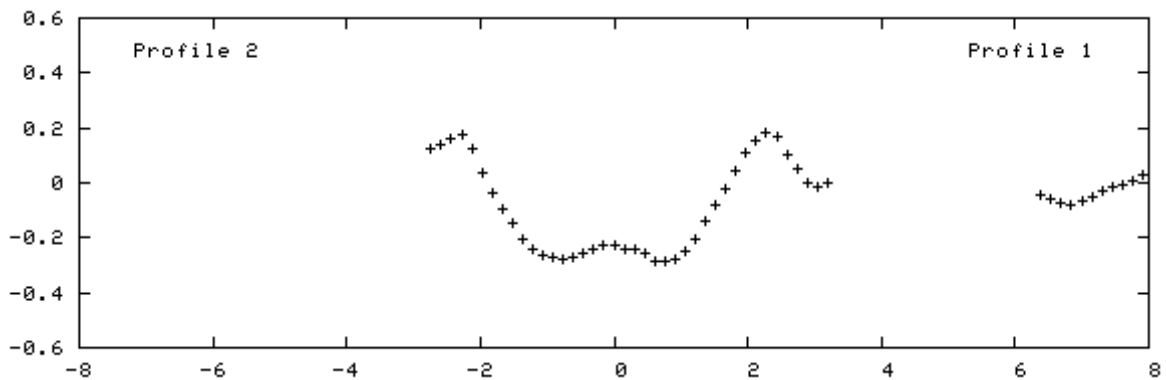


# GN13:189

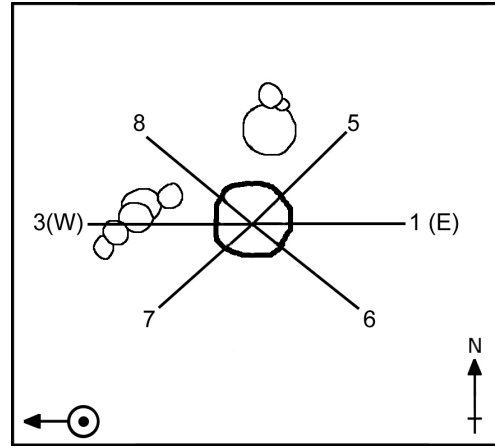
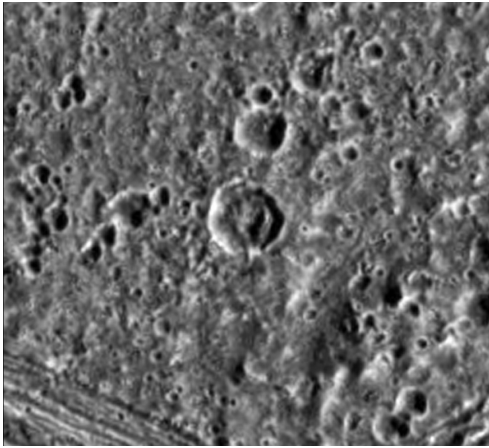


High sun angle, albedo variations and low resolution that will influence the quality of these profiles. ((Topography from Photoclinometry?))

Crater type	Central Peak
Approx. Diameter	4.6 km
Location:	12.8N: 189.3W
Terrain:	Dark Terrain
Excel file name	ans2

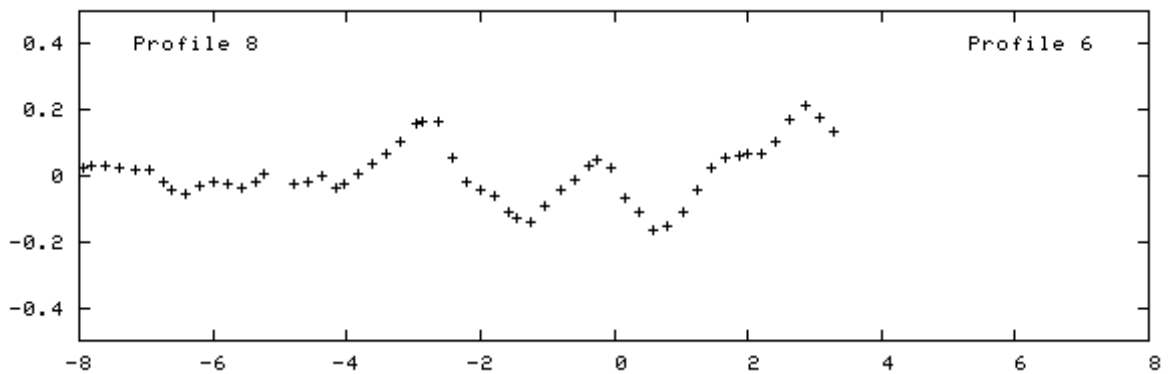
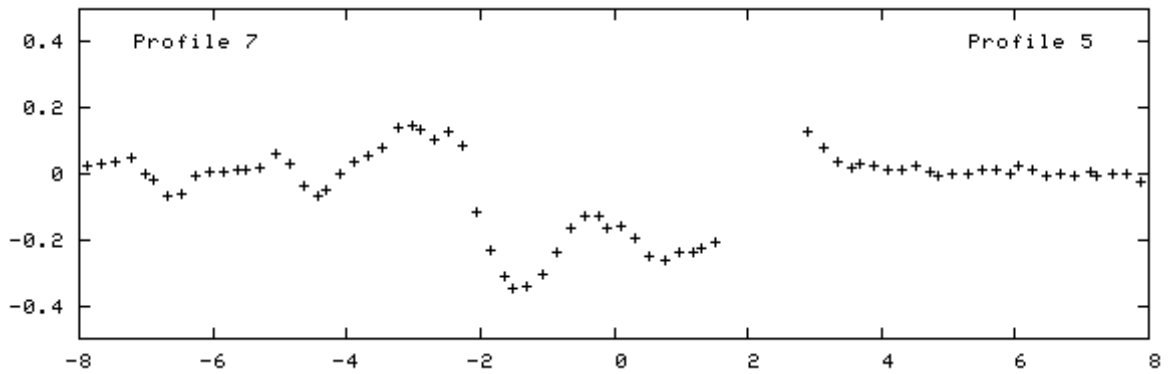
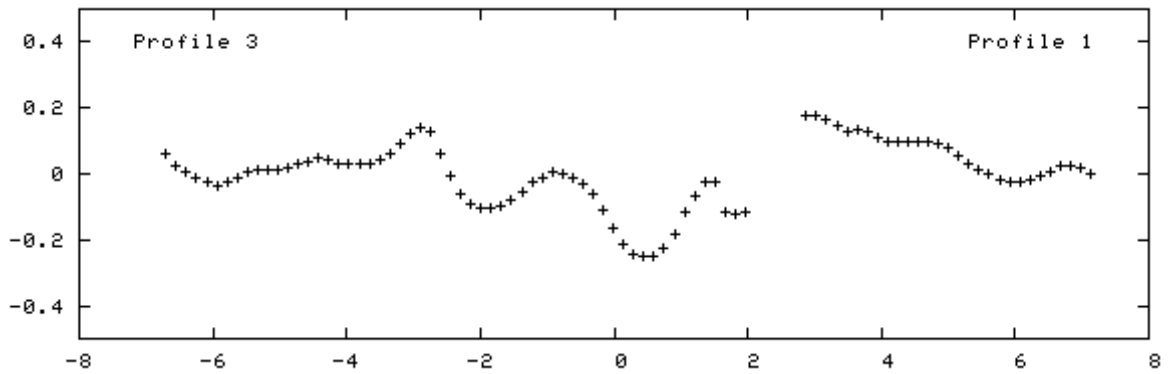


# GN13:190

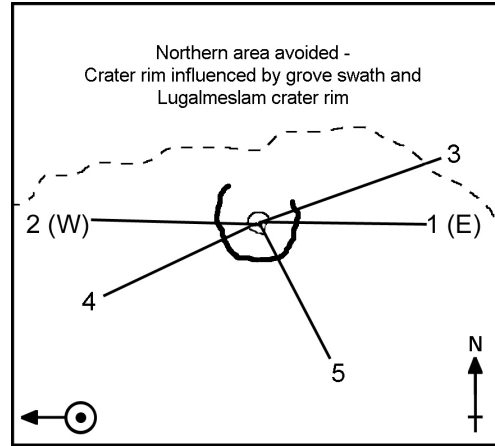
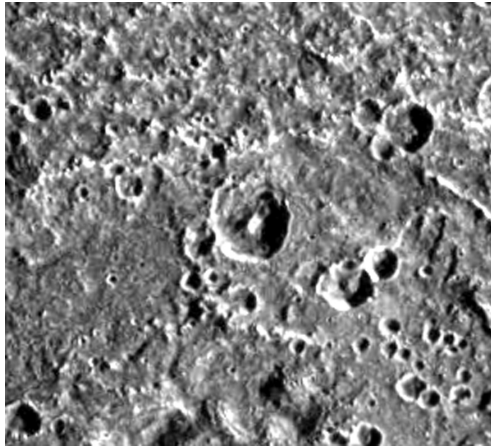


Anomalous central region (most obvious in profile 1). High sun angle, albedo variations and low resolution will affect the quality of the profiles.

Crater type	Unknown
Approx. Diameter	5.8km
Location:	12.26N : 190.05W
Terrain:	Dark Terrain
Excel file name	ans3

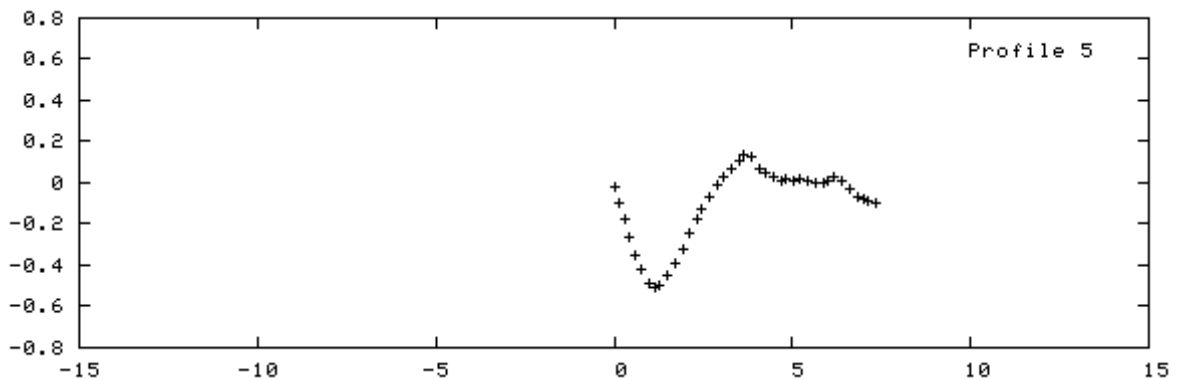
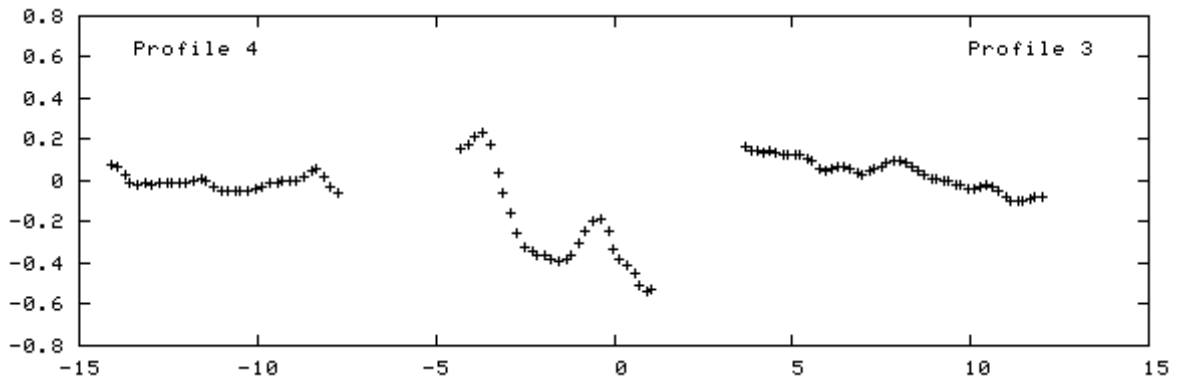
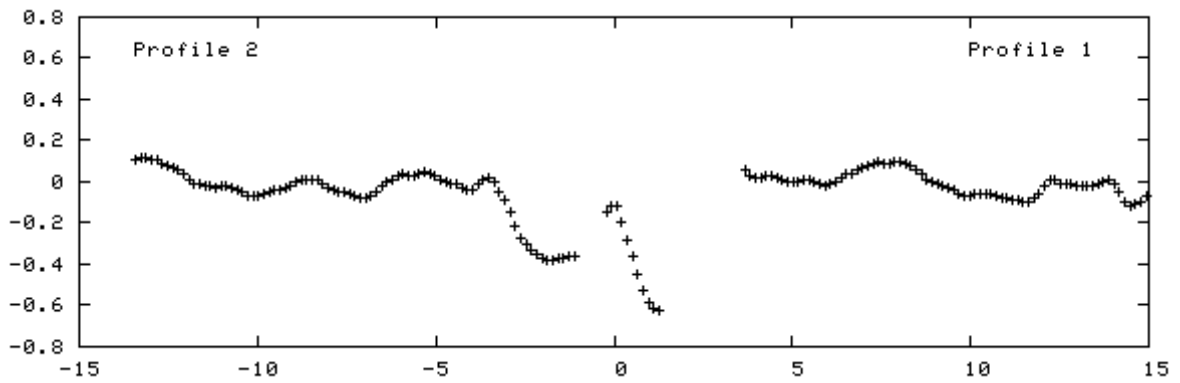


# GN24:194

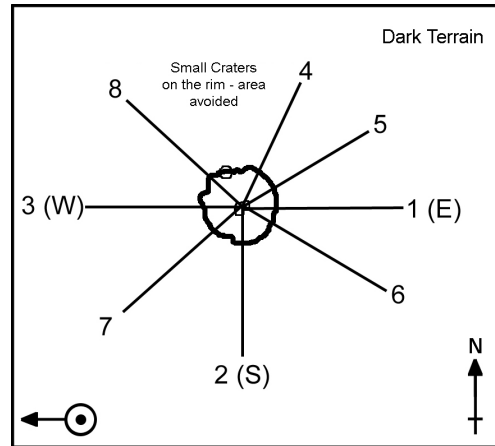
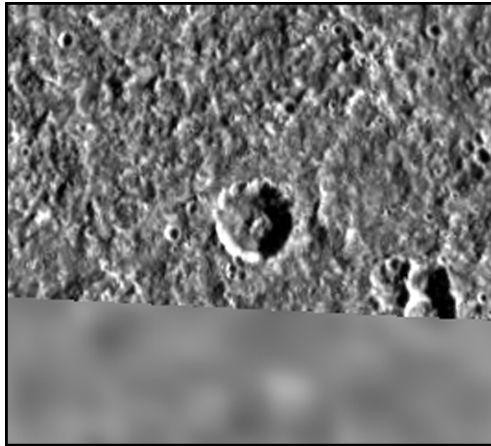


Good profiles due to the sun angle being 72degrees.((Topography from Photoclinometry))

Crater type	Central Peak
Approx. Diameter	7.3 km
Location:	24.4N : 193.7W
Terrain:	On existing crater
Excel file name	L1

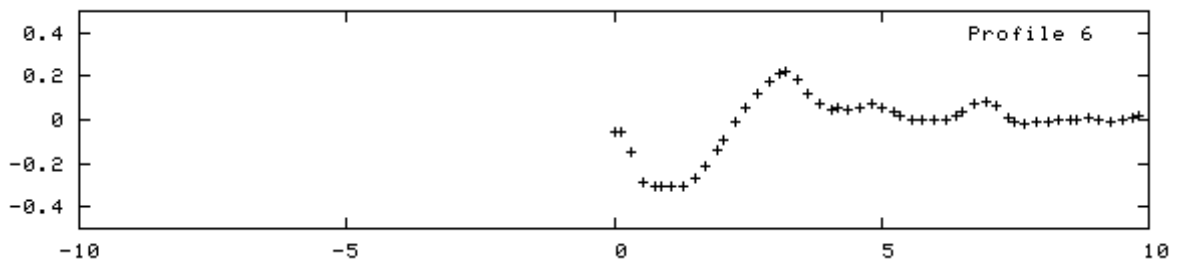
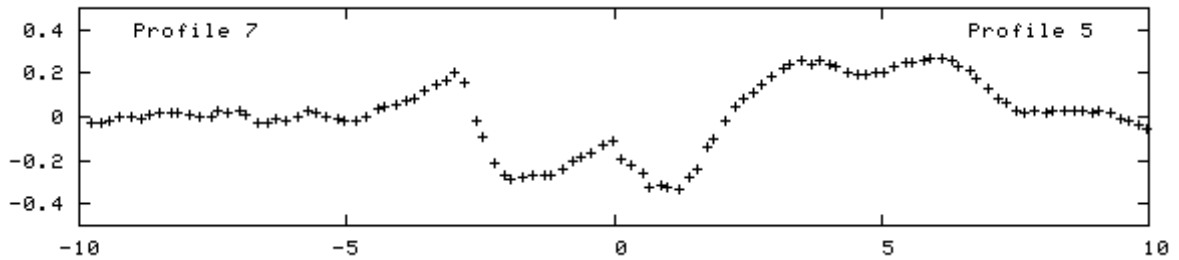
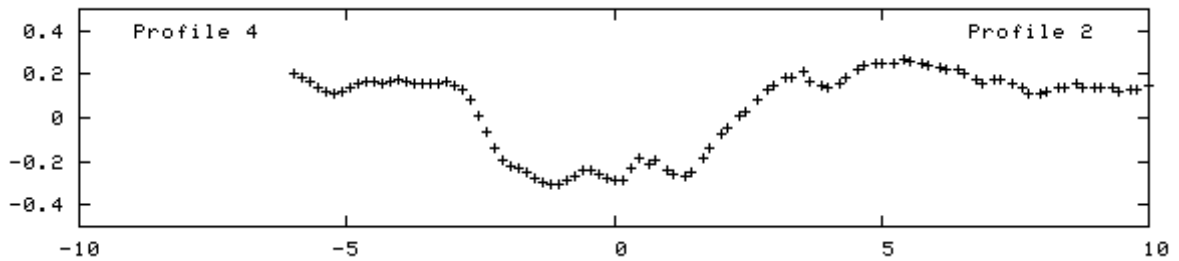
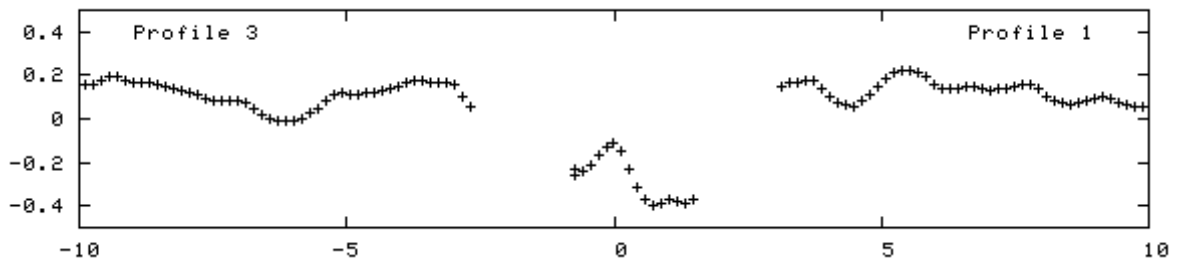


# GN23:194

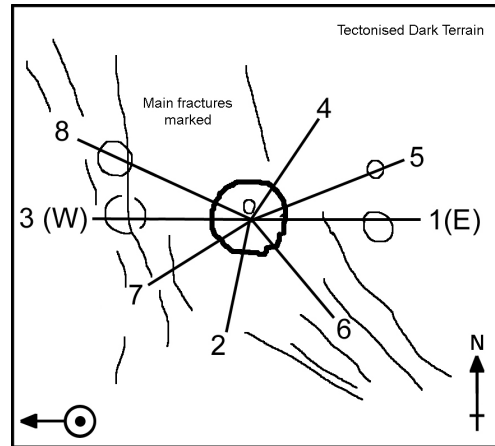
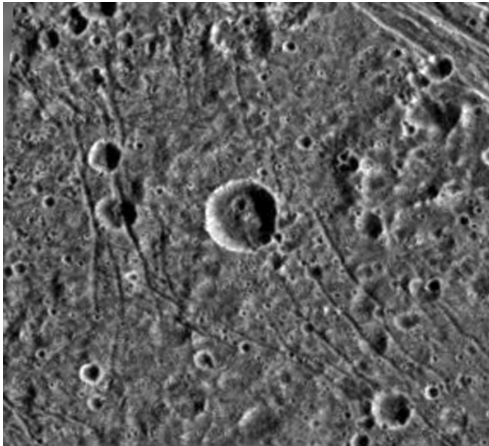


Good profiles due to the sun angle being 72degrees. ((Topography from Photoclinometry))

Crater type	Central Peak
Approx. Diameter	7 km
Location:	22.6N : 194.1W
Terrain:	Dark Terrain
Excel file name	L2

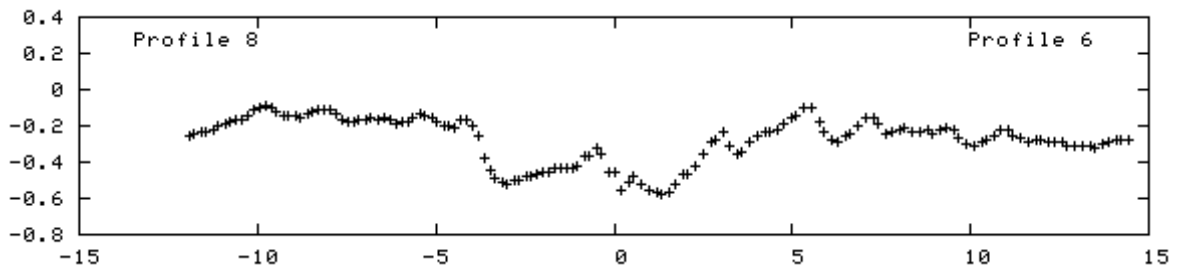
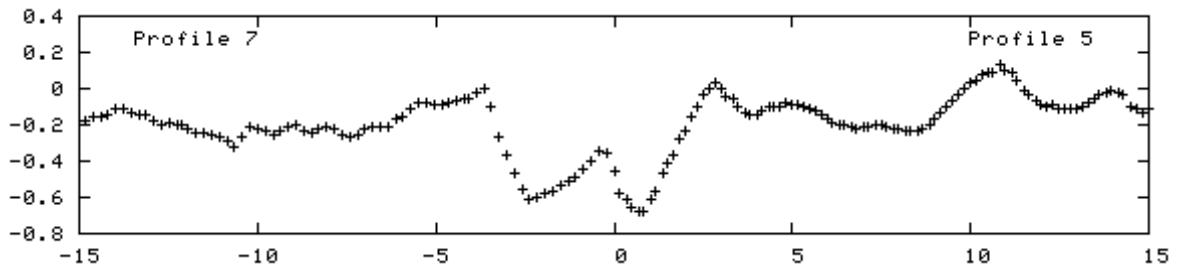
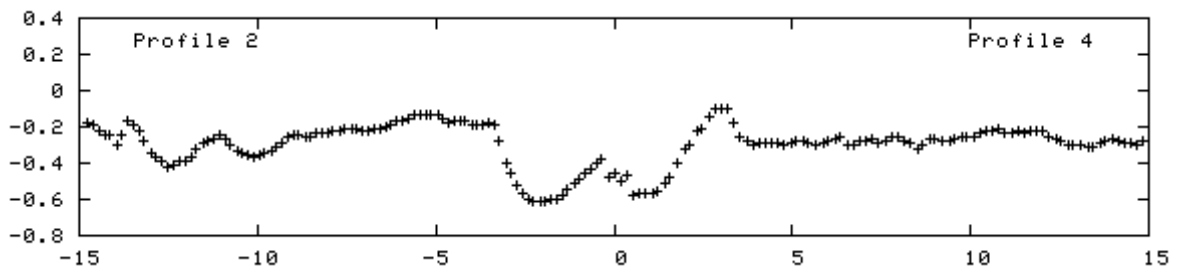
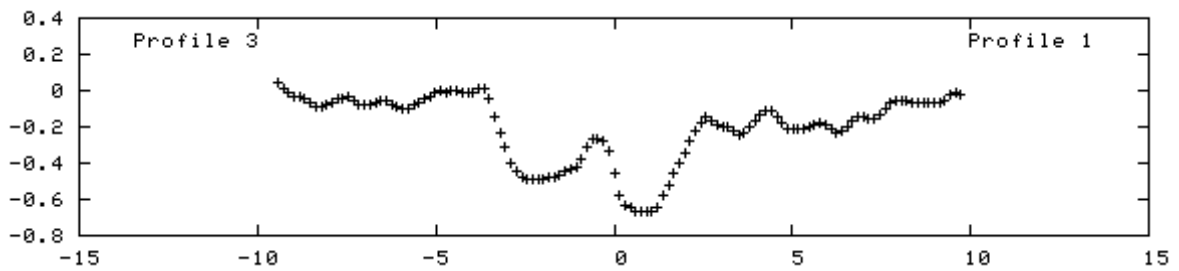


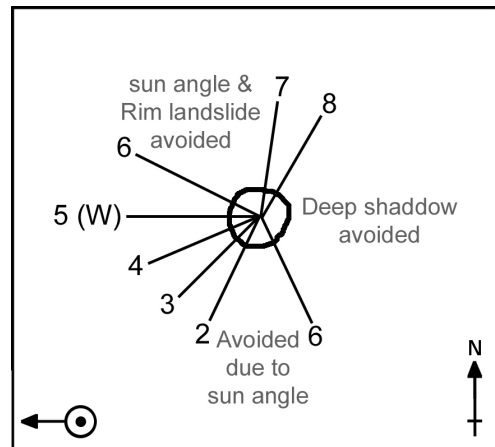
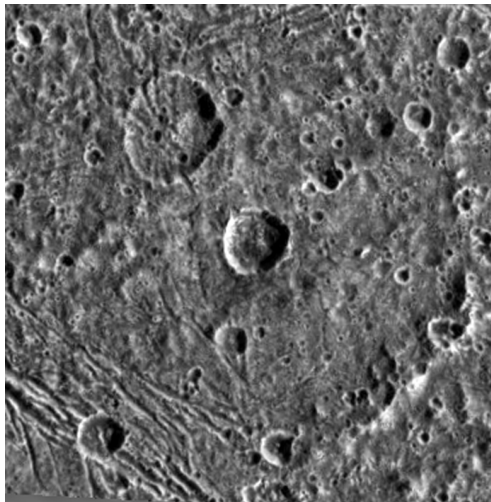
# GN13:193



High sun angle, albedo variations and low resolution may influence quality of profiles ((Topography from Photoclinometry?))

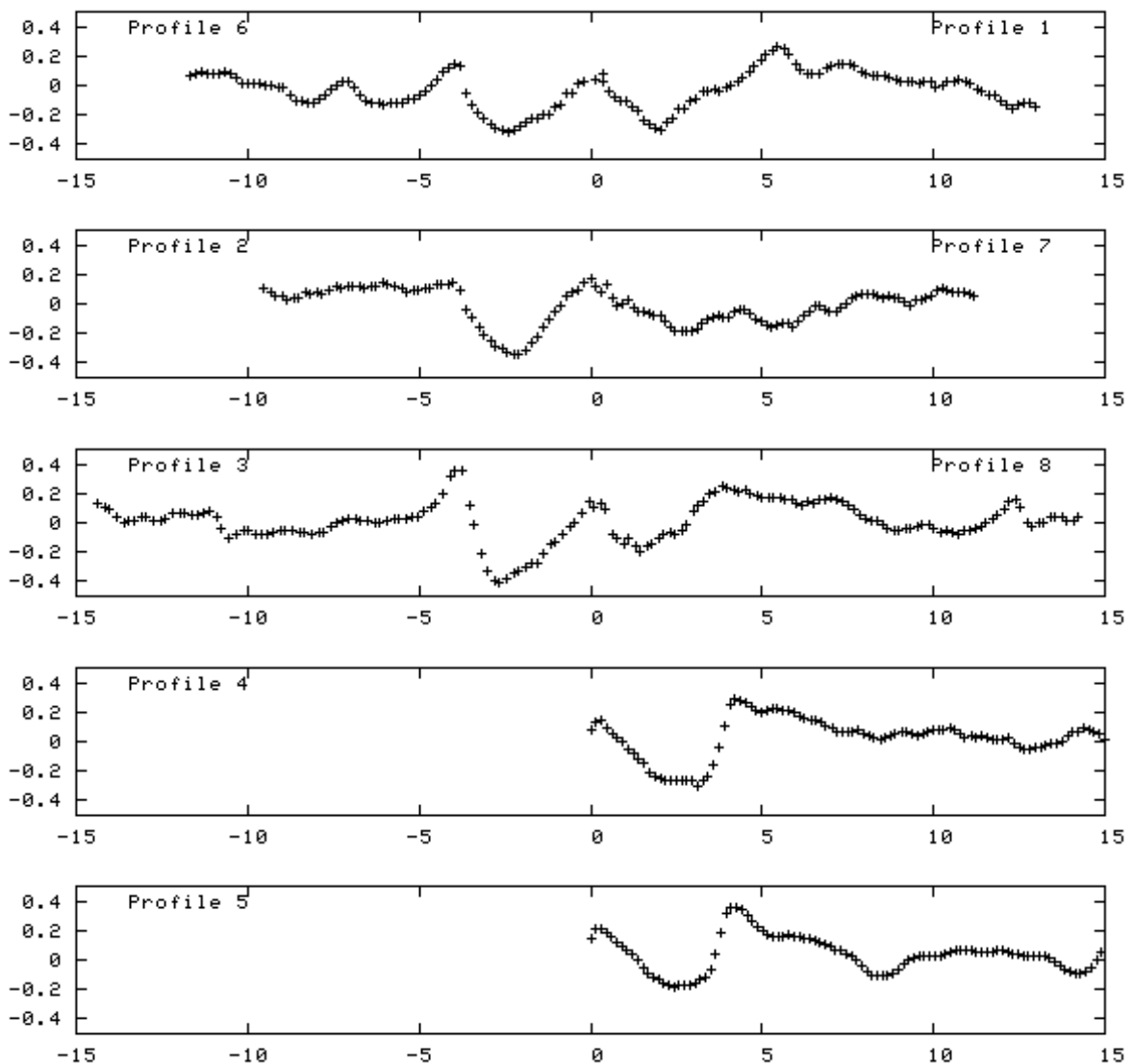
Crater type	Central Peak
Approx. Diameter	6.7 km
Location:	12.78N : 193.23W
Terrain:	Dark Terrain
Excel file name	ans1



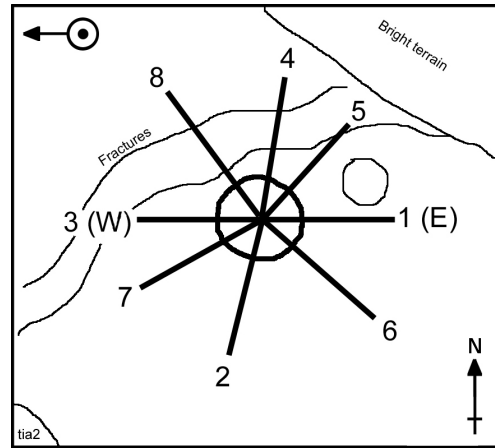
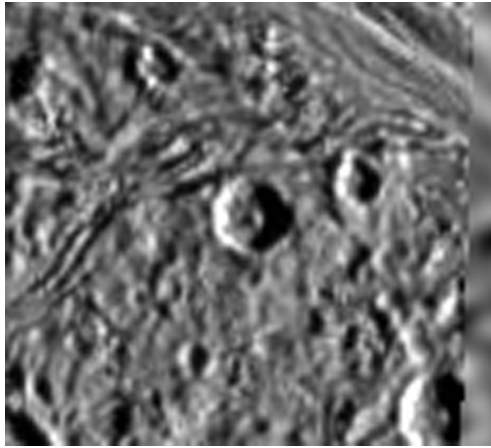


High sun angle, albedo variations and low resolution will influence the quality of the profiles. ((Topography from Pgotoclinometry))

Crater type	Central Peak
Approx. Diameter	8.8km
Location:	10.9N : 189.3
Terrain:	Dark Terrain
Excel file name	ans4

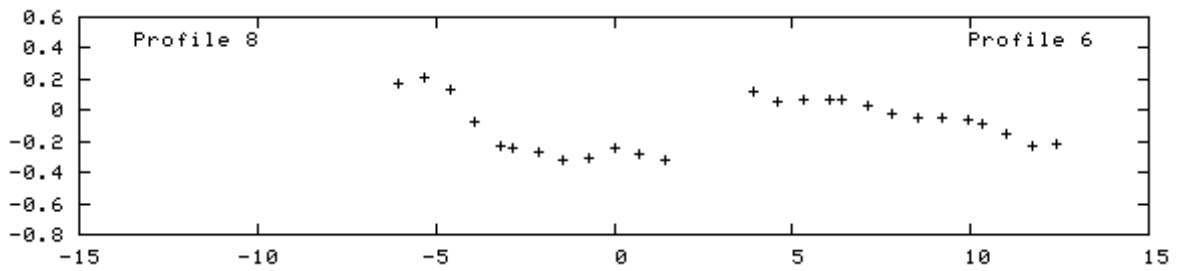
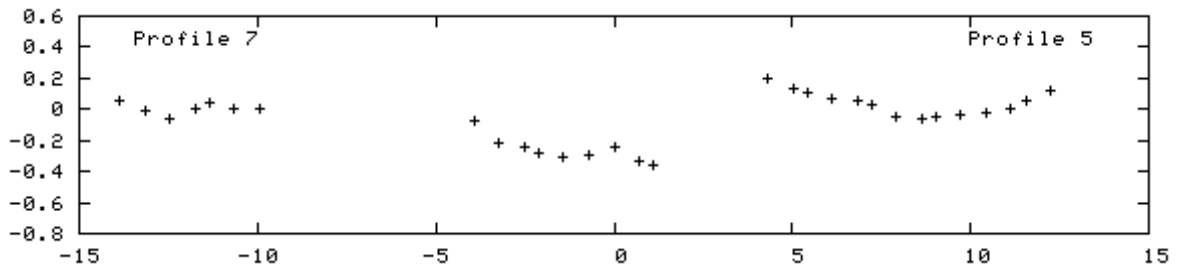
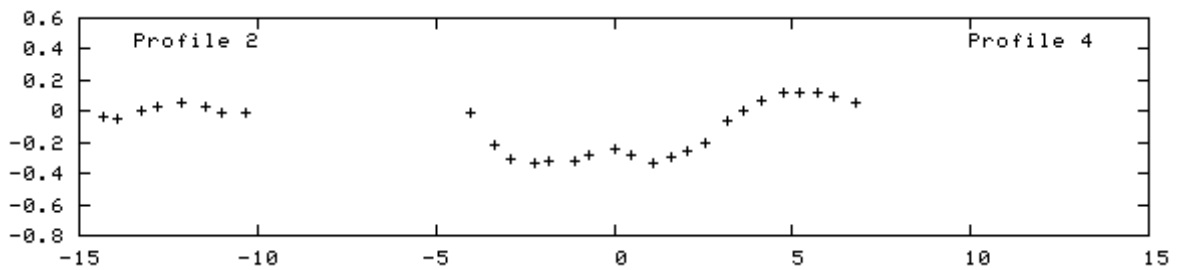
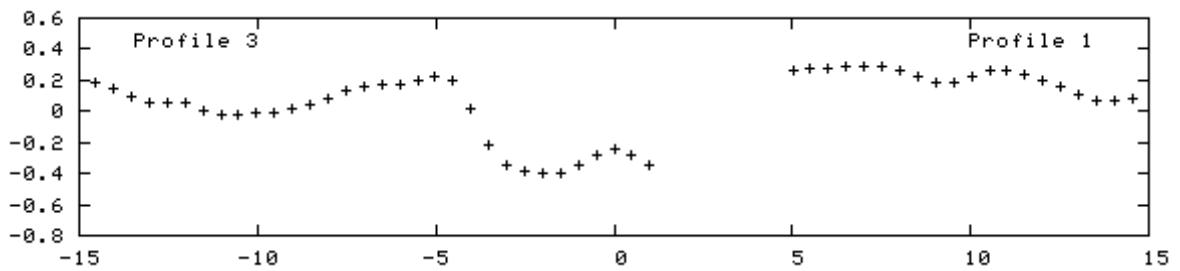


# GN1:201

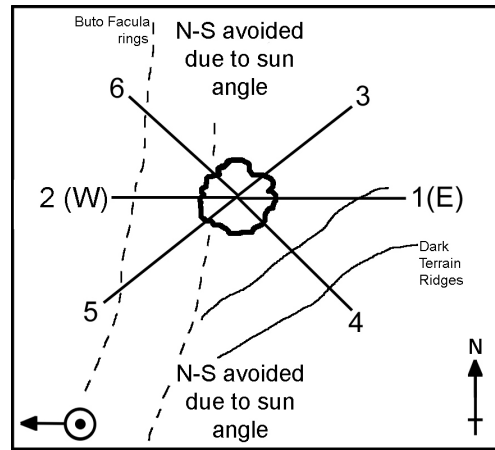
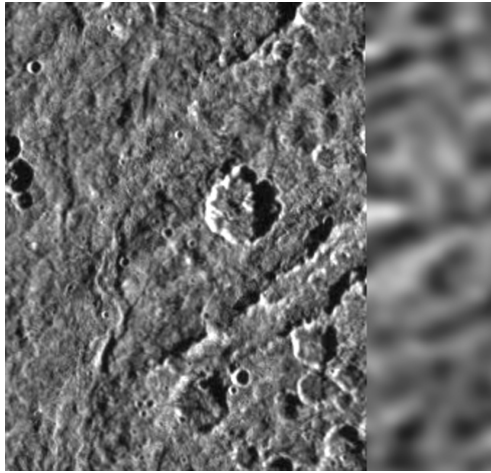


((Topography from Photoclinometry))

Crater type	Central Peak
Approx. Diameter	9.6 km
Location:	1.1N:200.7W
Terrain:	Dark Terrain
Excel file name	tia4

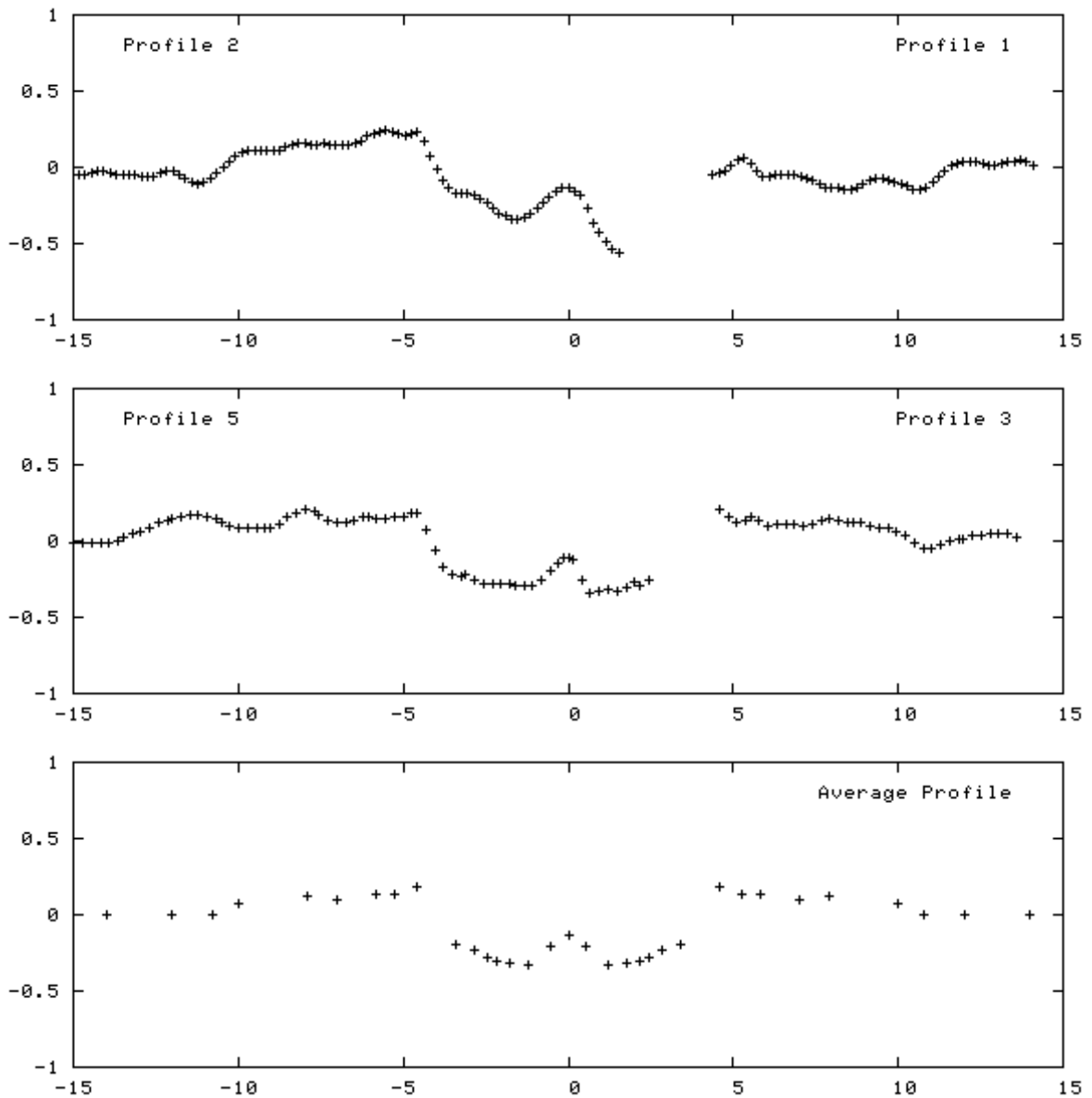


# GN13:200

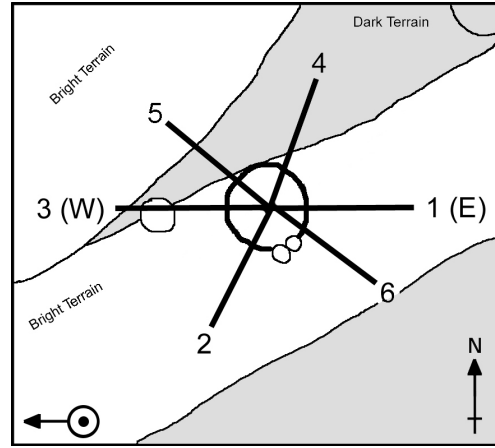
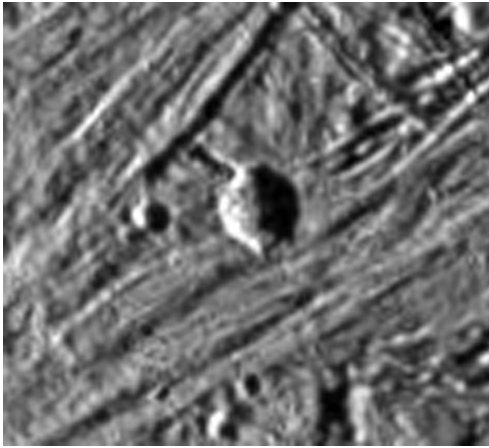


Crater lies in a trough between two ridges  
 ((Topography rom Photoclinometry))

Crater type	Central Peak
Approx. Diameter	9.1 km
Location:	13.2N : 200.4W
Terrain:	Dark Terrain
Excel file name	buto2

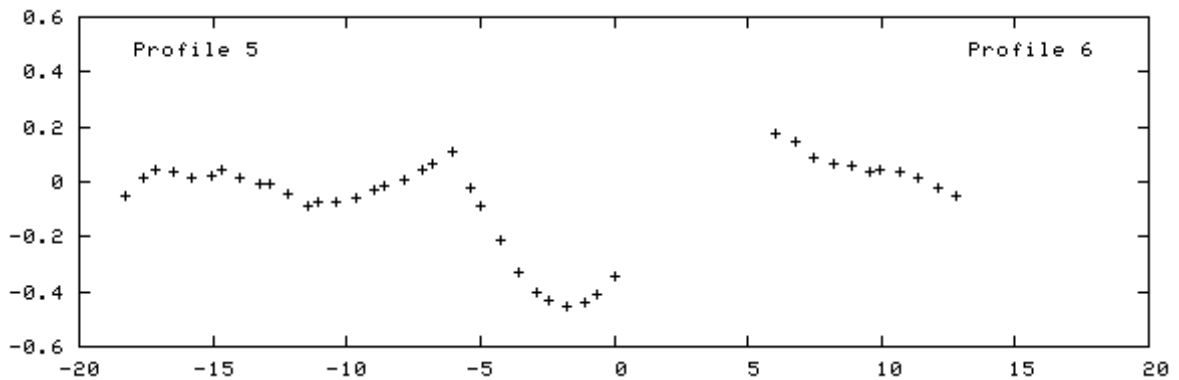
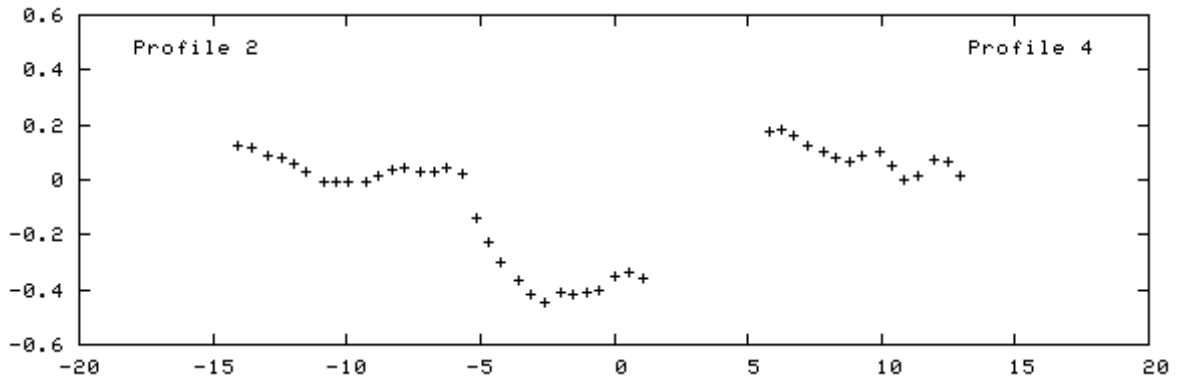
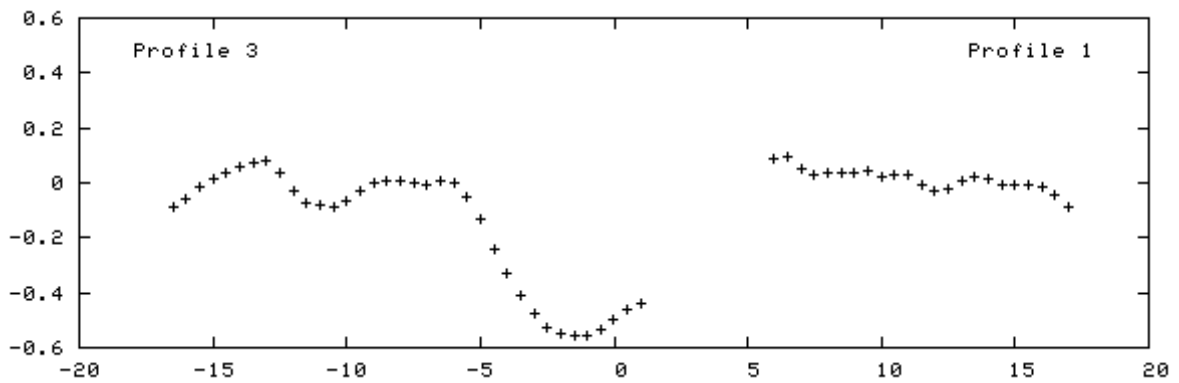


# GN2:202

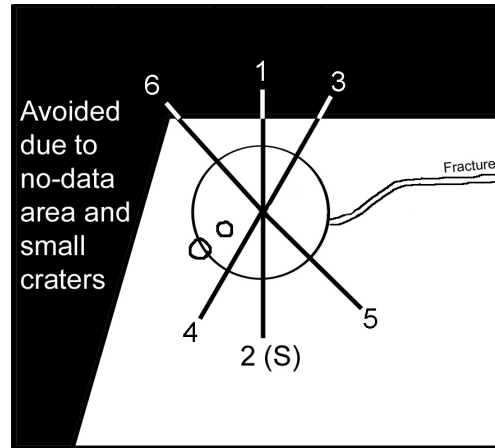
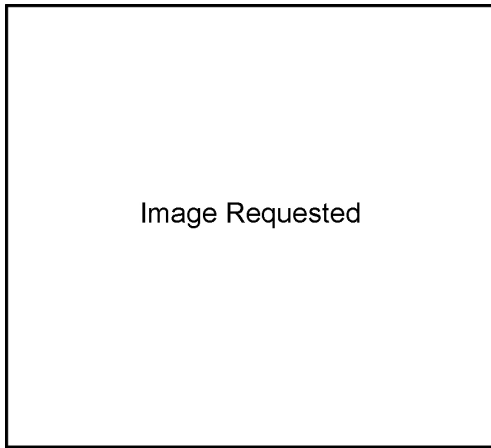


Care - significant shadow adds to data gaps and may hide central morphology. ((Topography from Photoclinometry))

Crater type	Central Peak
Approx. Diameter	9.9 km
Location:	1.6N:202.5W
Terrain:	Bright Terrain
Excel file name	tia6

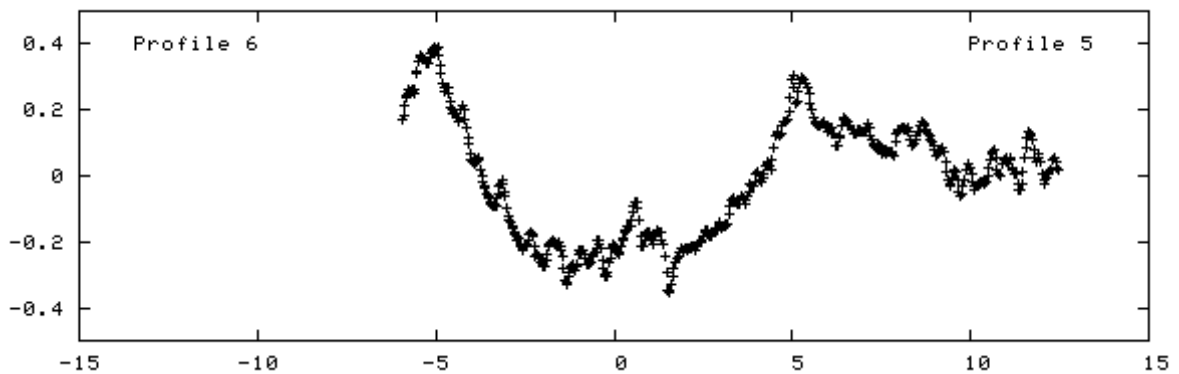
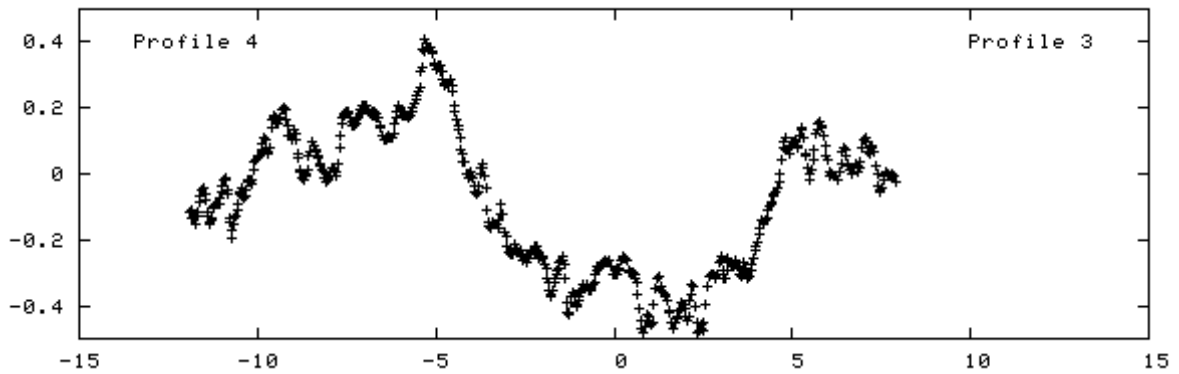
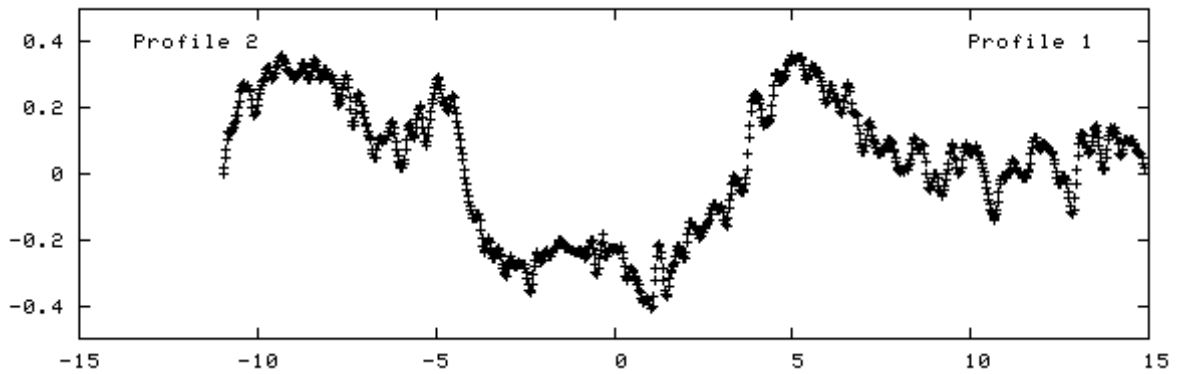


# GS15:337

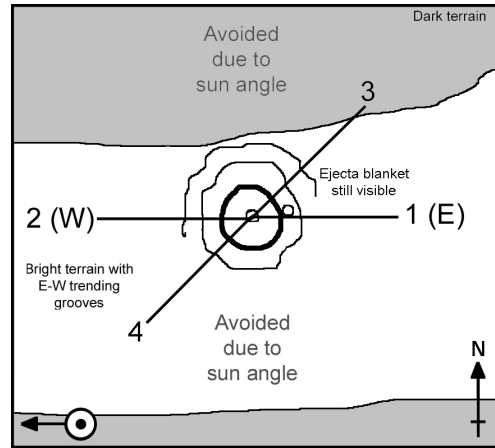
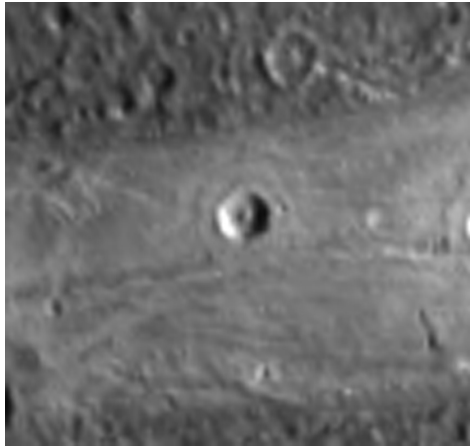


Heavily cratered. Shallower than expected for craters of this size. ((Topography from Stereo))

Crater type	Central Peak
Approx. Diameter	10.3 km
Location:	15.4S 336.5W
Terrain:	Dark Terrain
Excel file name	G28Dark

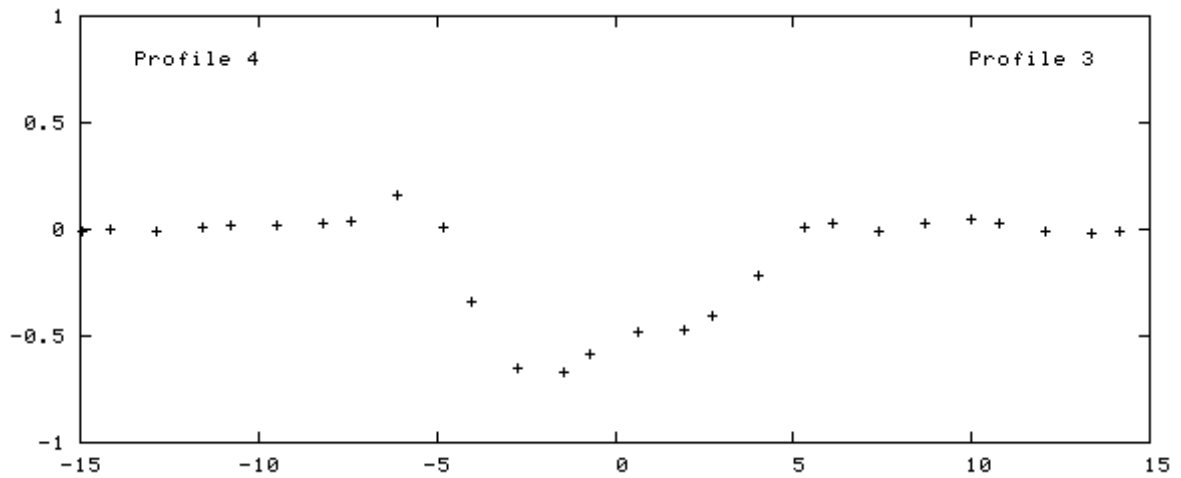
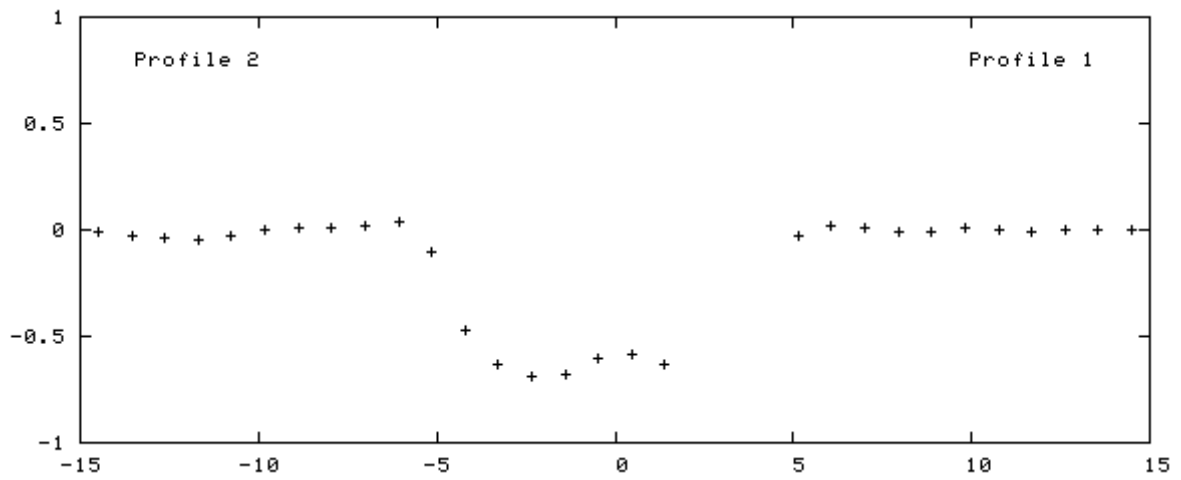


# GN39:193

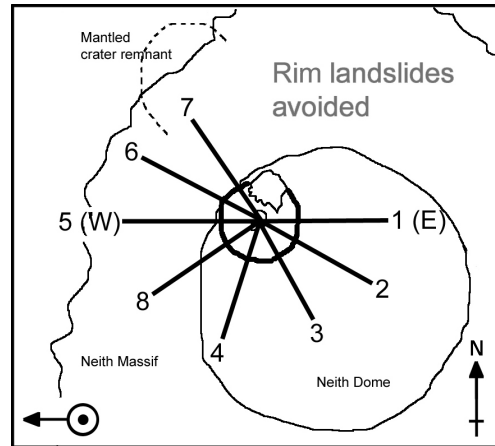


Care - low resolution for this size crater.  
 ((Topography from Stereo?))

Crater type	Central Peak
Approx. Diameter	12.2 km
Location:	39.3N 193.3W
Terrain:	Bright Terrain
Excel file name	G2

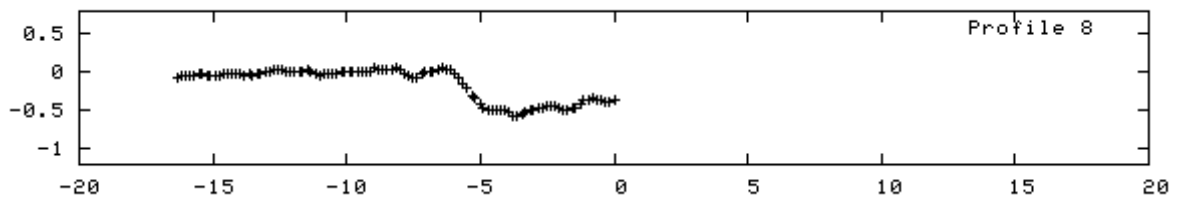
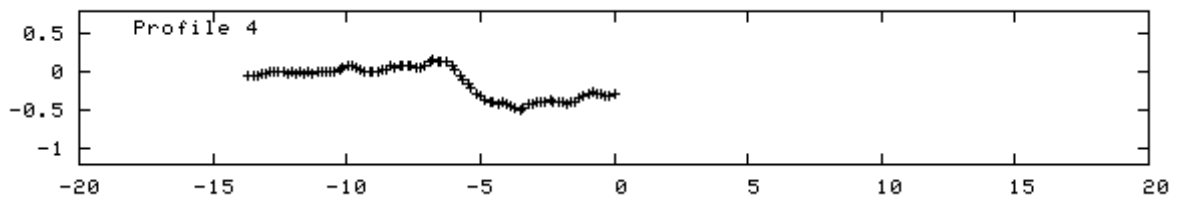
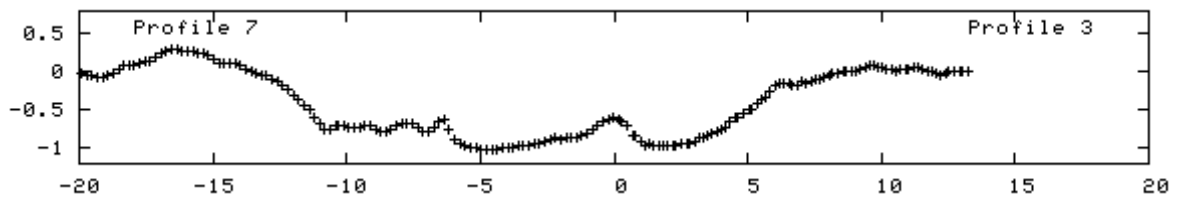
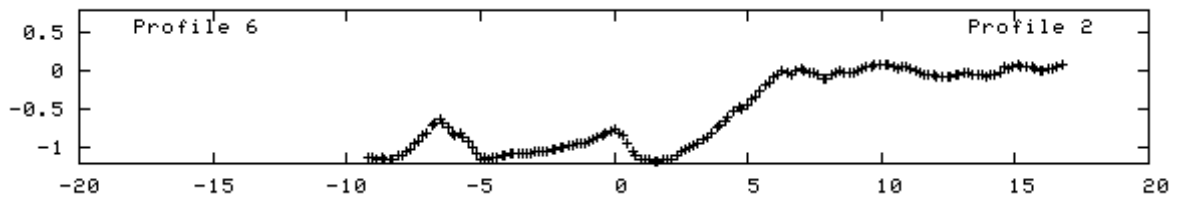
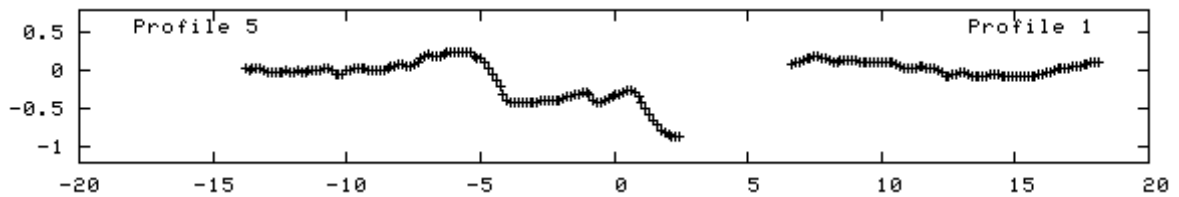


# GN30:8

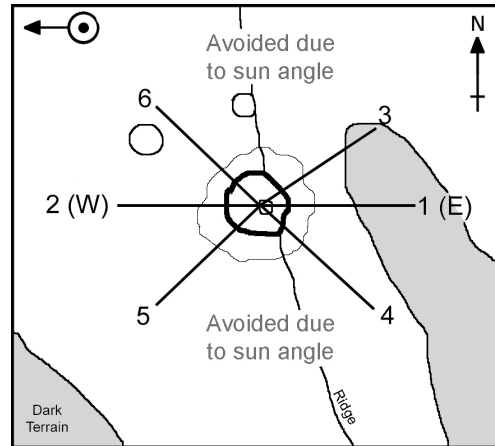
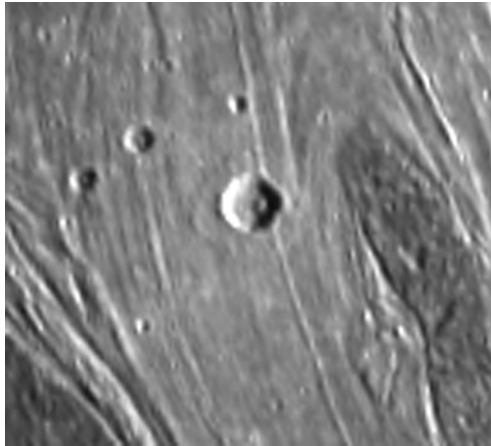


All NW profiles (7,6,5) will have been affected by the crater's location on the edge of Neith's central dome. Profiles 2,3,4 and 8 should be considered more representative for craters of this size. ((Topography from Photoclinometry))

Crater type	Central Peak
Approx. Diameter	13.4 km
Location:	29.8N, 7.6W
Terrain:	On Older Crater
Excel file name	F1

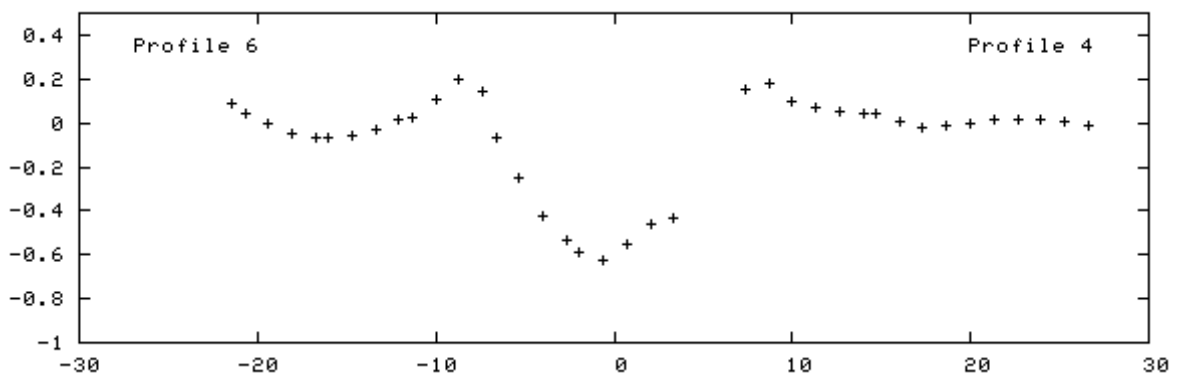
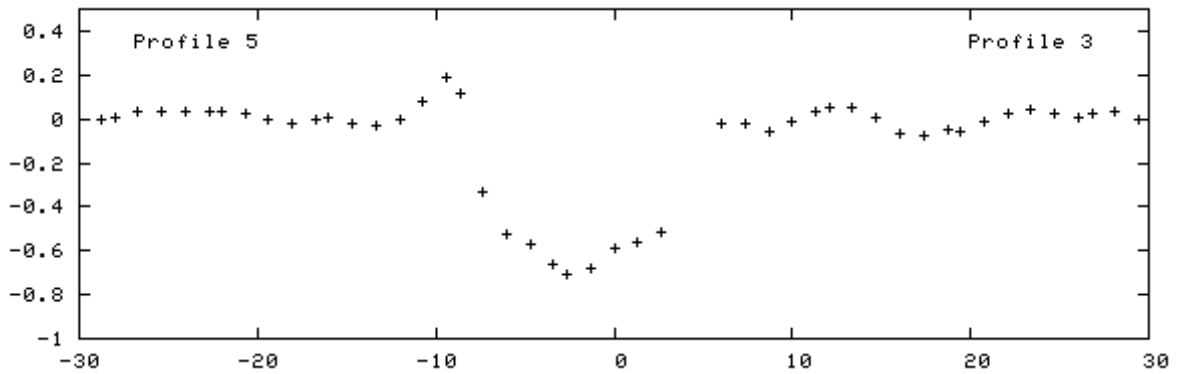
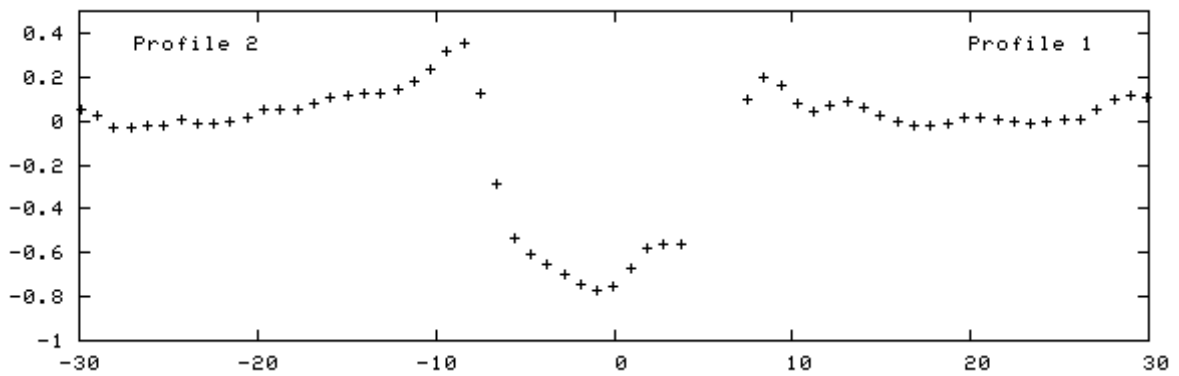


# GN50:192

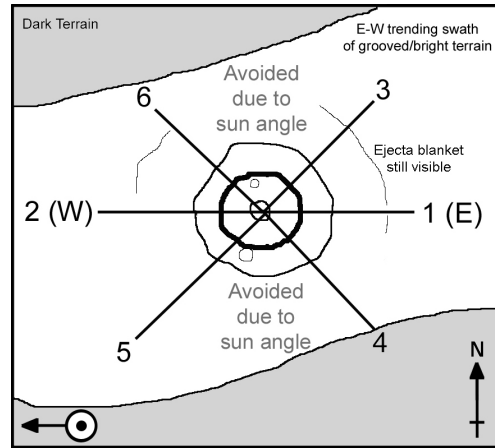
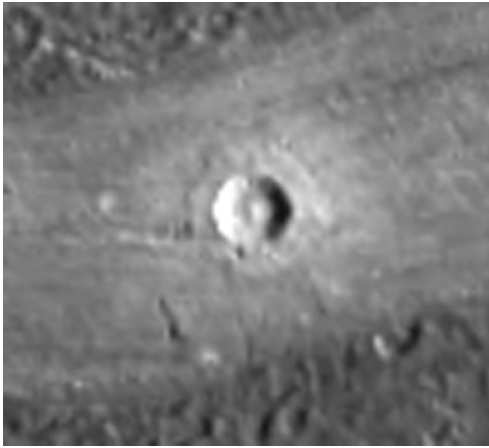


Offset central peak

Crater type	Central Peak
Approx. Diameter	17.1 km
Location:	50N : 192W
Terrain:	Bright Terrain
Excel file name	G1

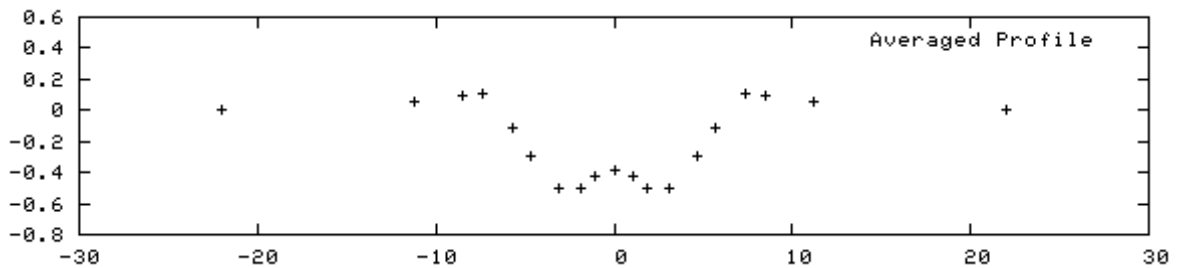
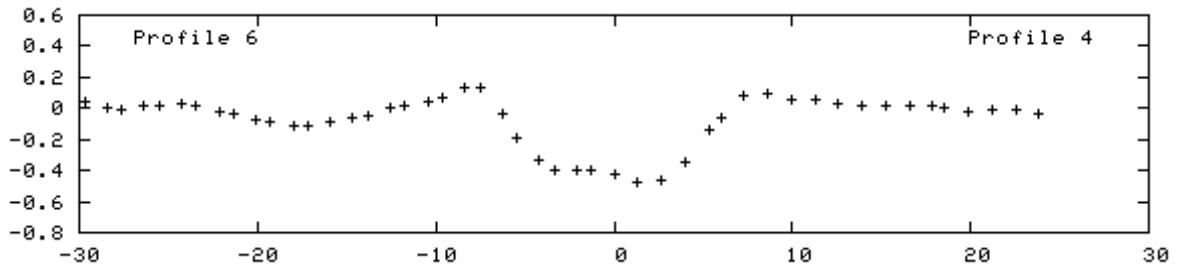
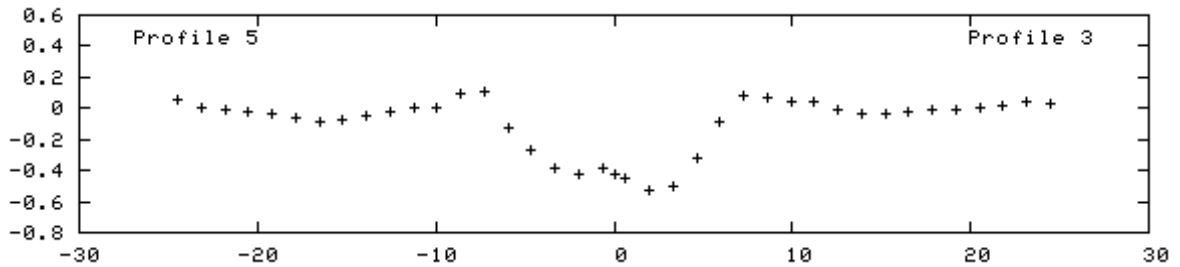
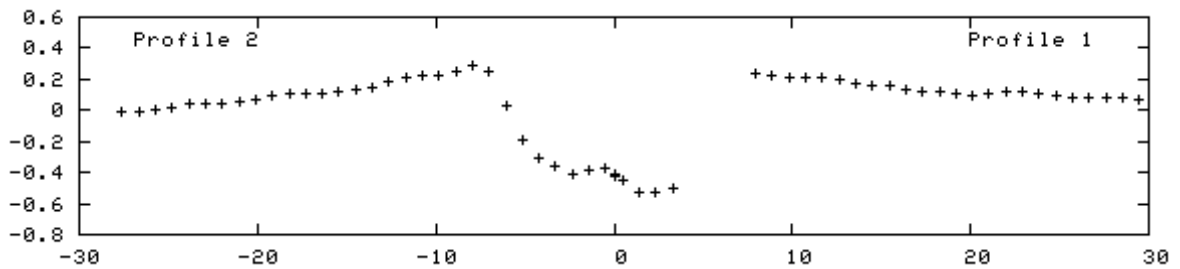


# GN39:192

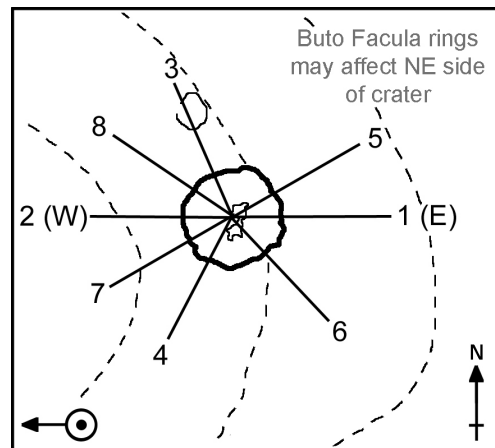
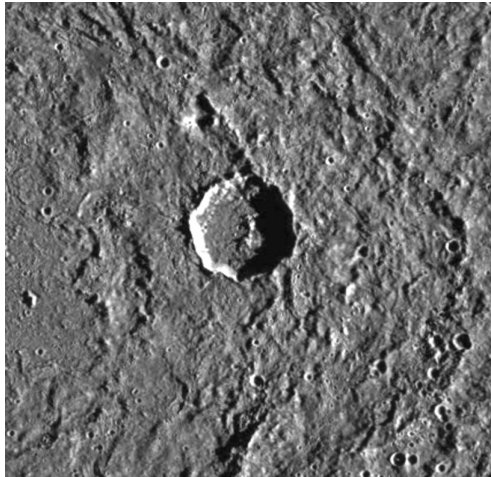


Care - low resolution for this size crater.  
 ((Topography from Stereo?))

Crater type	Central Peak
Approx. Diameter	14.7 km
Location:	39.2N : 191.7W
Terrain:	Bright Terrain
Excel file name	G3

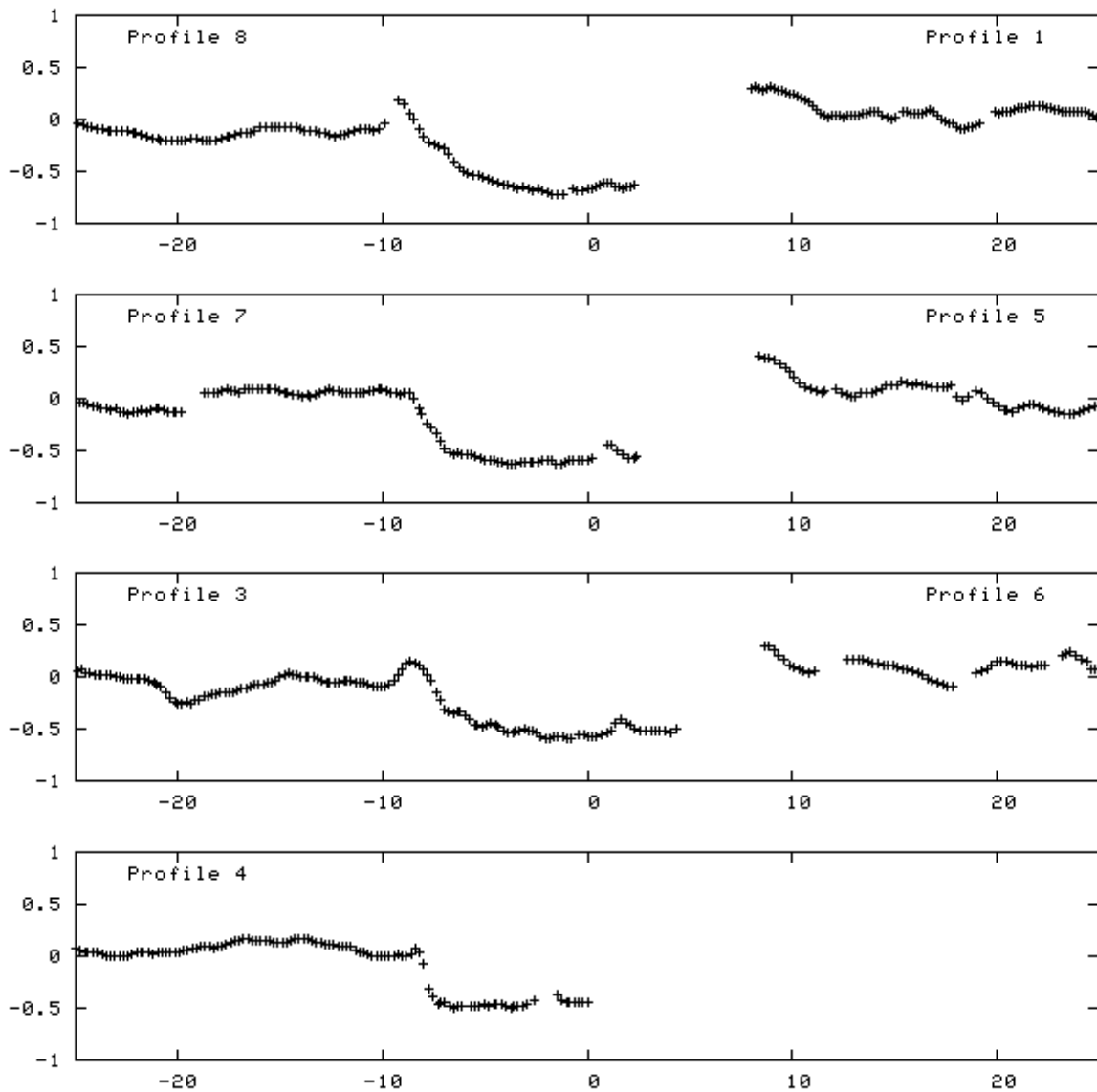


# GN14:202

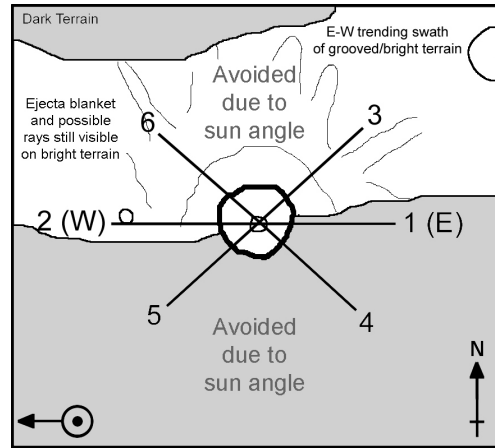


Offset and irregular central peak. ((Topography from Photoclinometry))

Crater type	Central Peak
Approx. Diameter	17.9 km
Location:	13.5N, 202.2W
Terrain:	On Older Crater
Excel file name	buto1

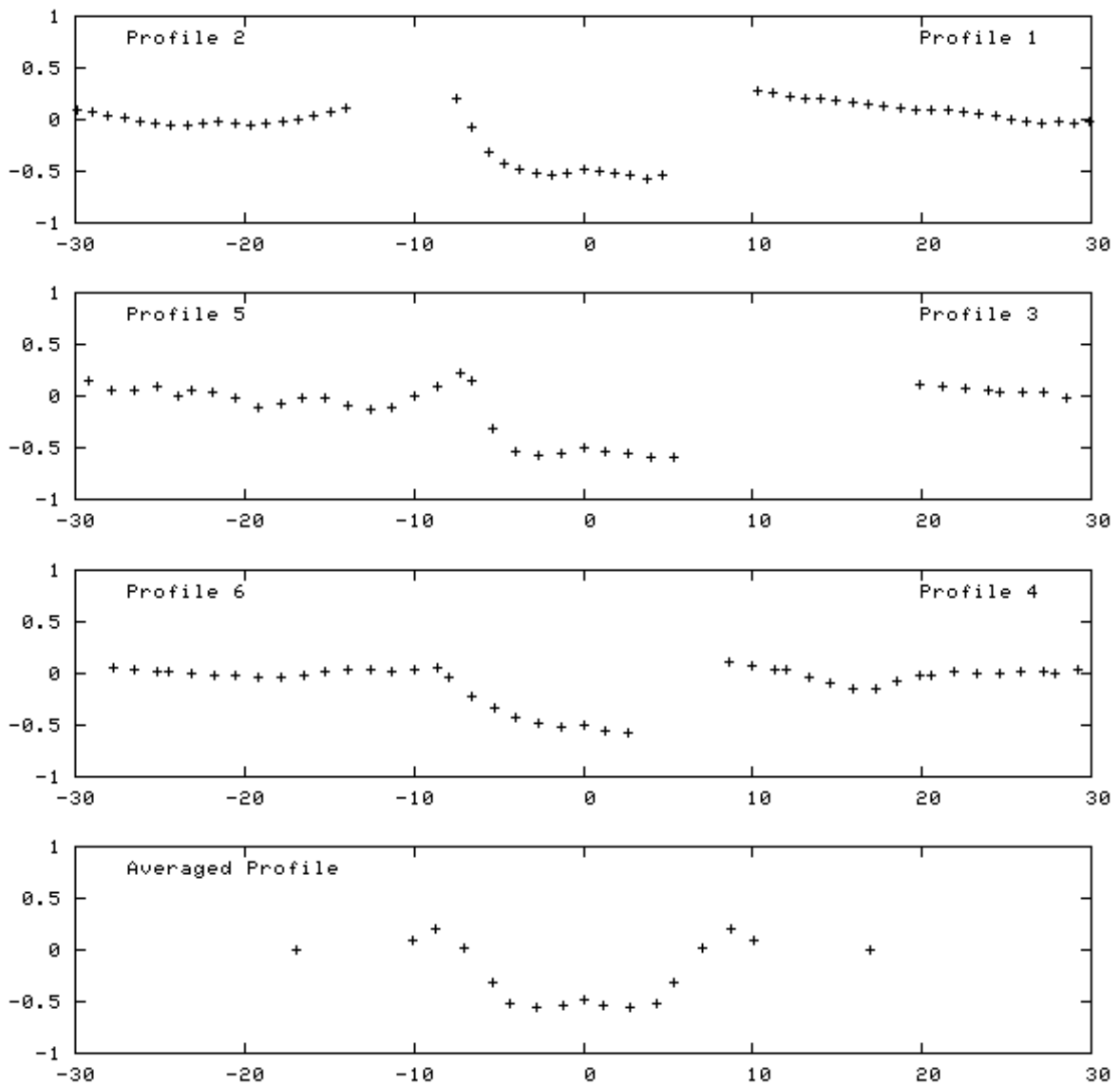


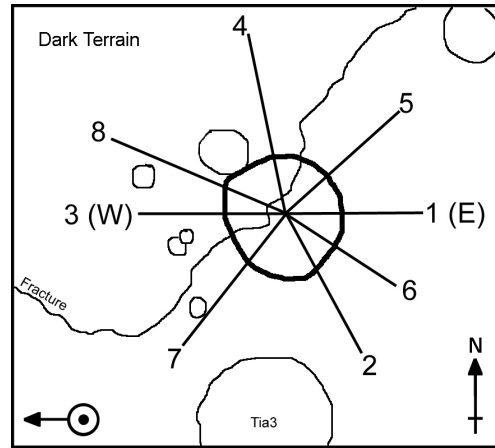
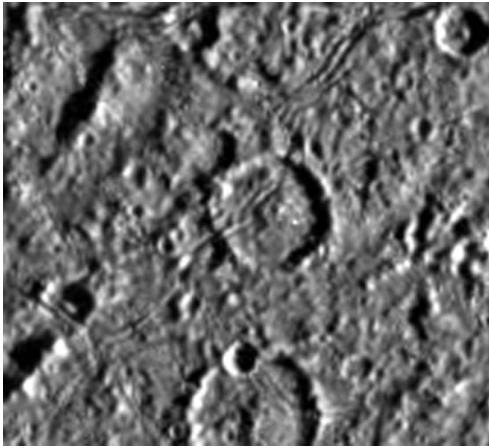
GN38:195



Care - low resolution for this size crater.  
 ((Topography from Stereo?))

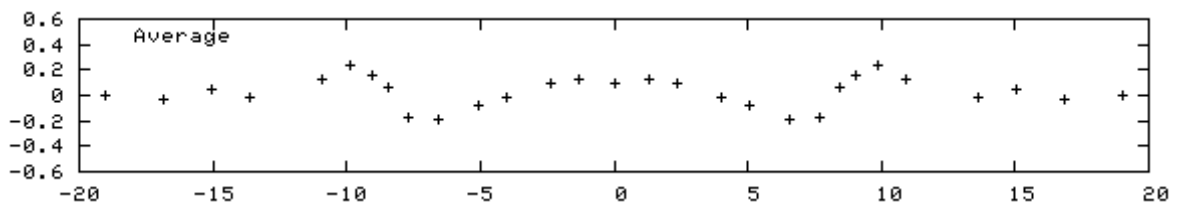
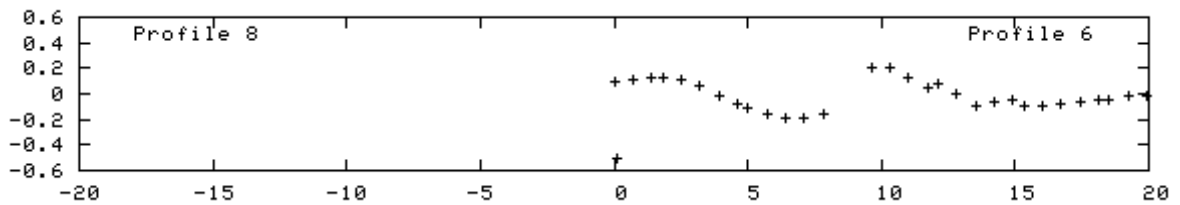
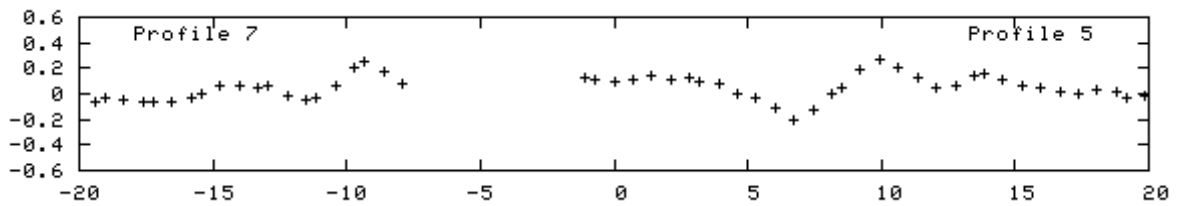
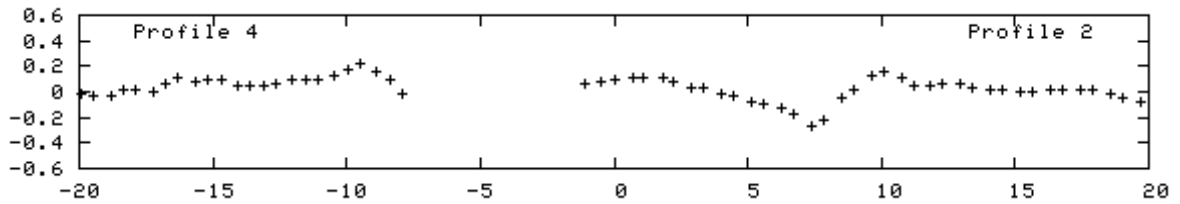
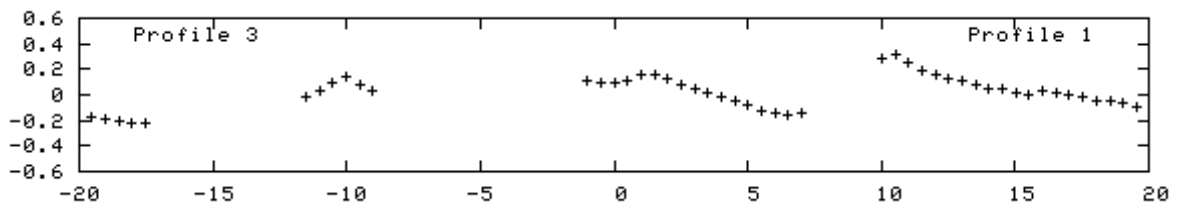
Crater type	Central Peak
Approx. Diameter	17.5 km
Location:	38.4N, 194.9W
Terrain:	Bright/Dark Terrain boundary
Excel file name	G4



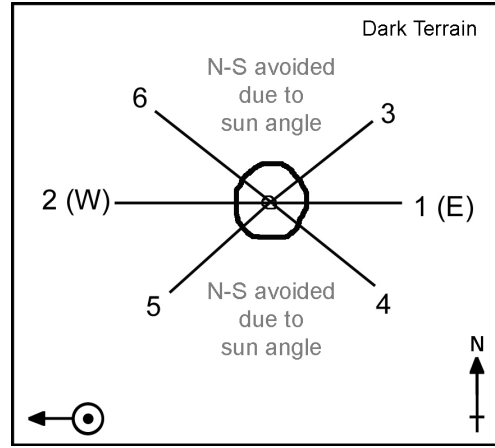
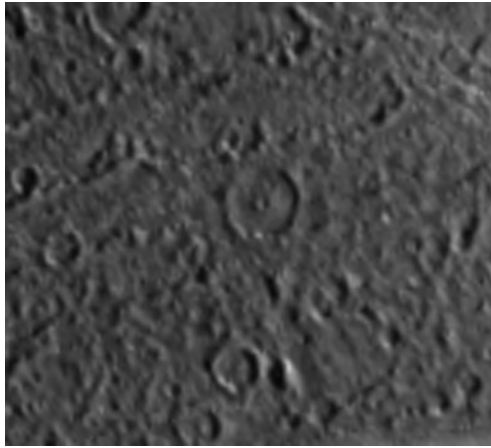


((Topography from Photoclinometry))

Crater type	Summit Pit
Approx. Diameter	19.7 km
Location:	0.4N : 201.4
Terrain:	Dark Terrain
Excel file name	Tia2

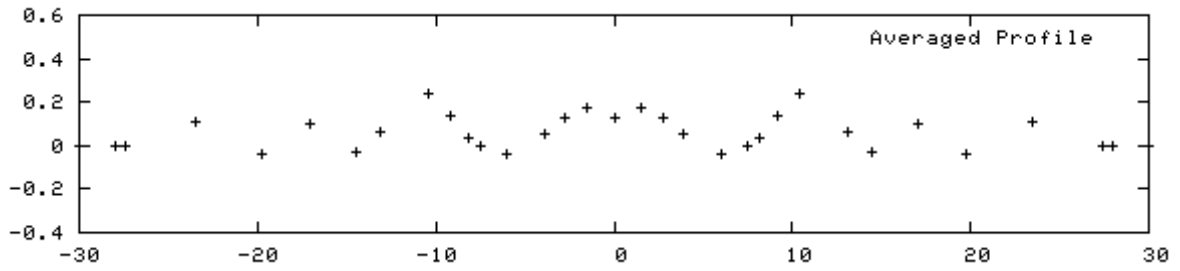
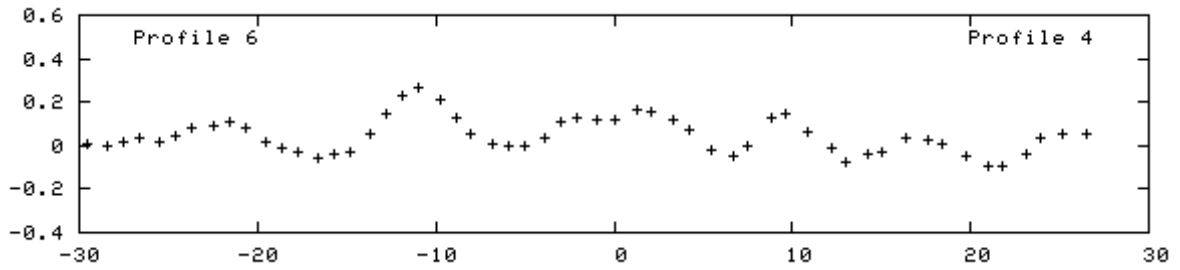
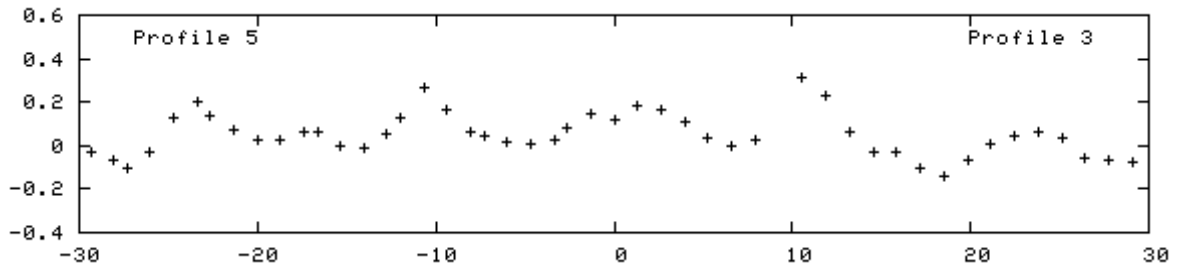
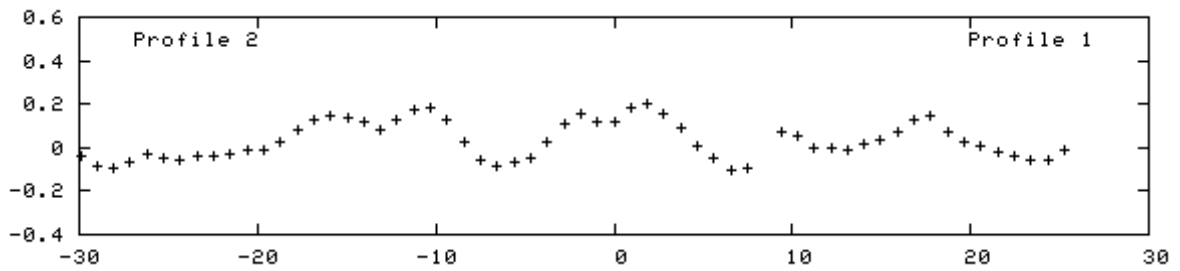


# GN41:195

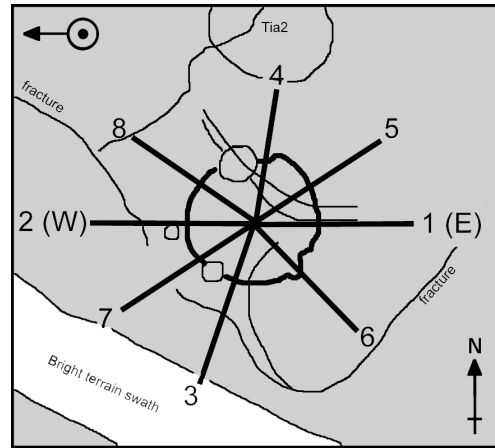
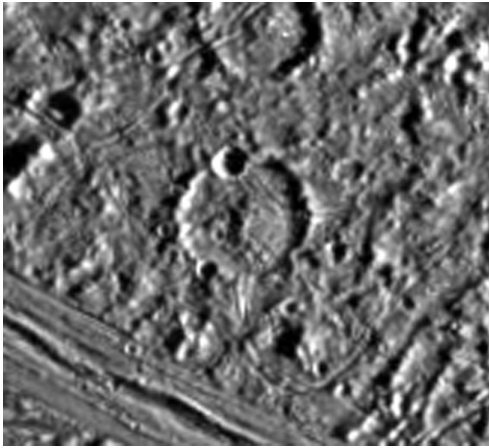


((Topography from Photoclinometry))

Crater type	Central Peak
Approx. Diameter	20.8 km
Location:	41N 195.4W
Terrain:	Dark Terrain
Excel file name	G7

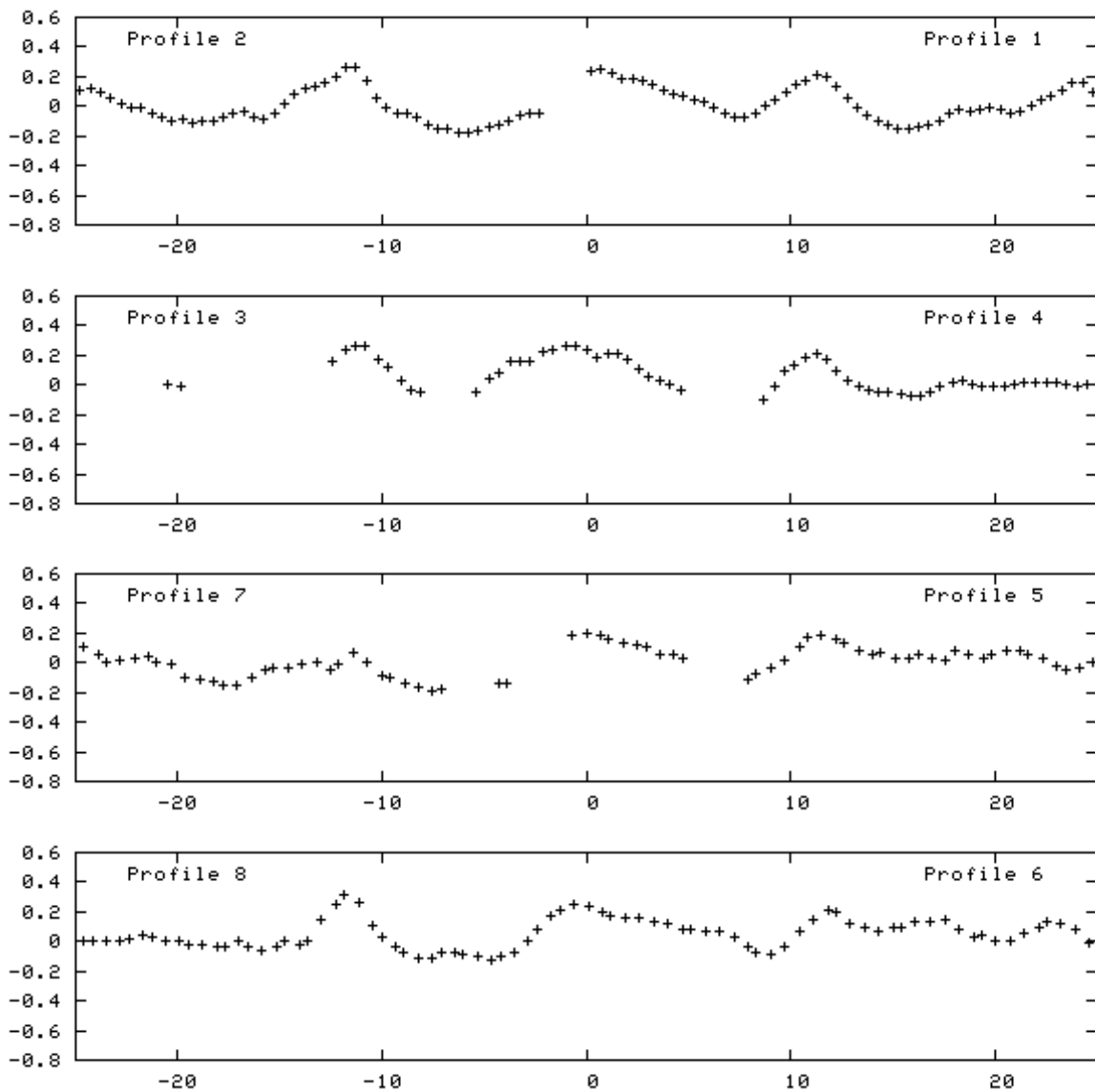


# GN0:202

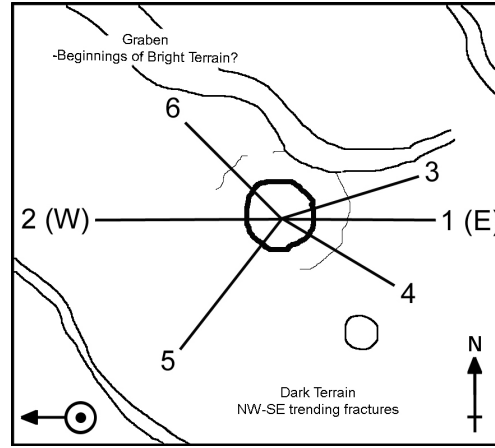
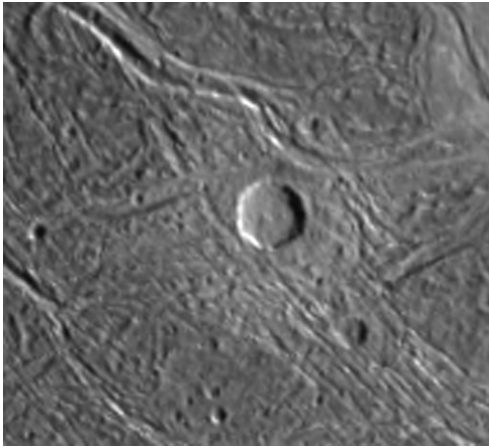


Relaxed, similar morphology to GN0201/Tia2 but without the pitted summit. ((Topography from Photoclinometry))

Crater type	Central Peak
Approx. Diameter	22.9 km
Location:	0.4N : 201.5W
Terrain:	Dark Terrain
Excel file name	Tia3

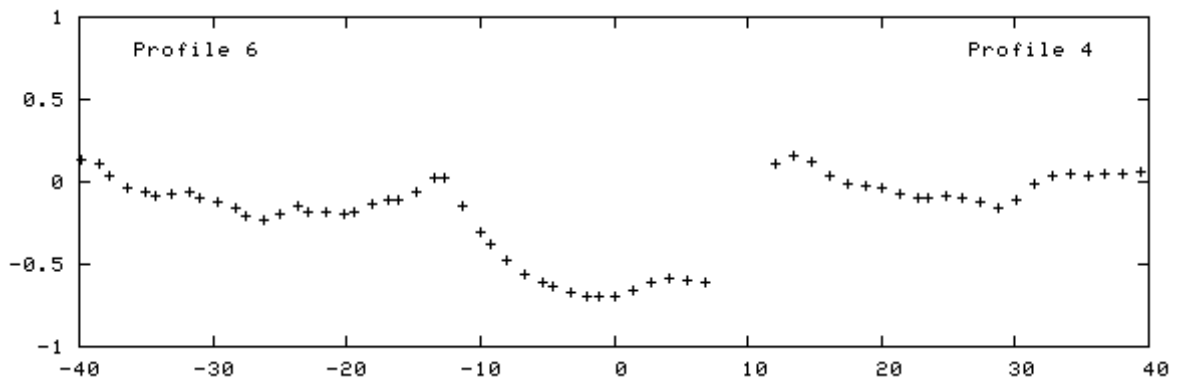
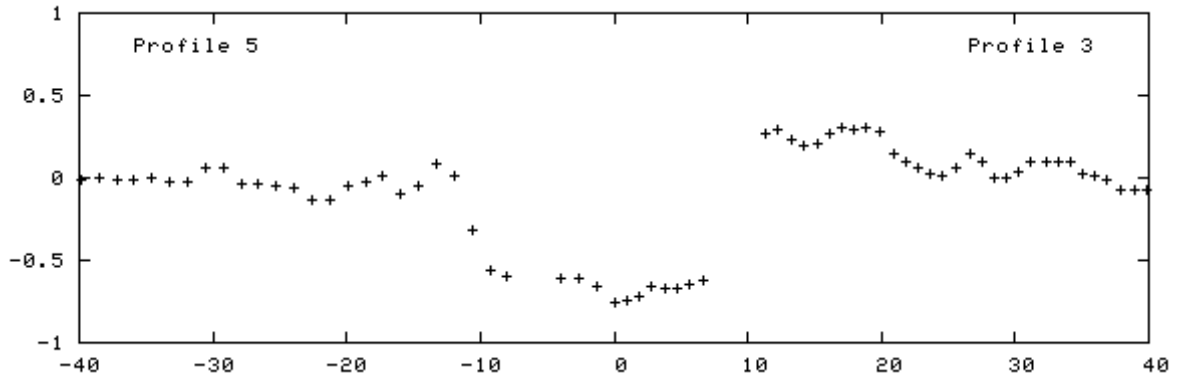
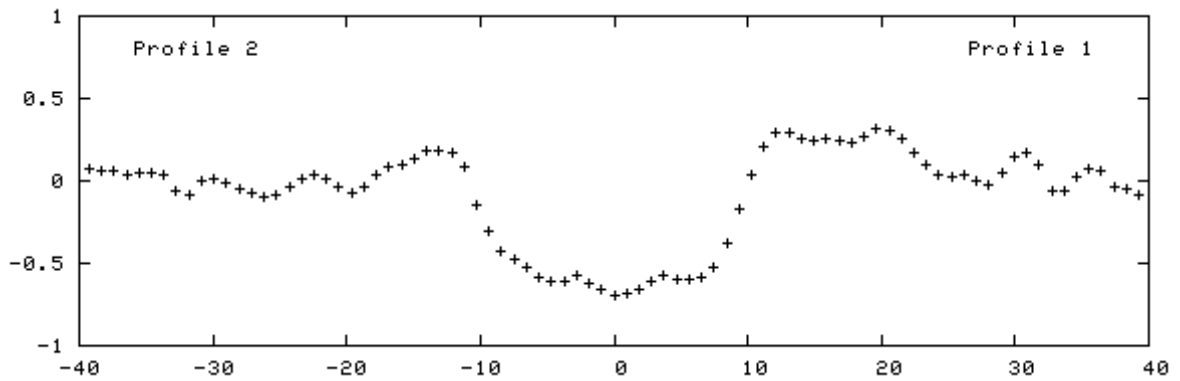


GN33:192

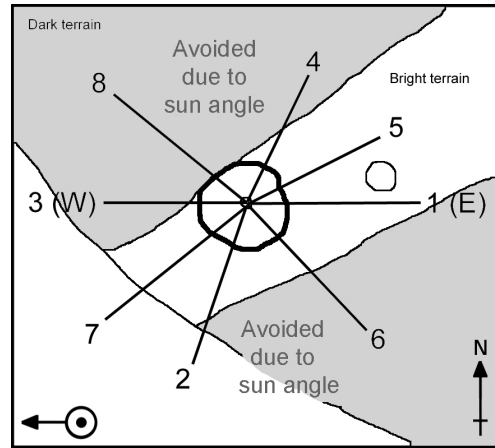
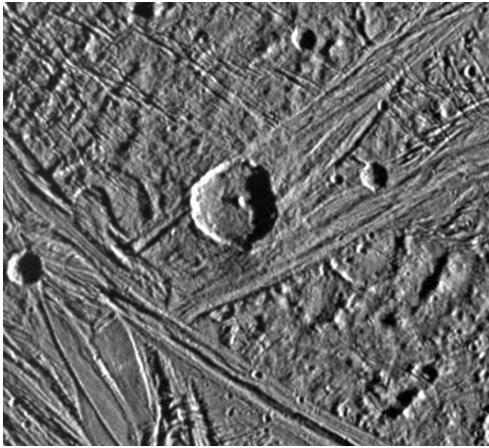


Ejecta still visible - lack of significant central topography is not necessarily due to degradation.

Crater type	Degraded/Floor Pit
Approx. Diameter	26 km
Location:	33N, 192W
Terrain:	Dark Terrain
Excel file name	G6

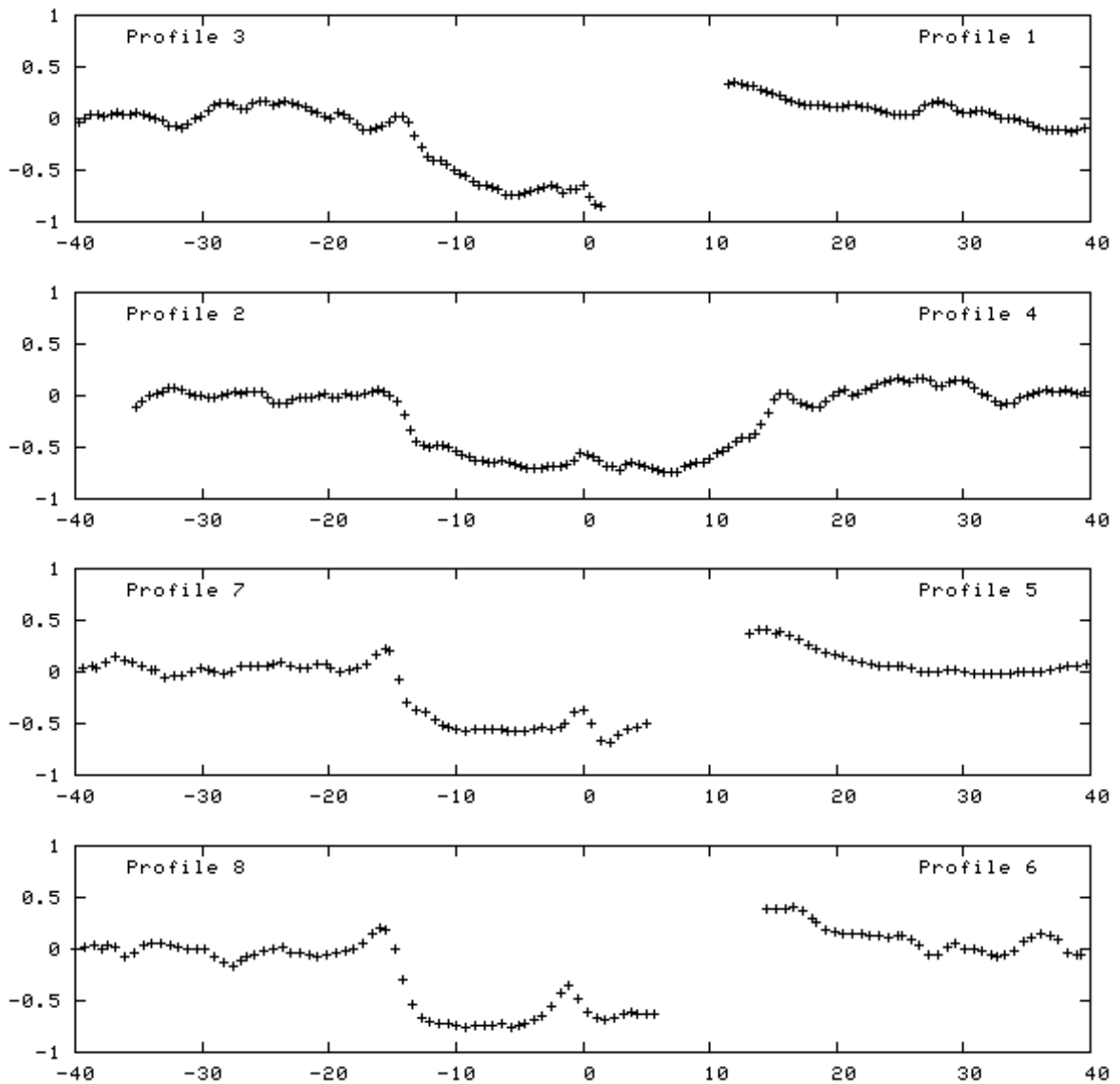


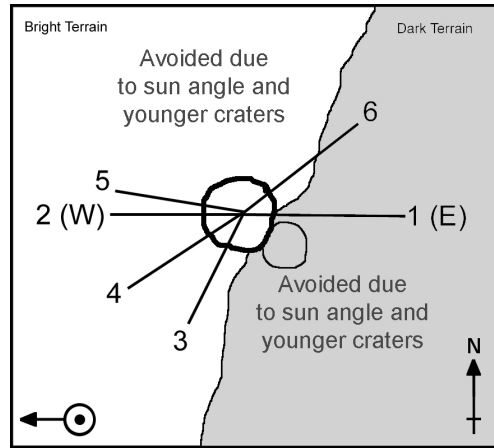
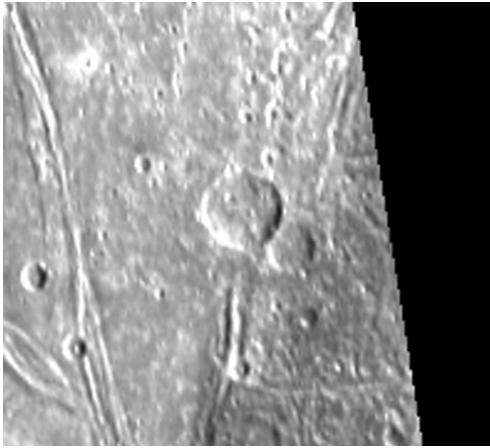
# GN1:204



((Topography from Photoclinometry))

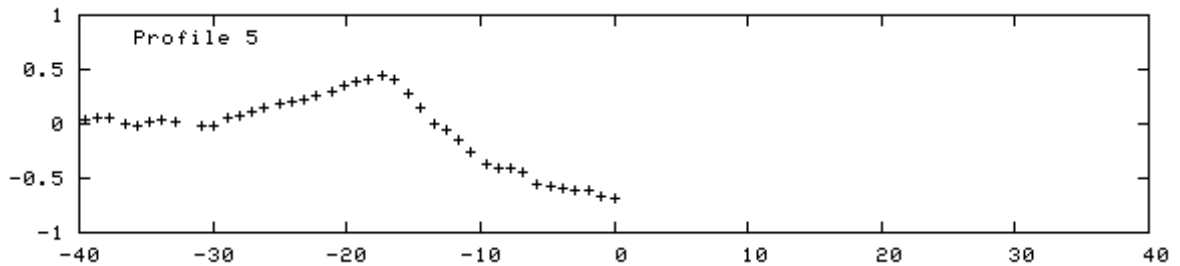
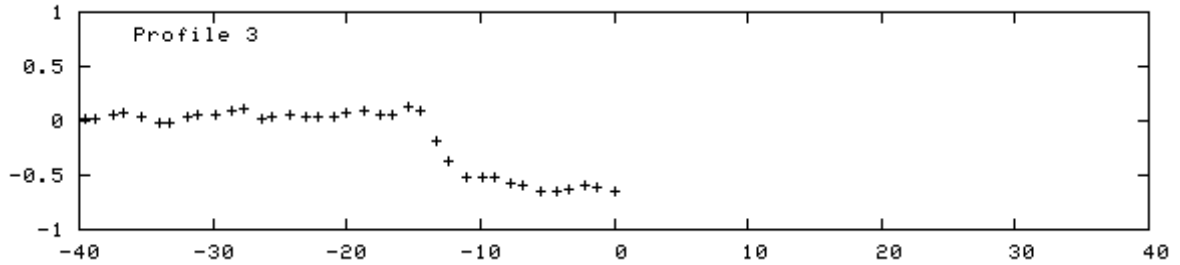
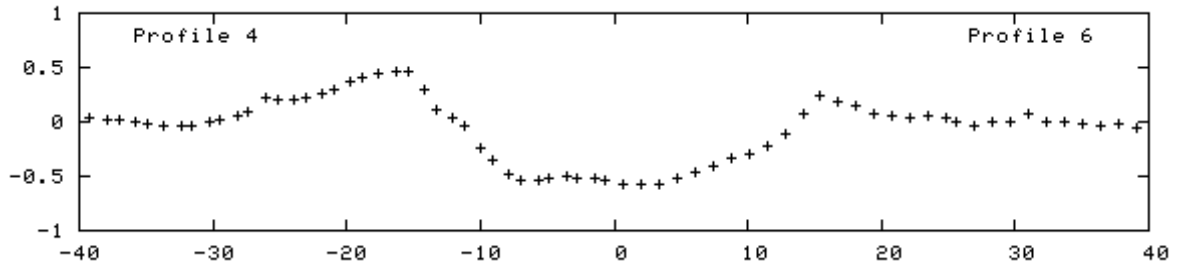
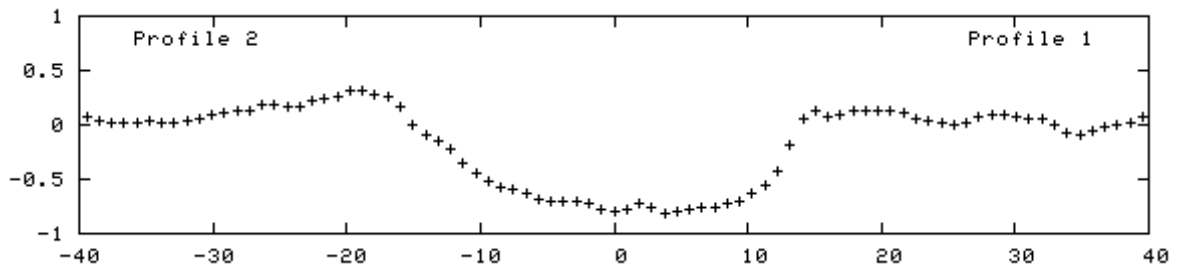
Crater type	Central Peak
Approx. Diameter	31.8 km
Location:	1.4N : 203.5
Terrain:	Bright Terrain
Excel file name	Tia1



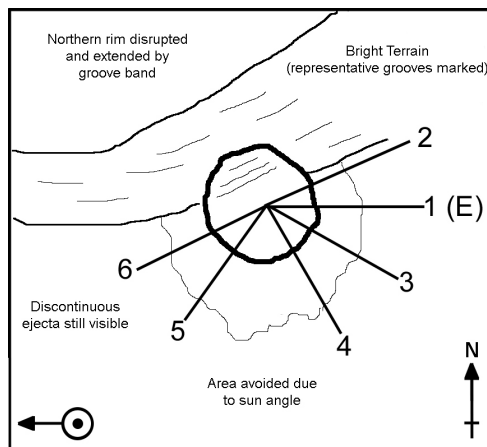


((Topography from Stereo))

Crater type	Degraded/Unknown
Approx. Diameter	35.2 km
Location:	49.4N, 183.5W
Terrain:	Bright Terrain
Excel file name	G5

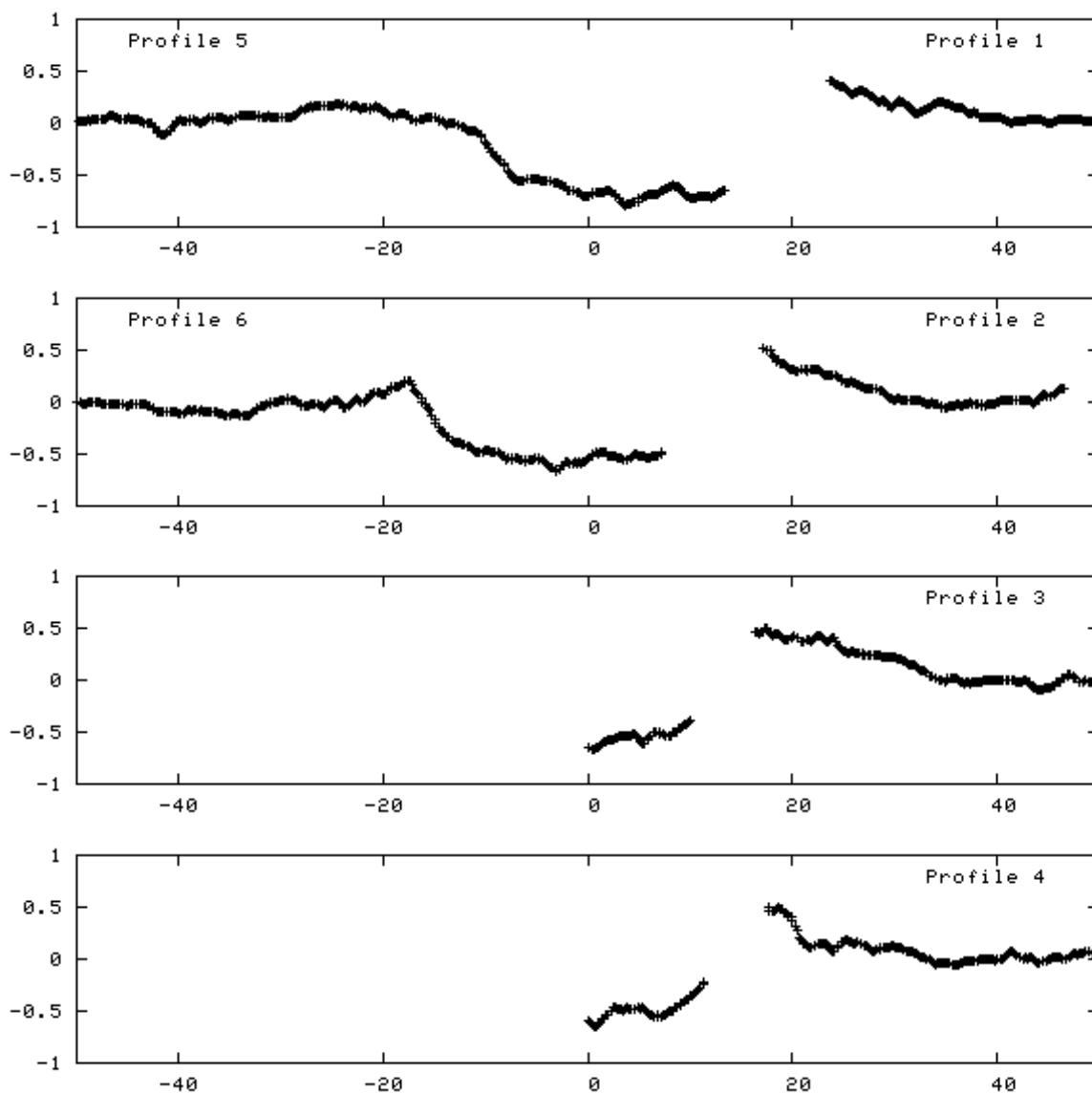


# Achelous

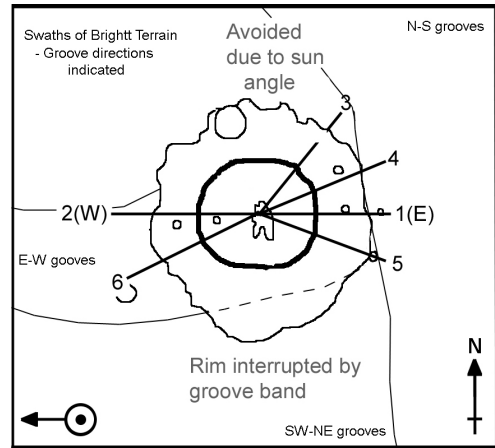
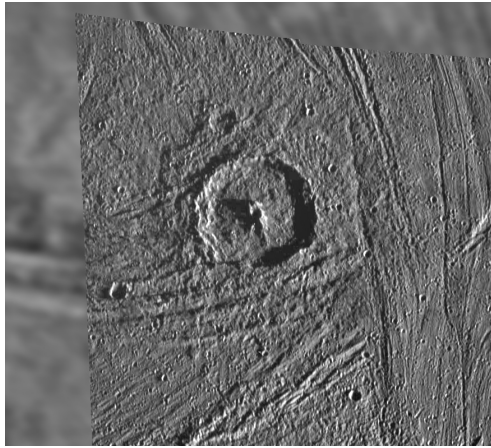


On same bright terrain unit as Gula, with similar diameter but strikingly different morphology. Internal features are more apparent in the image than topographic profile.

Crater type	Central pit/Flat Floored
Approx. Diameter	34.7 km
Location:	61.8N:11.7W
Terrain:	Bright Terrain
Excel file name	Achelous

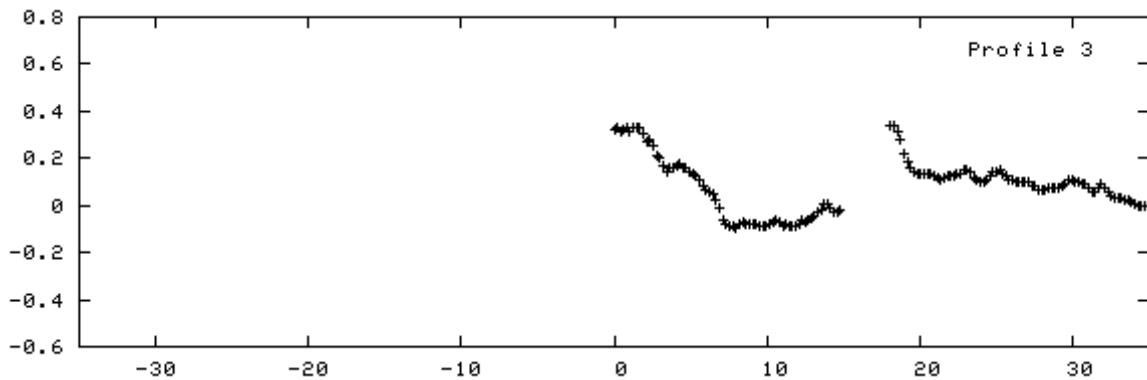
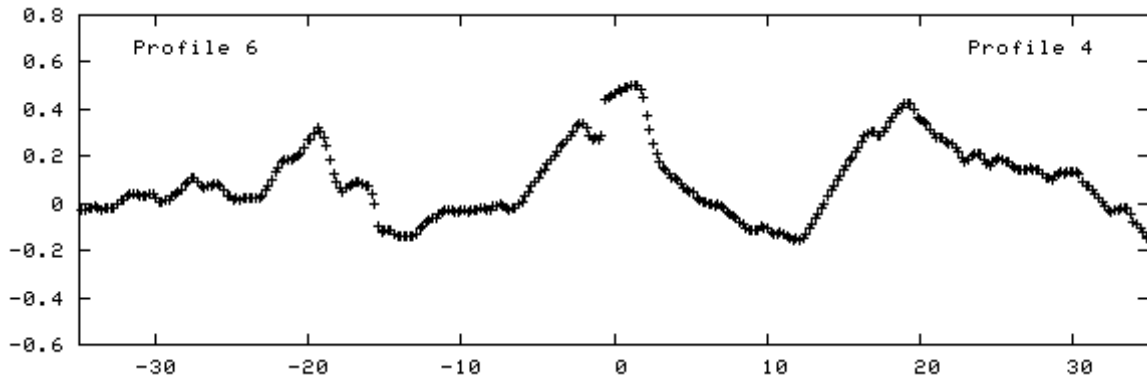
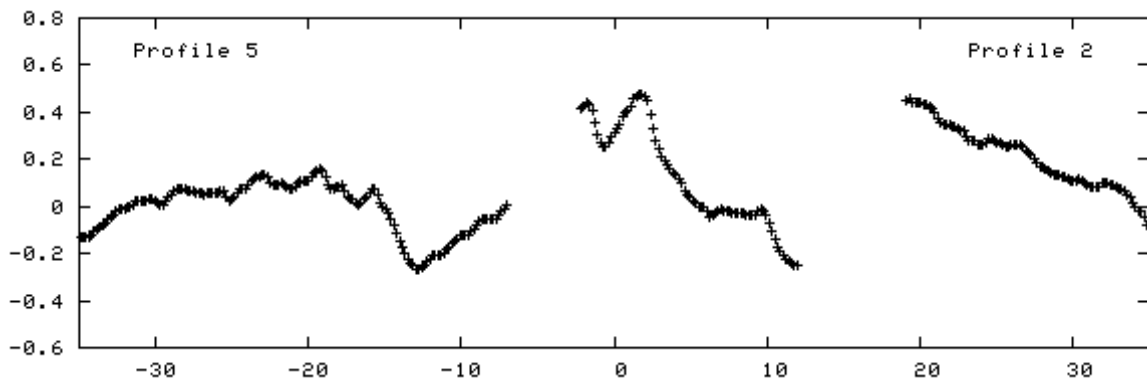


# Gula

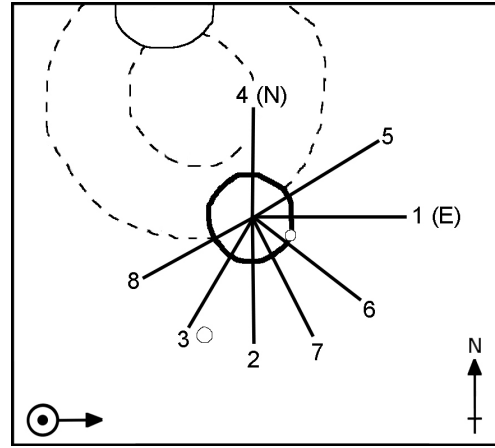
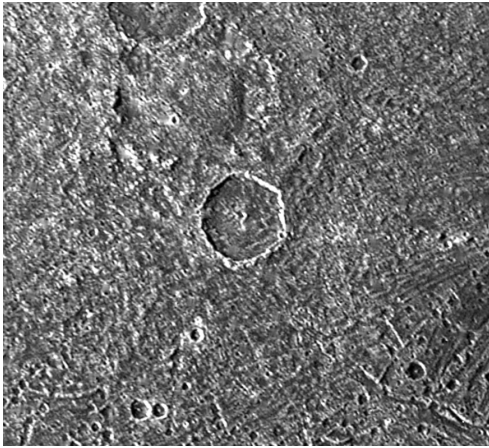


The central peak may not actually exceed the rim height, but more likely to be an artifact due to extreme shadowing. Commonly classified as a central peak crater.

Crater type	Summit Pit
Approx. Diameter	39.3 km
Location:	64.1N, 12.3W
Terrain:	Bright Terrain
Excel file name	Gula

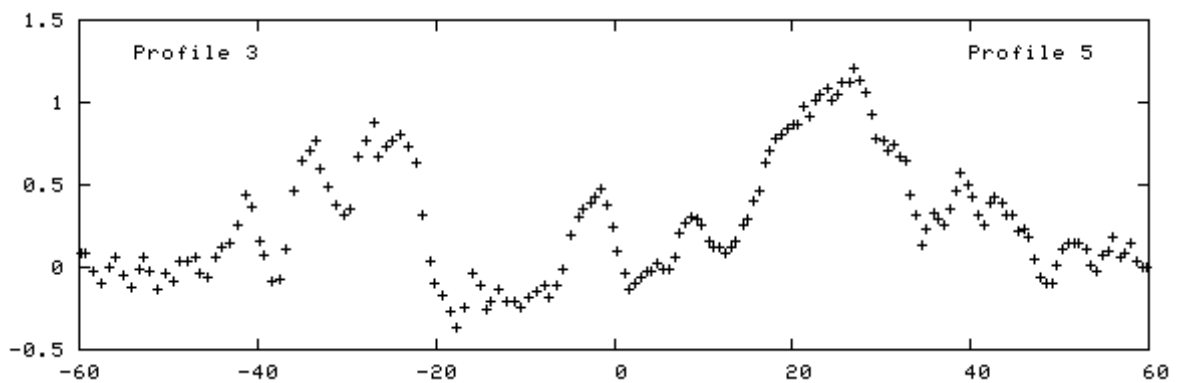
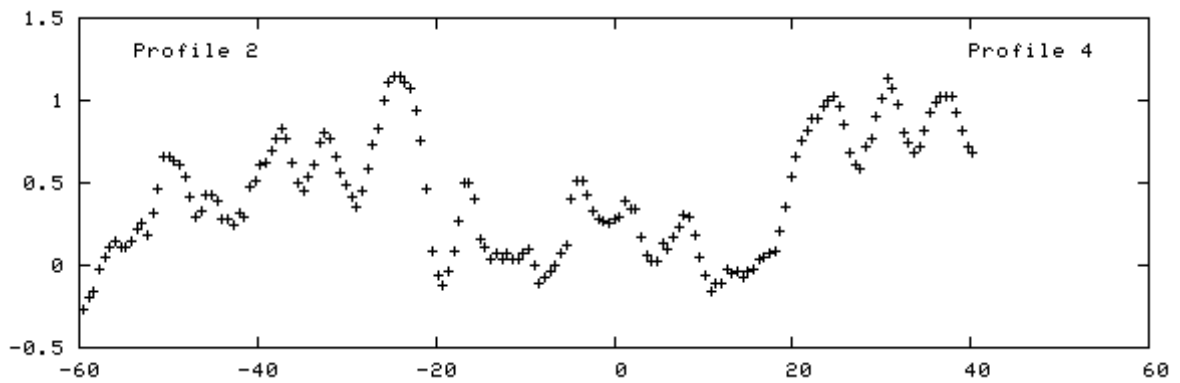
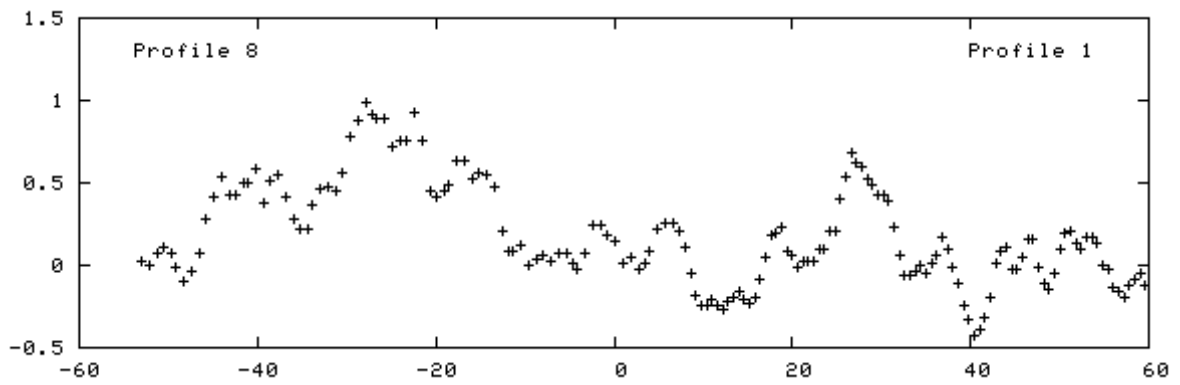


ZS37:139

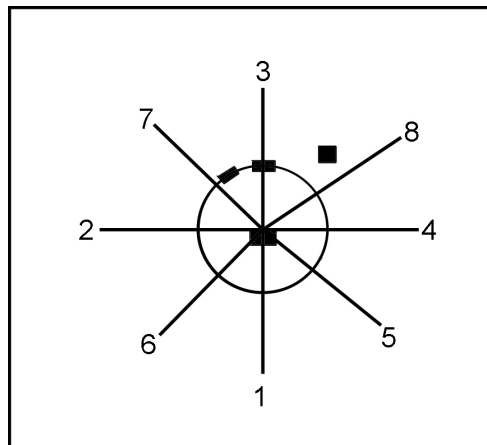
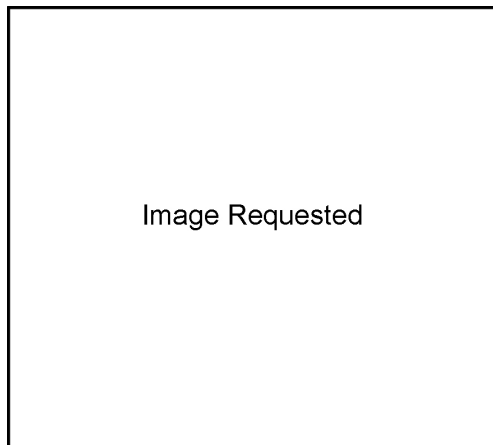


((Topography from Stereo))

Crater type	Central Pit
Approx. Diameter	52.1 km
Location:	37.7N:140.2W
Terrain:	On Older Crater
Excel file name	Z2

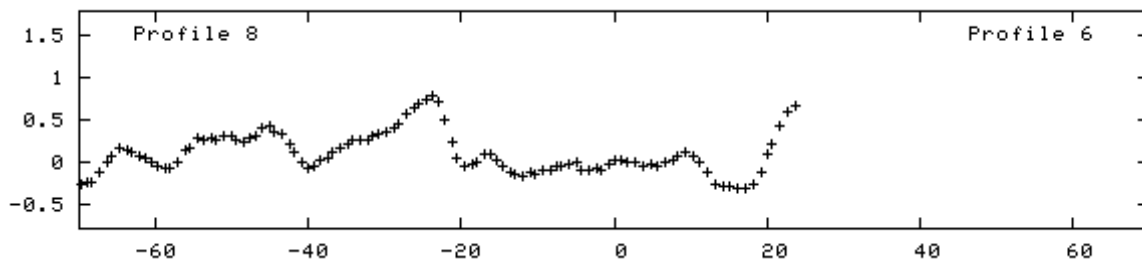
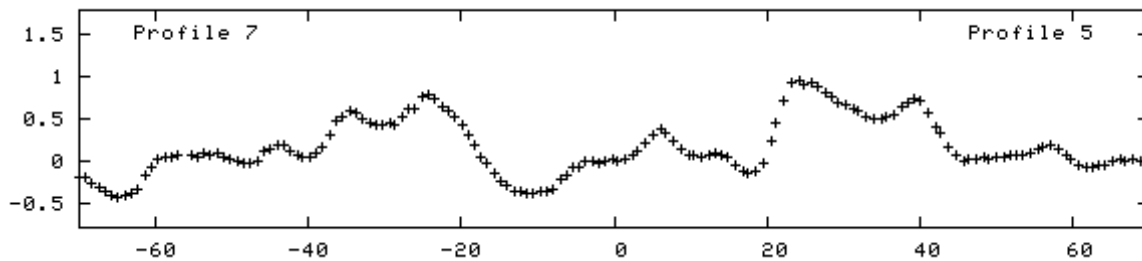
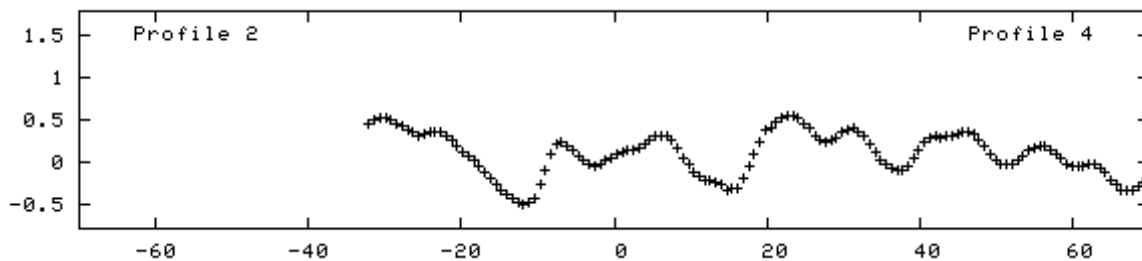
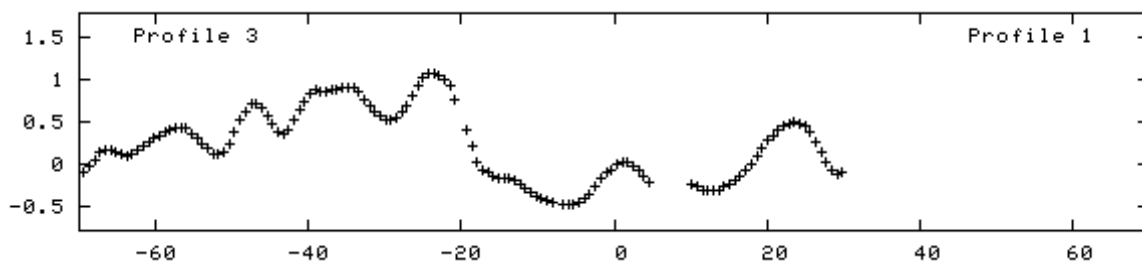


# GS69:231

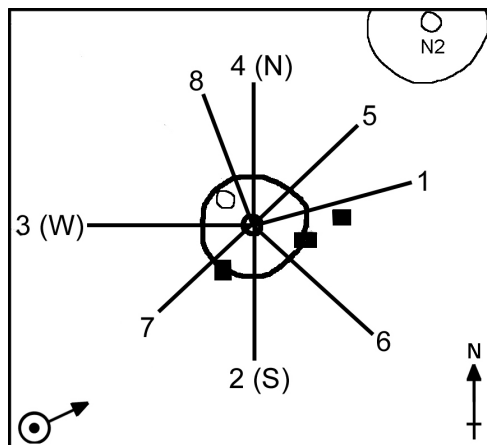
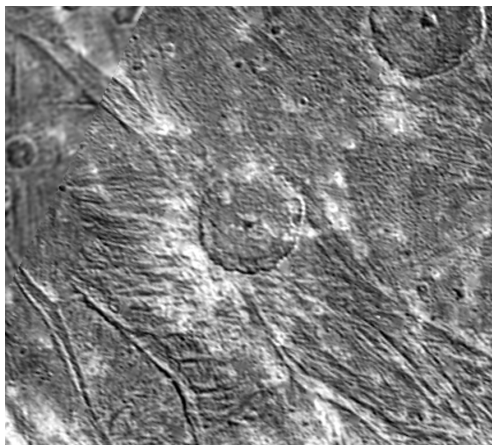


Frequent data gaps in this dataset - marked by blacked out areas. Inconsistent central morphology. Lack of image may cause artefacts to still be present in the profiles. ((Topography from Stereo))

Crater type	Central pit
Approx. Diameter	47.4 km
Location:	68.7S : 230.9W
Terrain:	Bright Terrain
Excel file name	bub4

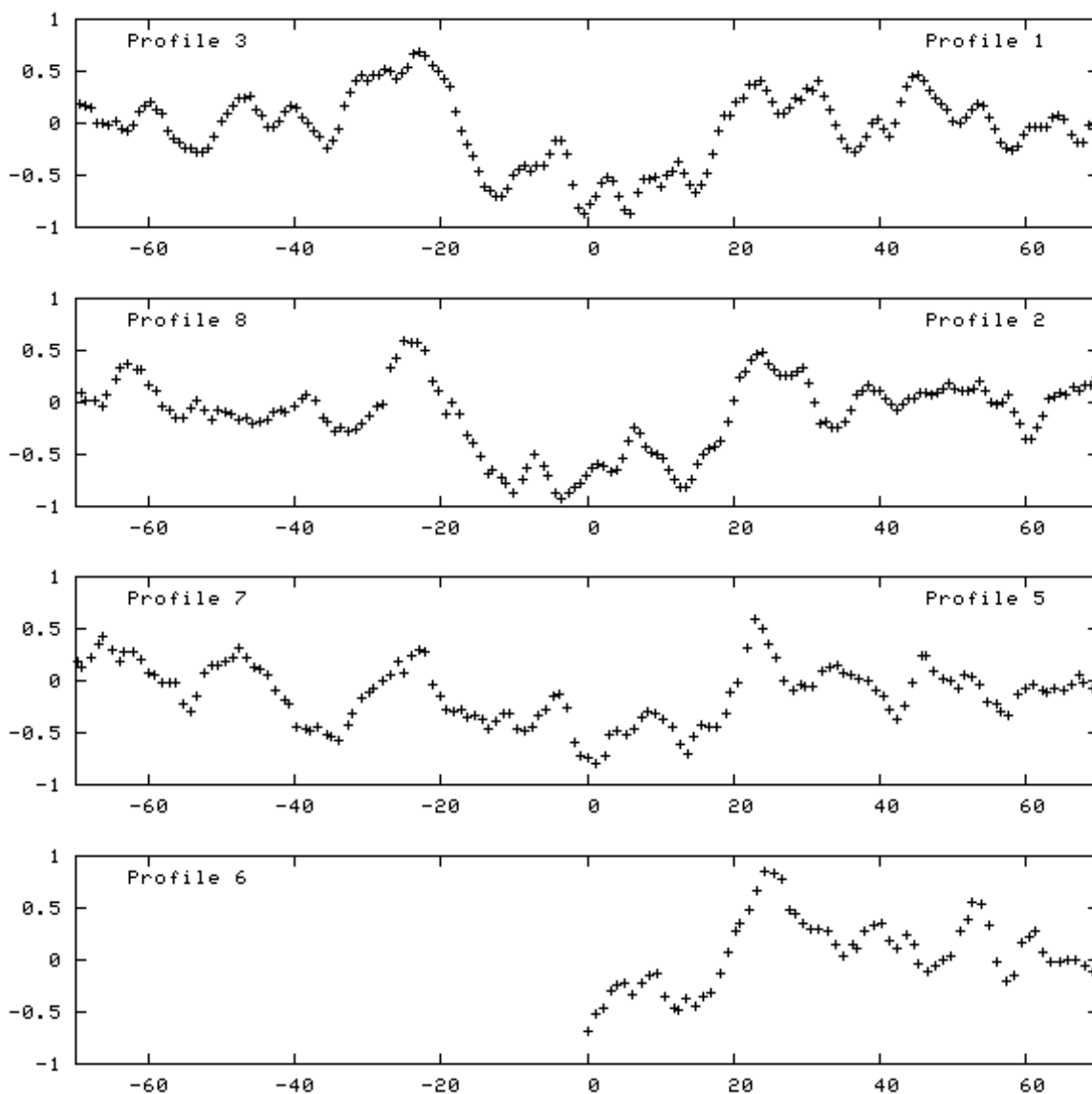


# GS31:170

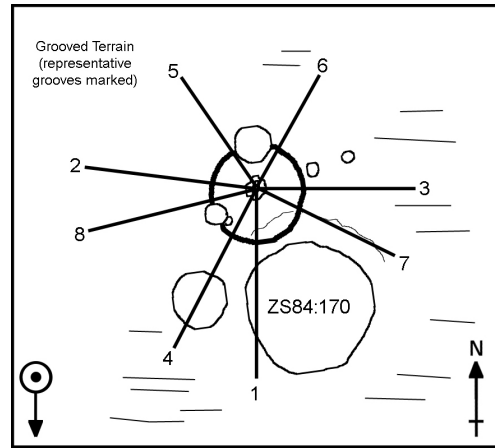
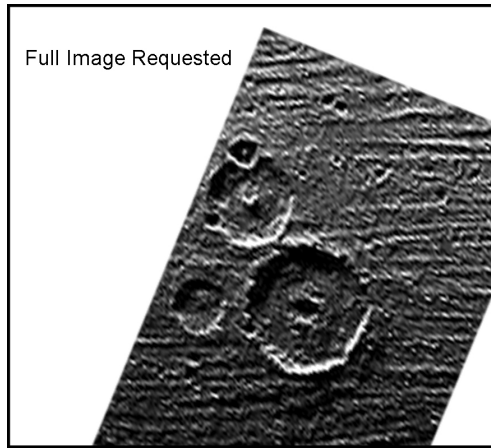


Frequent data gaps in this dataset - marked by blacked out areas.

Crater type	Central Pit
Approx. Diameter	47 km
Location:	30.8S : 169.7W
Terrain:	Bright Terrain
Excel file name	N3

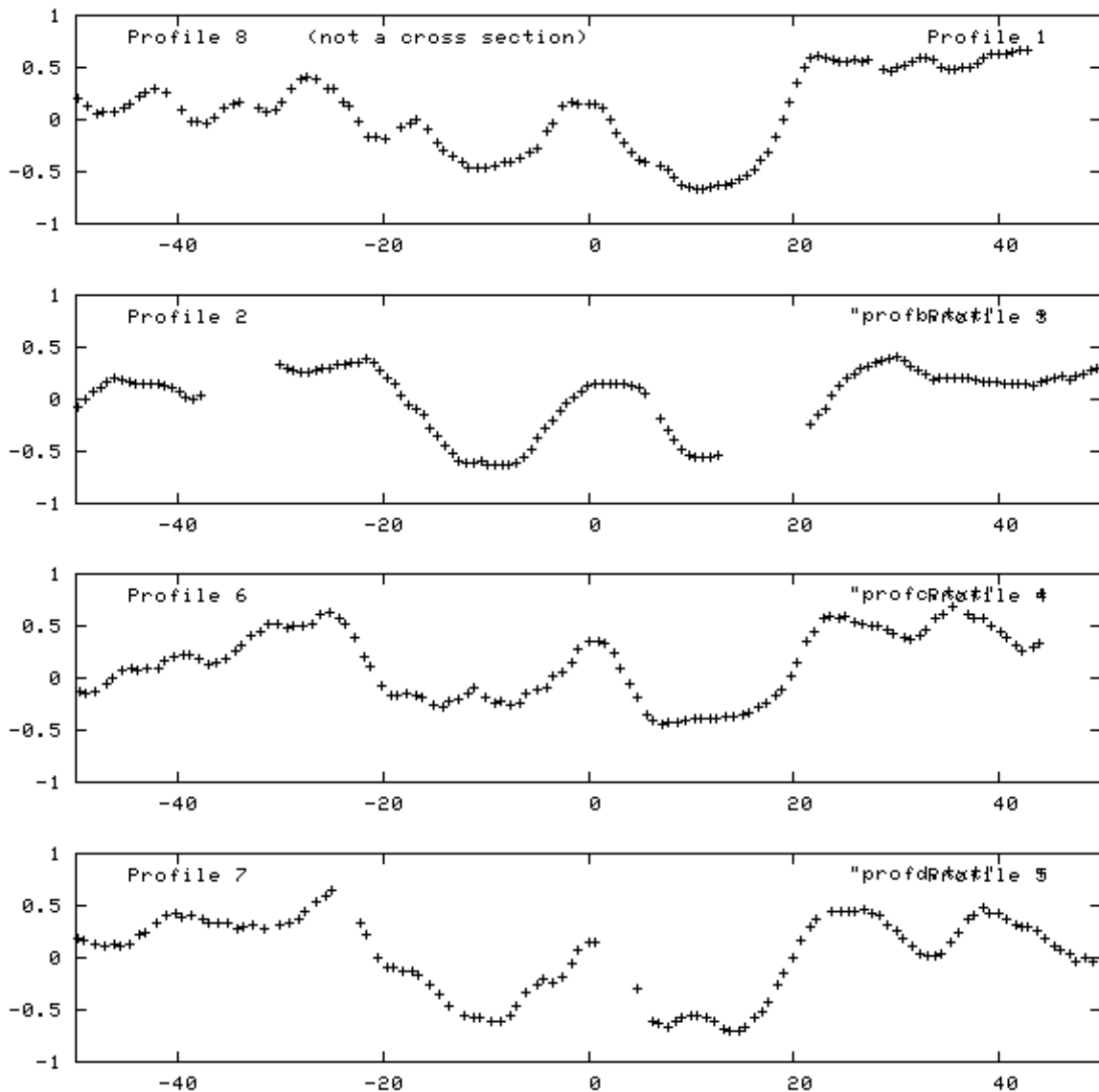


# GS83:198

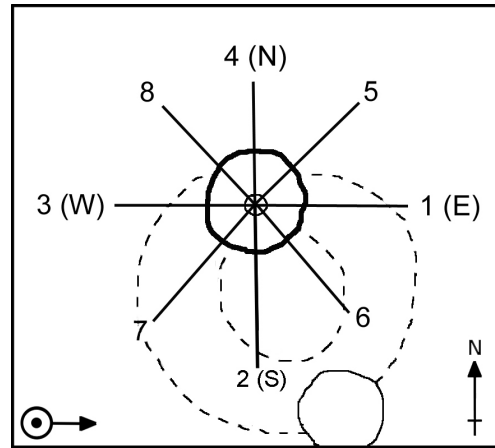
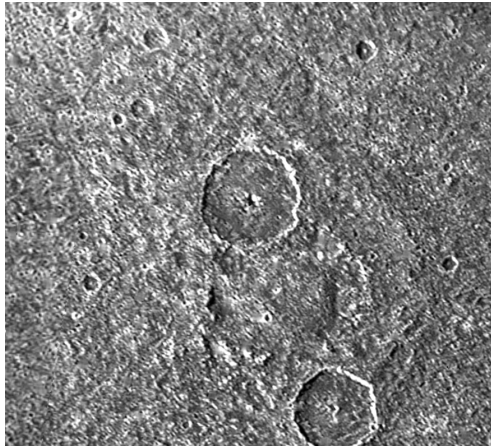


Frequent data gaps in this dataset - marked by blacked out areas. Image suggests this is a central pit crater, the profiles suggest it is a central peak crater. ((Topography from Stereo))

Crater type	Central pit (?)
Approx. Diameter	50.4 km
Location:	83.1S : 197.7W
Terrain:	Dark Terrain
Excel file name	bub1

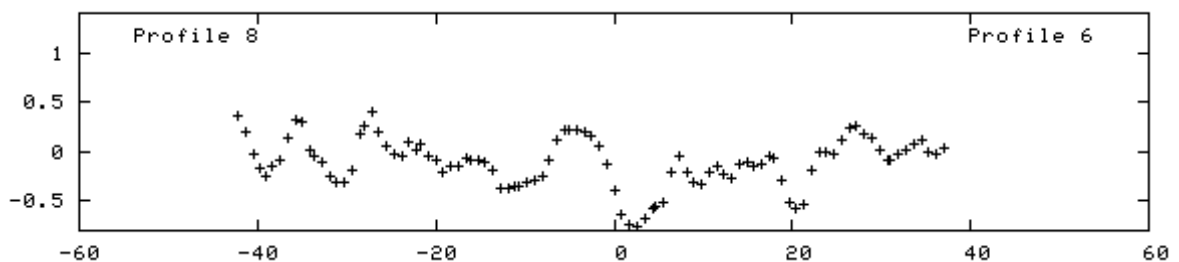
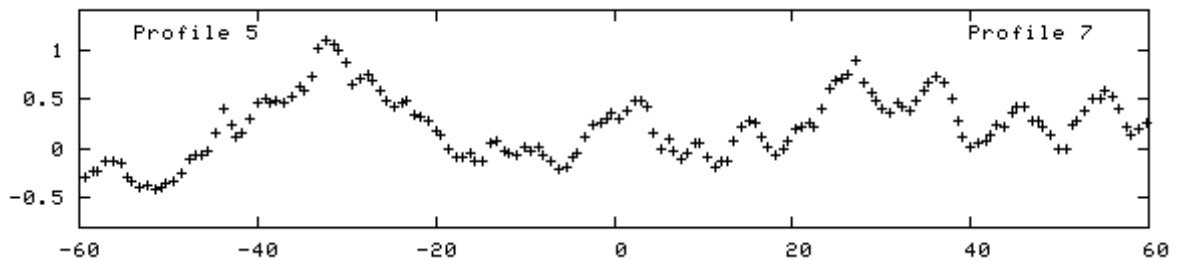
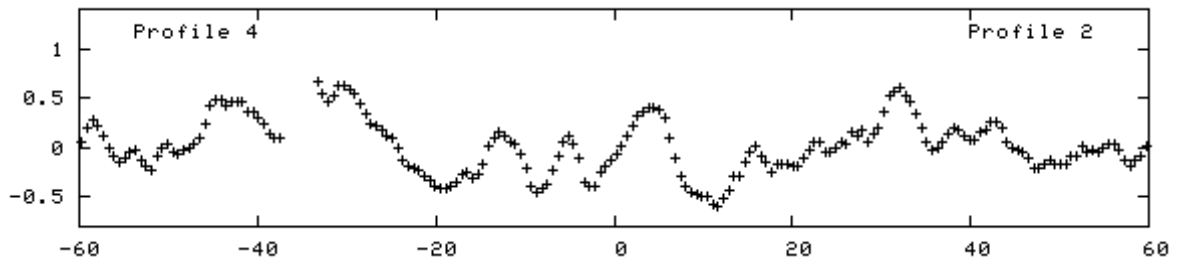
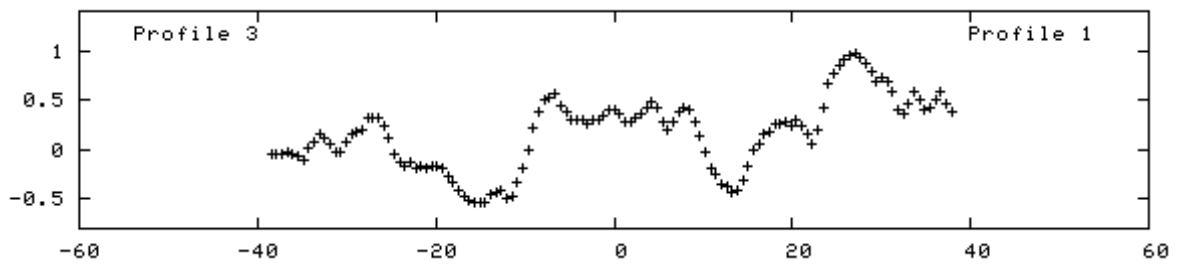


# ZS34:140

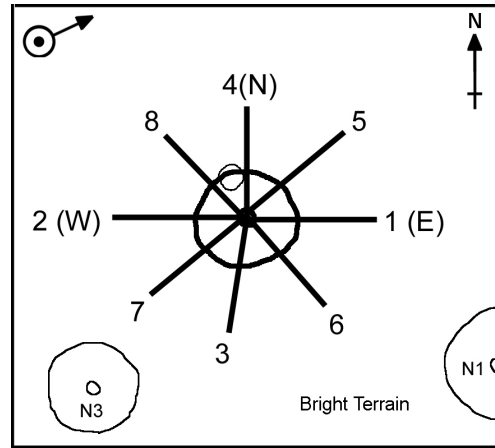


Obvious mosaic line running E-W central to the crater. This will have affected profiles 1 and 3. ((Topography from Stereo))

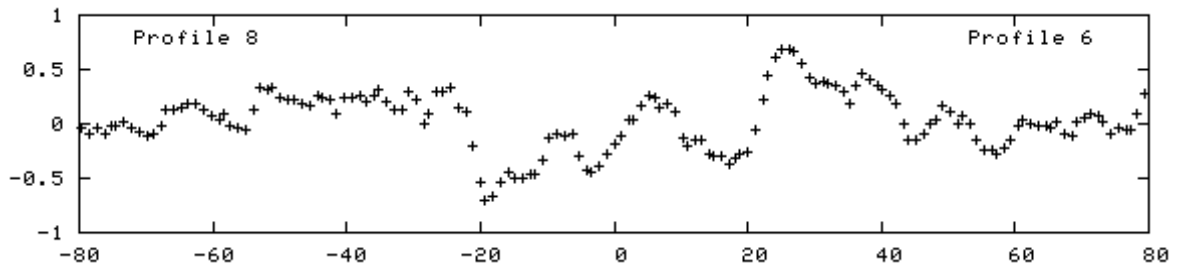
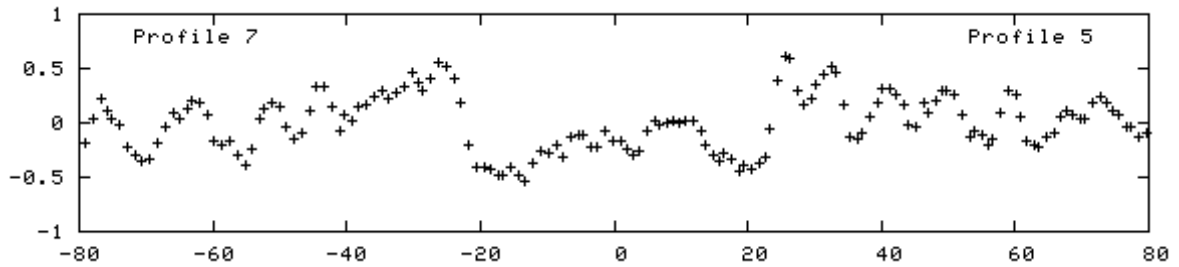
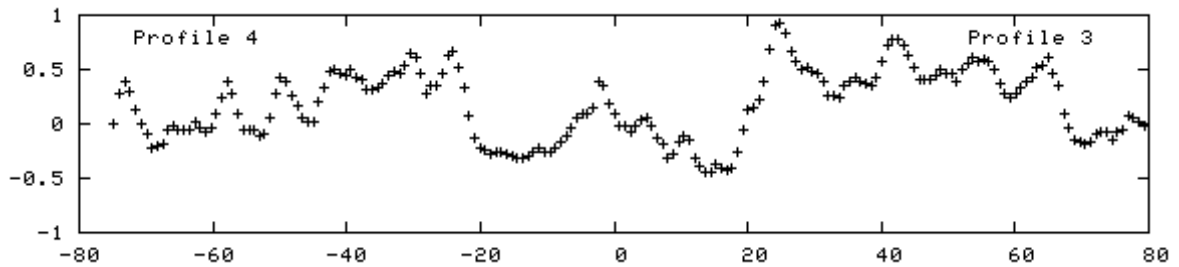
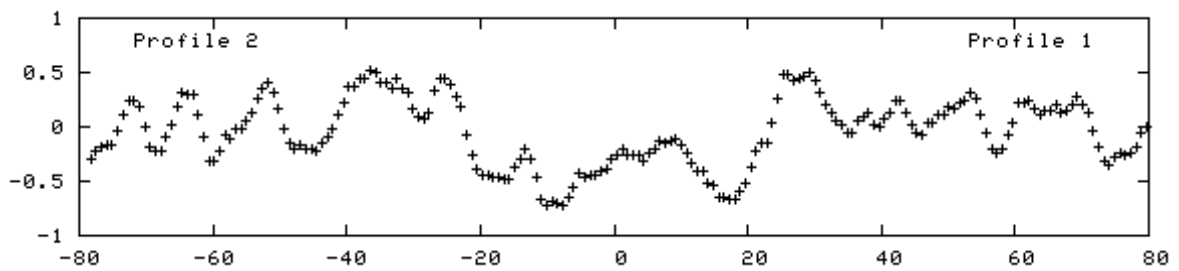
Crater type	Central Pit
Approx. Diameter	59.6 km
Location:	35.2N:141.4W
Terrain:	On Older Crater
Excel file name	Z1

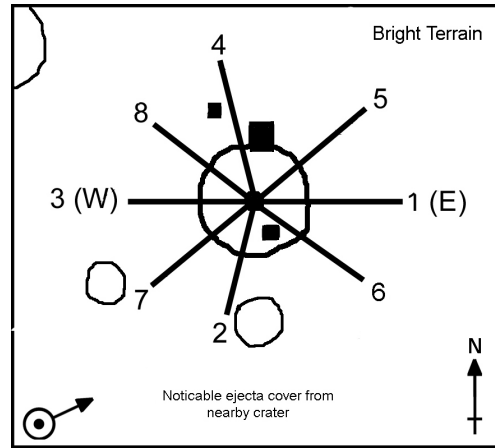


ZS29:167



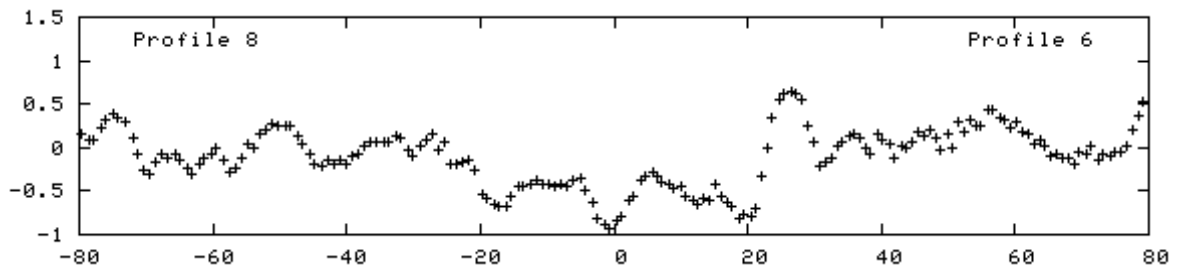
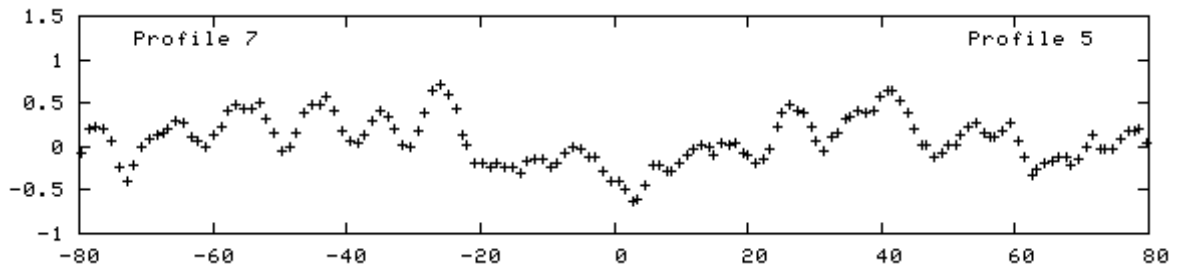
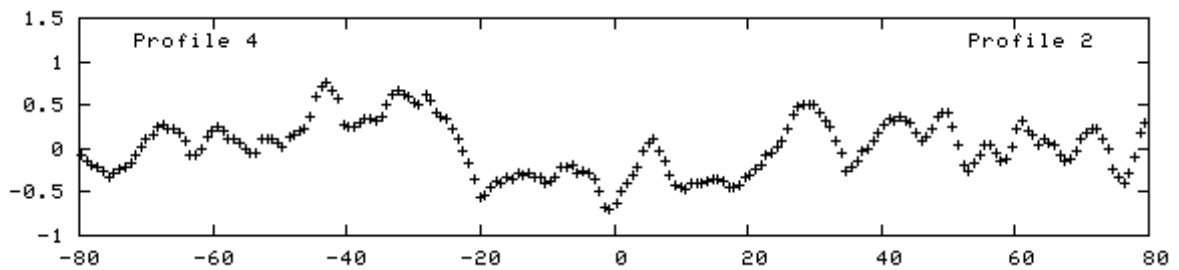
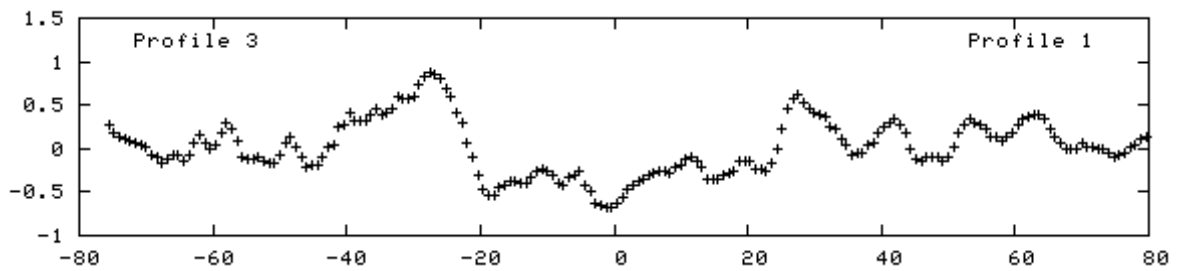
Crater type	Central Pit
Approx. Diameter	51.3 km
Location:	29S : 167.7W
Terrain:	Bright Terrain
Excel file name	N2



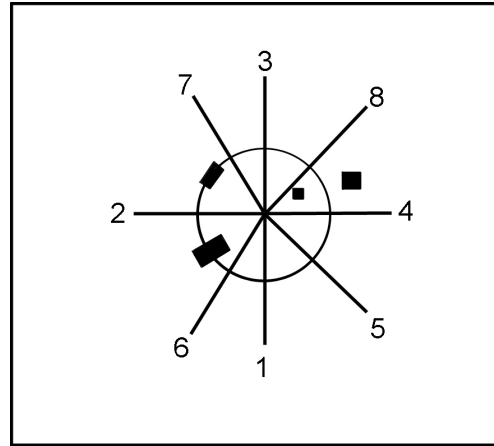
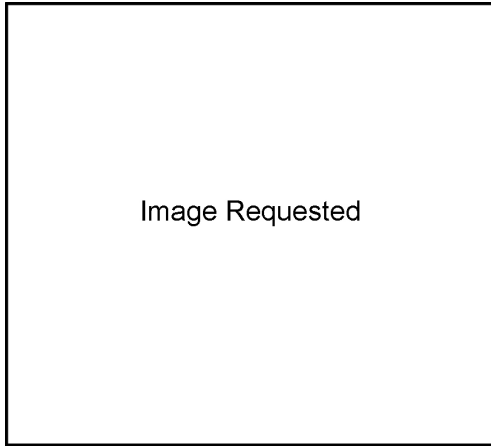


Area has noticeable mantling by light ejecta from another impact. This high albedo material could cause problems for photogrammetry.

Crater type	Central Pit
Approx. Diameter	56 km
Location:	30.7S : 164.6W
Terrain:	Bright Terrain
Excel file name	N1

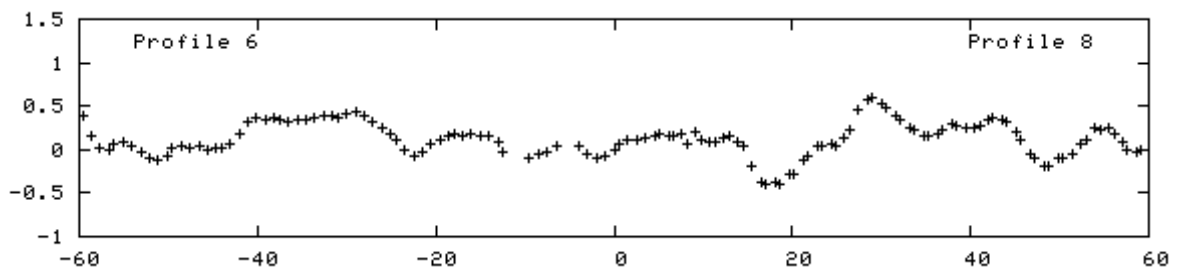
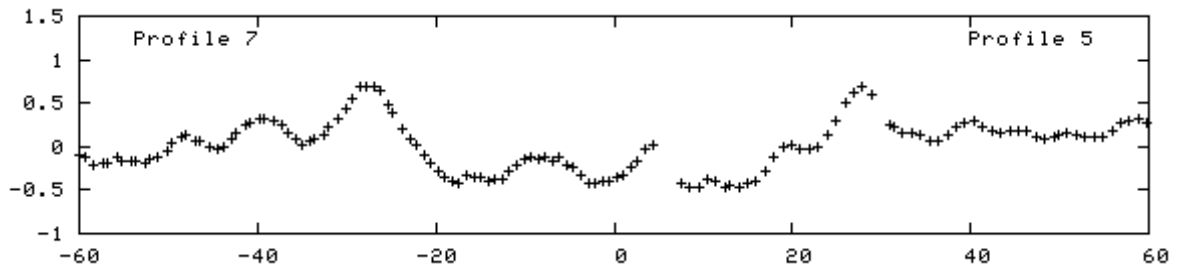
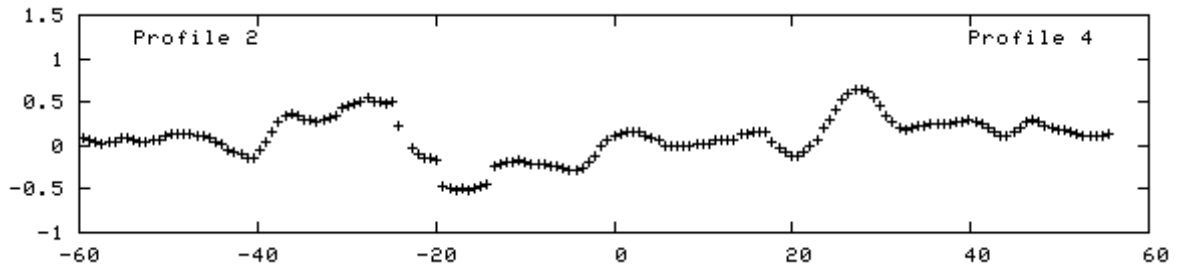
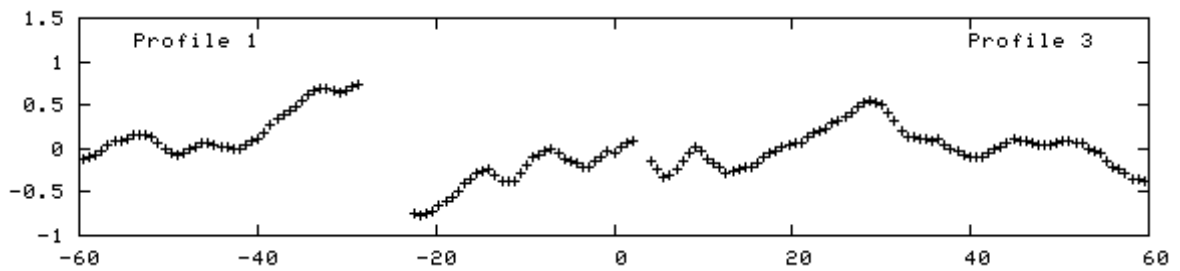


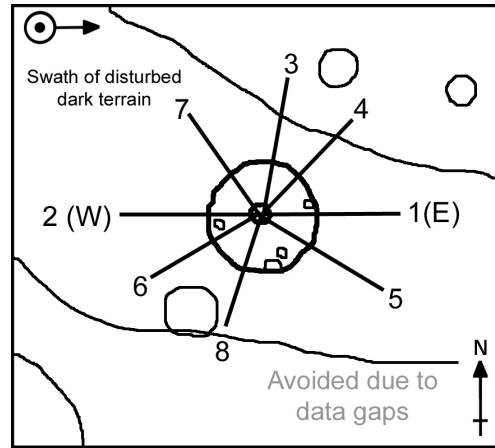
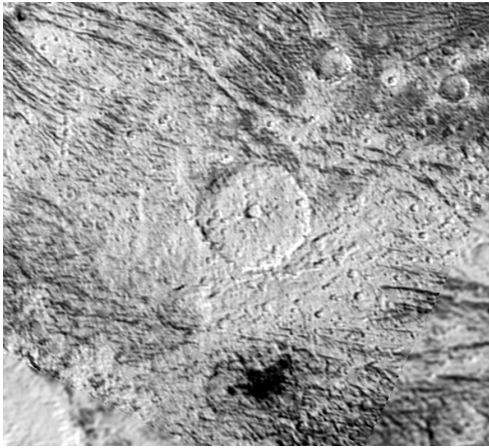
# GS74:152



Frequent data gaps in this dataset - marked by blacked out areas. ((Topography from Stereo))

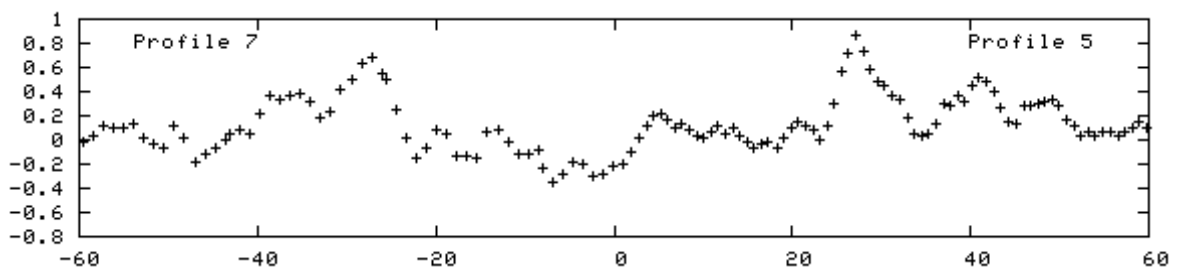
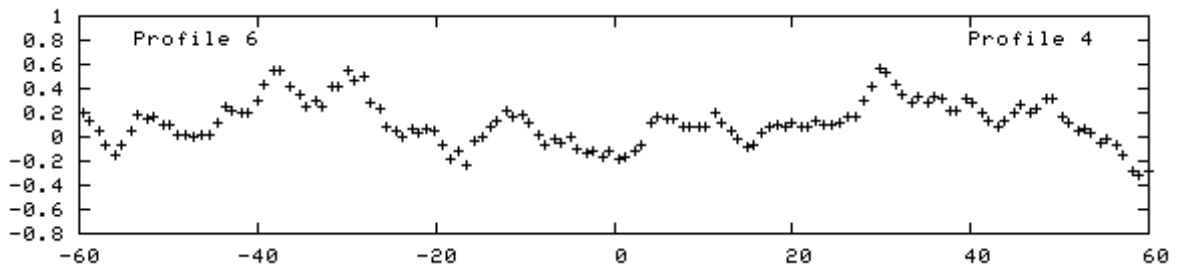
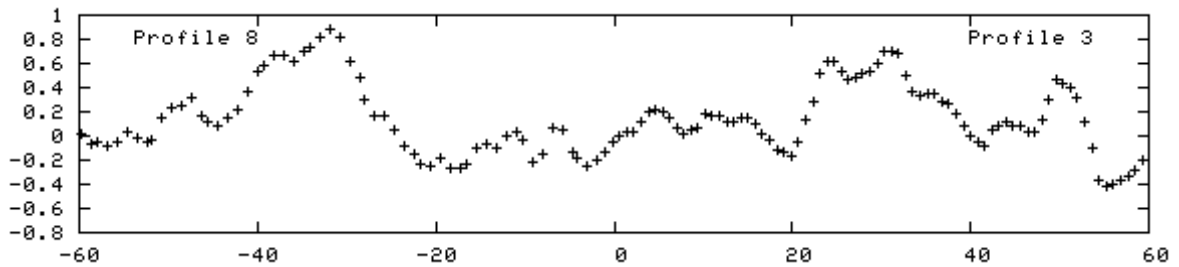
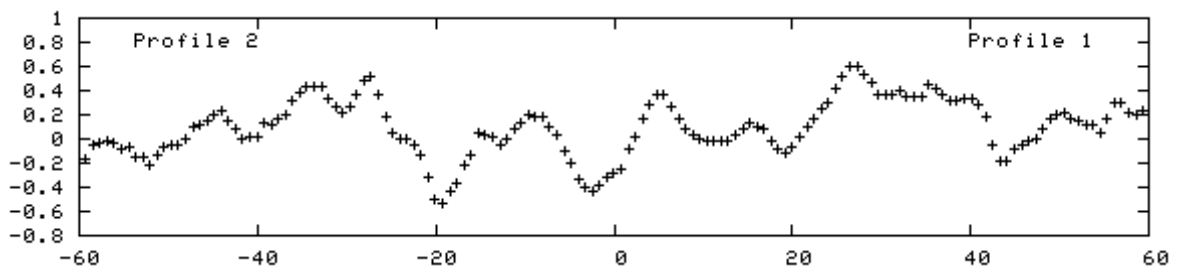
Crater type	Central pit
Approx. Diameter	56.7 km
Location:	74S : 151.9W
Terrain:	Bright Terrain
Excel file name	bub2



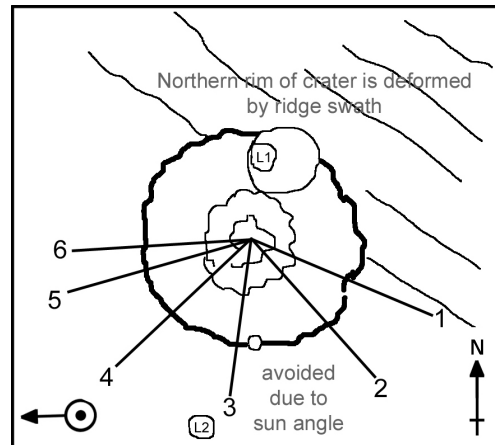
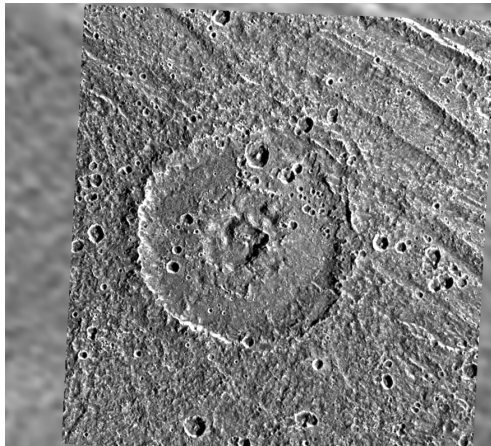


Frequent data gaps in this dataset - marked by blacked out areas.

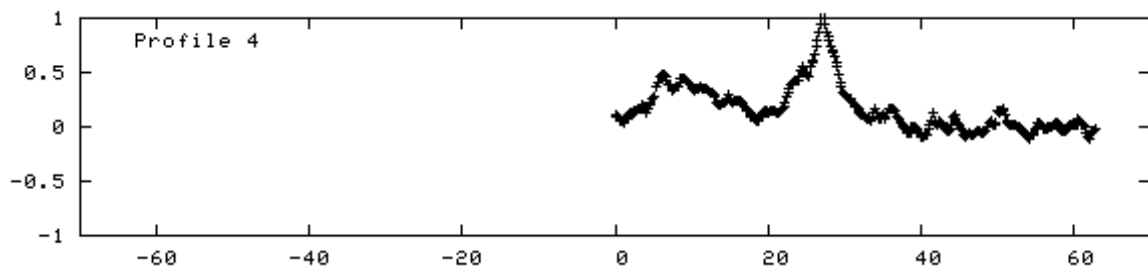
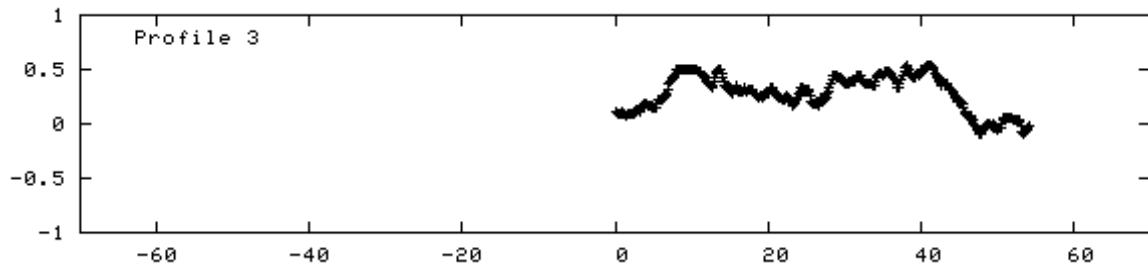
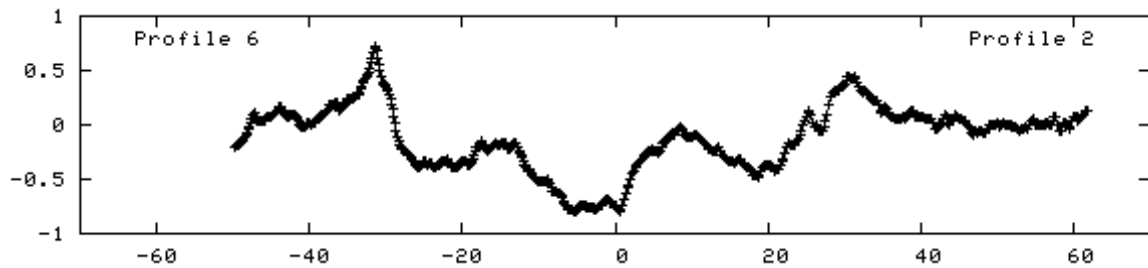
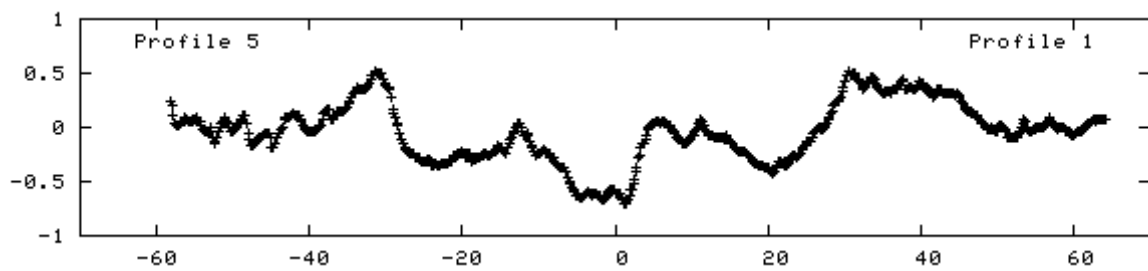
Crater type	Central Pit
Approx. Diameter	58.2 km
Location:	35.3S : 162.8W
Terrain:	Bright Terrain
Excel file name	Nosir

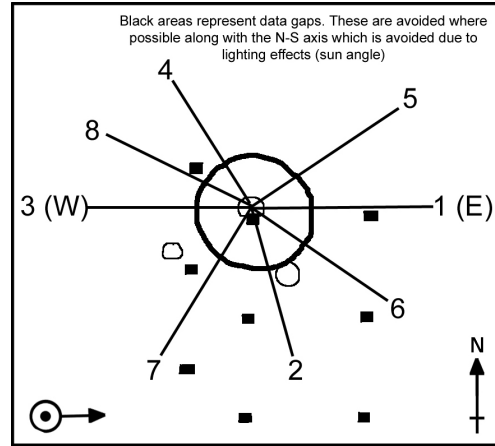
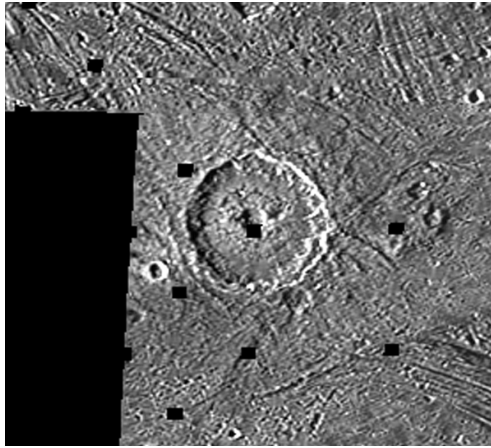


# Lugalmeslam



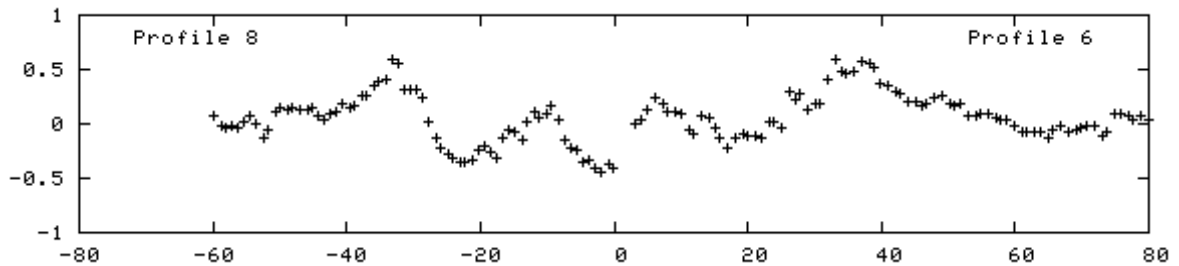
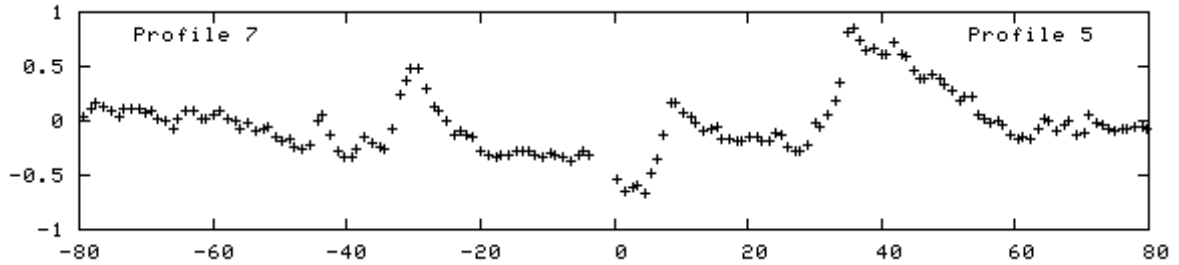
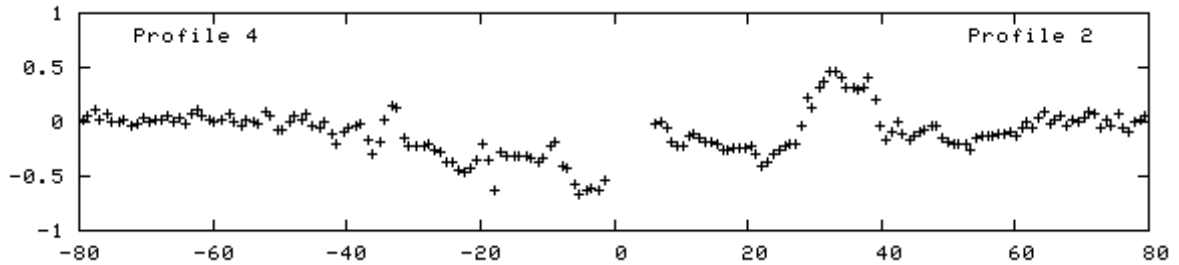
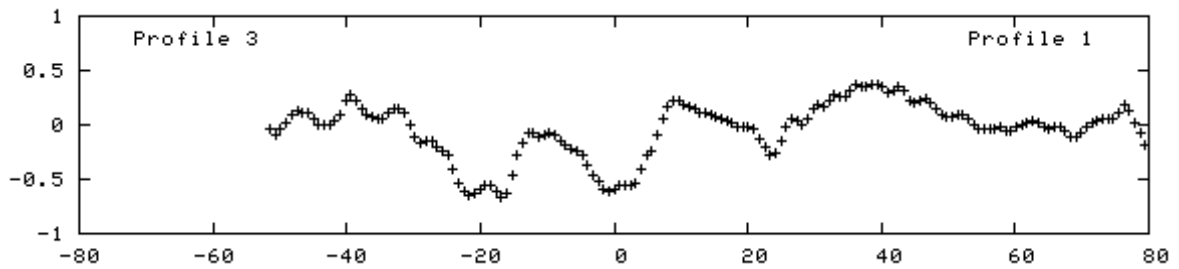
Crater type	Central Pit
Approx. Diameter	63 km
Location:	23.8N : 193.8W
Terrain:	Dark Terrain
Excel file name	Lugala



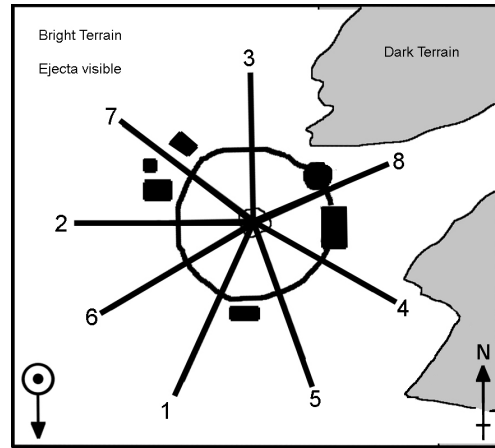
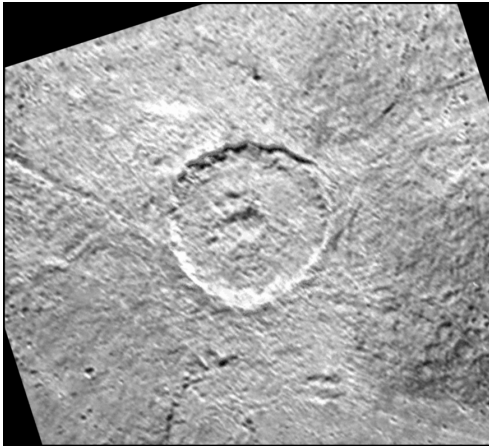


Frequent data gaps in this dataset - marked by blacked out areas.

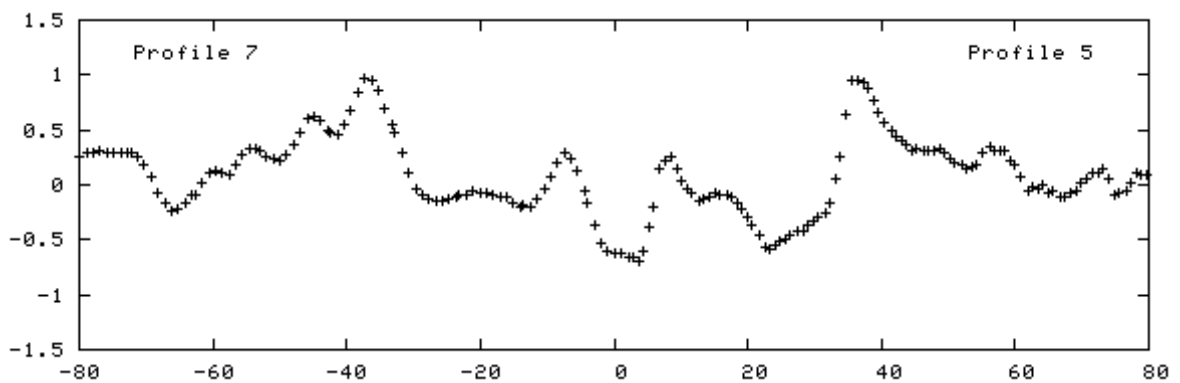
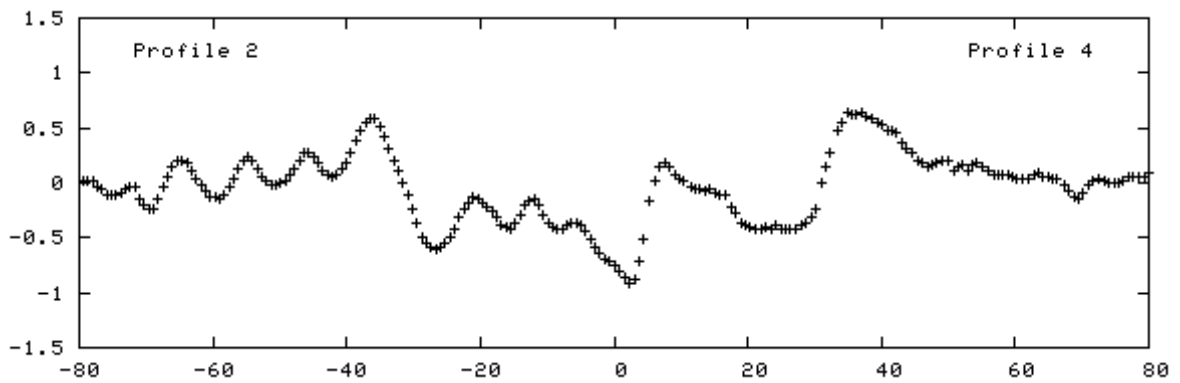
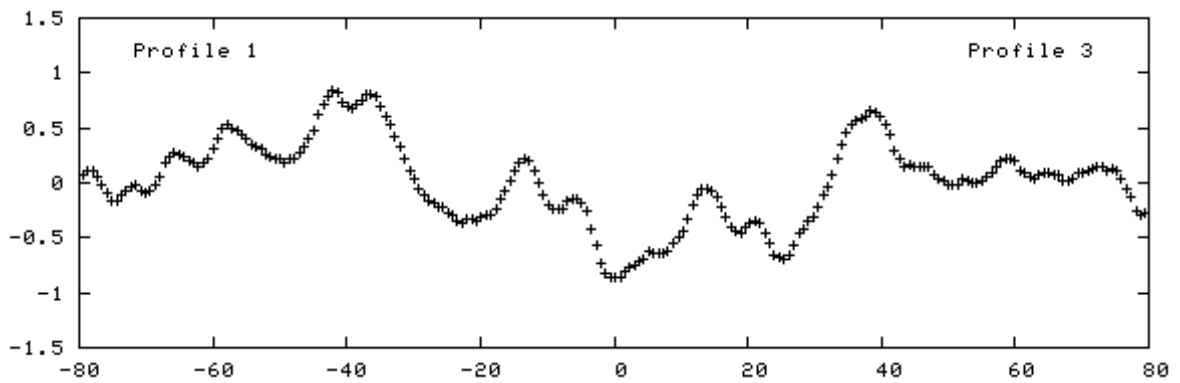
Crater type	Central pit
Approx. Diameter	68.9 km
Location:	19S : 126.7W
Terrain:	Bright Terrain
Excel file name	Ninki



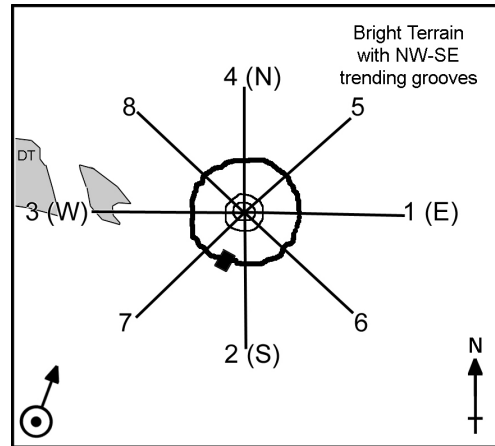
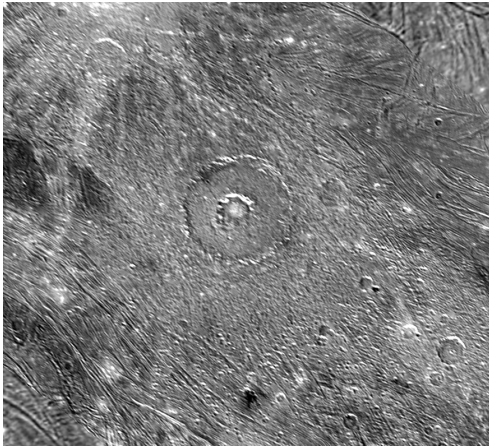
# Isis



Crater type	Cetnral Pit
Approx. Diameter	76.9 km
Location:	67.5S : 201.5W
Terrain:	Bright Terrain
Excel file name	Isis

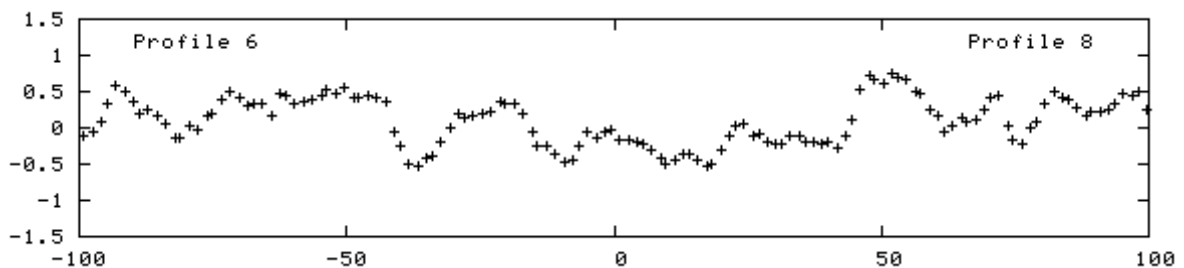
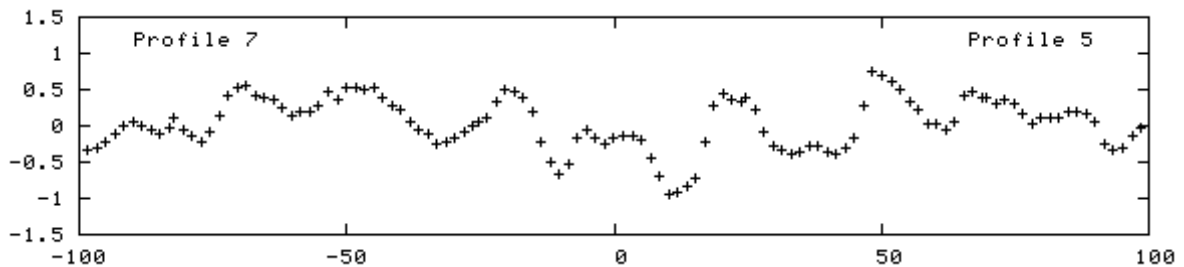
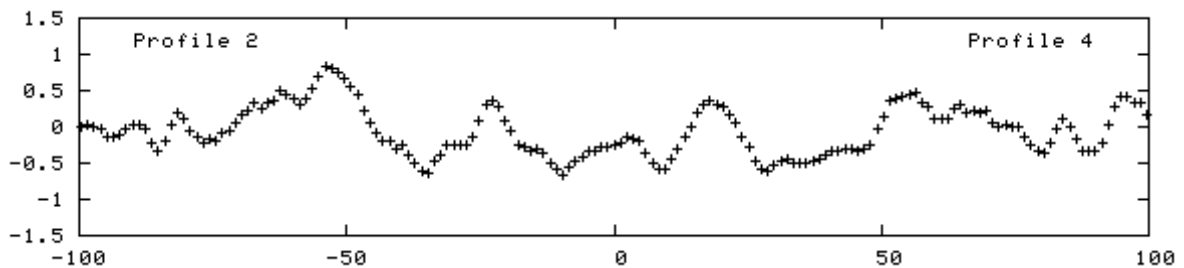
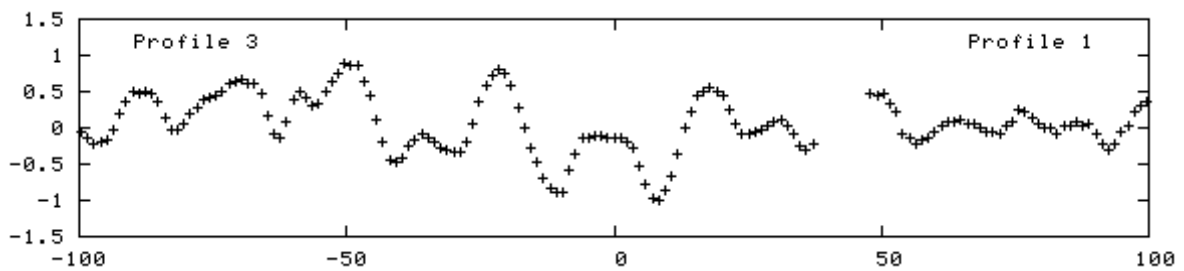


# Eshmun

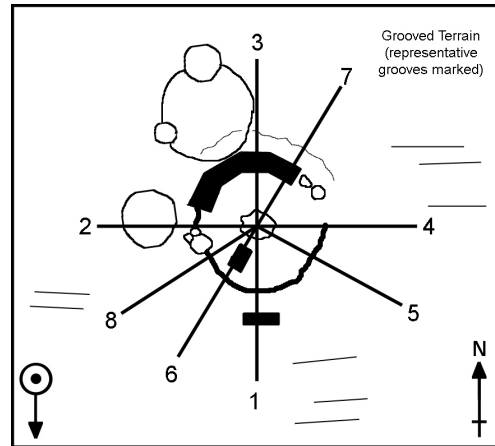


Care - Noisy data ((Topography from Stereo))

Crater type	Anomalous Dome
Approx. Diameter	102.2 km
Location:	17.3S, 192.2W
Terrain:	Bright Terrain
Excel file name	Eshmun

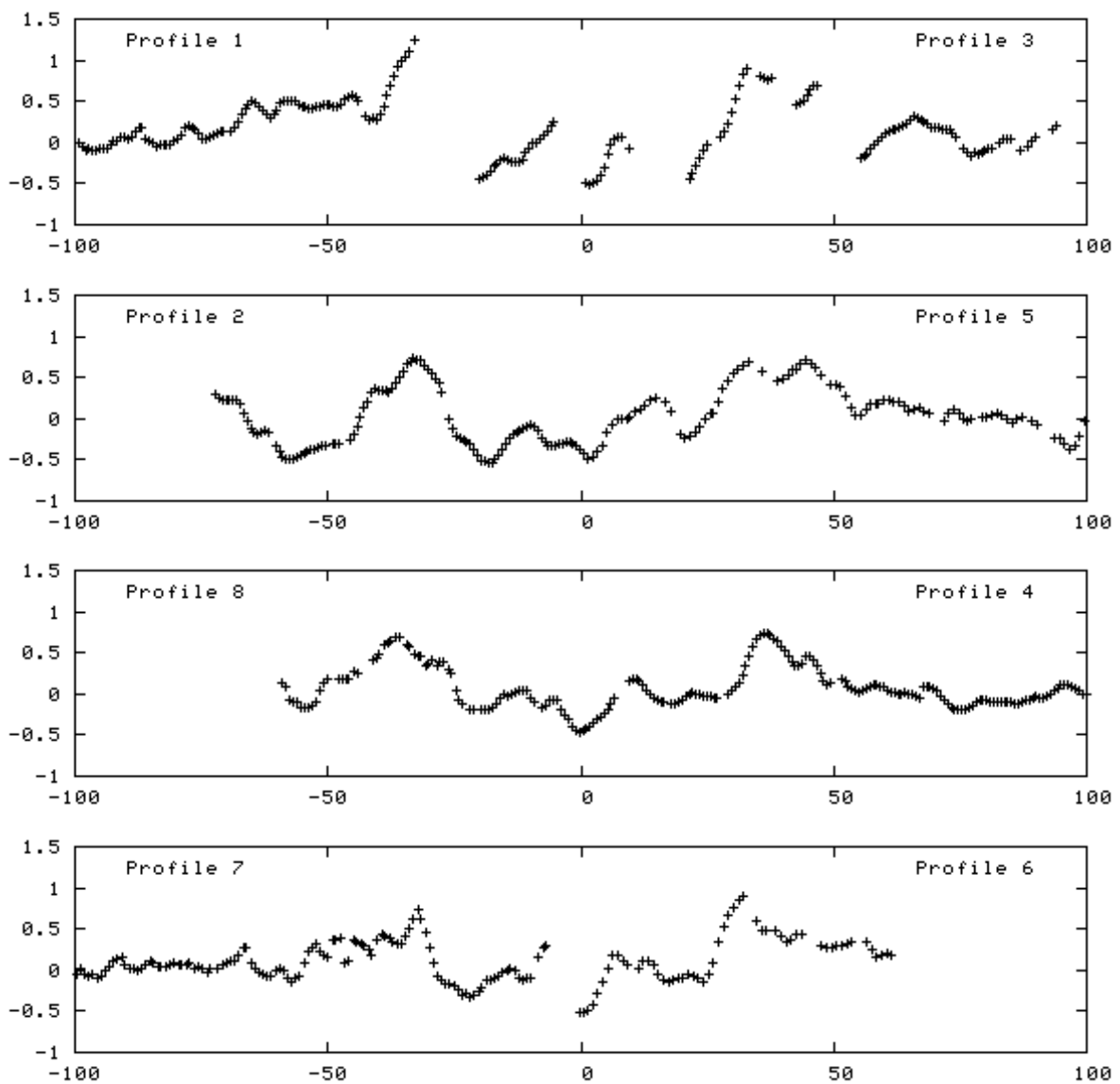


ZS84:170



Frequent data gaps in this dataset - marked by blacked out areas.

Crater type	Central pit
Approx. Diameter	67.1km
Location:	84.3S : 192.9W
Terrain:	Bright Terrain
Excel file name	bub3



## Appendix B

# Program to Compute the Hugoniot of Ice

```

*****
***
c  =====
c  Program to compute the Hugoniot of ice using the Tillotson
c  EoS and the energy equation
c
c
c  Coded by Veronica Bray                                2008-05
c
*****
***
c  implicit none
c
c  real den,den0,denmax,P0,Elow,Ehigh
c  real atillo,btillo,Atil,Btil,alpha
c  real beta,Eiv,Ecv,P,f,test
c  real mu,eta,Eguess,E0,free_unit
c
c  integer i,j,imin,imax,itermax,output_unit
c
c  start values for the real numbers are chosen based on tillotson
c  parameters as recorded in Melosh, 1989 (except for Atillo which
c  which is different in iSALE). Elow and Ehigh are designed to be
c  initially far from the correct E value
c
c  P0=0
c  den0=910.
c  denmax=2200.
c  imin=1
c  imax=100
c  Elow=1.D+0
c  Ehigh=1.D+6
c  atillo=0.3
c  btillo=0.1
c  Atil=9.8D+9
c  Btil=6.5D+9
c  alpha=10.D0
c  beta=5.D0
c  E0=7.D6
c  Eiv=7.73D+5

```

```

    Ecv=3.04D+6
    itermax=100
    output_unit=7705519
c
    open(unit=output_unit,file="output.txt",action="write")
    print*,'about to start outer do loop'
c
c The following do loop will assign a value for the density from den0
c to denmax in increments. When i=0 den=den0, when i=imax den=denmax
c
c Remember that den0 is the density at P=0 and E=0
c
    do i=imin,imax
        den=den0+float(i)*(denmax-den0)/float(imax)
        print*,'about to start inner do loop for density of',den
c
c The inner do loop finds the internal energy E, for the specified
density
c 'itermax' will stop the loop after a specified number of cycles
rather
c than letting the loop run until Etest<10D-6 as this may take eons!
c this option can be taken out once you know this actually works.
c
        eta=(den/den0)
        mu=eta-1
        do j=1,itermax
            Eguess=(Elow+Ehigh)*0.5
            P=(atillo+(btillo/(Eguess/(E0*(eta**2)+1))))*
            & (den*Eguess)+(Atil*mu)+(Btil*(mu**2))
            f=(0.5*((1./den0)-(1./den))*(P+P0))-Eguess
            print*,'Ehigh for loop',j,'=',Ehigh
            print*,'Elow for loop',j,'=',Elow
            print*,'Eguess for loop',j,'=',Eguess
            print*,'f for loop',j,'=',f
c
c The next section updates the Elow or Ehigh value ready for use
c in the next loop. If f is small enough, the loop is stopped and
c the value of Eguess returned for this density.
c
c using an absolute value for f to check the accuracy of the answer
c may cause problems at high E values as an accuracy of 10D-6 will be
c difficult to reach. Instead you can either make the accuracy less
c by increasing the number f is checked with (10D-6 ---> 0.1). Or,
c you can check the accuracy with a relative error by checking that
c f/Eguess is less than 10D-6
c
            test=f/Eguess

            if(abs(test).lt.(1.D-6)) then
                print*,'test',j
                go to 10
            elseif(f.gt.0) then
                Elow=Eguess
            elseif(f.lt.0) then
                Ehigh=Eguess
            endif
        enddo
10    continue
    print*,'Internal energy for density',i,'is',Eguess,'J/Kg'
    print*,'Pressure for this density',i,'is',P,'Pa'

```

```
c
c The next section writes the density, Internal Energy and Pressure
c to the text file.
c
```

```
    write(output_unit,*) den,Eguess,P
    Elow=Eguess
    Ehigh=100.*Eguess
enddo
close(output_unit)
end
```

## Appendix C

# Section of iSALE Script Implementing the Relationship of Melting Temperature with Ambient Pressure

```

implicit none

! Inputs/Outputs
  real*8 pressure, meltTempIce

  ! Local parameters
  real*8 pice0,pice1,pice2,pice3,pice4
  real*8 tice0,tice1,tice2,tice3,tice4
  parameter
  &
  (pice0=0.d0,pice1=0.2e9,pice2=0.34e9,pice3=0.61e9,pice4=2.17e9)
  parameter
  &
  (tice0=273.d0,tice1=252d0,tice2=257d0,tice3=274d0,tice4=354.8d0)

  ! Calculate melt temp as piecewise series of
  ! functions of pressure . . .
  if(pressure.le.pice1)then
    meltTempIce=tice0
  $      +(tice1-tice0)*(pressure-pice0)/(pice1-pice0)
  elseif(pressure.gt.pice1 .and. pressure.le.pice2)then
    meltTempIce=tice1
  $      +(tice2-tice1)*(pressure-pice1)/(pice2-pice1)
  elseif(pressure.gt.pice2 .and. pressure.le.pice3)then
    meltTempIce=tice2
  $      +(tice3-tice2)*(pressure-pice2)/(pice3-pice2)
  elseif(pressure.gt.pice3 .and. pressure.le.pice4)then
    meltTempIce=tice3
  $      +(tice4-tice3)*(pressure-pice3)/(pice4-pice3)
  elseif(pressure.gt.pice4)then
    meltTempIce=tice4*
  $      ((pressure-pice4)/1.253e9 +1)**(1./3.)
  endif
  return
end

```

# Bibliography

Ahrens, T. J. and O'Keefe, J. D. (1977). Equations of state and impact-induced shock-wave attenuation on the Moon. In *Impact and Explosion Cratering*. Edited by Roddy, D. J., Pepin, R. O. and Merrill, R. B. Pergamon Press (New York). Pp 639-656.

Alexopoulos, J. S. and McKinnon, W.B. (1994). Large impact craters and basins on Venus, with implications for ring mechanics on the terrestrial planets. In *Large Meteorite Impacts and Planetary Evolution*. Edited by Dressler, B. O., Grieve, R.A.F., and Sharpton, V. L. *Geol. Soc. Am. Spec. Pap.* 293:29-50.

Allen, C. C. (1975). Central peaks in lunar craters. *Earth, Moon and Planets.* 12(4):463-474.

Alzate, N. and Barlow, N. G. (2008). Characteristics and distribution of central pit craters on Ganymede: Implications for pit formation models. *Proceedings, Lunar Planet. Sci.* 39<sup>th</sup> Conf. Abs. 1714.

Amsden, A.A., Ruppel, H.M., and Hirt, C.W. (1980). SALE: A simplified ALE computer program for fluid flow at all speeds. Los Alamos National Laboratory LA-8095, Los Alamos, NM, 101.

Anderson, C. E. (1987). An overview of the theory of hydrocodes. *International Journal of Impact Engineering.* 5:33-59.

Anderson, G. D. (1968), The equation of state of ice and composite frozen soil material. *Res. Rep.* 257, Cold Regions Res. and Eng. Lab., Hanover, N. H.

Anderson, J. D., Schubert, G., Jacobson, R. A., Lau, E. L., Moore, W. B. and Sjogren, W. L. (1998). Europa's differentiated internal structure: Inferences from four Galileo encounters. *Science* 281:2019-2022.

- Artemieva, N., Karp, T. and Milkereit, B. (2004). Investigating the Lake Bosumtwi impact structure: Insight from numerical modelling. *Geochemistry, Geophysics, Geosystems* 5(11): doi: 10.1029/2004GC000733.
- Asay, J. R. and Shahinpoor, M. (1993). *High-pressure shock compression of solids*. Springer, New York.
- Barlow, N. G. (2006). Comparison of central pit craters on Mars and Ganymede. *Mars crater consortium 9*. Abstract.
- Barlow, N. G. and Alzate, N. (2008). Central pit craters on Mars and Ganymede: Characteristics, distributions and implications for formation models. *Large meteorite impacts and planetary evolution IV*. Abs. 3071.
- Beeman, M., Durham, W. B., and Kirby, S. H. (1988). Friction of ice, *J. Geophys. Res.* 93:7625-7633.
- Bingham, E. C. (1916). An investigation of the laws of plastic flow. *Bull. U. S. Bur. of Standards* 13(309).
- Bonner, W.J. and Schmall, R.A. (1973). A photometric technique for determining planetary slopes from orbital photographs. *US Geological Survey Professional Paper 812(A)*:1-16.
- Bray, V. J., Collins, G. S. and Morgan, J. V. (2006). Numerical modelling of impact cratering on the Moon and icy satellites. *37th Lunar and Planet. Sci. Conf.* Abs. 1175.
- Bray, V. J., Collins, G. S., Morgan, J. V., and Schenk, P. M. (2008). The effect of target properties on crater morphology: Comparison of central peak craters on the Moon and Ganymede. *Meteoritics and Planet. Sci.* Vol. 43(12):1979-1992.
- Bray, V. J., Schenk, P. M., Melosh, H. J., Collins, G. S. and Morgan, J. V. (2009). Dimensions of central pits in Ganymede craters, *40<sup>th</sup> Lunar and Planet. Sci. Conf.* Abs. 1350.

- Breneman, H. H. and Belton, M. J. S. (1998). Dark terrain on Ganymede: geological mapping and interpretation of Galileo Regio at high resolution. *Icarus*.135:317-344.
- Burchell, M.J., Cole, M.J., Lascelles, S.F., Khan, M.A., Barthet, C., Wilson, S.A., Cairns, D.B. and Armes, S.P. (1999). Acceleration of conducting polymer-coated latex particles as projectiles in hypervelocity impact experiments. *J. Phys. D: Appl. Phys.* 32:1719-1728.
- Carey, S.W. (1953). The Rheid concept in geotectonics. *J. Geol. Soc. Australia*.1:67-117.
- Carr, M.H., Crumpler, L.S., Cutts, J.A., Greeley, R., Guest, J.E. and Masursky, H. (1977). Martian impact craters and emplacement of ejecta by surface flow. *J. Geophys. Res.* 82:4055-4065.
- Chapman, C. R. and McKinnon, W. B. (1986). Cratering of planetary satellites in *Satellites*. Edited by Burns, J. A. and Matthews, M.S. University of Arizona Press, Tucson. pp. 492-580.
- Chyba C.F. (2000). Energy for microbial life on Europa. *Nature*. 403:381-382.
- de Cicco,, M. and Zucoloto, M. E. (2002). Appraisal of Brazilian astroblemes and similar structures. *Meteoritics and Plan. Sci.* 37:A40.
- Colburn, D. S. and Reynolds, R. T. (1985). Electrolytic currents in Europa. *Icarus* 63:39-44.
- Collins, G. S. (2000). Numerical modelling of large impact crater collapse. Ph.D. Thesis. Imperial College, London, U.K.
- Collins, G. S., Melosh, H. J., Morgan, J. V., and Warner, M. R. (2002). Hydrocode simulations of Chicxulub crater collapse and peak ring formation. *Icarus*. 157:24-33.
- Collins, G. S., Melosh, H. J. and Ivanov, B. A. (2004). Damage and deformation in numerical impact simulations. *Meteoritics and Planet. Sci.* 39:217-231.
- Collins, G. S., Kenkmann, T., Osinski, G. R. and Wunnemann, K. (2008). Mid-sized complex crater formation in mixed crystalline sedimentary targets: Insight from modelling and observation. *Meteoritics and Planetary Science*. Vol. 43(12):1955.

- Consolmagno, G.J. and Lewis, J.S. (1977). Preliminary thermal history models of icy satellites in *Planetary Satellites*. Edited by Burns, J. A. pp. 492-500.
- Cooper, J. F., Johnson, R. E., Mauk, B. H., Garrett, H. B. and Gehrel, N. (2001), Energetic ion and electron irradiation of the icy Galilean satellites. *Icarus* 149, 133-159
- Croft, S. K. (1981). Cratering on Ganymede and Callisto: comparisons with the terrestrial planets. 12<sup>th</sup> Lunar Planet. Sci. Conf. pp 187-189.
- Croft, S. K. (1983). A proposed origin for palimpsests and anomalous pit craters on Ganymede and Callisto. *J. Geophys. Res. Suppl.* 88:B17-B89.
- Croft, S. K. (1985). The scaling of complex craters. *Proceedings, Lunar. Planet. Sci. 13<sup>th</sup> Conf. 13<sup>th</sup>*. *J. Geophys. Res.* 90:C828 -C842.
- Croft, S. K., Kargel, J. S., Kirk, R. L., Moore, J. M., Schenk, P. M. and Strom, R. G. (1995). The geology of Triton. In *Neptune and Triton*. Edited by Cruikshank, D. P. Univ. of Arizona Press, Tucson. pp. 879-948.
- Crozier, W. D. and Hume, W. (1957). High-velocity, light-gas gun. *Jour. Appl. Phys.* 28:892-894.
- Datchi, F., Loubeyre, P. and Le Toullec, R. (2000). Extended and accurate determination of the melting curves of argon, helium, ice (H<sub>2</sub>O), and hydrogen (H<sub>2</sub>). *Phys. Rev. B* 61:6535-6546.
- Davis, P. A. and Soderblom, L. A. (1984). Modeling crater topography and albedo from monoscopic Viking Orbiter images. I – methodology. *J. Geophys. Res.* 89:9449-9457.
- Dence, M. R. (1973). Dimensional analysis of impact structures. *Meteoritics* 8:343-344.
- Dombard, A.J., and McKinnon, W.B. (2006). Elastoviscoplastic relaxation of impact crater topography with application to Ganymede and Callisto. *J. Geophys. Res.* 111, E01001, doi:10.1029/2005JE002445.

- Dressler, B.O. and Sharpton, V. L. (1997). Breccia formation at a complex impact crater: Slate Islands, Lake Superior, Ontario, Canada. *Tectonophysics*. 275(4):285-311.
- Dubrovinskaia, N. and Dubrovinsky, L. (2003). Melting curve of water studied in externally heated diamond-anvil cell. *High Press. Res.* 23(3):307-312.
- Durham, W. B. and Stern, L. A. (2001). Rheological properties of water ice—Applications to the satellites of the outer planet, *Annu. Rev. Earth Planet. Sci.* 29:295-33.
- Durham, W. B., Heard, H. C., and Kirby, S. H. (1983). Experimental deformation of polycrystalline H<sub>2</sub>O ice at high pressure and low temperature: Preliminary results. *Proceedings. Lunar planet. Sci. 14<sup>th</sup> Conf. J. Geophys. Res.* 88:B377-B392.
- Efford, N. (1991). Sources of error in the photoclinometric determination of planetary topography - A reappraisal. *J. Earth, Moon, and Planets.* 54:19-58.
- Elbeshausen, D., Wünnemann, K. and Collins, G.S. (2007). Three-dimensional numerical modeling of oblique impact processes: Scaling of crater efficiency. 36<sup>th</sup> Lunar and Planet. Sci. Conf. Abs. 1952.
- Fechtig, H., Gault, D.E., Neukum, G. and Schneider, E. (1972). Laboratory Simulation of Lunar Craters. *Naturwissenschaften* 59:151-157.
- Fletcher, N. A. (1970). *The Chemical Physics of Ice*. Cambridge monographs on physics. New York: Cambridge University Press.
- French, B.M. (1998). *Traces of Catastrophe*. Lunar and Planet. Inst. Contribution 954, Houston.
- Gaffney, E. S., and T. J. Ahrens (1980), Identification of ice VI on the Hugoniot of ice Ih. *Geophys. Res. Lett.*, 7(6), 407–409.
- Gaffney, E.S. and Melosh, H. J. (1982). Noise and target strength degradation accompanying shallow-buried explosions. *J. Geophys. Res.* 87:1871–79.

- Gaidos, E.J., Neelson, K.H., and Kirschvink, J.L. (1999). Life in ice-covered oceans. *Science*. 284:1631-1633.
- Gault, D. E. and Wedekind, J. A. (1978). Experimental studies of oblique impact. *Proc. Lunar Planet. Sci. Conf. 8<sup>th</sup>*. pp. 3843–3875.
- Gault, D. E., Quaide, W. L. and Oberbeck, V. R. (1968). Impact Cratering Mechanics and Structures, in *Shock Metamorphism of Natural Materials*. Edited by French, B. M. and Short, N. M. Mono, Baltimore, USA. pp. 87-99.
- Geissler, P. E. (2004). Origin of chaos terrain. Europa's Icy Shell Workshop. Abstract #7050.
- Gilbert, G.K. (1983). The Moon's Face: a Study of the Origin of Its Features. *Bull. Philosoph. Soc., Washington*. 12:241-292.
- Greeley, R. (1999). *The New Solar System, Fourth Addition*. Edited by Beatty, J. K., Collins Petersen, C. and Chakin, A. Cambridge University Press.
- Greeley, R., Fink, J. H., Gault, D. E. and Guest, J. E. (1982). Experimental simulation of impact cratering on icy satellites. In *Satellites of Jupiter*. Edited by Morrison, D. University of Arizona Press, Tucson, Arizona. pp. 340-378.
- Grieve, R.A.F. (1978). The petro-chemistry of the melt rocks at Brent Crater and their implications for the conditions of impact. *Meteoritics*. 13(4):484-487.
- Grieve, R.A.F. (1987). Terrestrial impact structures. *Annu. Rev. Earth Planet. Sci.* 15:245-270.
- Grieve, R. A. F. (2006). Impact structures in Canada. *Geol. Ass. Can.* pp. 210.
- Grieve, R. A. F. and Pilkington, M. (1996). The signature of terrestrial impacts. *AGSO Journal of Australian Geology and Geophysics*. 16:399-420.
- Grieve, R. A. F., Dence, M. C. and Robertson, P. B. (1977). Cratering processes: As interpreted from the occurrence of impact melts. In *Impact and Explosion Cratering*.

- Edited by Roddy, D.J., Pepin, R.O. and Merrill, R. B. Pergamon Press, New York, pp 791-814.
- Hale, W. and Grieve, R. A. F. (1982). Volumetric analysis of complex lunar craters: Implications for basin ring formation. Proceedings, Lunar Planet. Sci. 13<sup>th</sup> Conf. J. Geophys. Res. 87:A65-A76.
- Hale, W. and Head, J. W. (1980). Central peaks in mecurian craters:Comparisons to the Moon. Proc. Lunar. Planet. Sci. Conf. 11th. pp. 2191-2205.
- Hartmann, W. K. and Wood, C. A. (1971). Origin and evolution of multi-ring basins. The Moon 3:3-78.
- Heather, D. J. and Dunkin, S. K. (2002). Geology and stratigraphy of King crater, lunar farside. Icarus 163:307-329.
- Hildebrand, A. R., Penfield, G. T., King, D. A., Pilkington, M., Camaro, A. Z., Jacobson, S. B. and Boynton, W. B. (1991). Chicxulub Crater: a possible Cretaceous/Tertiary boundary impact crater on the Yucatan Peninsula, Mexico. Geology 19:867-871.
- Hodges, C. A., Shew, N.B. and Clow, G.D. (1980). Distribution of central pit craters on Mars. Proc. 11<sup>th</sup> Lunar Planet. Sci. Conf. pp. 450-452.
- Hoek, E. (1983). Strength of jointed rock masses. Geotechnique 33(3):187-223.
- Hoppa, G. V., Tufts, B. R., Greenberg, R. and Geissler, P. (1999). Formation of Cycloidal Features on Europa. Science 285:1899-1902.
- Howard, A. D., Blasius, K. R. and Cutts, J A. (1982). Photoclinometric determination of the topography of the Martian north polar cap. Icarus 50:245-258.
- Hussmann, H. and Spohn, T. (2004). Europa's ice shell thickness derived from thermal-orbital evolution models. Workshop on Europa's Icy shell: past present and future. Abs. #7012.

- Hussmann, H., Spohn, T. and Wiczerkowski, K. (2002). Thermal equilibrium states of Europa's ice shell: Implications for internal ocean thickness and surface heat flow. *Icarus* 156:143-151.
- Ivanov, B. A. (2000). Crust and mantle deformation under Chicxulub: Test for models. *Catastrophic Events Conference: Impacts and Beyond*. pp. 78–79
- Ivanov, B. A. and Artimieva, N. (2002). Numerical Modeling of the formation of large impact craters. *GSA Special Paper 256*:619-630.
- Ivanov, B. A. and Deutsch, A. (1999). Sudbury impact event: Cratering mechanics and thermal history. In *Large Meteorite Impacts and Planetary Evolution II*. Special Paper 339. Edited by Dressler, B. O., and Sharpton, V. I. Geol. Soc. Am., Boulder, CO. pp. 389-397.
- Ivanov B.A., and Kostuchenko V. N. (1998). Impact crater formation: Dry friction and fluidization influence on the scaling and modification. *Proceedings, Lunar Planet. Sci. 29<sup>th</sup> Conf.* pp 1654.
- Ivanov, B.A., Kocharyan, G.G., Kostuchenko, V.N., Kirjakov, A.F., Pevzner, L. (1996). Puchezh Katunki impact crater: preliminary data on recovered core block structure. 26<sup>th</sup> Lunar and Planet. Sci. Conf. Abs. #1655.
- Ivanov, B. A., Deniem, D., and Neukum, G. (1997). Implementation of dynamic strength models into 2D hydrocodes: Applications for atmospheric breakup and impact cratering. *Int. J. Impact Engineering*. 20:411-430.
- Jaeger, J. C. and Cook, N. G. W. (1969). *Fundamentals of Rock Mechanics*, Mathuen, London.
- Jankowski, D. G. and Squyres, S. W. (1991). Sources of error in planetary photoclinometry. *J. Geophys. Res.* 96:20,907-20,922.
- Ji, S. and Shen, H. H. (2006). Contrasting terrestrial and lunar gravity: angle of repose and incline flows. *Proc. 10th ASCE Aerospace Division Int. Conf. on Engineering, Construction and Operations in Challenging Environments (Earth and Space 2006)*.

Edited by Malla, R. B., Binienda, W. K. and Maji, A. K (Reston, VA: Aerospace Division of the American Society of Civil Engineers).

Johnson, T. V. (1999). Io. In *The New Solar System*. Fourth edition. Edited by Beatty, J. K., Collins Peterson, C. and Chaikin, A. Cambridge University Press.

Jones, K. B., head, J. W., Pappalardo, R. T. and Moore, J. M. (2003). Morphology and origin of palimpsests on Ganymede based on Galileo observations. *Icarus* 164(1):197-212.

Kagy, H. M. and Barlow, N. G. (2008). Topography of northern hemisphere Martian central pit craters. 39<sup>th</sup> Lunar and Planet. Sci. Conf. Abs. #1166.

Kargel, J. S. and Consolmagno, G. J. (1996). Magnetic Fields and the Detectability of Brine Oceans in Jupiter's Icy Satellites. 27<sup>th</sup> Lunar Planet. Sci. Conf. Abs. #643.

Kargel, J.S., Kaye, J.Z., Head, J.W., Marion, G.M., Sassen, R., Crowley, J. K., Prieto-Ballesteros, O. and Hogenboom, D. L. (2000). Europa's crust and ocean: origin, composition and the prospects for life. *Icarus* 148:226–265

Kenkmann, T. (2002). Folding within seconds. *Geology*. 30:231-234.

Khurana, K. K., M. G. Kivelson, D. J. Stevenson, G. Schubert, C. T. Russell, R. J. Walker and C. Polansky (1998). Induced magnetic fields as evidence for subsurface oceans in Europa and Callisto. *Nature* 395:777-780.

Kieffer, S. W., (1977). Sound speed in liquid-gas mixtures: Water-air and water-stream, *J. Geophys. Res.* 82, 2895–2904.

Kim, H. and Keune, J. (2007). Compressive strength of ice at impact strain rates. *J. of Materials Science*. 42:2802-2806.

Kivelson, M. G., Khurana, K. K., Joy, S., Russel, C.T., Southwood, D.J., Walker, R.J., Polansky, C. (1997). Europa's magnetic signature: report from Galileo's pass on 19 December 1996. *Science* 276:1239-1241.

- Klaybor, K. and Barlow, N. G. (2006). Interior morphologies of impact craters on Ganymede. Lunar and Planet. Sci. Conf. Abs. #1360.
- Klinger, J. (1980). Influence of a phase transition of ice on the heat and mass balance of comets. *Science* 209:271–272.
- Kutter, G. S. (1987). *The Universe and Life: Origins and Evolution*. Boston: Jones and Bartlett Publishers.
- Lajtai, E.Z., Duncan, E.J.S. and Carter, B.J. (1991). The effect of strain rate on rock strength. *Rock Mechanics and Rock Engineering*, 24:99-109.
- Larson, D. B., G. D. Bearson, and J. R. Taylor (1973). Shock-wave studies of ice and two frozen soils. In *Permafrost: The North American Contribution to the Second International Conference*, pp. 318–325, Natl. Acad. of Sci., Washington, D. C.
- Lin, J., Militzer, B., Stuzhkin, V., Gregoryanz, E., Hemley, R. and Mao, H. (2004). High pressure-temperature Raman measurements of H<sub>2</sub>O melting to 22 GPa and 900 K. *J. Chem. Phys.* 121:8423-8427.
- Lucchitta, B.K. and Soderblom, L.A. (1982). In *Satellites of Jupiter*, Tucson: Univ. Ariz. Press. Edited by Morrison, D.
- Lundborg, N. (1968). Strength of rock-like materials. *International Journal of Rock Mechanics and Mining Sciences*. 5:427-454.
- McCord, T. B., G. B. Hansen, F. P. Fanale, R. W. Carlson, D. L. Matson, T. V. Johnson, W. D. Smythe, J. K. Crowley, P. D. Martin, A. Ocampo, C. A. Hibbitts, J. C. Granahan, and The NIMS team. (1998). Salts on Europa's surface detected by Galileo's near infrared mapping spectrometer. *Science*, 280:1242-1245.
- McEwen, A. S. (1991). Photometric functions from photoclinometry and other applications. *Icarus*. 92:298-311.
- McEwen, A. S., C. J. Hansen, W. A. Delamere, E. M. Eliason, K. E. Herkenhoff, L. Keszthelyi, V. C. Gulick, R. L. Kirk, M. T. Mellon, J. A. Grant, N. Thomas, C. M. Weitz,

- S. W. Squyres, N. T. Bridges, S. L. Murchie, F. Seelos, K. Seelos, C. H. Okubo, M. P. Milazzo, L. L. Tornabene, W. L. Jaeger, S. Byrne, P. S. Russell, J. L. Griffes, S. Martínez-Alonso, A. Davatzes, F. C. Chuang, B. J. Thomson, K. E. Fishbaugh, C. M. Dundas, K. J. Kolb, M. E. Banks, J. J. Wray. (2007). A closer look at water-related geologic activity on Mars. *Science* 317(5845):1706-1709.
- McHone J. F. (1986). Terrestrial impact structures: Their detection and verification with new examples from Brazil. University of Illinois at Urbana-Champaign, Urbana, Illinois. pp. 210
- McKinnon, W. B. (1999). Convective instability in Europa's floating ice shell. *Geophys. Res. Lett.* 26:951-954.
- McKinnon, W. B., Chapman, C. R., and Housen, K. R. (1991). Cratering of the Uranian satellites, In *Uranus*, edited by Miner, J.T., and Matthews, L.D. Univ. of Arizona Press. Tucson. pp. 629–692.
- Melosh, H. J. (1979). Acoustic Fluidization: a new geologic process? *J. Geophys. Res.* 84:7513:7520.
- Melosh, H. J. (1982). A schematic model of crater modification by gravity. *J. Geophys. Res.* 87:371-380.
- Melosh H. J. (1983). Acoustic fluidization. *Am. Sci.* 71:158-65.
- Melosh, H. J. (1986). The physics of very large landslides. *Acta Mechanica* 64:89-99.
- Melosh, H. J. (1989). *Impact Cratering: a Geological Process*. Number 11 in Oxford monographs on geology and geophysics. New York: Oxford Univ. Press.
- Melosh, H. J. (1996). Dynamical weakening of faults by acoustic fluidization, *Nature*, 379:601-606.
- Melosh, H. J. and McKinnon, W. B. (1978). The mechanics of ringed basin formation. *Geophys. Res. Lett.* 5:985-988.

- Melosh, H. J. and Ivanov, B. A. (1999). Impact crater collapse. *Annu. Rev. Earth Planet. Sci.* 27:385-415.
- Melosh, H. J., E. V. Ryan, and E. Asphaug. (1992). Dynamic Fragmentation in Impacts: Hydrocode Simulation of Laboratory Impacts. *Jour. Geophys. Res.* 97. 14:735-14,759.
- Milton, D. J., Barlow, B. C., Brett, R., Brown, A R., Glikson, Y., Manwaring, E. A., Moss, F. L., Sedmik, E. C. E., Vanson, J. and Young, G. A. (1972). Gosses Bluff impact structure. *Science* 175:1199-2007.
- Moore, H. J. (1971). Large blocks around lunar craters. In *Analysis of Apollo 10 photography and visual observations*, pp. 26-27. NASA-SP 232, Washington, D. C.
- Moore, J. and Malin. M. (1988). Dome craters on Ganymede. *Geophys. Res. Let.* 15:225-228.
- Moore, J.M., Horner, V. M., and Greeley, R. (1985). The geomorphology of Rhea. *Proceedings, Lunar Planet. Sci. 15<sup>th</sup> Conf. J. Geophys. Res.* 90:C785-C795.
- Jeffrey M. Moore, Erik Asphaug, Robert J. Sullivan, James E. Klemaszewski, Kelly C. Bender, Ronald Greeley, Paul E. Geissler, Alfred S. McEwen, Elizabeth P. Turtle, Cynthia B. Phillips, B. Randy Tufts, James W. Head III, Robert T. Pappalardo, Kevin B. Jones, Clark R. Chapman, Michael J. S. Belton, Randolph L. Kirk, David Morrison. (1998). Large impact features on Europa: results of the Galileo nominal mission. *Icarus* 135:127-145.
- Moore, J.M., Asphaug, E., Belton, M.J.S., Bierhaus, B., Breneman, H.H., Brooks, S.M., Chapman, C.R., Chuang, F.C., Collins, G.C., Giese, B., Greeley, R., Head J.W., III, Kadel, S., Klaasen, K.P., Klemaszewski, J.E., Magee, K.P., Moreau, J., Morrison, D., Neukum, G., Pappalardo, R.T., Phillips, C.B., Schenk, P.M., Senske, D.A., Sullivan, R.J., Turtle, E.P., and Williams K.K. (2001). Impact features on Europa: Results of the Galileo Europa Mission (GEM). *Icarus.* 151:93-111.
- Moore, J. M., Schenk, P.M., Bruesch, L. S., Asphaug, E., McKinnon, W. B., (2004). Large impact features on middle-sized icy satellites. *Icarus*, 171:421-443.

- Morgan, J. V. and Warner, M. (1999). Morphology of the Chicxulub impact: Peak-ring crater or multi-ring basin? In *Large Meteorite Impacts and Planetary Evolution ii*. Edited by Dressler, B. O. and Sharpton, V. L. pp. 281-290.
- Morgan, J. V., Warner, M. R., Collins, G. S., Melosh, H. J., and Christenson, G. L. (2000). Peak-ring formation in large impact craters: Geophysical constraints from Chicxulub. *Earth Planet. Sci. Lett.* 193:347-354.
- Murray, J. B. (1979). Oscillating peak model of basin and crater formation. *Earth, Moon and Planets.* 22(3):269-291.
- Nimmo, F. and Manga, N. (2002). Causes, characteristics and consequences of convective diapirism on Europa. *Geophys. Res. Lett.* 29:2109.
- Nimmo, F., Giese, B. and Pappalardo, R. (2003). Estimates of Europa's ice shell thickness from elastically supported topography. *Lunar and Planet. Sci. Conf. Abs.* 1296.
- Nolan, M., Asphaug, E., Melosh, H. J., and Greenberg, R. (1996). Impact craters on asteroids: does strength or gravity control their size? *Earth and Planetary Sci. Lett.*, 183:347-354.
- O'Keefe, J. D. and Ahrens, T. J. (1982). Cometary and meteorite swarm impact on planetary surfaces. *J. Geophys. Res.* 87:6668-6680.
- O'Keefe, J. D. and Ahrens, T. J. (1993). Planetary cratering mechanics. *J. Geophys. Res.* 98:17001-17028.
- O'Keefe, J. D. and Ahrens, T. J. (1999). Complex craters: Relationship of stratigraphy and rings to impact conditions. *J. Geophys. Res.* 104:27091-27104.
- Ohnaka M (1995) A shear failure strength law of rock in the brittle-plastic transition regime. *Geophysical Research Letters* 22: 25-28
- Pappalardo, R. T. (1999). Ganymede and Callisto. Pp. 263-275. In *The New Solar System*, 4<sup>th</sup> ed. Edited by J. K. Beatty, C.C. Petersen and A. Chaikin. Cambridge University Press.

- Pappalardo, R. T. and Sullivan, R. J. (1996). Evidence for Separation across a Gray Band on Europa. *Icarus* 123:557-567.
- Pappalardo, R. T., Head, J. W., Greeley, R., Sullivan, R. J., Pilcher, C., Schubert, G., Moore, W. B., Carr, M. H., Moore, J. M., Belton, J. S. and Goldsby, D. L. (1998). Geological evidence for solid-state convection in Europa's ice shell. *Nature* 391:365-368.
- Parmetier, R. T. and Head, J. (1981). Viscous relaxation of impact craters in icy planetary surfaces: determination of viscosity variation with depth, *Icarus* 47:100-111.
- Passey, Q. R. (1982). Viscosity structure of the lithospheres of Ganymede, Callisto, and Enceladus, and of the Earth's mantle. Ph.D. Thesis. Calif. Inst. Technol. Pasadena. USA.
- Passey, Q. R. and Shoemaker, E. M. (1982). Craters and basins on Ganymede and Callisto: Morphological indicators of crustal evolution. In *Satellites of Jupiter*, edited by Morrison, D. Tucson: Univ. of Arizona Press. pp. 340-378.
- Pater, I. and Lissauer, J. (2001). *Planetary Sciences*. Cambridge University Press.
- Peale, S.J., and Lee, M. H. (2002). A primordial origin of the Laplace relation among the Galilean satellites. *Science* 298:593-597.
- Pearce, S. J. and Melosh, H. J. (1986). Terrace width variations in complex lunar craters. *Geophys. Res. Lett.* 13:1419-1422.
- Pierazzo E. and Melosh, H. J. (2000a). Understanding oblique impacts from experiments, observations, and modeling. *Ann. Rev. Earth Planet. Sci.* 28:141-167
- Pierazzo E. and Melosh, H. J. (2000b). Melt production in oblique impacts. *Icarus* 145:252-261.
- Pierazzo, E., Vickery, A. M., and Melosh, H. J. (1997). A reevaluation of impact melt production. *Icarus*. 127:408-423.
- Pierazzo, E., Artemieva, N. A., Baldwin, E. C., Cazamias, J., Coker, R. F., Collins, G. S., Crawford, D. A., Davison, T., Holsapple, K. A., Housen, K. R., Korycansky, D. G., and

- Wünnemann, K. (2008). The Impact Hydrocode Benchmark and Validation Project: Results of Validation. 39<sup>th</sup> Lunar Planet. Sci. Conf. Abs. 1391.
- Pierazzo, E. and Collins, G. (2004). A brief introduction to hydrocode modelling, in Cratering in Marine Environments and on Ice. Springer Verlag Berlin Heidelberg, Dypvik, D., Burchell, M. and Claeys, P. eds. pp. 323-340.
- Pike, R. J. (1976). Crater dimensions from Apollo data and supplemental sources. *The Moon*. 15:463-477.
- Pike, R. J. (1977). Size-dependence in the shape of fresh impact craters on the moon. In Impact and explosion cratering, edited by Roddy, D.J., Pepin, R. O., and Merrill, R. B. New York: Pergamon Press. pp 489-509.
- Pike, R. J. (1980). Formation of complex impact craters: Mars. *Icarus*. 43:1-19.
- Pike, R. J. (1985). Some morphologic systematics of complex impact structures. *Meteoritics* 20:49-68.
- Pike, R. J. (1988). Geomorphology of impact craters on Mercury. In Mercury, edited by Vilas, F., Chapman, C., and Matthews, M, Tucson:Univ. Ariz. Press. pp. 165-273
- Pilkington, M., Hildebrand, A.R. and Ortiz-Aleman, C. 1994. Gravity and magnetic-field modeling and structure of the Chicxulub crater, Mexico. *J. Geophys. Res.* 99:13147-13162.
- Pistorius, C. W. F. T., Pistorius, M. C., Blakeley, J. P. and Admiraal, L. J. (1963). Melting curve of ice VII to 200 kbar. *J. Chem. Phys.* 38:600-602.
- Quaide, W. L. and Oberbeck, V. R. (1968). Thickness determinations of the lunar surface layer from lunar impact craters. *J. Geophys. Res.* 73:5247-5270.
- Reimold, W. U., Cooper, G.R.J., Romano, R., Cowan, D. and Koeberl, C. (2004). A SRTM investigation of Serra Da Cangalho Impact structure, Brazil. *Proc. Lunar and Planet. Sci. Conf. Abs.* #1232.

- Rist, M. A. and Murrell S. A. F. (1994). Ice triaxial deformation and fracture. *J. Glaciology*. 40:305-318.
- Roddy D. J., Boyce J. M., Colton G. W., and Dial A. L. (1975). Meteor Crater, Arizona, rim drilling with thickness, structural uplift, diameter, depth, volume, and mass-balance calculations. *Proc. Lunar Sci. Conf.* 6:2621-2644.
- Ruiz, J., Alvarez-Gomez, J. A., Tejero, R. and Sanchez, N. (2007). Heat flow and thickness of a convective ice shell on Europa for grain size-dependent rheologies. *Icarus*. 190:145-154.
- Schenk, P. M. (1989). Crater formation and modification on the icy satellites of Uranus and Saturn: Depth/diameter and central peak occurrence. *J. Geophys. Res.* 94:3813–3832.
- Schenk, P. M. (1991). Ganymede and Callisto: Complex crater formation and planetary crusts. *J. Geophys. Res.* 96:15635-15664.
- Schenk, P. M. (1993). Central pit and dome craters: Exposing the interiors of Ganymede and Callisto. *J. Geophys. Res.* 98:7475-7498.
- Schenk, P. M. (2002). Thickness constraints on the icy shells of the Galilean satellites from a comparison of crater shapes. *Nature*. 417:419-421.
- Schenk, P. M. and McKinnon, W. B. (1991). Dark ray and dark floor craters on Ganymede and the provenances of large impactors in the Jovian system. *Icarus*. 89:318-346.
- Schenk, P.M., and Bulmer, M. H. (1998). Origin of mountains on Io by thrust faulting and large-scale mass movements. *Science* 279:1514-1518.
- Schenk, P. M. and Moore, J. M. (2004). High-resolution mapping of Europa's impact craters: comparison with Ganymede. *Europa's Icy Shell Workshop. Abstract #7051.*
- Schenk, P. M and Moore, J. M. In prep. Large impact craters and palimpsests on large icy satellites: Ganymede and Callisto.

- Schenk, P., McEwen, A., Davies, A., Davenport, T. and Jones, K. (1997). Geology and topography of Ra Patera, Io, in the Voyager era: Prelude to eruption. *Geophys. Res. Lett.* 24:2467-2470.
- Schenk, P., McKinnon, W. B., Gwynn, D. and Moore, J. M. (2001). Flooding of Ganymede's bright terrains by low-viscosity water-ice lavas. *Nature* 410:57-60.
- Schenk, P. M., Wilson, R. R., and Davies, A. G. (2004). Shield volcano topography and rheology of lava flows on Io. *Icarus*. 169:98-110.
- Schmidt, R.M. and Housen, K.R. (1987). Some recent advances in the scaling of impact and explosion cratering. *Int. J. Impact Eng.* 5:543-560.
- Schultz, P. H. (1992). Atmospheric effects on ejecta emplacement and crater formation on Venus from Magellan. *J. Geophys. Res.* 97:16,183-16,248.
- Seed, H. B. and Goodman, R. E. (1964). Earthquake stability of cohesionless soils. *J. of the Soil Mechanics and Foundation Division*. 90 (SM6), ASCE, 4128.
- Shoemaker, E. M. (1963). Impact mechanics at Meteor Crater, Arizona. Middlehurst, B.M. and Kuiper, G.P., eds., *The Moon, Meteorites and Comets*, University of Chicago Press, Chicago.
- Shoemaker, E. M., Lucchitta, B. K., Plescia, J. B., Squyres, S. W. and Wilhelms, D. E. (1982). The geology of Ganymede. In *Satellites of Jupiter*, edited by Morrison, D. Tucson:Univ. of Arizona Press. pp. 435-520.
- Showman, A. P., Mosquera, I., and Head, J. W. (2004). On the resurfacing of Ganymede by liquid-water volcanism. *Icarus*. 172:625-640.
- Shrine, R. G., Burchell, M. J. and Grey, I. D. S. (2002). Velocity scaling of impact craters in water ice over the range 1 to 7.3 km s<sup>-1</sup>. *Icarus*. 155:475-485.
- Smith, E. I. (1976). Comparison of the crater morphology-size relationship for Mars, Moon and Mercury. *Icarus* 28:543-550.

- Sotin, C. and Tobie, G. (2004). Internal structure and dynamics of the large icy satellites. *Comptes Rendus Physique* 5(7):769-780.
- Spray, J. and Thompson, L. (1995). Friction melt distribution in a multi-ring impact basin. *Nature*. 373:130-132.
- Spudis, P. D., Hawke, B. R. and Lucey, P. (1984). Composition of Orientale basin deposits and implications for the lunar basin-forming process. *Proc. Lunar Planet. Sci. Conf. 15th, Part 1, J. Geophys. Res.* 89:197-210.
- Squyres, S. W. and Veveřka, J. (1981). Voyager photometry of surface features on Ganymede and Callisto. *Icarus* 46:137–155.
- Stewart, S.T., and Ahrens, T.J. (2005). Shock properties of H<sub>2</sub>O ice. *J. Geophys. Res.* 110, E03005, doi:10.1029/2004JE002305.
- Therriault, A.M., Grieve, R.A.F. and Reimold, W.U. (1997). Original size of the Vredefort Structure: implications for the geological evolution of the Witwatersrand Basin. *Meteoritics Planet. Sci.* 32:71–77
- Thompson, S. L. and Lauson, H.S. (1972). Improvements in the Chart-D radiation–hydrodynamic code III: Revised analytic equations of state. Tech. Rep. SC-RR-71 0714, Sandia National Laboratories.
- Tillotson, J. M. (1962). Metallic equation of state for hypervelocity impact. General Atomic Report GA-3216. Advanced Research Project Agency, San Diego, pp. 141.
- Tornabene, L.L., McEwen, A.S., Osinski, G.R., Mouginiš-Mark, P.J., Boyce, J.M., Williams, R.M.E., Wray, J.J., Grant, J.A., and the HiRISE Team. (2007). Impact melting and the role of subsurface volatiles: Implications for the formation of valley networks and phyllosilicate-rich lithologies on early Mars. In: *Seventh International Conference on Mars*. Abstract #3288
- Turcotte, D.L. and Schubert, G. (1982). *Geodynamics: applications of continuum physics to geological problems*. Wiley, New York.

- Turtle, E. P. and Pierazzo, E. (2001). Thickness of a European ice shell from impact crater simulations. *Science*. 294:1326-1328.
- Weertman, J. and Weertman, J. R. (1975). High temperature creep of rock and mantle viscosity. *Ann. Rev. Earth Planet. Sci.* 3:293-315.
- Weiss, J. and Schulson, E. M. (1995). The failure of fresh-water granular ice under multi-axial compressive loading. *Acta Metall. Mater.* 43:2303-2315.
- Wetherill, G.W. (1971). Cometary versus asteroidal origin of chondritic meteorites. In *Physical studies of minor planets*, edited by Gehrels, T. NASA SP-267. pp. 447-460.
- Wieczorek, M. A. and Phillips, R. J. (1999). Lunar multi-ring basins and the cratering process. *Icarus* 139:246-259.
- Wilson, L., Brown, M. A., Parmentier, E. M., and Head, J. W. (1983). 14<sup>th</sup> Lunar Planet. Sci. Conf. Abs. #849.
- Wood, C. A. (1973). Central peak heights and crater origins. *Icarus*. 20:503.
- Wood, C. A. (1980). Martian double-ring basins: new observations. 11<sup>th</sup> Lunar Planet. Sci. Conf. pp. 2221-2241.
- Wood, C.A. and Head, J. W. (1976). Comparison of impact basins on Mercury, Mars and the Moon. *Proc. Lunar Planet. Sci. Conf.* 7:3629-3651.
- Wood, C. A. and Anderson, L. (1978). New morphometric data for fresh lunar craters. 9<sup>th</sup> Lunar Planet. Sci. Conf. pp. 3669-3689.
- Wood, C. A., Head, J. W., and Cintala, M. J. (1978). Interior morphology of fresh Martian craters: the effects of target characteristics. 9<sup>th</sup> Lunar Planet. Sci. Conf. pp. 3691-3709.
- Worthington, A. M. (1963). *A study of splashes*. New York: MacMillan.

- Wünnemann K. and Ivanov B. A. (2003). Numerical modelling of impact crater depth-diameter dependence in an acoustically fluidized target. *Planetary and Space Science*. 51:831-845.
- Wünnemann, K., Morgan, J., and Jodicke, H. (2005). Is Ries crater typical for its size? An analysis based upon old and new geophysical data and numerical modelling. In *Large Meteorite Impacts III*, Edited by Kenkmann, T., Horz, F., and Deutsch, A. Boulder, Co, USA. The Geological Society of America. pp 67 – 84.
- Wünnemann, K., Collins, G. S., and Melosh, H. J. (2006). A strain-based porosity model for use in hydrocode simulations of impacts and implications for transient-crater growth in porous targets. *Icarus*. 180:514-527.
- Zahnle, K., Dones, L., and Levison, H. F. (1998). Cratering rates on the Galilean satellites. *Icarus*. 136:202-222.
- Zimmer, C., Khurana, K. K. and Kivelson, M. G. (2000), Subsurface Oceans on Europa and Callisto: Constraints from Galileo Magnetometer Observations. *Icarus* 147:329-347.